REPORT DOCUMENTATION PAGE	*Form Approved* *OMB No. 0704-0188*

1. REPORT DATE *(DD-MM-YYYY)* 21-05-2012	**2. REPORT TYPE** Final Technical Report	**3. DATES COVERED** *(From - To)* From 12/01/2009 to 03/31/2012

4. TITLE AND SUBTITLE
Dynamics-based Nondestructive Structural Monitoring Techniques

5a. CONTRACT NUMBER
FA9550-10-C-0020

5b. GRANT NUMBER

5c. PROGRAM ELEMENT NUMBER

6. AUTHOR(S)
Michael J. Aviol
Fei Yan
Joseph L. Rose

5d. PROJECT NUMBER

5e. TASK NUMBER

5f. WORK UNIT NUMBER

7. PERFORMING ORGANIZATION NAME(S) AND ADDRESS(ES)
FBS, Inc.
3340 West College Ave
State College, PA 16801-2503

8. PERFORMING ORGANIZATION REPORT NUMBER

9. SPONSORING/MONITORING AGENCY NAME(S) AND ADDRESS(ES)
Air Force Office of Scientific Research Aerospace, Chemical, and Material Sciences
875 N. Randolph Street
Suite 325, Room 3112
Arlington VA, 22203-1768

10. SPONSOR/MONITOR'S ACRONYM(S)

11. SPONSOR/MONITOR'S REPORT NUMBER(S)

12. DISTRIBUTION/AVAILABILITY STATEMENT
Approved for public release; distribution is unlimited

13. SUPPLEMENTARY NOTES

14. ABSTRACT

A novel Ultrasonic Modal Analysis Technique (UMAT) capable of damage detection in 3-dimensional, non-homogeneous, anisotropic structures based on ultrasonic vibration signatures was developed and implemented into a portable inspection system. The system contains an annular array actuator that is capable of providing various guided wave modes and frequencies as the loading functions to achieve high sensitivity to different defects. An analytical theory on guided wave excitations by annular arrays with/without time delays was developed. The theory can be applied for optimizing annular array designs for UMAT and also conventional transient ultrasonic guided wave applications. Key experiments were conducted on different test samples including realistic aircraft composite structures to demonstrate the high damage detection sensitivity of UMAT as well as its capability of damage differentiation.

15. SUBJECT TERMS

16. SECURITY CLASSIFICATION OF:			**17. LIMITATION OF ABSTRACT**	**18. NUMBER OF PAGES**	**19a. NAME OF RESPONSIBLE PERSON**
a. REPORT	**b. ABSTRACT**	**c. THIS PAGE**			Michael J. Avioli
U	U	U	UU	183	**19b. TELEPHONE NUMBER** *(Include area code)* 8142343437

Reset

Final Report

For

Dynamics-based Nondestructive Structural Monitoring Techniques
Contract # FA9550-10-C-0020

Submitted to

Civ USAF AFMC AFOSR/NA

Attn: David Stargel
Structural Mechanics program manager
Air Force Office of Scientific Research (AFOSR)
875 N. Randolph St., Arlington, VA 22203

david.stargel@afosr.af.mil

By

FBS, Inc.
Michael J. Avioli / Fei Yan
3340 West College Ave
State College, PA 16801-2503
Mavioli@fbsworldwide.com
Fyan@fbsworldwide.com

Pennsylvania State University
Joseph L. Rose
411E EES Building
University Park, PA 16801
jlresm@engr.psu.edu

On

May 21, 2012

Table of contents

1. Summary:

A novel Ultrasonic Modal Analysis Technique (UMAT) capable of damage detection in 3-dimensional, non-homogeneous, anisotropic structures based on ultrasonic vibration signatures was developed and implemented into a portable inspection system. The system contains an annular array actuator that is capable of providing various guided wave modes and frequencies as the loading functions to achieve high sensitivity to different defects. An analytical theory on guided wave excitations by annular arrays with/without time delays was developed. The theory can be applied for optimizing annular array designs for UMAT and also conventional transient ultrasonic guided wave applications. A guided wave mode expansion method was developed to study the connections between transient guided wave propagations and steady-state vibrations. It was shown that steady-state vibrations can be decomposed into superposition of guided waves propagating in different directions. The interferences of the guided waves form the steady-state vibration patterns. It was also shown that by applying specific guided wave modes and frequencies, the vibration modes that are tightly associated with the guided wave mode and frequency inputs can be efficiently excited. Therefore, via annular array actuators, different guided wave loading functions can be used to excite different ultrasonic vibration modes for damage detection. Due to the fact that different vibration modes are sensitive to different damage types, it is therefore possible to achieve high sensitivity to different damage types by varying the guided wave loading functions. It is also feasible to differentiate different damage types. The control hardware for the UMAT system was designed for both UMAT and transient guided wave applications. To drive annular array actuators, the hardware outputs up to 8 channel tone-burst or sine signals with controlled phase shifts among the channels. An 8 channel A/D card is included in the system to receive ultrasonic vibration or transient guided wave signals. The hardware system is controlled by a laptop. Control software with a user-friendly interface was developed. Key experiments were conducted on different test samples including realistic aircraft composite structures to demonstrate the high damage detection sensitivity of UMAT as well as its capability of damage differentiation.

2. Ultrasonic Guided Wave Vibration Theory

Ultrasonic guided wave inspection techniques are a powerful tool in the practice of non-destructive evaluation (NDE) and structural health monitoring (SHM). Guided wave techniques have several advantages over conventional bulk wave ultrasonic NDE/SHM techniques. Some of these advantages are outlined in Table I. However, in addition to the advantages of guided waves comes an inherent complexity beyond that of bulk wave mechanics. Fortunately, this complexity can be used to one's advantage if the guided wave mechanics are thoroughly understood and appropriately utilized.

Table I *Some of the benefits of guided waves as compared to bulk wave*

Benefits of Guided Waves over Bulk Wave Inspection Techniques	
Guided Wave	*Bulk Wave*
Line scan	Single-point scan
Full structural coverage	Local structural coverage
Faster inspection	Slower inspection
Long inspection distance	Short inspection distance
Numerous possible modes	Very limited modes
Ability to inspect hidden structures	Require direct inspection access

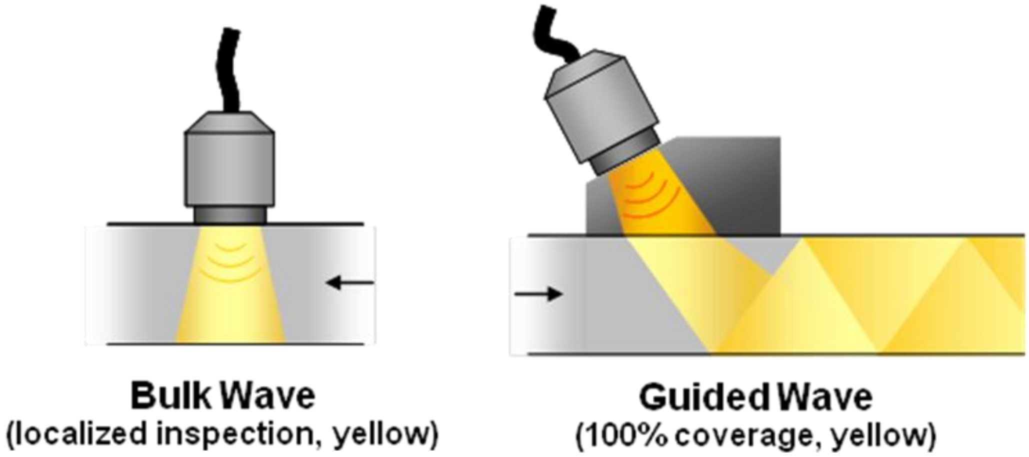

Fig. 1 Illustration of bulk wave (left) propagation and guided wave (right) propagation in a plate.

While there exist only three different modes (one longitudinal and two shear) in bulk wave ultrasonics, there are an infinite number of modes for guided waves. This means that there are theoretically an infinite number of different mode-frequency combinations and thus an infinite number of wave structures possible in a guided wave.

In reality, the frequency range of interest is limited by our ability to design transducers, the size of the defects to be detected, and the attenuation properties of the material. We are also limited by which guided wave modes we can realistically activate. Even with these limitations, there exists a plethora of options for designing a guided wave inspection system. It is up to the engineer to choose the optimal mode-frequency combinations for the task at hand, and the consequences of mode-frequency selection can often determine the success (or failure) of the system. While there are a number of factors that go into guided wave mode-frequency selection, including penetration power, excitability, etc., wavestructure plays a primary role in terms of defect detection sensitivity. Optimal wavestructure selection is dependent upon choosing the appropriate mode-frequency combination and being able to excite the selected point on the dispersion curve.

The development of UMAT seeks the feasibility of applying modal analysis to high frequency vibrations introduced by controlled ultrasonic guided wave inputs. In a UMAT test, modal analyses are applied to the long time structural responses to a specifically defined ultrasonic guided wave input. Thanks to the fact that the long time structural responses result from multiple reflections and scatterings of the input guided wave energy, an overall coverage of the structure can be reached from a very small number of test positions. In Phase I of this project, we have demonstrated in experiments that the forced vibration of a structure is a function of the ultrasonic guided wave mode and frequency that is applied as the vibration loading function [1]. By selecting an appropriate mode and frequency based on the guided wave sensitivity to a specific defect type, we have shown that excellent sensitivity can be achieved for the defect type. It is therefore possible to obtain good sensitivities to all different kinds of defects by varying the input guided wave modes and frequencies. Various guided wave transducers including angle beam transducers, electromagnetic acoustic transducers (EMATs), and piezoelectric comb transducers are available for guided wave mode and frequency control [2, 3]. In this project, time delay annular array transducers are employed as the UMAT actuator. The main advantages of using such actuators are their omni-directional guided wave excitation and the capability of automatic mode and frequency tuning through electrical time delay circuits. A theoretical model was developed for studying guided wave excitation spectra of annular array type actuators. Based on the theoretical understanding, phased annular array transducers were developed as a powerful tool for guided wave mode and frequency control.

The new UMAT approach is expected to bridge together conventional low frequency vibration methods with high frequency guided wave methods. It is an objective of the project to keep the benefits of both methods in the new UMAT approach while overcoming the disadvantages of the two different technologies. More particularly, the high defect detection sensitivity of guided wave methods and the fast and complete coverage of vibration tests with small numbers of accessible positions are to be combined in the UMAT approach. One basic hypothesis of UMAT is that the long time structural response depends on the initial ultrasonic loading functions (guided wave modes and frequencies). Furthermore, a vibration mode decomposition method was also developed to assess the defect sensitivity of plate vibration modes by the same transverse wave structure analysis approach that has proved to be successful for transient guided waves. It was demonstrated that vibration modes can be decomposed into a superposition of guided waves traveling in different directions. The vibration resonances that are associated with certain guided wave modes may preserve the defect sensitivity of the guided wave modes. Such theoretical findings therefore validate the basic hypothesis of UMAT and can serve as the theoretical foundation of the UMAT development.

2.1 Guided Wave Excitation by an Annular Array

2.1.1 Introduction

A number of guided wave transducers are available for mode and frequency control, including angle beam transducers, piezoelectric comb transducers, electromagnetic acoustic (EMATs), and magnetostrictive transducers. Through a selection of an incident angle, an angle beam transducer excites and receives guided waves with a phase velocity determined by Snell's law. The mode selection capability of an angle beam transducer can thus be described by a straight horizontal line in the phase velocity dispersion curve space [4]. Mode and frequency selections of piezoelectric comb transducers, EMATs, and magnetostrictive transducers are typically realized through wavelength matches. All three types of transducers can be made with multiple rectangular elements equally spaced into a comb shape. The efficiency of guided wave excitation and reception becomes optimal when the wavelengths of the guided waves match with the element spacing. In these cases, a straight line with the slope equal to the element spacing can be used to describe the mode selection capability [4]. As an effort to achieve mode and frequency tuning electronically, Li and Rose [5] demonstrated that the excitation line of a comb type transducer can be bent into curved lines by applying time delays to the comb elements. The studies on time delay comb transducers were further carried out and applied to guided wave inspections of plate structures by Yan and Rose [6]. In many guided wave applications, omnidirectional transducers or sectioned annular transducers are used to radiate guided wave energies axisymmetrically into all directions to obtain complete coverage. Following comb transducer theory, Gao, et al, designed and fabricated circular and fan-shaped PVDF transducers for SHM applications with controlled guided wave modes and frequencies [7]. Wilcox used EMATs with circular coils in a guided wave phased array application [8]. Guided wave excitation and reception of the circular EMATs were analytically investigated by Wilcox in another paper coauthored with Lowe and Cawley [9]. Point source solution for circular crest guided wave excitation in a plate was used as the basis for their analytical model. Cesnik and his colleagues have developed wedge-shaped guided wave SHM transducers with interdigital sector elements, called CLoVER [10, 11]. Guided wave excitations of the CLoVERs have been studied by them as well. Selective guided wave excitations using annular array patches were recently studied by Glushkov et al, [12]. An optimization approach was developed to maximize the energy ratio of the selected wave mode to the total guided wave excitation. Their wave excitation model was derived based on Fourier integrals of wave equations. The numerical simulation results presented in the paper showed that selective excitations of two different modes: S0 and A0 modes can be achieved by applying different amplitude factors and phase delays to the tone-burst driving signals for the five elements of an annular array.

In the course of this project, a theoretical model was developed, in analogy with the comb transducer model in reference [6], for studying guided wave excitation spectra of axisymmetric sources. It was shown that, similar to comb transducers, the amplitudes of guided wave modes excited by an axisymmetric source are also determined by two separable terms: the excitabilities of the guided wave modes and the excitation spectrum of the source. The guided wave excitabilities are the same for comb transducers and axisymmetric sources, which depend solely on the wave structures. The excitation spectrum of an axisymmetric source can be calculated from a Hankel transform of the axial source loading profile. This is different from the comb transducer cases, in which the excitation spectra are calculated from spatial Fourier transforms of the loading profiles. The excitation spectra were used to investigate guided wave excitation capability of annular array transducers. The effects of applying phase delays to the array elements were studied as well. Based on the theoretical understanding, phased annular array transducers were developed as a powerful tool for guided wave mode and frequency control in both transient guided wave and UMAT inspections.

2.1.2 Analytical Development

The excitation spectrum of a transducer array is a direct result of the spatial distribution of the loading that the array exhibits on the structure to which it is applied. Thus to develop relations for the excitation spectra of transducer arrays, the spatial loading distribution functions of the arrays must first be developed. Two general array geometries will be considered: linear comb arrays (Figure 2.1) and annular arrays (Figure 2.2). The linear comb arrays are examined in a plane strain formulation and can thus be assumed to extend to $z = \pm\infty$. The geometric parameters of these arrays are the center-to-center element spacing, s, the element width, w, and the inner radius, r_0 (for the case of an annular array), as shown in Figures 2.1 and 2.2.

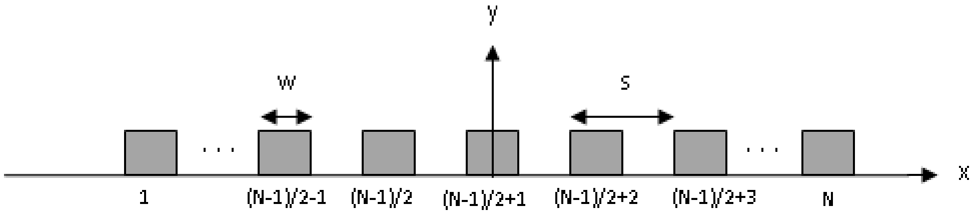

Fig. 2.1 Plane strain geometry of a generalized N-element comb array transducer with inner element width w and center-to-center spacing s.

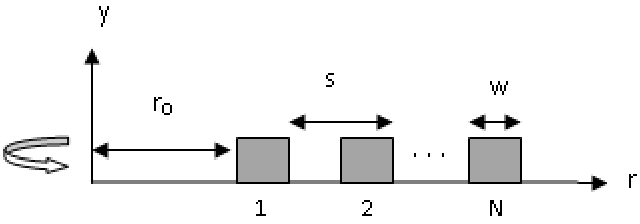

Fig. 2.2 Axisymmetric geometry of a generalized N-element annular array transducer with inner radius r_0, element width w, and center-to-center spacing s.

Assuming a piston-type loading, the spatial distribution of the load applied by the comb and annular arrays can be defined in terms of rectangle functions, denoted by $\prod_a(x)$ and $\prod_a(r)$, respectively. These rectangle functions are defined in (1), in which *a* is any positive value.

$$\prod_a(x) = \begin{cases} 1, & -a \le x \le a \\ 0, & x < -a \ \ or \ \ x > a \end{cases}, \tag{1a}$$

$$\prod_a(r) = \begin{cases} 1, & 0 \le r \le a \\ 0, & r > a \end{cases}. \tag{1b}$$

Thus the spatial loading distribution function for an *N*-element comb transducer with generalized element spacing and width parameters *s* and *w* can be described as

$$f_c(x) = \sum_{n=0}^{N-1} \prod_{w/2}(x - ns) \,. \tag{2a}$$

Similarly for an N-element annular array, the mathematical description of the spatial loading distribution function is

$$f_a(r) = \sum_{n=0}^{N-1} [\prod_w(r - ns - r_0)] \,, \tag{2b}$$

which can be written alternatively as

$$f_a(r) = \sum_{n=0}^{N-1} [H(r - ns - r_0) - H(r - ns - r_0 - w)] \,, \tag{2c}$$

in which *H(r)* is the Heaviside step function.

Array Transducer Excitation by Huygens' Principle

The development of the model for guided wave excitations by axisymmetric sources can be initialized from the understanding of the guided wave excitation of a point source applied to the surface of a plate structure. Based on previous work on point source guided wave excitations [9, 13], the guided wave surface displacement fields excited by out-of-plane point sources applied to the point ($r = 0$, $z = d/2$) or in-plane point sources applied to the same point in the $\theta = 0$ direction can be expressed as:

$$\boldsymbol{u}_\nu\left({}^{d}/_{2}\right) = \left[\boldsymbol{E}_\nu^{(3D)} \cdot (t_r\hat{\boldsymbol{e}}_r,\ t_\theta\hat{\boldsymbol{e}}_\theta,\ t_z\hat{\boldsymbol{e}}_z)^T\right]^T H_0^{(1)}(k_\nu r)e^{-i\omega t} \qquad (3)$$

where $\boldsymbol{E}_\nu^{(3D)}$ is a 3D excitability matrix for point sources [9, 13], t denotes the surface traction introduced by the point source, r, θ, and z are the three orthogonal directions in a cylinder coordinate system whose origin is located in the center of the plate, d is the plate thickness, k_ν is the wave number of the ν^{th} guided wave mode, ω is the radian frequency, and $H_0^{(1)}$ is a zero order first kind Hankel function. The 3D excitability in Eq. (3) can be calculated from the free guided wave solutions and is independent of the applied source. By combining the point source solution with the Huygen's principle, it can be shown that the far field guided wave excitations of any axisymmetric sources can be described as:

$$\boldsymbol{u}_\nu = \left\{2\sqrt{\frac{2\pi}{k_\nu r i}}\left[\boldsymbol{E}_\nu^{(3D)} \cdot (t_r\hat{\boldsymbol{e}}_r,\ t_\theta\hat{\boldsymbol{e}}_\theta,\ t_z\hat{\boldsymbol{e}}_z)^T\right]^T e^{-ik_\nu r}\right\}\left\{\int_0^\infty rf(r)J_0(k_\nu r)\,dr\right\} \qquad (4)$$

where J_0 denotes zero order first type Bessel function, and $f(r)$ is the spatial distribution of the axisymmetric source in r direction.

Eq. (4) shows that the far field guided wave displacements excited by an axisymmetric source can be expressed into a product of two terms, while the first term enclosed in the first curly bracket is dependent on the excitabilities of the guided wave modes and the second term enclosed by the second curly bracket is purely a function of the spatial distribution of the source. This is similar to the comb cases we studied earlier, in which the guided wave field solutions can also be separated into excitabilities and Fourier transforms of the spatial distributions. We have used the Fourier transforms of the spatial distributions of comb transducers to investigate the excitation spectrums of the transducers. According to Eq. (4) here, we can actually use a zero order Hankel transform to calculate the excitation spectra of annular arrays (notice that the integral included in the equation is actually a zero order Hankel transform). The Hankel transform will lead to the excitation spectra in wavenumber domain.

Wavenumber-Domain Excitation Spectrum by Spatial Fourier Transforms

To analyze the geometries of the linear comb and annular arrays in the wavenumber k domain, the spatial Fourier transforms of the respective geometry functions must be taken. For the comb array case, the Fourier transform is as follows.

$$\mathcal{F}\{f(x)\}(k) = \frac{1}{\sqrt{2\pi}}\int_{-\infty}^{\infty} f(x)e^{-ikx}dx \qquad (5)$$

Thus for the comb array geometry, let $k = k_x$, and

$$F_c(k) = \mathcal{F}\{f_c(x)\} = \frac{1}{\sqrt{2\pi}}\int_{-\infty}^{\infty}\left\{\sum_{n=0}^{N-1}\Pi_{w/2}(x - ns)\right\}e^{-ikx}dx \qquad (6)$$

However, this can be simplified by first taking the Fourier transform of a single element centered about the origin and exploiting the modulation property of the Fourier transform. Thus, by assuming constant element spacing and width, any element n can be described by combining as

$$\mathcal{F}\{f_c(x)\} = \frac{w}{\sqrt{2\pi}} \sum_{n=0}^{N-1} sinc\left(\frac{kw}{2}\right) e^{ikns} \qquad (7)$$

Thus equation (7) is the spatial Fourier transform of the geometry function of the N-element comb array.

To describe the excitation spectrum of the annular array, the 2-dimensional Fourier transform of the annular array geometry function must be taken. However, since the geometry function of the annular array is axisymmetric, the 2D spatial Fourier transform can be simplified as a 0^{th}-order Hankel transform.

$$F_a(k) = \mathcal{H}_0\{f_a(r)\}(k) = \int_0^\infty f_a(r) r\, J_0(kr)\, dr \qquad (8)$$

By substituting in the annular array geometry function from equation (2c), the Hankel transform becomes

$$\mathcal{H}_0\{\Pi_w(r - ns - r_0)\} = \mathcal{H}_0\{H(r - ns - r_0) - H(r - ns - r_0 - w)\} \qquad (9)$$

in which *H(r)* is the Heaviside step function. By using Bessel function integral recurrence relations and integrating each term in the summation, we find the following.

$$\mathcal{H}_0\{H(r)\} = \frac{1}{k}\, [u\, J_1(u)]|_0^\infty \qquad (10)$$

$$\mathcal{H}_0\{\Pi_w(r - ns - r0)\} = \frac{1}{k}\, [u\, J_1(u)]|_{ns+r0}^{ns+r0+w} \qquad (11)$$

Two types of annular arrays were included in our study. The arrangement shown in Figure 2.3a has the inner circle element as an "active" or non-zero element, while the configuration in Figure 2.3b has an "inactive" or zero-valued element in the center, along with an arbitrary inner radius distance r_0. These arrangements will be referred to as "active-center" and "inactive-center" geometries, respectively. Thus the 0^{th}-order Hankel transform of the inactive-center geometry function of the N-ring annular array is given in equation (12).

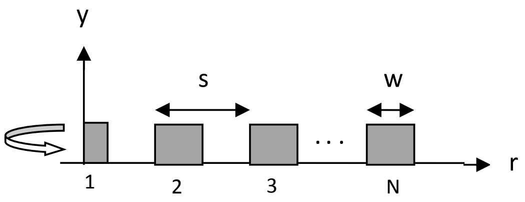

Fig. 2.3a Axisymmetric geometry of an active-center annular array.

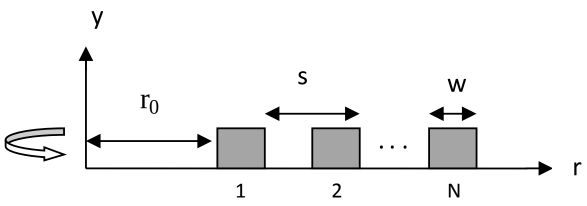

Fig. 2.3b Axisymmetric geometry of an inactive-center annular array.

$$F_{a_{inactive}}(k) = \frac{1}{k}\sum_{n=0}^{N-1}\{(r_0+ns+w)\,J_1[(r_0+ns+w)k] - (r_0+ns)\,J_1[(r_0+ns)k]\} \tag{12}$$

It can also be shown that for the case of the active-center annular array, the Hankel transform is that given in equation (13).

$$F_{a_{active}}(k) = \frac{1}{k}\left[\frac{w}{2}J_1\left[k\frac{w}{2}\right] + \sum_{n=1}^{N-1}\left\{\left(ns+\frac{w}{2}\right)J_1\left[\left(ns+\frac{w}{2}\right)k\right] - \left(ns-\frac{w}{2}\right)J_1\left[\left(ns-\frac{w}{2}\right)k\right]\right\}\right] \tag{13}$$

To convert these complex-valued k-domain functions into absolute real values, equation (14) can be invoked, in which $\tilde{F}$ denotes the complex conjugate of F.

$$\Phi(k) = |F(k)| = \sqrt[2]{F(k)\cdot\tilde{F}(k)} \tag{14}$$

Using the relation $\lambda = {}^{2\pi}/_{k}$, the functions $\Phi_c(k)$, $\Phi_a(k)$, $\Phi_c(\lambda)$, and $\Phi_a(\lambda)$ can be plotted against k and λ, respectively.

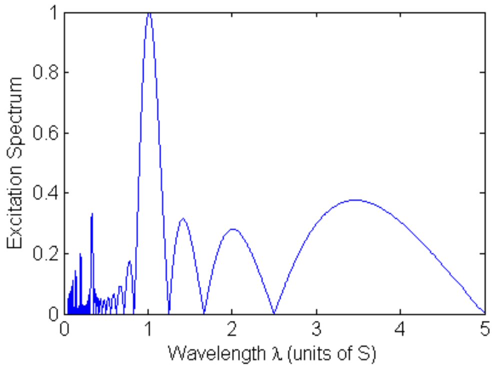

Fig. 2.4a Inactive-center annular array excitation spectrum vs. λ.

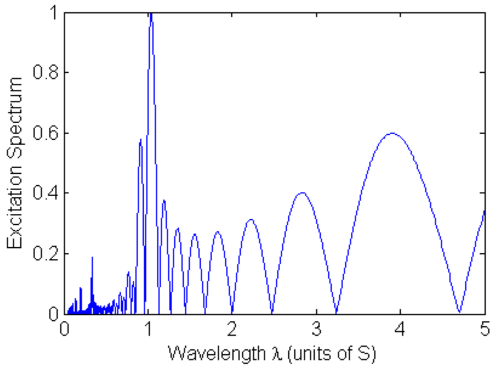

Fig. 2.4b Comb array excitation spectrum vs. λ.

As can be seen, the excitation spectrum of the comb transducer has its maximum value when the wavelength equals to the element spacing. However, it is not the case for the annular array excitation spectrum. Although the annular array can still well select the guided waves with wavelengths close to the element spacing, the excitation spectrum maximum is a little away from $\lambda = s$. In addition, for the same 3 elements in the annular array and the comb transducer, the sidelobe of the excitation spectrum appears more severe for the annular array case. This demonstrates that for active-center annular arrays, it is necessary to use the new annular array model to analytically study the guided wave excitations, rather than simply use the comb approximations.

2.1.3 Parametric Analysis of Various Annular Array Design Parameters

Various design parameters, such as number of elements (N), element spacing (s), element width (w), inner radius (r_0), and the choice of active- or inactive-center array geometry can dramatically affect the excitation spectrum of the annular array and must thus be carefully considered. Using the theoretical models developed here, we will attempt to separate and analyze the effect of each of these parameters and how they can be optimized to design an array best-suited for each purpose. Excitation spectrum features such as amplitude of the primary peak(s), peak bandwidth, sidelobe bandwidth, and others were considered as quality indicators for the parametric study.

Active- vs. Inactive-Center Arrays

The difference between an “active-center” vs. an “inactive-center” annular array was examined. Next, in Figure 2.5, is an example plot of the excitation spectra in the λ-domain for both active- and inactive-center annular arrays with $N = 3$ and $s = 2w$. Apparently, the active-center annular array, in this case, has much worse mode selection capability as compared to the inactive-center array. We have also done comparisons between the two types of annular arrays using the excitation spectrums for different element width to element spacing ratios (WSRs). The results showed that the shape of the excitation spectra is strongly affected by the choice of an active-center vs. inactive-center annular array. It was also concluded that the effective excitation bandwidth is greater for the active-center case. Thus, in most cases, inactive-center array geometry is preferred. From this point on, we will consider only inactive-center arrays.

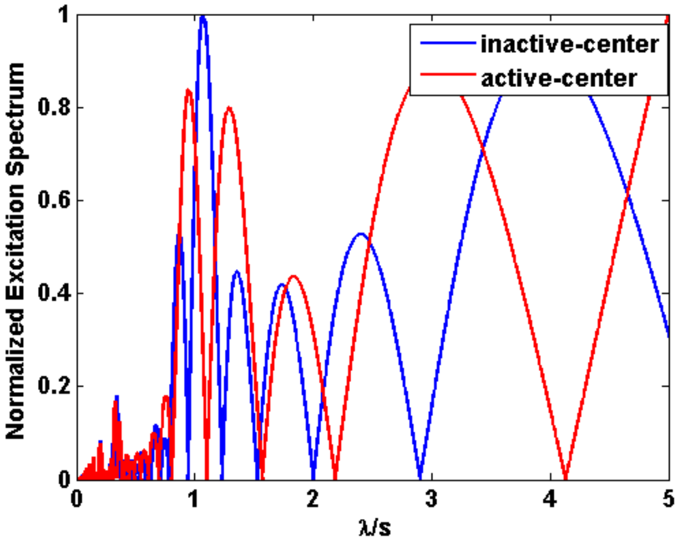

Fig. 2.5 Comparison between an inactive-center array and an active-center array; for the inactive-center array, r_0=2mm. Number of elements N=3 elements, element width w=2 mm, and spacing s=4 mm.

Inner Radius r_0

It has been shown that the inactive-center array geometry is preferable over the active-center geometry. This leaves the question of the influence of the inner radius of the array, i.e. the distance from the center of the array to the inside of the first element. For the array to be considered an inactive-center array, $r_0 > 0$. The excitation spectra for various values of r_0 are given in Figures 2.6 and 2.7 for an annular array with a WSR value of 0.5 and 5 elements. The excitation spectrum for a comb array with similar WSR and *N* values is included for comparison. There are two fundamental cases for optimizing the inner radius that must be considered. The first of which is the case in which $r_0 < s$, and the second is the case in which $r_0 > s$. Case 1 is investigated in Figure 2.6 and case 2 is investigated in Figure 2.7.

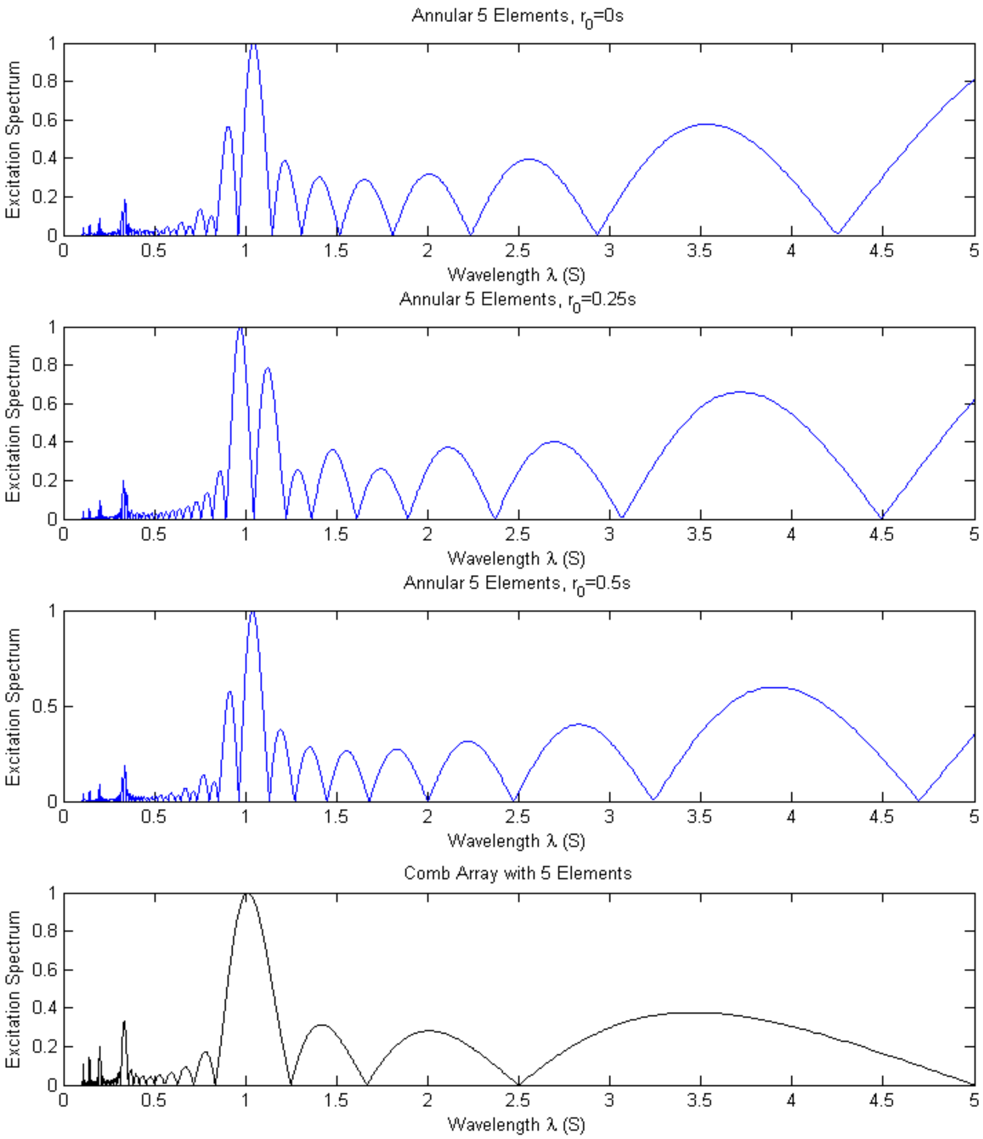

Fig. 2.6 Comparison of the excitation spectra for various values of $r_0 < s$ and N=5 elements. The bottom plot is the comb case.

In Figure 2.6 it is apparent that the case of $r_0 = 0.25s$, the ratio of the 1st-2nd peaks is undesirably larger than in the case of $r_0 = 0s$ and $r_0 = 0.5s$. The differences between the $r_0 = 0s$ and $r_0 = 0.5s$ cases is negligible, except for in the upper end of the λ-domain, in which the amplitudes are slightly lower for the $r_0 = 0.5s$ case. Figure 2.7 details the effect of an inner radius greater than 1*s*. It is apparent in Figure 2.7 that the broad envelope of the excitation spectra near the primary peak are independent of r_0, for the case in which $r_0 \gg s$. However, as r_0 increases, the number of zeros within the displayed λ range increases, and the function comes to more closely resemble the comb case with the same number of elements. Since the effective excitation in real-world applications only has a certain wavelength resolution, it can be approximated that the primary excitation peak for $r_0 = 15s$ and even $r_0 = 8s$ can be considered equivalent to the comb array case.

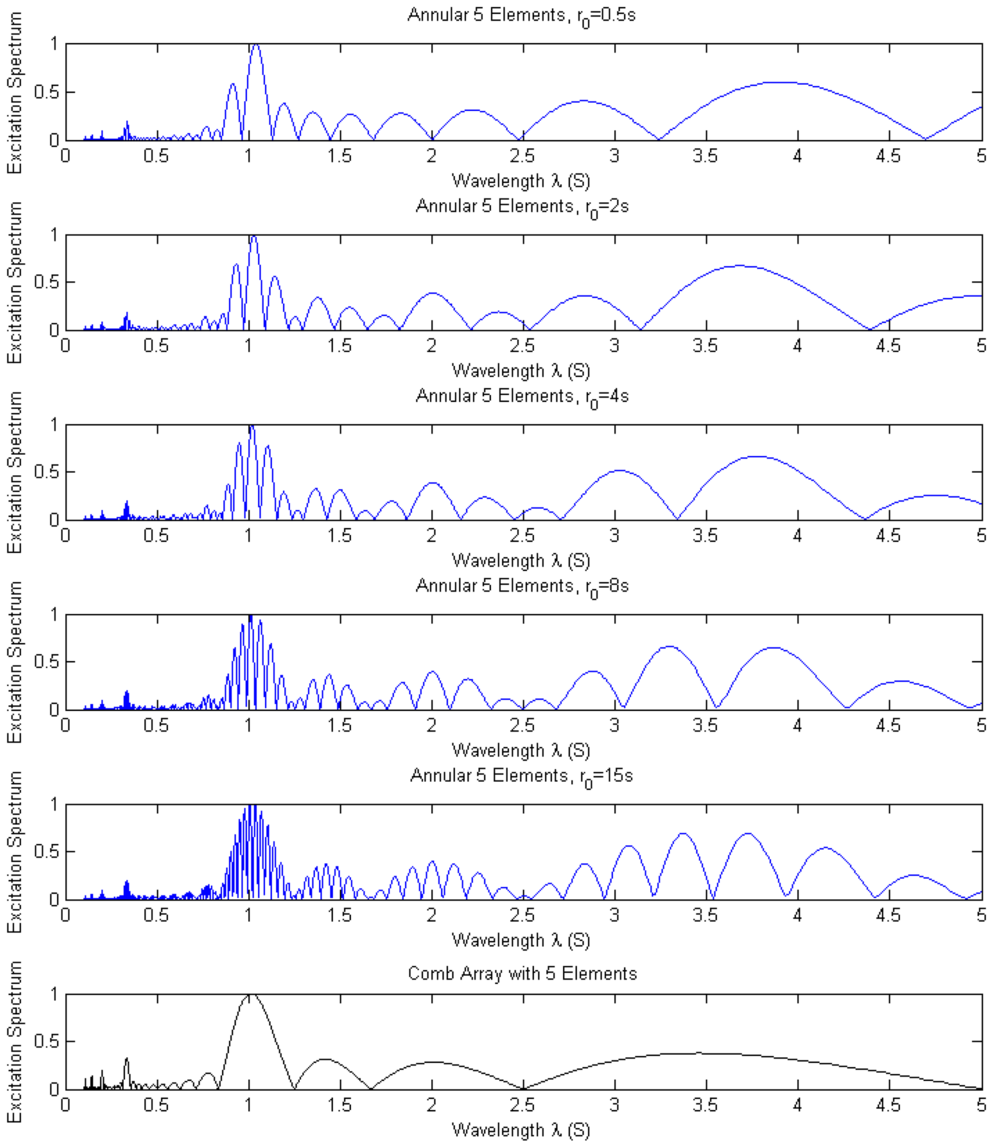

Fig. 2.7 Comparison of the excitation spectra for various values of r_0 and N=5 elements. The bottom plot is the comb case.

To perform a complete analysis on the effect of the inner radius of the annular array on the subpeaks of the primary excitation peak, Figures 2.8 and 2.9 can be studied.

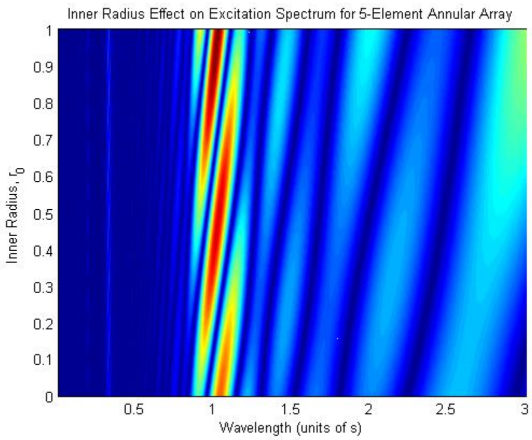

Fig. 2.8 The effect on the excitation spectrum of altering the inner radius from 0s to 1s.

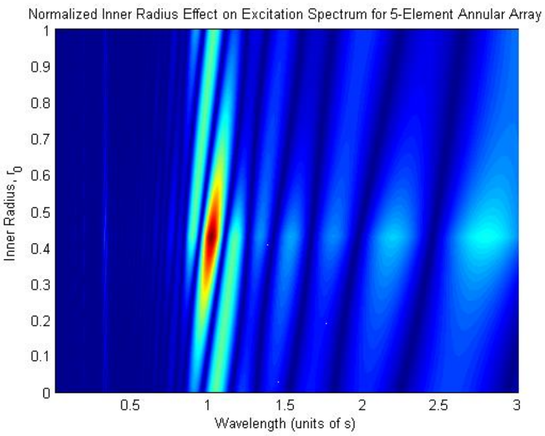

Fig. 2.9 Plot showing the critical inner radius, at which the main peak is maximized with respect to its subpeaks.

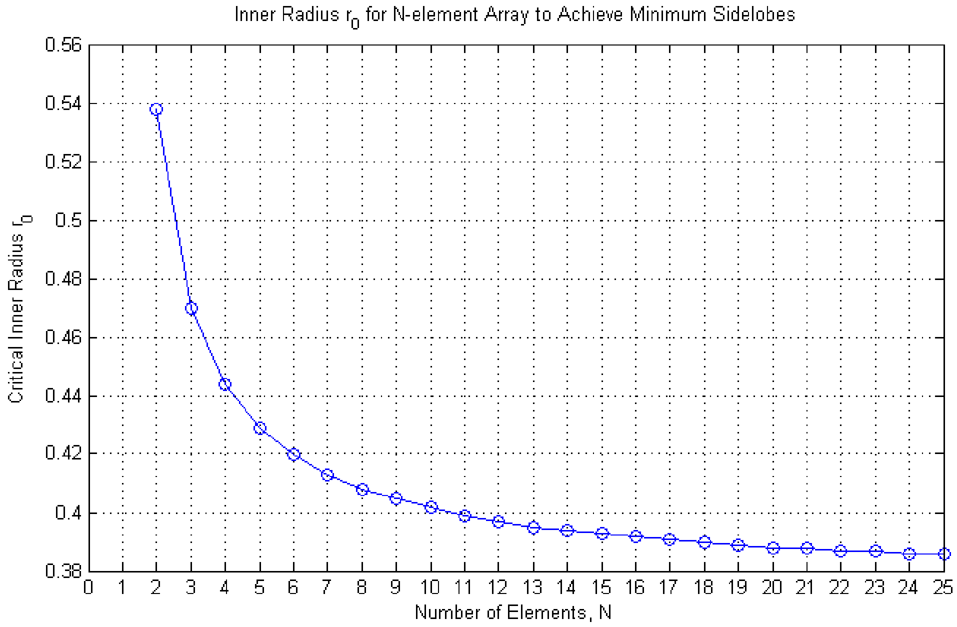

Fig. 2.10 The critical inner radius, r_c, for which the amplitudes of the subpeaks are minimized (and equal), can be found for any number of elements in an annular array.

Note that at any given value of r_0, the subpeaks are due to the adjacent angled regions of high excitation. The explicit value of the excitation increases as r_0 increases, due to the increased area of physical excitation, since a greater loaded area on the structure means greater excitation (assuming constant traction density). In order to understand the maximum value of the center peak with respect to its subpeaks for any given r_0 value, we can normalize the plot as shown in Figure 2.9 for each r_0 value. The maximum point shown corresponds to the location where the sidelobes on each side of the main peak are minimized (and equal). The example shown in Figure 2.9 is for a 5-element array. This critical r_0 value can be found for any number of elements, N, as shown in Figure 2.10.

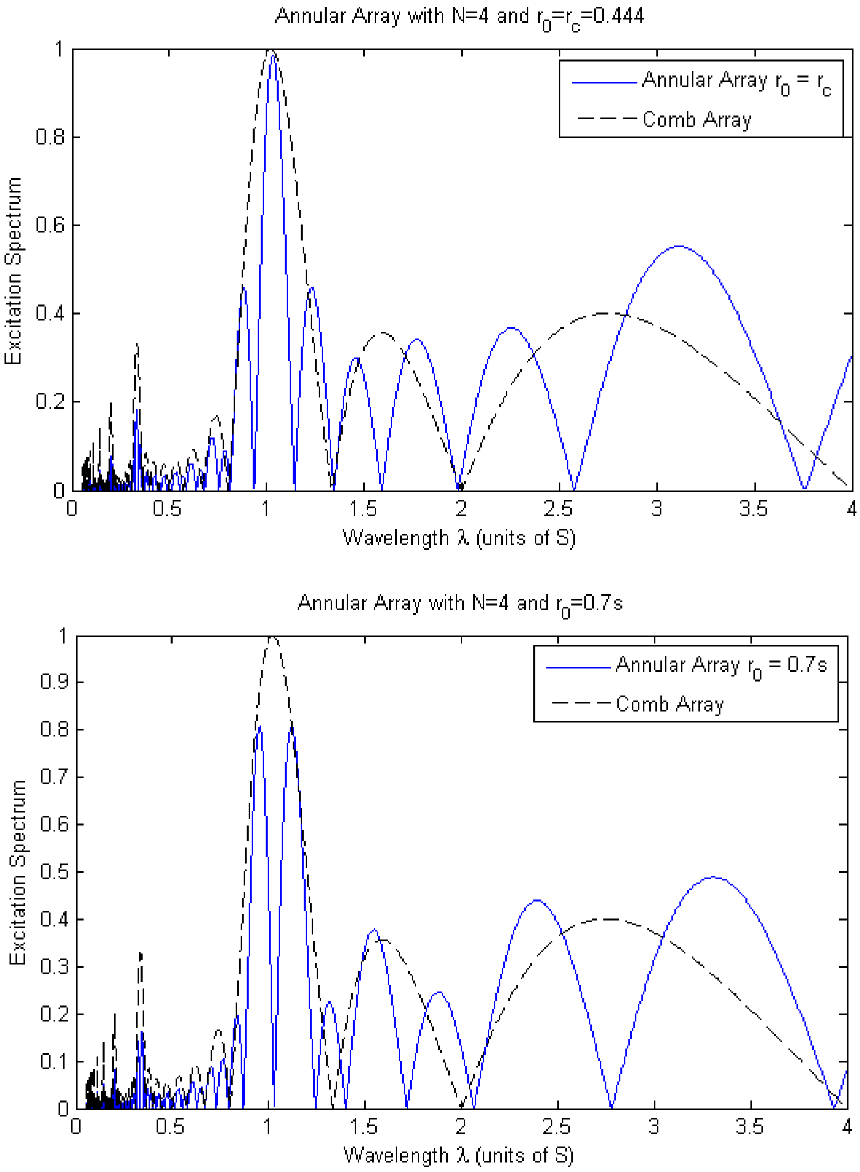

Fig. 2.11 Example of a 4-element annular array transducer with $r_0 = 0.444s = r_c$ and $r_0 = 0.7s$.

An example of the effect of choosing an inner radius equal to or far from the critical inner radius, r_c, is given in Figure 2.11. The bottom excitation spectrum is an extreme case of a poor choice for r_0 in which there is a completely split central peak of excitation. Thus it can be concluded that the optimum inner radius for a particular annular array depends on the number of elements that comprise it. To simplify further calculations, as well as to accommodate simpler array fabrication, for the remainder of this paper the 'standard' inner radius for an annular array will be taken to be 0.5s. Although this is not optimal for all number of elements, it will not greatly affect the subsequent calculations and will facilitate simpler fabrication for experiments. In practice, however, it may be ideal to optimize the inner radius using the chart in Figure 2.11 in order to suppress the subpeaks.

Element-Width-to-Spacing Ratio (WSR)

The ratio of the element width and element spacing of the arrays can be written as $\frac{w}{s}$, or WSR. This value can range from the limiting cases of 0 to 1. An array with a WSR value of 0 would have no elements at all, while an array with a WSR value of 1 will essentially be a solid. The plots in Figure 12 show the effect of WSR values from 0.1-0.9 for an annular array.

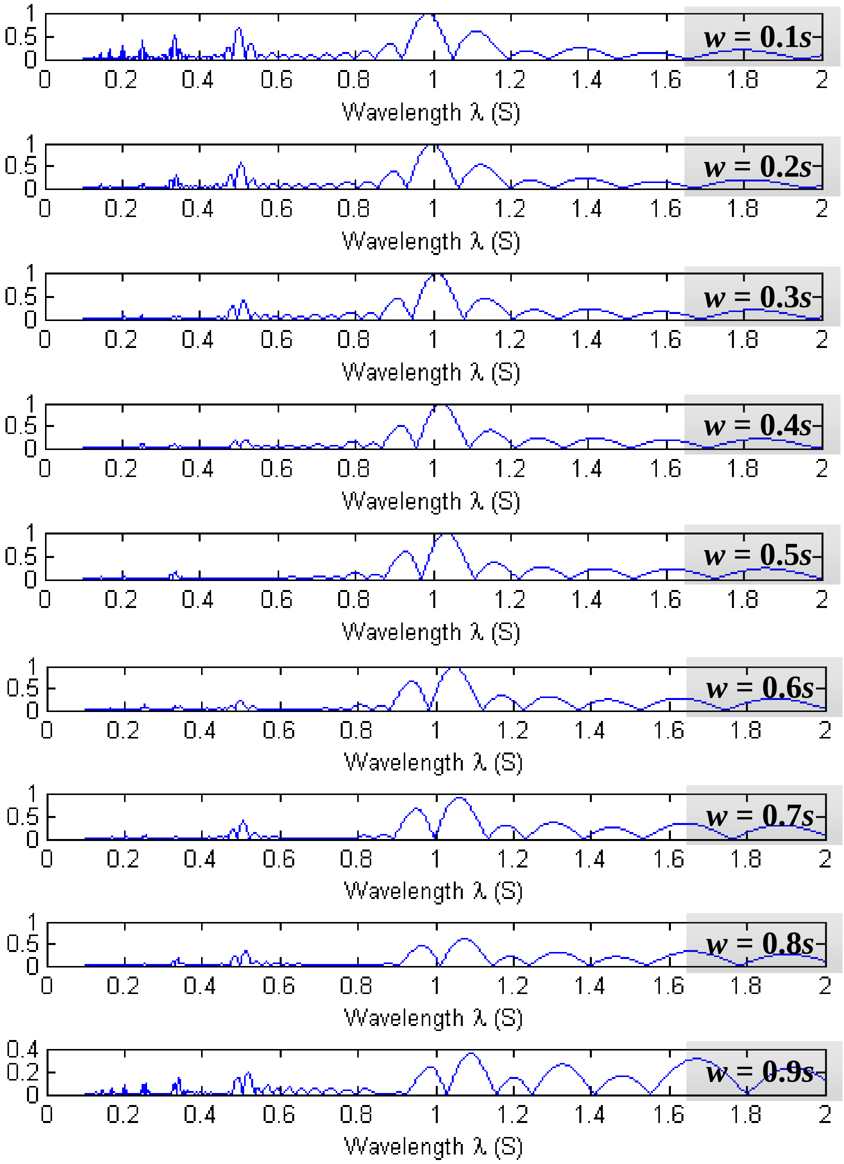

Fig. 2.12 Excitation spectra for various WSR values from 0.1-0.9 (from top to bottom) for an N = 6 annular array.

Further analysis can be performed by analyzing the amplitudes of the harmonics and sidelobes relative to the primary peak amplitude. This is done in Figures 2.13 and 2.14

below. Thus we cannot control the amplitude of all harmonics by simply varying the WSR value of the array. However, we must consider the relative importance of each of the harmonics as well as their relative amplitude to each other for various WSR cases.

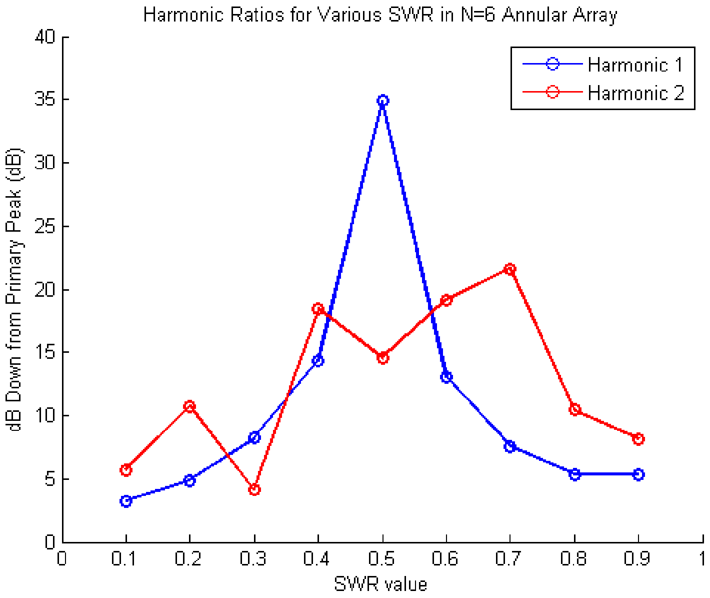

Fig. 2.13 Harmonic ratios for first and second harmonics relative to the main peak in an N=6 annular array with various WSR values.

It can be shown that, in general, the amplitude of the harmonics is significantly less for the annular array in comparison to those of a comparable comb array. Thus we will only focus on the first and second harmonics in the annular array spectra, as the other harmonics are often insignificant. Figure 2.13 shows that the behavior of the second harmonic is somewhat complex, but the amplitude of the first harmonic is clearly minimized when WSR = 0.5. For this case, the first harmonic is -35dB down from the main peak, compared to -15dB down at WSR = 0.4 or 0.6. Thus, due to the dominance of the first harmonic, we can conclude that with respect to minimizing harmonics, WSR = 0.5 or a value within this neighborhood, is ideal for the annular array. We must also analyze the size of the sidelobes, which are more substantial in the annular array case than in a comparable comb array case. Figure 2.14 shows the trend of the relative amplitudes of the sidelobes as WSR varies.

By analyzing Figure 2.14 as well as Figure 2.12, we can separate the behavior of the sidelobes into two categories. The first category is comprised of the first large sidelobe on each side of the primary peak. We will refer to these as subpeaks. The second category is comprised of all other sidelobes within each period (i.e. between harmonics). We will continue to refer to these as sidelobes. In Figure 2.12, for WSR values from 0.1 to 0.5, we can see that the primary peak and both subpeaks gradually reverse themselves symmetrically about $\lambda = s$. Then for WSR values above 0.5, the amplitude of one subpeak increases at the same rate that the other sidelobe decreases in amplitude. Thus the ideal WSR value, with respect to sidelobe and subpeak amplitude, is at WSR = 0.25 (or 0.75).

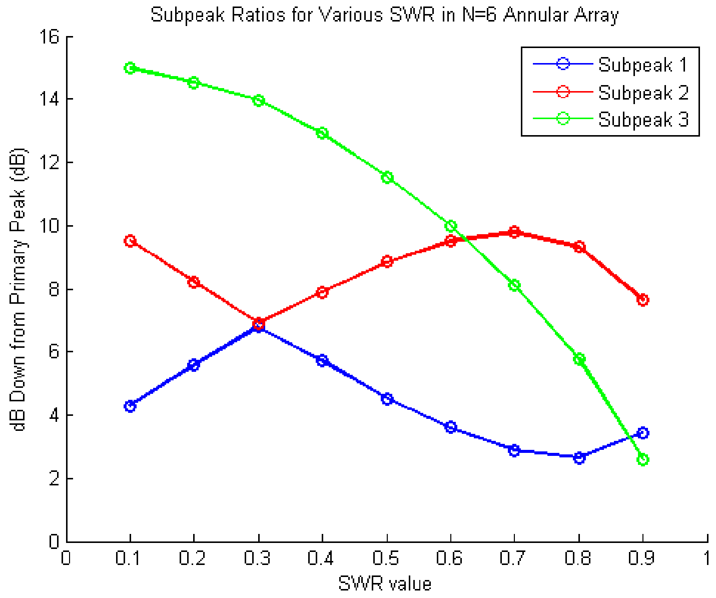

Fig. 2.14 Sidelobe amplitude ratios relative to the main peak in an N=6 annular array with various WSR values.

At this point, the two subpeaks have reached a point where they are equal, and the overall subpeak amplitude is minimized. Another factor that must be investigated is the λ location of the main peak, which shifts for various WSR values. It can be seen the main peak reaches a maximum at exactly λ = *s* for WSR = 0.25 and WSR = 0.75. We have just determined that for subpeak and sidelobe amplitude reasons, WSR = 0.25 would be the preferable of the two. A plot of the excitation spectrum for the annular array with this WSR value and N = 6 elements is shown in Figure 2.15.

The only downside to this value of WSR is that the first harmonic is approximately 28 dB higher than in the WSR=0.5 case. This case is plotted for comparison in Figure 2.16. It is obvious that even though the main peak is now centered at λ=*s* and the subpeaks are minimized, the tradeoff in terms of harmonic amplitudes is substantial. In most cases, this tradeoff will most likely not be worthwhile, and the WSR = 0.5 case will still be ideal. However, there could be situations in which the amplitudes of the harmonics are not so significant and it would be preferable to use an array with a WSR value of 0.25. In addition to these two WSR values, any value of WSR ≤ 0.5 could be used with the annular array in order to minimize one sub peak or the other near the main peak. This may be useful for certain regions of the dispersion curve. For instance, for a case which a mode with a wavelength slightly shorter than the desired wavelength is easily excited while no modes exist with a slightly longer wavelength (at the chosen frequency), then it would be preferable to use an array with an WSR value of 0.1 (as long as harmonics are not a significant issue).

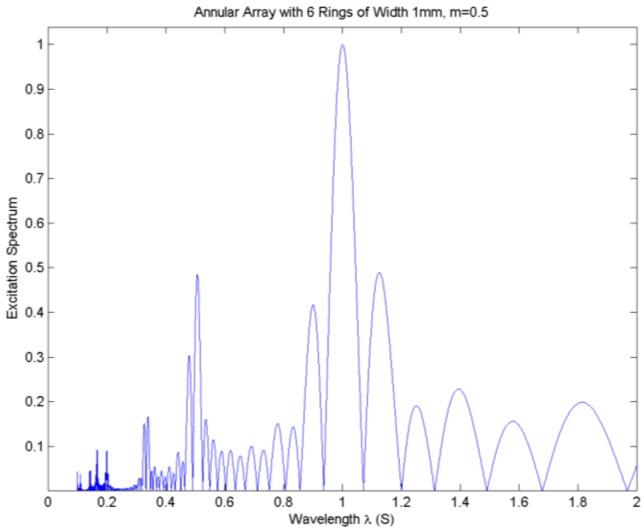

Fig. 2.15 Excitation spectrum for an annular array with N=6 and WSR = 0.25.

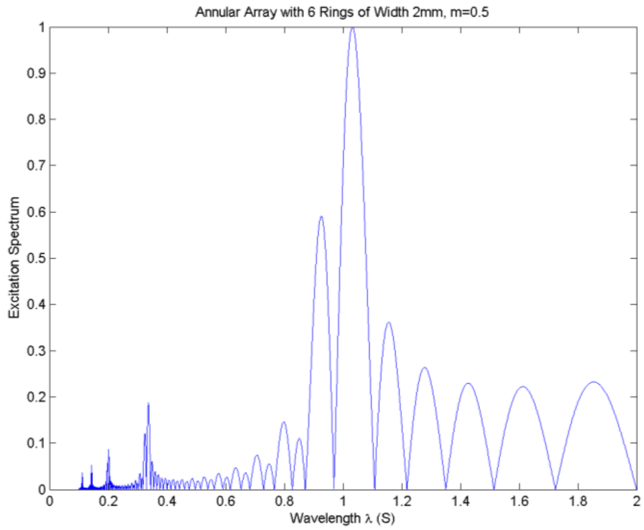

Fig. 2.16 Excitation spectrum for an annular array with N=6 and WSR = 0.5.

Spacing Compensation Factor

To design an annular or comb array with optimal excitation at the desired wavelength, it is important to understand the relationship between the wavelength of peak excitation and the array spacing, as well as how this ratio depends on N and r_0. This ratio can be considered to simply be a "spacing compensation factor", α, when designing an array transducer. Note that a compensation factor less than 1 corresponds to a transducer with spacing smaller than the desired wavelength. It has often been approximated that for a comb array in which $w = 0.5s$, the wavelength of peak excitation is equal to the spacing of the array elements, i.e. the compensation factor is unity. Figure 2.17 shows that this approximation is accurate for comb arrays with large a large number of elements, but is slightly less accurate with fewer elements. The relationship between the wavelength of peak excitation and the array spacing for an annular array is slightly more complex, since it depends on both the number of elements, N, and the inner radius, r_0, of the array, as is shown in Figure 2.18.

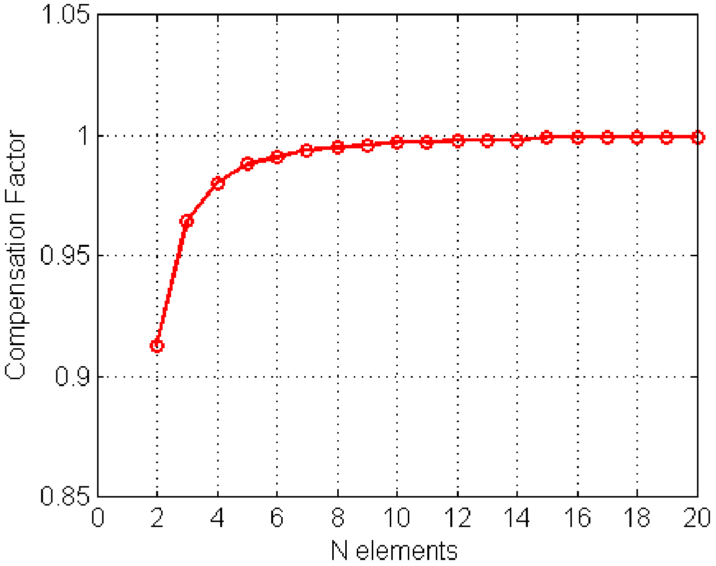

Fig. 2.17 Relationship between number of elements in an array and the ratio of the element spacing and the wavelength of peak excitation in the excitation spectrum.

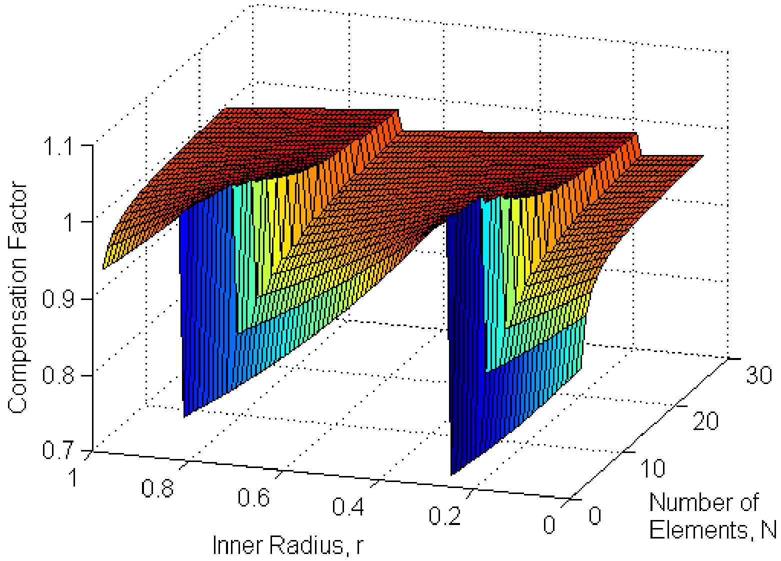

Fig. 2.18 Correction factor as a function of N and r_0.

It is apparent that for the comb array case, the main peak is within 3% of $\lambda=1s$ for $N>3$. Even with only two elements, the main peak is still within 10% of $\lambda=1s$. However, for the annular array case, the compensation factor can be as low as 0.75 or as high as 1.06, depending on the inner radius and the number of elements. The strong variations with r_0 in the trend of the compensation factor for an increasing number of elements is due to the role that the inner radius plays in determining the interference of the outward-propagating waves and the inward-propagating waves, which pass through the center of the array. This is also the cause of the split primary peak in the annular array excitation spectrum. It is clear that for particular inner radii, such as near 0.2s and 0.7s, the compensation factor undergoes a dramatic shift. This corresponds to the points at which the two peaks that comprise the split primary peak in the excitation spectrum switch in magnitude.

Although one's instinct may initially be to minimize the compensation factor, or choose an inner radius with a compensation factor that varies minimally with changes in N, this is of no real advantage; in fact, designing an annular array with an inner radius such that the compensation factor is minimized may in some cases be detrimental due to the change this incurs in the properties of the excitation spectrum such as lower order peak amplitudes and primary peak bandwidth. As long as a plot such as that shown in Figure 18 is referenced to determine the compensation factor for *s*, any annular array, regardless of inner radius or number of elements, can be designed to optimally excite a particular wavelength.

In addition to analyzing the numerical value of the compensation factors, it is equally useful to evaluate the effect of *not* utilizing the compensation factors, which is related to the width of the primary peak in the excitation spectrum. This can be done by evaluating the value of the excitation spectrum at the point $\lambda = s$ and comparing that to the peak value at the wavelength with the compensation factor $\lambda = s/\alpha$. The ratio of these two values, converted to the decibel scale, is hereafter referred to as the "excitation loss" for a particular array. The excitation loss for comb arrays with various values of *N* are shown in Figure 2.19 and the same is done for annular arrays with various values of *N* and r_0 in Figure 2.20.

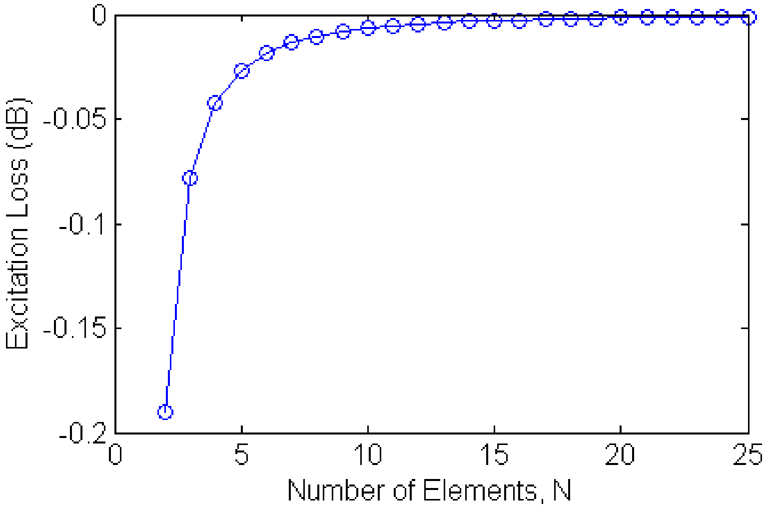

Fig. 2.19 Values of the excitation spectra for a comb transducer with N elements at $\lambda = s$.

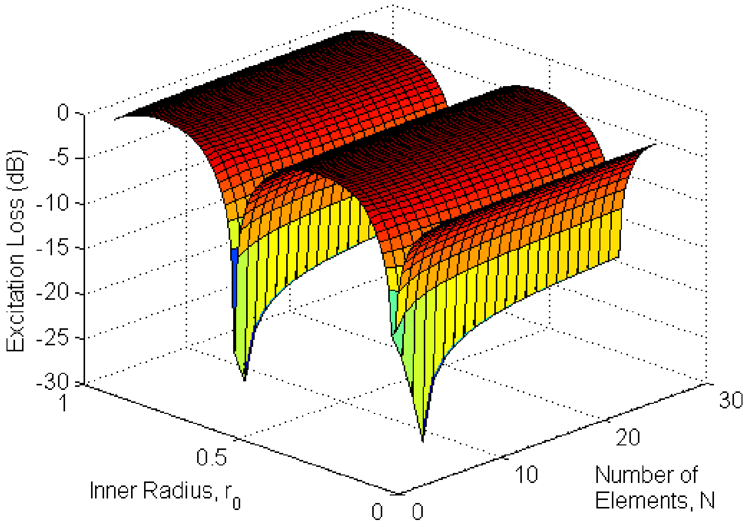

Fig. 2.20 Values of the excitation spectra for annular arrays with N elements and inner radius r_0 at $\lambda = s$.

Note that the excitation losses for the comb array are quite small, on the order of -0.1 dB in the worst cases. Thus, in nearly all cases, the compensation factor is not critical with comb array applications. This is due to the combined factors of rather small compensation factors and a rather broad primary peak in the excitation spectra for comb arrays. This single broad primary peak is not present in the annular array excitation spectrum due to the added complication of the interfering inward- and outward-propagating waves, which cause a split in the primary peak that is dependent on the inner radius of the array. The conclusion that the compensation factor is not critical for comb arrays is in good agreement with the fact that comb transducers have been successfully utilized with the $\lambda = s$ design assumption for decades. However, as shown in Figure 2.20, this is not the case with annular arrays. Depending on the inner radius, the effect of the compensation factor can be quite extreme, even when the value of the compensation factor is rather small. However, the excitation loss for an annular array can be beyond -25 dB. Here it can be seen that the variation of the excitation loss does not vary heavily with the number of elements in the annular array, but it does vary significantly with the inner radius. At some r_0 values, the use of the compensation factor will not be critical, since the value of the excitation spectrum without it is nearly identical to that with it. Yet at other r_0 values, the excitation loss is dramatic. Examples of the extreme cases at $r_0 = 0.37s$ and $r_0 = 0.63s$, as well as the case of inner radius $r_0 = 0.5s$, are given in Figures 2.21, 2.22, and 2.23.

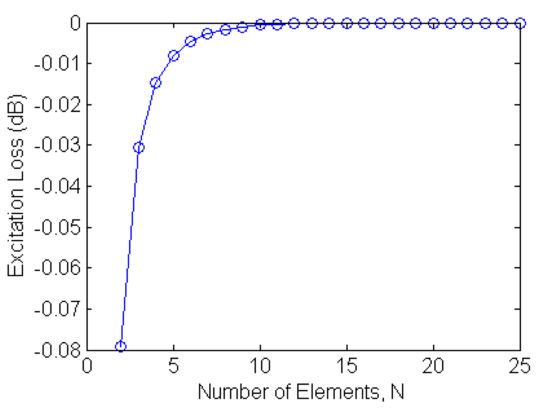

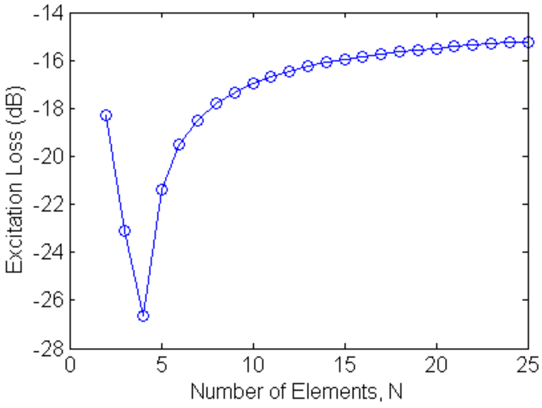

Fig. 2.21 Values of the excitation spectra for annular arrays with N elements and inner radius r_0=0.37*s* at $\lambda = s$. For this case, the correction factor has a minor effect on the excitation spectrum amplitude.

Fig. 2.22 Values of the excitation spectra for annular arrays with N elements and inner radius r_0=0.63*s* at $\lambda = s$. For this case, the correction factor has a severe effect on the excitation spectrum amplitude, which is from 5-7% of the value of the excitation spectrum with the correction factor.

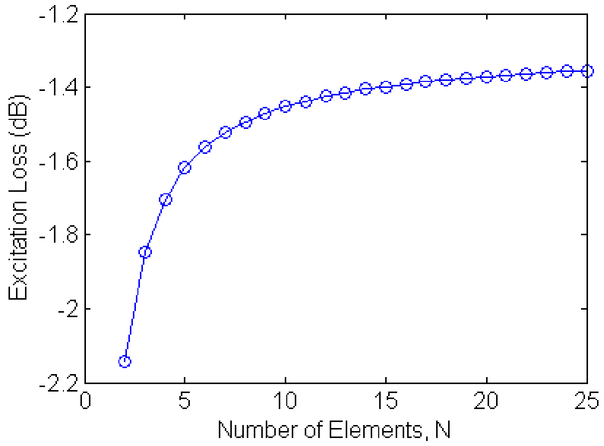

Fig. 2.23 Values of the excitation spectra for annular arrays with N elements and inner radius $r_0 = 0.5s$ at $\lambda = s$. This is the most common inner radius for our purposes, and the correction factor has a significant effect, albeit not as extreme as in some cases.

Number of Elements

The broad effect of the number of elements in an array is obvious, and in the ideal case, a very large number of elements would be used. However, the size and cost considerations in array design dictate that the fewest elements possible should be used to achieve the goal of the array. To analyze the effect of the number of elements, *N*, we can compare them graphically in Figure 2.24. It is apparent that as $N \to \infty$, the envelope of the primary peak in the excitation spectrum narrows. The finer differences for reasonable ranges of *N* values lies in the specific peaks and zeros within this envelope. One factor to take into consideration is λ sensitivity, i.e. how focused the excitation spectrum must be. For applications with high λ sensitivity, more elements will be necessary to reduce the bandwidth of the primary excitation peak and to reduce the amplitude of the sidelobes.

Factors such as this will determine the necessary number of elements, *N*, that must be included in an annular array.

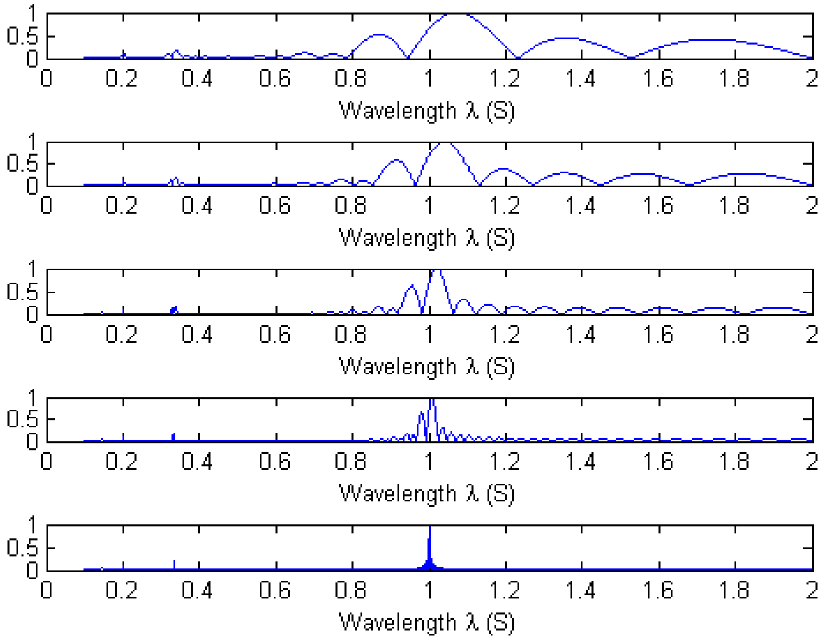

Fig. 2.24 Influence of the number of elements, N, on the excitation spectrum of an annular array. The excitation spectra above are for identical arrays with elements numbers of N=3, 5, 10, 25, and 200 respectively.

2.1.4. Time Delay Phasing of Annular Arrays

The ability of a comb or annular array transducer to selectively excite particular wavelength regions of a dispersion curve makes it a powerful tool in guided wave inspection techniques. However, the other side of the coin is that the excitation ability of an array is limited by its construction. To enhance the capabilities of a single array, time delays can be applied across its elements, which effectively increase or decrease the physical spacing between the elements. If applied appropriately, time delays can allow the user to selectively excite any region on the dispersion curve to one degree or another. [5, 6] However, the key here is the ability to understand and predict the response of the transducer to applied time delays.

Comb Array Time Delays

The analysis of the effect of time delays on the excitation spectrum of a comb transducer is relatively straight-forward. By applying the appropriate time delay term onto the summation term for each element, we can predict the associated excitation spectrum of the array as follows.

$$\mathcal{F}\{f_c(x)\} = \frac{w}{\sqrt{2\pi}} \sum_{n=0}^{N-1} sinc\left(\frac{kw}{2}\right) e^{ikns} e^{-i\omega n\Delta t} \qquad (15)$$

In this case, linear time delays are applied across each element, relative to the first element. This can be rearranged as in (16).

$$\mathcal{F}\{f_c(x)\} = \frac{w}{\sqrt{2\pi}} \sum_{n=0}^{N-1} sinc\left(\frac{kw}{2}\right) e^{in(ks-\omega\Delta t)} \qquad (16)$$

Note that the term ω·Δt where ω is the angular frequency and Δt is the time delay, is equivalent to a phase delay Δφ. In equation (16) it can be seen that the time delays are effectively shifting the *ks* term. This causes the entire excitation spectrum to shift in the k-domain, as is demonstrated in Figure 2.25 for a 5-element comb array. In this figure, it can be seen that the symmetry about k = 0 has been broken. The result of this is that the waves propagating from each end of the comb array are no longer identical. The excitation spectra of the forward and backward propagating waves can be separated by analyzing the positive and negative k-domains separately. The forward-propagating spectra for this comb array are shown in the wavelength-domain in Figure 2.26. The spectra for the backward case are simply the spectra for the forward case in with time delays in reversed order, and vice-versa.

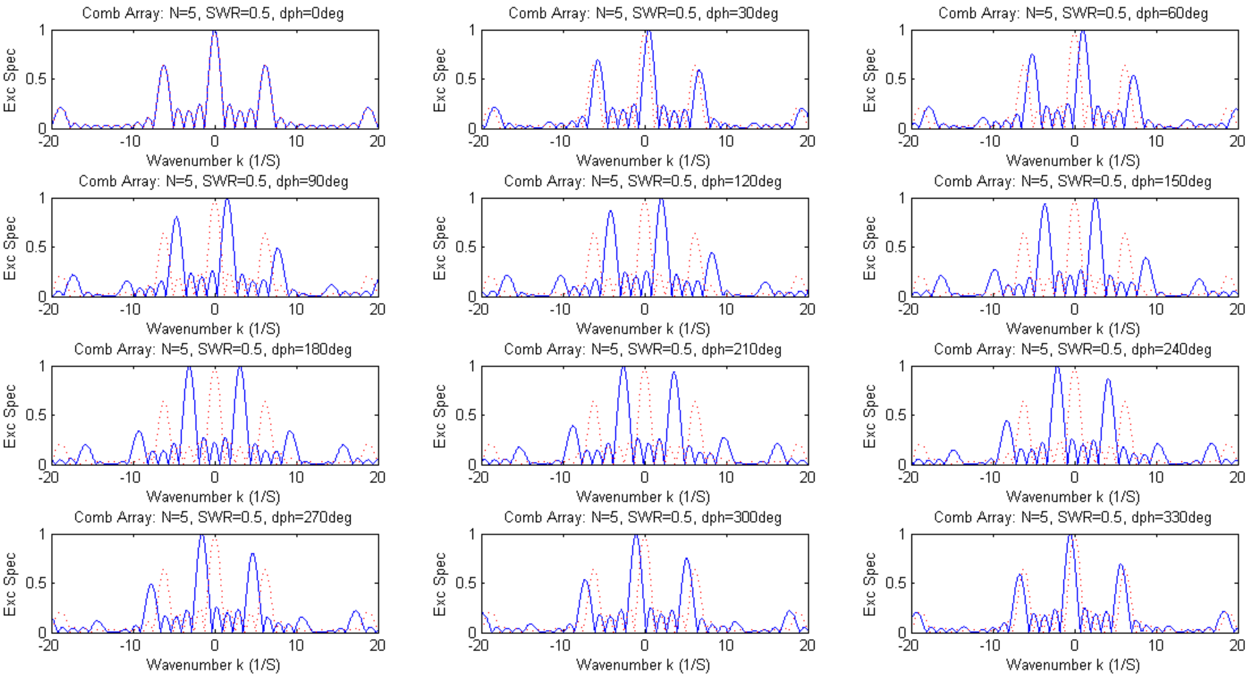

Fig. 25 Excitation spectrum of linearly-phased 5-element comb array in k-domain.

The fact that the forward and backward propagating waves have different spectra in the wavelength-domain allows us to select a time delay parameter such that an ideal mode will be propagated forward and no mode, or a very weak mode, will be propagated backward. This gives us directional control of the comb array. This is not the case with an annular array, which we will address shortly.

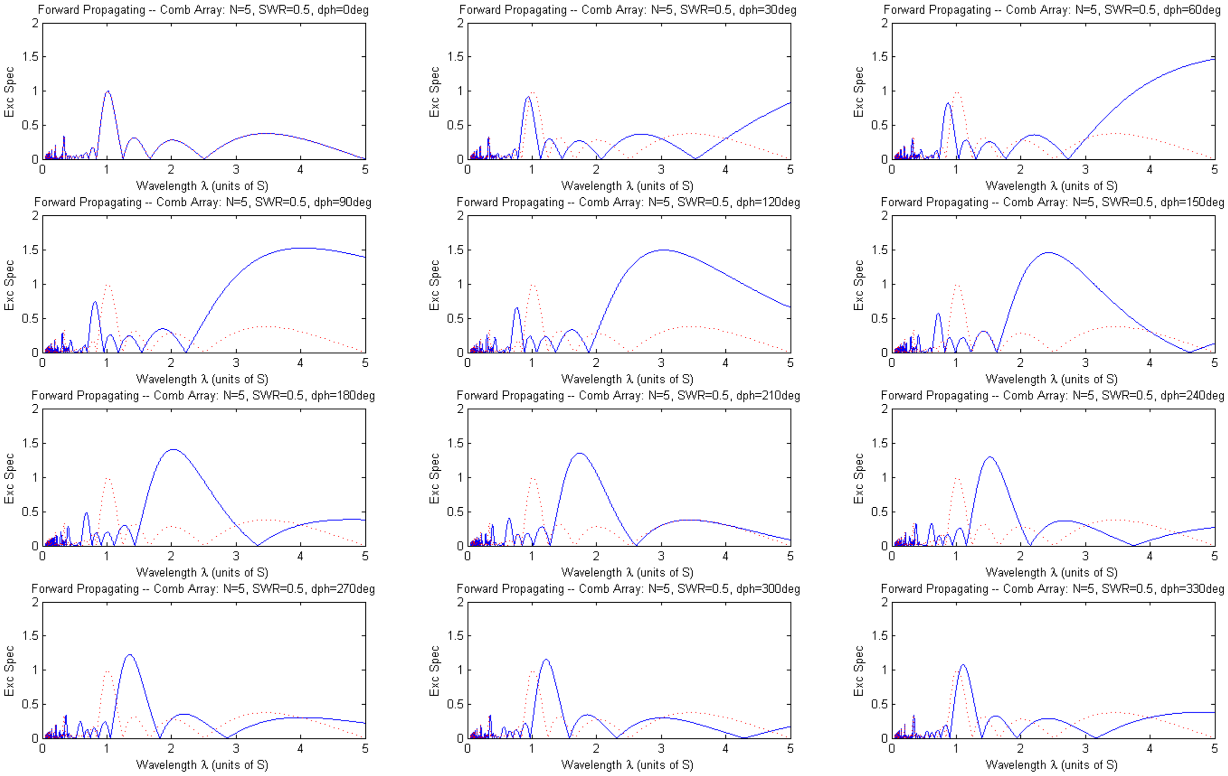

Forward Propagating -- Comb Array: N=5, SWR=0.5, dph=0deg
Forward Propagating -- Comb Array: N=5, SWR=0.5, dph=30deg
Forward Propagating -- Comb Array: N=5, SWR=0.5, dph=60deg
Forward Propagating -- Comb Array: N=5, SWR=0.5, dph=90deg
Forward Propagating -- Comb Array: N=5, SWR=0.5, dph=120deg
Forward Propagating -- Comb Array: N=5, SWR=0.5, dph=150deg
Forward Propagating -- Comb Array: N=5, SWR=0.5, dph=180deg
Forward Propagating -- Comb Array: N=5, SWR=0.5, dph=210deg
Forward Propagating -- Comb Array: N=5, SWR=0.5, dph=240deg
Forward Propagating -- Comb Array: N=5, SWR=0.5, dph=270deg
Forward Propagating -- Comb Array: N=5, SWR=0.5, dph=300deg
Forward Propagating -- Comb Array: N=5, SWR=0.5, dph=330deg

Fig. 2.26 Excitation spectrum forward propagating wave from a linearly-phased 5-element comb array in wavelength-domain.

Annular Array Time Delays

Following a similar process as was done for the comb case, the excitation spectra for annular arrays is given by equation (17).

$$F_a(k) = \frac{1}{k}\sum_{n=0}^{N-1}\{R_{2_n}\, J_1[R_{2_n}k] - R_{1_n}\, J_1[R_{1_n}k]\}e^{-in\omega\Delta t} \qquad (17)$$

However, it is apparent that this cannot be simplified into a form in which the time delay term causes a direct shift in the excitation spectrum, as was possible in the comb case. This leads us to the conclusion that linear time delays applied to an annular array will not simply shift the excitation spectrum. In fact, the excitation spectra for a 5-element linearly-phased annular array are as shown in Figure 2.27 for the wavenumber domain and Figure 2.28 for the wavenumber domain.

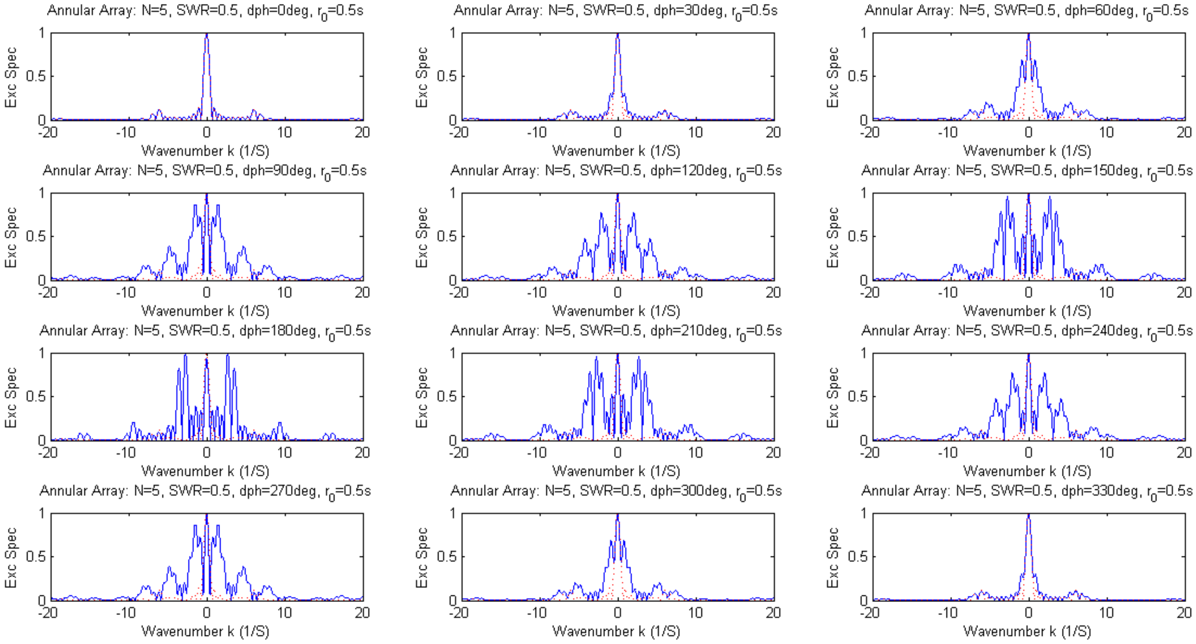

Fig. 2.27 Excitation spectrum for a linearly-phased 5-element annular array in wavenumber-domain.

It is important to notice the fact that the symmetry of the k-domain excitation spectra for the annular array about k = 0 is preserved after time delays are applied. This is true for any time delays that are applied to the array, linear or otherwise. This means that the inward and outward propagating waves are not separated in the wave-length domain. This makes sense, because the inward-propagating wave from any infinitesimal element will cross through the center of the array and interact with the outward propagating wave from the symmetrically opposite infinitesimal element. In the same way, the inward propagating wave from this second infinitesimal element will interact identically with the outward propagating wave from the first infinitesimal element. Thus the wave that the excitation spectra are describing is the *sum* of the inward and outward propagating waves, described by the radial k-domain value k_r. This is accurate, however in reality, due to the finite excitation period (pulse) in the time-domain, it is possible for the inward and outward propagating waves to in fact be separated, dependent upon a sufficiently large inner radius of the array. This will be further explored in the FEM analysis section of this report.

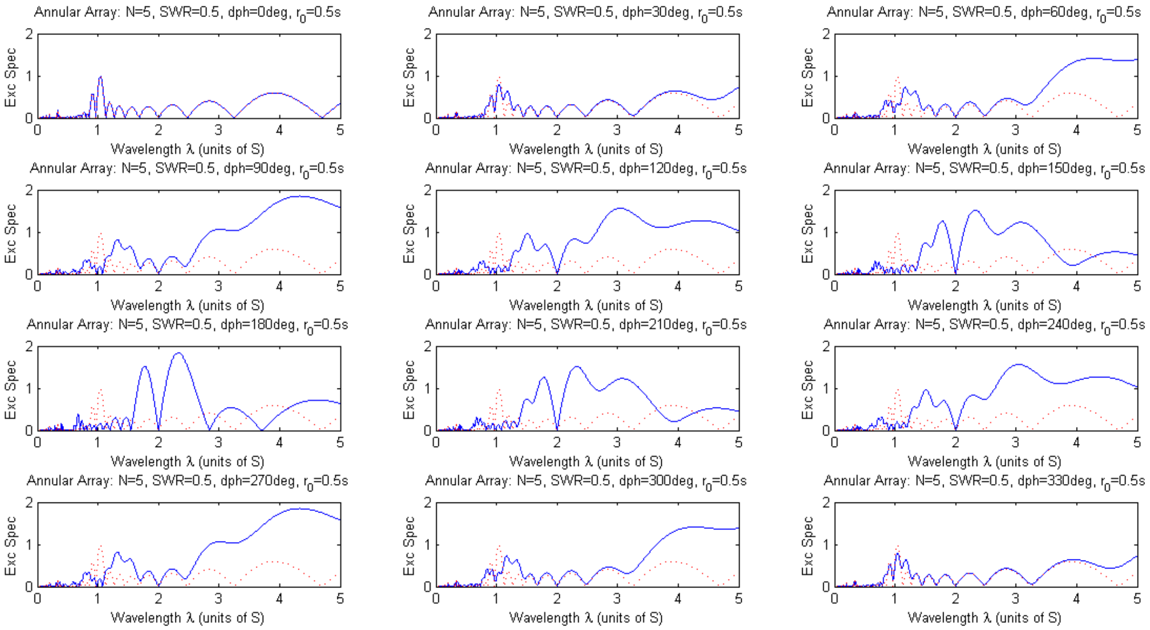

Fig. 2.28 Excitation spectrum for a linearly-phased 5-element annular array in wavelength-domain.

Another interesting feature that occurs due to this symmetry is that the linear phasing can be positive or negative (i.e. starting from the innermost element or the outermost element) and the excitation spectra will be identical. For the comb case, however, this would swap the forward and backward propagating waves.

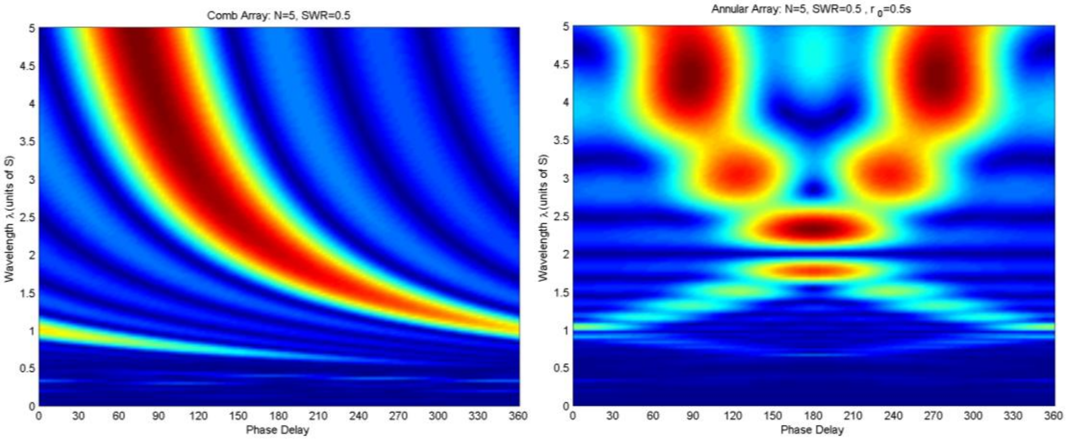

Fig. 2.29 Contour plot of excitation in the wavelength domain versus applied phase delay for comb transducer (left) and annular array transducer (right) with 5 elements and central radius 0.5*s*.

The effect of time delays on comb and annular arrays determines the ability of the array to excite various regions of the dispersion curve. By plotting the excitation spectrum of an array (at a central frequency) versus the phase delay applied across its elements, we can gain insight into how the delay alters the excitation spectrum of a particular array.

Several plots showing this relationship for comb and annular arrays are given in Figures 2.29-2.32. Note the symmetry apparent in the annular array spectra and the similarities to the comb spectra. The symmetry and the interference pattern are effects of the inward and outward wave interference.

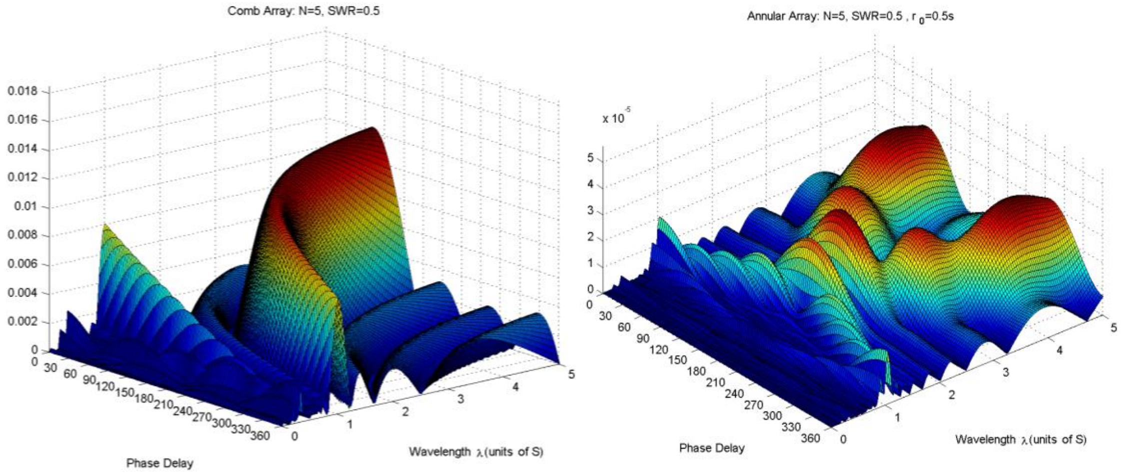

Fig. 2.30 Surface plot of excitation in the wavelength domain versus applied phase delay for comb transducer (left) and annular array transducer (right) with 5 elements and central radius 0.5*s*.

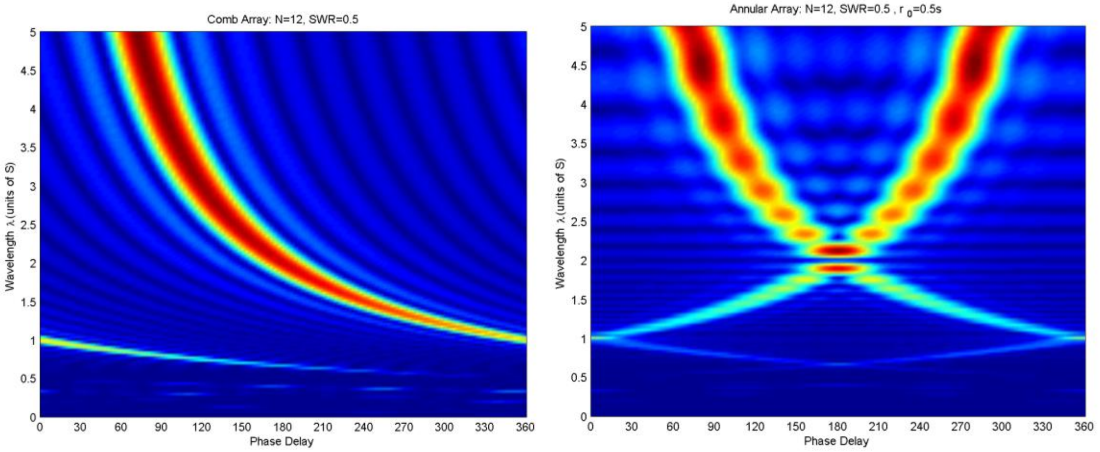

Fig. 2.31 Contour plot of excitation in the wavelength domain versus applied phase delay for comb transducer (left) and annular array transducer (right) with 12 elements and central radius 0.5*s*.

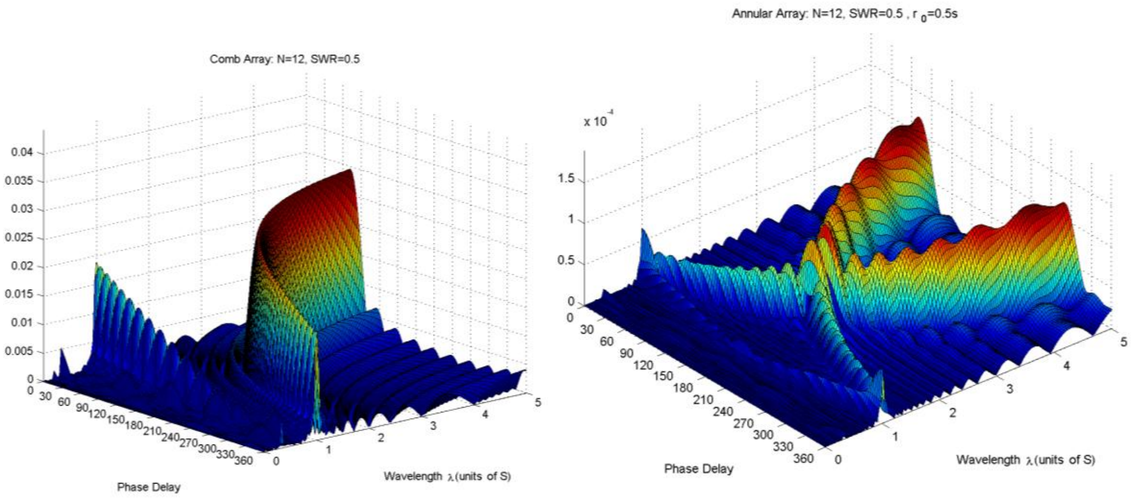

Fig. 2.32 Surface plot of excitation in the wavelength domain versus applied phase delay for comb transducer (left) and annular array transducer (right) with 12 elements and central radius 0.5*s*.

Separation of the Inward- and Outward-Propagating Annular Array Waves

Due to the fact that the excitation spectrum, as derived previously for the annular array, describes the sum of the outward and inward propagating waves, we were unable to separate the two in our wavelength-domain analysis. In order to consider the spectra of these waves individually, we will need to better define the inward and outward propagation.

Figure 2.33 shows a generalized disk and a point $(r,0)$ to which a wave is propagating. Here ρ is the radial distance to an infinitesimal transducer element from the center of the array, θ is the angle to that element from vector $\vec{r}$, and $\vec{d}$ is the vector from the element to the measurement point. The angle α is the angle between a line parallel to $\vec{r}$ and the vector $\vec{d}$, and ψ is the angle from $\vec{d}$ to the tangent of the radial vector $\vec{\rho}$.

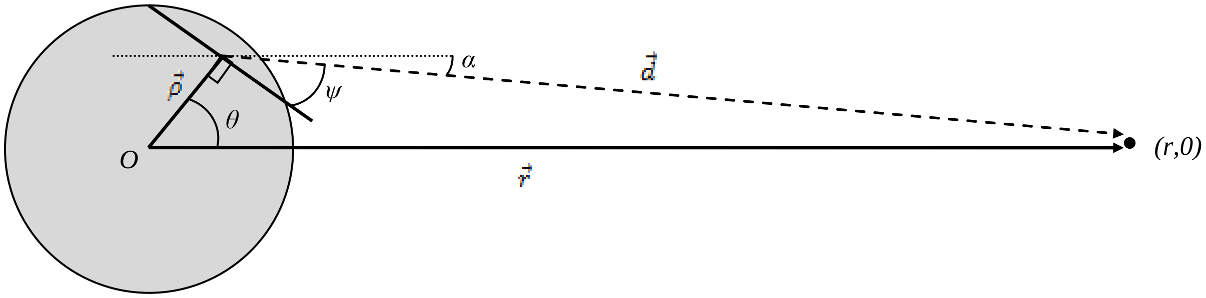

Fig. 2.33 Geometry of transducer disk and measurement point $(r,0)$.

From this geometry, we can draw the following conclusions:

$$\vec{d} = \vec{r} - \vec{\rho} \qquad\qquad \psi = \frac{\pi}{2} - \alpha - \theta \tag{18a}$$

$$\vec{d} = [r - \rho\cos(\theta)]\,\hat{\imath} + [\rho\sin(\theta)]\,\hat{\jmath} \tag{18b}$$

$$\Rightarrow \quad \begin{cases} r - \rho\cos(\theta) = d\cos(\alpha) \\ \rho\sin(\theta) = d\sin(\alpha) \end{cases}$$

$$\Rightarrow \quad \tan^{-1}\left(\frac{\rho\sin(\theta)}{r - \rho\cos(\theta)}\right) = -\alpha = \psi + \theta - \frac{\pi}{2} \tag{18c}$$

Now by examining a small annular ring element located at a radial distance ρ and angle θ from the origin, we can define the inward and outward propagating waves. In Figure 34, ψ is the angle between the wavenumber vector $\vec{k}$ and the tangent to the radial vector $\vec{\rho}$. The inward and outward waves can then be defined as in equation (19).

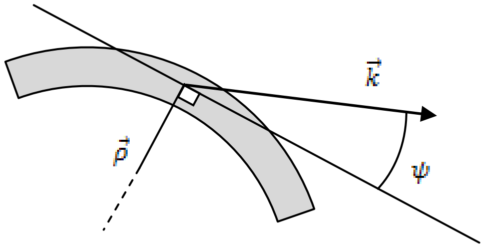

Fig. 2.34 Local geometry for small element of an annular ring.

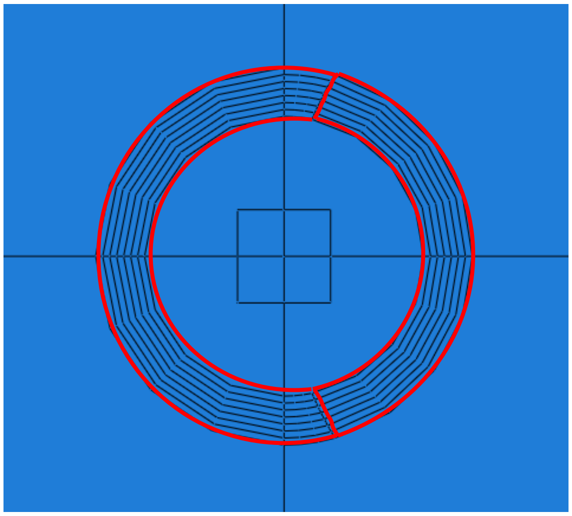

Fig. 2.35 Separation of the portions of the annular array responsible for the outward (right) and inward (left) propagating waves for the case with $\frac{r}{R} = 3.7$.

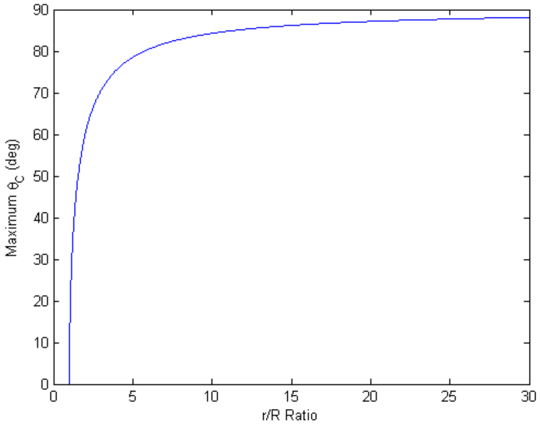

Fig. 2.36 Critical angle θ_c at the edge of the annular array for various values of the $\frac{r}{R}$ ratio.

$$\begin{cases} -\pi < \psi < 0 & outward \\ \pi > \psi > 0 & inward \end{cases} \qquad (19)$$

Due to the radial symmetry of the array, we can select an angle of $\theta = 0$ to examine without losing generality. This selection, along with equations (18c) and (19) allows us to identify the maximum angles $\pm\theta_c$ for any value of ρ for which any outward propagating waves can reach an arbitrary point (*r*,*0*).

$$\tan^{-1}\left(\frac{\rho\sin(\theta_c)}{r - \rho\cos(\theta_c)}\right) = \theta_c \pm \frac{\pi}{2} \qquad (20)$$

With some trigonometric manipulation, this yields equation (21).

$$\theta_c = \pm\cos^{-1}\left(\frac{\rho}{r}\right) \qquad (21)$$

Thus the outward propagating wave incident at point *(r,0)* is entirely described by the rightward-propagating wave from the annular array segment enclosed between these angles. The inward propagating wave incident at (*r*,*0*) is similarly due entirely to the rightward-propagating wave from the remainder of the array, as shown in Figure 2.35.

As we can see from equation (21) and Figure 2.36, for relatively large distances from the transducer, which is the typical assumption for guided wave mechanics, the critical angle can be approximated as $\theta_c = \frac{\pi}{2}$. Therefore we can approximate that the outward-propagating wave is due to the nearest semi-annular portion of the array from the point of interest, and the inward-propagating wave is due to the far semi-annular portion. Thus to calculate the wavenumber excitation spectra of these two wave packets individually, we need to take the 2D spatial Fourier transform of a semi-annular array section. In doing so, we will no longer have the axisymmetric geometry that allowed us to convert the 2D spatial Fourier transform into a radial Hankel transform. For simplicity in this derivation, we will consider only a single semi-annular element at first, and we will then generalize the array geometry for the final equations.

$$\mathcal{F}\{f(x,y)\}(k_x,k_y) = \frac{1}{2\pi}\int_{-\infty}^{\infty}\int_{-\infty}^{\infty} f(x,y)e^{-i(k_x x + k_y y)}\,dxdy \qquad (22)$$

This can be converted into polar coordinates as

$$\mathcal{F}\{f(r,\theta)\}(k_r,\varphi) = \frac{1}{2\pi}\int_{-\infty}^{\infty}\int_{-\pi}^{\pi} f(r,\theta)e^{-irk_r\cos(\varphi-\theta)}\,rd\theta dr \qquad (23)$$

By substituting the semi-annular element geometry function into this equation, we find

$$F_s(k_r,\varphi) = \frac{1}{2\pi}\int_{R_1}^{R_2}\int_{-\pi/2}^{\pi/2} e^{-irk_r\cos(\theta)}\, r\,d\theta\,dr \tag{24}$$

As straight-forward as this integral may at first appear, it in fact has no analytical solution. Thus to solve this equation analytically, we must expand the geometry function of the semi-annular element into a Fourier series in the angular domain.

$$\mathcal{F}\{f(r,\theta)\} = F(k_r,\theta) = \sum_{m=-\infty}^{\infty} 2\pi i^{-m} e^{im\varphi}\int_0^{\infty} f_m(r)\,J_m(k_r r)\,r\,dr \tag{25}$$

Substituting the annular array geometry functions into (25) yields the 2D polar Fourier transform of a semi-annular element in equation (26).

$$\begin{aligned} &F_s(k_r,\theta) \\ &= \sum_{m=-\infty,\ m\neq 0}^{\infty}\left[\frac{2}{m} i^{-m}\sin\left(m\frac{\pi}{2}\right) e^{im\varphi}\int_{R_1}^{R_2} r\,J_m(k_r r)\,dr\right] \\ &+ \frac{\pi}{k_r}\left[R_2\,J_1(k_r R_2) - R_1\,J_1(k_r R_1)\right] \end{aligned} \tag{26}$$

Since we are concerned only with the outward and inward propagating waves, we can evaluate the excitation spectrum for waves propagating in the φ=0 and φ=π, respectively. The result of this evaluation, as well as introduction of the time delay term and summation over all N elements is given in the following equations.

$$F_{s+}(k_r,\theta) = \left\{\sum_{m=-\infty}^{\infty} i^{-m}\int_{-\pi/2}^{\pi/2} e^{-im\theta}\,d\theta\int_{R_1}^{R_2} r\,J_m(k_r r)\,dr\right\} e^{-in\omega\Delta t} \tag{27a}$$

$$F_{s-}(k_r,\theta) = \left\{\sum_{m=-\infty}^{\infty} (-1)^m\, i^{-m}\int_{-\pi/2}^{\pi/2} e^{-im\theta}\,d\theta\int_{R_1}^{R_2} r\,J_m(k_r r)\,dr\right\} e^{-in\omega\Delta t} \tag{27b}$$

This agrees with solutions found in [10] and [11], and can be further simplified through several trigonometric and Bessel function relations to contract the number of terms over which the summation is evaluated. Neglecting the time delays:

$$F_{s+}(k_r,\theta) = \sum_{m=1}^{\infty}\left[-\frac{4}{m} i\int_{R_1}^{R_2} r\,J_m(k_r r)\,dr\right] + \frac{\pi}{k_r}\left[R_2\,J_1(k_r R_2) - R_1\,J_1(k_r R_1)\right] \tag{28a}$$

$$F_{s-}(k_r,\theta) = \sum_{m=1}^{\infty} \left[\frac{4}{m} i \int_{R_1}^{R_2} r\, J_m(k_r r)\, dr \right] + \frac{\pi}{k_r} \left[R_2\, J_1(k_r R_2) - R_1\, J_1(k_r R_1) \right] \qquad (28b)$$

Note that the Bessel function integral can no longer be analytically integrated for all values of *m*, due to the varying order of the Bessel function. Thus these equations must be evaluated numerically for a chosen number of terms, *m*.

Once convergence has been established, the inward and outward excitation spectra can be analyzed versus the applied phase delays. In this way, the trends of the individual waves as a function of phase delay can be understood and compared to those of the comb and complete annular arrays. The surface and contour plots showing this relationship for an annular array with 8 elements are given in Figures 2.37 and 2.38. Note that the inward and outward excitation spectra are identical only for applied phase delays of 0° and 180°. A significant result of this separation is that we can now see that the inward-propagating annular array spectrum is quite similar to the forward comb excitation spectrum, and the same is true for the outward-propagating annular and backward comb spectra.

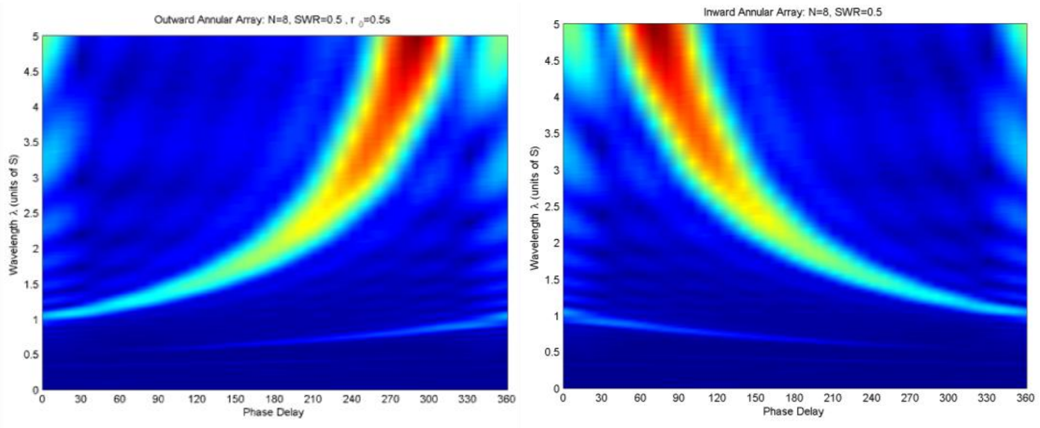

Fig. 2.37 Contour plots of excitation in the wavelength domain versus applied phase delay for outward- (left) and inward-propagating (right) waves from an annular array transducer with 8 elements and central radius 0.5*s*.

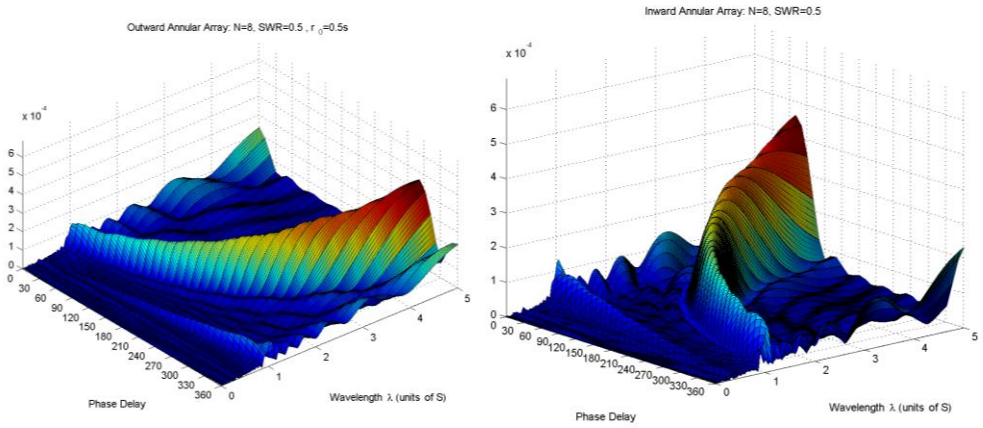

Fig. 2.38 Surface plots of excitation in the wavelength domain versus applied phase delay for outward- (left) and inward-propagating (right) waves from an annular array transducer with 8 elements and central radius 0.5*s*.

It can be seen in Figures 2.37 and 2.38 that the excitation spectra for the inward and outward waves are similar, although not identical, to the excitation of a comb transducer. This difference exists due to the plane wave nature of the comb excitation as compared to the circularly-crested wave nature of the annular array excitation. To understand the effect of the number of elements on the inward and outward excitation spectra of an annular array, see Figure 2.39. Only the inward-propagation spectra are given due to the symmetry of the inward and outward spectra.

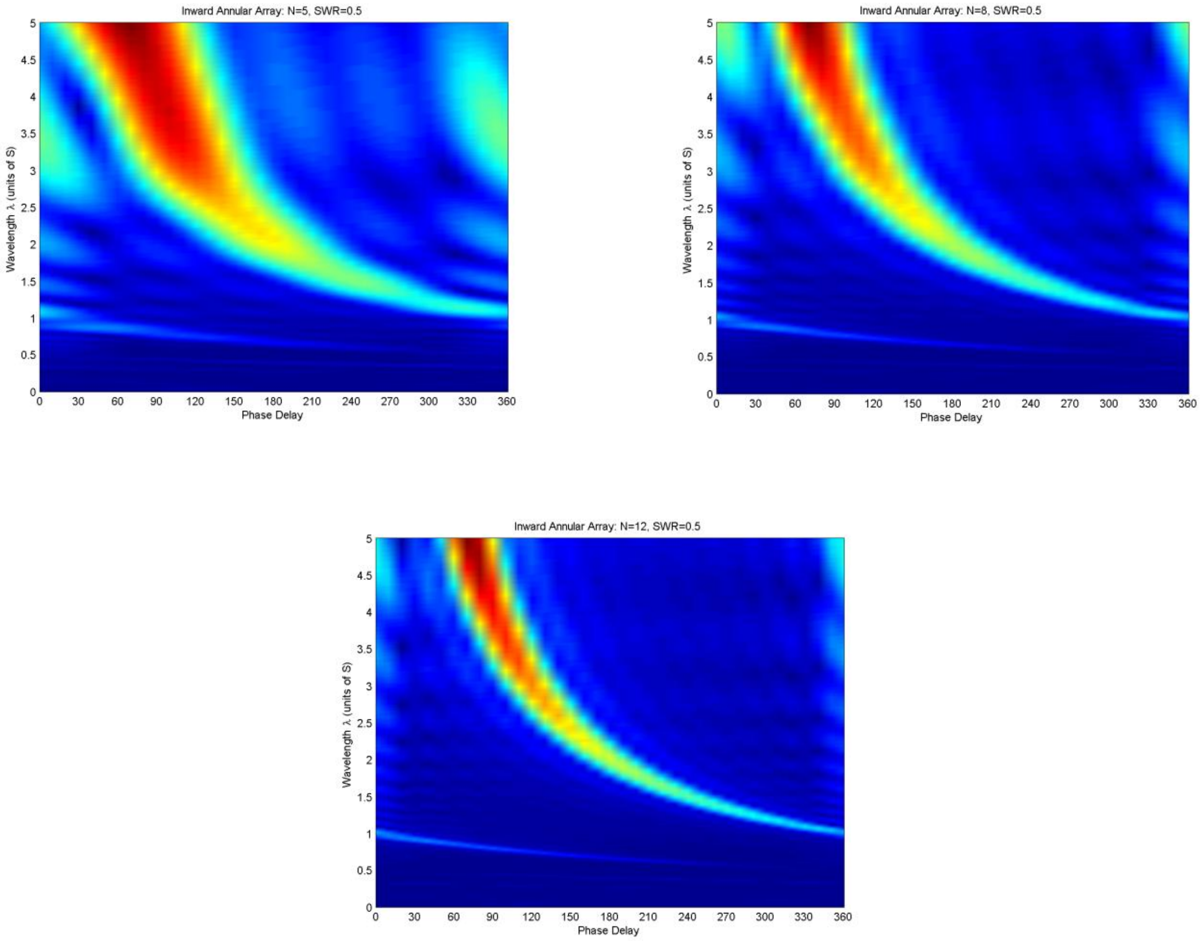

Fig. 2.39 Contour plots of excitation in the wavelength domain versus phase delay for inward-propagating waves from a transducer with (clockwise from upper left) 5, 8, and 12 elements.

The Influence of Guided Wave Mode Excitability

Thus far, we have discussed the excitation spectrum of the transducer arrays in the dispersion curve space domain (wavelength, wavenumber, phase velocity). This has provided us complete generality in terms of waveguide structure and transducer loading. Thus these results are applicable to all structures and all loading scenarios (i.e. shear, normal, etc.). However, in addition to the excitability spectrum, the mode excitability always plays a role in guided wave mode excitation. To understand the effect of mode excitability, we will need to incorporate the effects of specific guided wave mode excitability that will, in conjunction with the wavelength-domain excitation spectra, allow us to exactly predict unique waveforms generated by a particular transducer.

To derive the excitability of various guided wave modes, the normal mode expansion technique is employed. This technique is based on the orthogonality and completeness of the Lamb wave modes. The orthogonality relation for Lamb waves is:

$$P_{\nu\mu} = -\frac{1}{4}\int_{-d/2}^{d/2} \left(\mathbf{v}_{\nu}^{*} \cdot \mathbf{T}_{\mu} + \mathbf{v}_{\mu} \cdot \mathbf{T}_{\nu}^{*}\right) \cdot \hat{\mathbf{e}}_{x}\, dz \qquad (29a)$$

in which

$$\begin{cases} P_{\nu\mu} = 0\,, & \nu = \mu \\ P_{\nu\mu} \neq 0\,, & \nu \neq \mu \end{cases} \qquad (29b)$$

$$P_{\nu\nu} = Re\left(\frac{1}{2}\int_{-d/2}^{d/2} \left(\mathbf{v}_{\nu}^{*} \cdot \mathbf{T}_{\nu}\right) \cdot \hat{\mathbf{e}}_{x}\, dz\right) \qquad (29a)$$

Here $P_{\nu\nu}$ is the time-averaged power, or Poynting vector in the $\hat{\mathbf{e}}_x$ direction for the ν^{th} mode, $\mathbf{v}_\mu$ is the velocity vector for the μ-th mode, $\mathbf{T}_\mu$ is the stress tensor for the μ-th mode, and the plate thickness is *d*. The asterisk denotes complex conjugation. According to the orthogonality and completeness of the Lamb wave modes, any velocity or stress field can be represented by an expansion of Lamb wave modes.

$$\mathbf{v}(x,z) = \sum_{\mu} A_{\mu}(x)\mathbf{v}_{\mu}(z) \qquad (30a)$$

$$\mathbf{T}(x,z) = \sum_{\mu} A_{\mu}(x)\mathbf{T}_{\mu}(z) \qquad (30b)$$

In addition to the orthogonality of the wave modes, a complex reciprocity relation also holds. In fact, this is the relation from which the orthogonality can be derived.

$$\nabla \cdot \left(\mathbf{v}_{2}^{*} \cdot \mathbf{T}_{1} + \mathbf{v}_{1} \cdot \mathbf{T}_{2}^{*}\right) = 0 \qquad (31)$$

Without proceeding through the entire derivation, the amplitude of a guided wave mode ν due to a point traction load **t** on the surface of a plate according to equation (32).

$$A_{\nu}(x) = \frac{e^{ik_{\nu}^{*}x}}{4P_{\nu\nu}} \int_{-\infty}^{\infty} e^{-ik_{\nu}^{*}\zeta} \; \mathbf{v}_{\nu}^{*}(d/2) \cdot \mathbf{t}(\zeta) d\zeta \tag{32}$$

We can then use this amplitude value to exactly describe the displacement field of the ν^{th} guided wave mode excited by the specified traction.

$$\mathbf{u}_{\nu}(x,z) = \left[\frac{\mathbf{v}_{\nu}^{*}(d/2)}{4P_{\nu\nu}} \cdot \int_{-\infty}^{\infty} \mathbf{t}(\zeta) e^{-ik_{\nu}^{*}\zeta} \; d\zeta \right] \bar{\mathbf{u}}_{\nu}(z) e^{i(k_{\nu}^{*}x - \omega t)} \tag{33}$$

We can decompose this expression into two components. The first component is dictated by the wavestructure, while the second is dictated by the loading. The dot product of these two components yields displacement field of the excited mode. We can extract the wavestructure component, also known as the excitability matrix, as shown in equation (34).

$$\mathbf{E}_{\nu} = \frac{1}{4P_{\nu\nu}} [\bar{\mathbf{u}}_{\nu}(d/2)]^{T} \times \mathbf{v}_{\nu}^{*}(d/2) \tag{34}$$

The excitability matrix $\mathbf{E}_{\nu}$ has 9 components. It can be shown that for circularly crested waves in cylindrical coordinates (i.e. 3D and not planar space), the 3D excitability matrix $\mathbf{E}_{\nu}^{3D}$ can be expressed in terms of the corresponding plane wave excitability matrix components derived here.

By multiplying the 3D excitability matrix with the geometry-based excitability spectrum (in the k-domain), we can construct an expression for the total wave mode excitability for any phased annular array or comb transducer loading. Multiplying by the surface traction density ρ_{Tr} and including the wave propagation terms to account for spatial and dispersion and time harmonic oscillation, we can predict the surface displacements at a given distance due to each guided wave mode. This can then be used to determine the entire displacement, velocity, or stress field in the structure, if necessary. The surface displacement predictions due to mode ν at a distance *r* for a phased annular array transducer are given in equations (35).

$$u_{r\nu} \approx \sqrt{\frac{2\pi}{ik_{\nu}r}} E_{xz_{\nu}} \rho_{Tr} \left[\sum_{n=0}^{N-1} \left\{ R_{2_n} J_1[R_{2_n}k] - R_{1_n} J_1[R_{1_n}k] \right\} \right] e^{i(k_{\nu}r - n\omega\Delta t)} \tag{35a}$$

$$u_{z\nu} \approx \sqrt{\frac{2\pi}{ik_{\nu}r}} E_{zz_{\nu}} \rho_{Tr} \left[\sum_{n=0}^{N-1} \left\{ R_{2_n} J_1[R_{2_n}k] - R_{1_n} J_1[R_{1_n}k] \right\} \right] e^{i(k_{\nu}r - n\omega\Delta t)} \tag{35b}$$

The approximation is due to the Hankel function approximation used for circularly crested waves. Here $R_{1_n} = r_0 + ns$ is the inner radius of the n^{th} element, and $R_{2_n} = r_0 + ns + w$ is the outer radius of the n^{th} element. Note that the excitability matrix components shown in equations (35) are actually those for the plane wave case, and that the appropriate correction factors are used to convert the components to the 3D circular crested wave case as shown here.

Now that the mode excitability has been defined as a function of guided wave mode and transducer loading, we can examine the effects of annular array phasing on actual mode excitation. This requires not only the description of the transducer dimensions, as was needed for the excitation spectrum calculations, but also knowledge of the waveguide on which the transducer will act. For the examples shown here, a 1-mm thick Aluminum plate with the following properties (see Table 2.II) was chosen to demonstrate mode excitation due to annular array phasing. The transducer used in the model had the dimensions shown in Table 2.III.

Aluminum Properties	
c_L = 6300 m/s	λ = 56.29 GPa
c_T = 3100 m/s	μ = 26.43 GPa
ρ = 2750 kg/ m^3	

Table 2.II Aluminum material properties used for mode excitation calculations.

Annular Array Transducer Dimensions
N=8
r_0 = 2.5 mm
w = 2.5 mm
s = 5.0 mm

Table 2.III Annular array dimensions used for mode excitation calculations.

Various attributes of the excited modes can be analyzed. By using the power-normalized amplitudes of the guided wave wavestructures calculated with the global matrix method, the explicit guided wave amplitudes can be plotted. However, a more meaningful value for guided wave inspection may be the energy in a particular mode. Additionally, it is easier to interpret the plots if the % of total energy in the waveguide is broken up into individual modes. Thus the plot in Figure 2.39 shows the % of the total guided wave energy that can be attributed to each excited guided wave mode as a function of frequency and phase delay.

In Figure 2.40 the % total energy for the S0 mode is plotted from 1-5 MHz, over the full range of phase delays 0-360°. From these plots, we can see that at many frequencies for each mode, we can exhibit excellent control over the dominant mode in the structure by applying phase delays to the annular array transducer. However, there are also regions for which the transducer cannot effectively excite a particular mode above the others. This lack of control is due to the excitability of the guided wave modes at that frequency in conjunction with the transducer loading (i.e. out-of-plane), as well as the bandwidth of the annular array excitation spectrum at that wavelength.

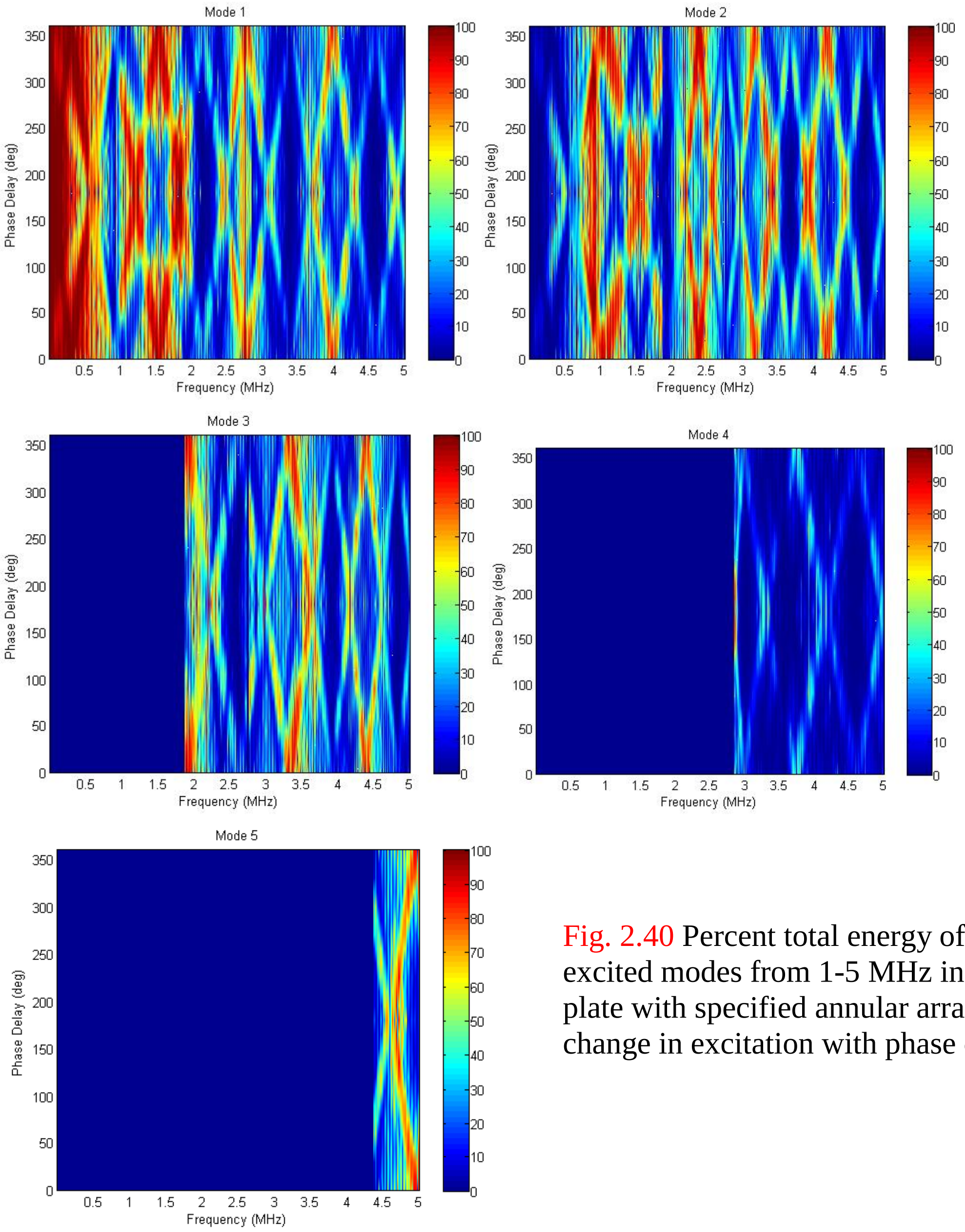

Fig. 2.40 Percent total energy of the first 5 excited modes from 1-5 MHz in 1-mm Al plate with specified annular array, showing change in excitation with phase delay.

Effective Range of Wavelength Control for a Phased Annular Array

By applying phase delays to the elements of an annular array, we have shown that the mode selection capability of the array can be expanded. Different mode and frequency combinations can be selectively excite under different phase delays and frequencies. However, it has to be mentioned that the annular array is in general most effective for a certain wavelength range. Beyond such an effective wavelength range, the mode selection capability is limited even with different phase delays. The excitation spectrum for a given phase delay can provide a good indication of the effectiveness of the array at selectively exciting a particular region of the dispersion curve. Clearly a narrow peak in this spectrum would correspond to highly-selective excitation, while a broad peak would correspond to broad excitation with poor selectivity.

If we consider an annular array with 4 elements that are each 0.1 mm wide, and spaced 0.1 mm apart, for a total transducer diameter of 1.6 mm, it seems highly unlikely that such an array would be able to effectively control wavelengths on the order of 1-2 cm by phasing the individual elements. This can be seen by examining the contour plot of excitation for an annular array as shown in Figure 2.41. For wavelength higher than 1 cm which is 10 times *s*, the selectivity is poor. The poor selectivity can be clearly seen when looking at the 2D excitation spectrum plots.

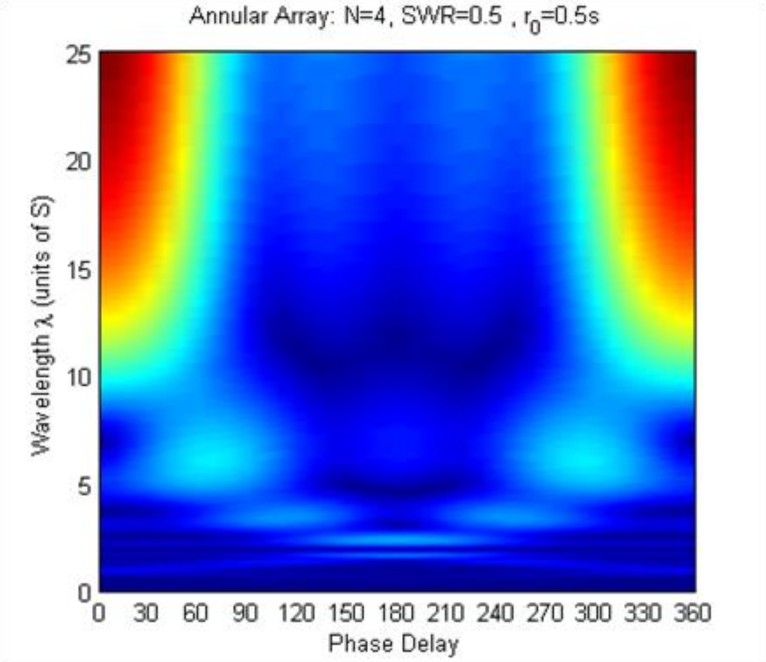

Fig. 2.41 Contour plot of excitation in the wavelength domain for a 4-element annular array over various phase delay values. Notice the poor selectivity in the upper region of $\lambda > 10$s.

Figure 2.42 shows the normalized excitation spectrum plots for a 4 element annular array. The x-axis of the plot is the wavelength in unit of the element spacing *s* and the y-axis is the normalized excitation spectrum values. Different colors are for different phase delays. Note the region in Figure 2.42 where the excitation spectrum rolls off into a large shoulder. At this point in the wavelength domain, there is clearly very little selectivity. For instance, attempting to excite a mode with λ= 20s while suppressing a mode with λ= 25s, would be highly unsuccessful with this annular array (not taking into account the mode excitability, of course, the limitations of which are independent of transducer geometry).

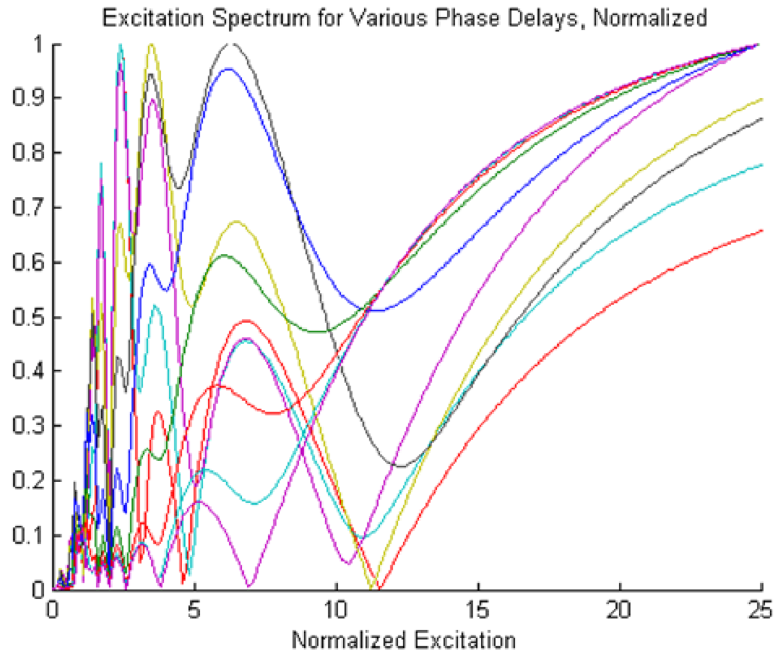

Fig. 2.42 Normalized plots of the excitation spectrum for an N=4 annular array, showing effect excitation range in the wavelength domain.

We can more precisely analyze the effective range for mode selections of annular arrays by examining the wavelength value at which the final minima occurs in the excitation spectrum of an N element annular array for various phase delays. Figure 2.43 shows the results for various N.

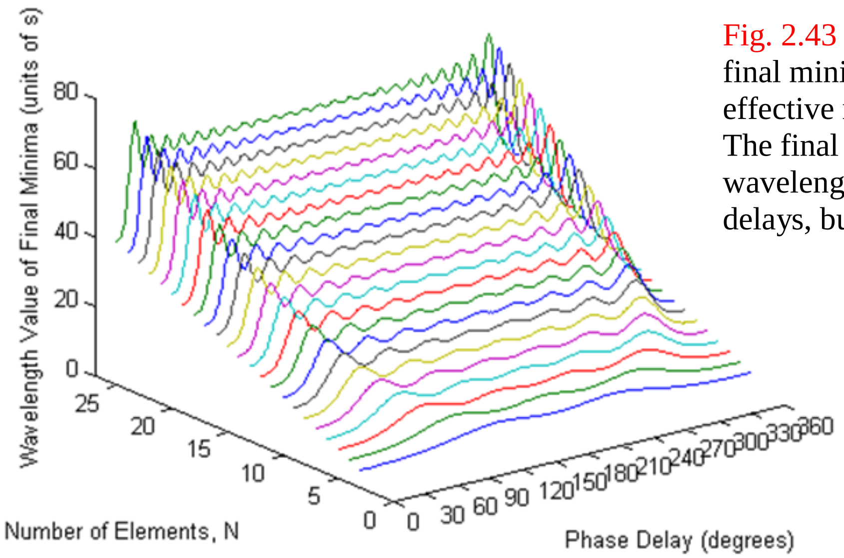

Fig. 2.43 Wavelength at which the final minima occurs. This dictates the effective range of the annular array. The final minima occur at different wavelength values for various phase delays, but a clear pattern is present.

It is interesting to note that the number of peaks in the curves shown above is equal to the N-1, where N is the number of elements for that array. As the number of elements increases, it is easy to see that the value at which the final minima occurs oscillates about a constant value as the phase delays are changed (with the exception of 0 and 360°). By averaging over curves, we can calculate an upper limit for wavelength range of an array with N elements. This average value is plotted vs. N in Figure 2.44 and a clear linear relationship can be observed. This allows one to calculate the effective operating range for a given annular array.

Table 2.IV shows the upper limit of the effective wavelength range for annular arrays ranging from 2-20 elements. The wavelength range, λ_{max} is in terms of the spacing. Thus a wavelength range of 10 for a 4-element array means that it can potentially control wavelengths up to 10 times the array spacing *s*. Such a table is very useful when designing annular array probes. After determining the wavelength range to use for a certain guided wave applications including UMAT applications, one can use the table to determine the minimum number of elements that can ensure reasonable mode selection capability.

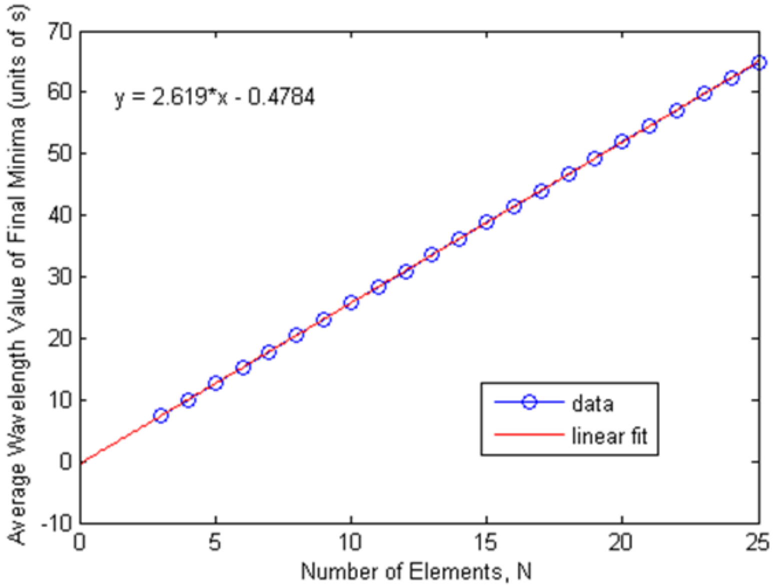

Fig. 2.44 The average wavelength at which the final minima occurs over various phase delay values for an N-element array. An excellent linear fit is achieved.

N	λ_{max} (s)	N	λ_{max} (s)
2	4.76	12	31.0
3	7.33	13	33.6
4	9.98	14	36.2
5	12.6	15	38.8
6	15.2	16	41.4
7	17.9	17	44.1
8	20.5	18	46.7
9	23.1	19	49.3
10	25.7	20	51.9
11	28.3		

Table 2.IV Effective maximum range for N-element annular array transducers.

2.1.5 Concluding Remarks on Annular Array Theory

Theoretical understanding of guided wave excitations in plate structures by axisymmetric sources, in particular, annular arrays, is established. It is shown that, similar to comb transducers, the guided wave excitations of an annular array can be separated into two factors: mode excitabilities and an excitation spectrum. The excitation spectrum can be calculated through a Hankel transform of the axial source loading profile. For comparison, comb transducer excitation spectra are determined by Fourier transforms of the loading profiles. The excitation spectrum of an active-center annular array or an inactive-center annular array with a small inner diameter is quite different from the one of a comb transducer with the same number of elements and element spacing. This is due to the difference in Hankel transform and Fourier transform. It is therefore necessary to the model developed in this paper, instead of the comb transducer model, for the investigations of guided wave excitations by active-center annular arrays and inactive center annular arrays with small inner diameters. By using the large argument approximation of the Bessel function included in the Hankel transform, however, it is not hard to show that the excitation spectrum of an inactive annular array with an inner diameter much larger than the element spacing is approximately identical to that of the corresponding comb transducer. A theoretical solution for excitation spectra of phased annular array transducers is also developed. Such a solution can be used for annular array transducer design and the selection of appropriate phase delays to achieve desired guided wave mode and frequency selection. Based on the theoretical solution, it is also clear that phased annular array transducers can be used to select different guided wave modes and frequencies by varying the phase delays and driving frequencies applied to different array elements.

2.2 Guided Wave Mode Expansion Method for Vibration Study

2.2.1 Introduction

The basic idea of the ultrasonic vibration method that has been developed under this project is that certain vibration modes with special sensitivity to defects of interest can be excited using the guided wave loading functions provided by annular array actuators. The strong ties between vibration modes and guided wave modes are the foundation of the work for this project. Different actuator loading functions (in terms of frequency and phased transducer elements) lead to different steady-state vibration fields in the interrogated structure. The differences in these fields are due to the superposition of various structural modes excited with relative amplitudes and phases. It was initially theorized that a relationship may exist between the transient guided waves initially propagating from the actuator and the final steady-state structural vibration due to the superposition of the interfering wave reflections. In order to further explore this concept theoretically, it was proposed that the final steady-state structural vibrations could be decomposed into the propagating guided wave modes for the structure with relative amplitudes and phases.

Classical thin plate theories, including Kirchhoff and Mindlin theories, are based on the assumption of simplified through-thickness displacement distributions in the plate during vibration.[13,14] These simplifications allow for closed-form analytical solutions of the vibration equations to a reasonable degree of accuracy for calculating general mode shapes and resonant frequencies. However, these theories become inapplicable if the full three-dimensional through-thickness displacement field is of interest, the shear modes are of interest, or thick plates are being investigated.[15, 16] Several approaches exist to solving the three-dimensional elasticity plate vibration problem, including those pioneered by Srinivas[15], Liew[17], Ljunggren[18], and others.

The ultrasonic guided wave vibration formulation was developed on the premise of the partial wave technique, which is a powerful method used in guided wave theory to predict the existence of guided wave modes in isotropic and anisotropic single- or multilayer plate-like structures. The partial wave method relies on the principle of superposition and assumes that all possible bulk wave modes exist in a structure and travel in both the positive and negative transverse directions in the waveguide with unknown amplitude and phase. By applying the concept of superposition, only a finite number of relative amplitude and phase combinations for the various wave modes can collectively satisfy the boundary conditions of the structure. This approach was modified by analyzing the propagation of all possible propagating and evanescent guided wave modes traveling in the positive and negative lengthwise directions of a semi-infinite plate-like structure.

Full-field elasticity solutions of structural vibration problems are often achieved by expanding the solution as a superposition of complete orthogonal functions in the thickness and/or other dimensions of the structure.[15-17] Such sets of complete orthogonal functions include trigonometric functions, Chebyshev polynomials, and other orthogonally generated polynomials. The technique described in this paper can be viewed as a similar expansion in the thickness dimension coupled with a traveling wave assumption in the length dimension. However, in this case of this formulation, the set of complete orthogonal functions utilized for the expansion is not simply chosen based on mathematical convenience. The set of functions used here are the transverse displacement and stress field solutions for the propagating and evanescent guided wave modes in the structure, which satisfy the requirements of a complete and orthogonal set[3]. Thus the relative amplitude and phase vector for any vibration solution will yield physical insight into the connection between transient guided wave and steady-state structural vibration of the structure.

2.2.2 Guided Wave Vibration for Semi-Infinite Plates

The initial structures to be investigated for the guided wave vibration formulation theory were semi-infinite plate-like structures. Such structures have a finite constant thickness, a finite length in one dimension, and an approximately infinite length in the other dimension. Such a model would be representative of any plate-like structure in which one of the dimensions is much greater than the others.

Theoretical Development

The elastic field that satisfies the harmonic equilibrium condition of a semi-infinite plate-like structure in steady-state vibration can be expanded as a superposition of propagating and evanescent guided wave modes traveling in the positive and negative *x*-directions. This can be written in terms of stresses $\boldsymbol{\sigma}$ as

$$\boldsymbol{\sigma}(x,z) = \sum_{\mu=1}^{\infty} \alpha_\mu \bar{\boldsymbol{\sigma}}_\mu(z) e^{i(k_\mu x - \omega t)} + \sum_{\mu=1}^{\infty} \alpha'_\mu \bar{\boldsymbol{\sigma}}_\mu(z) e^{i(k_\mu(x-L) - \omega t)}, \tag{36}$$

in which μ signifies the guided wave mode number, α and α' are the relative complex amplitude coefficient for each mode in the + and –*x*-directions, *k* is the wavenumber, *L* is the length of the plate, ω is the angular frequency, and $\bar{\boldsymbol{\sigma}}$ is the transverse stress field (i.e. wavestructure) solution for each guided wave mode. The first term corresponds to waves traveling in the +*x*-direction and the second term to waves traveling in the –*x*-direction.

The plate was then discretized with *N* nodes along the thickness direction, as shown in Fig. 2.45, and the semi-analytical finite element (SAFE) method [19-22] was utilized to develop the dispersion curves and wavestructure solutions for the desired frequency range in the structure. The result of a SAFE dispersion analysis with *N* nodes is a set of 3*N* guided wave solutions in each *x*-direction.

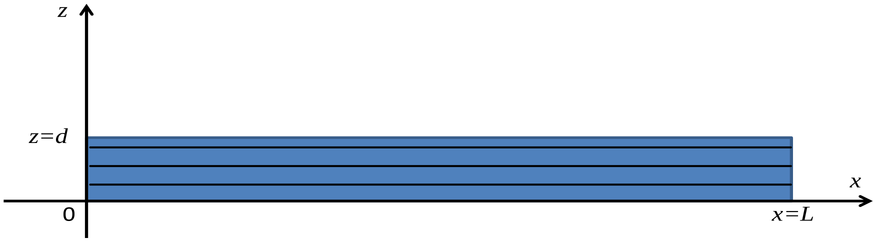

Fig. 2.45 An example of a possible discretization of the semi-infinite plate in the thickness dimension, in which 5 nodes were used in this case.

All six possible combinations of the three classical boundary conditions (free, simply-supported, and clamped) for the semi-infinite plate were successfully considered. The free-free boundary conditions, given as one example, are

$$\begin{cases} \sigma_{xx}(x=0,z) = \sigma_{xx}(x=L,z) = 0 \\ \sigma_{xz}(x=0,z) = \sigma_{xz}(x=L,z) = 0\ . \\ \sigma_{xy}(x=0,z) = \sigma_{xy}(x=L,z) = 0 \end{cases} \tag{37}$$

Upon applying the boundary conditions (37), by the collocation principle, to the discretized equation (36), a matrix equation is developed as a function of frequency:

$$\begin{bmatrix} \sigma_{xx}^{1}(z_1) & \cdots & \sigma_{xx}^{3N}(z_1) & \sigma_{xx}^{1}(z_1)e^{-ik_1L} & \cdots & \sigma_{xx}^{3N}(z_1)e^{-ik_{3N}L} \\ \sigma_{xz}^{1}(z_1) & \cdots & \sigma_{xz}^{3N}(z_1) & \sigma_{xz}^{1}(z_1)e^{-ik_1L} & \cdots & \sigma_{xz}^{3N}(z_1)e^{-ik_{3N}L} \\ \vdots & \vdots & \vdots & \vdots & \vdots & \vdots \\ \sigma_{xy}^{1}(z_N) & \cdots & \sigma_{xy}^{3N}(z_N) & \sigma_{xy}^{1}(z_N)e^{-ik_1L} & \cdots & \sigma_{xy}^{3N}(z_N)e^{-ik_{3N}L} \\ \sigma_{xx}^{1}(z_1)e^{ik_1L} & \cdots & \sigma_{xx}^{3N}(z_1)e^{ik_{3N}L} & \sigma_{xx}^{1}(z_1) & \cdots & \sigma_{xx}^{3N}(z_1) \\ \sigma_{xz}^{1}(z_1)e^{ik_1L} & \cdots & \sigma_{xz}^{3N}(z_1)e^{ik_{3N}L} & \sigma_{xz}^{1}(z_1) & \cdots & \sigma_{xz}^{\prime 3N}(z_1) \\ \vdots & \vdots & \vdots & \vdots & \vdots & \vdots \\ \sigma_{xy}^{1}(z_N)e^{ik_1L} & \cdots & \sigma_{xy}^{3N}(z_N)e^{ik_{3N}L} & \sigma_{xy}^{1}(z_N) & \cdots & \sigma_{xy}^{3N}(z_N) \end{bmatrix} \begin{Bmatrix} \alpha_1 \\ \alpha_2 \\ \alpha_3 \\ \vdots \\ \alpha_{6N} \end{Bmatrix} = \begin{Bmatrix} 0 \\ 0 \\ 0 \\ \vdots \\ 0 \end{Bmatrix} \tag{38}$$

Here the vector of complex amplitudes α is the only unknown and is a function of frequency. This can be written in a simpler manner by representing the large matrix as $\boldsymbol{\Lambda}$:

$$[\Lambda]\{\alpha\} = \{0\} \tag{39}$$

Thus all nontrivial solutions to this matrix equation must correspond to the frequencies at which the determinant of $\boldsymbol{\Lambda}$ is equal to zero:

$$|\boldsymbol{\Lambda}| = 0 \tag{40}$$

This determinant was plotted as a function of ω and an iterative root-finding algorithm was used to locate the frequencies at which equation (40) is approximately satisfied. These frequencies are the natural resonant frequencies of the structure.

In order to determine the complex amplitude vector α associated with each natural resonant frequency, the nullspace of $\boldsymbol{\Lambda}$ at each resonant frequency must be determined. However, since discrete values of ω and a finite number of guided wave modes were used in the superposition formulation, the matrix is not an exact representation of the system. Thus it is possible that all rows of the matrix can be linearly independent, which leads to a situation in which the rank of matrix $\boldsymbol{\Lambda}$ is $6N$ and the nullspace of the matrix subsequently does not exist. To overcome this, an artificial eigenvalue problem can be developed as in equation (41).

$$\boldsymbol{\Lambda\alpha} - \boldsymbol{\lambda\alpha} = 0 \quad ; \boldsymbol{\lambda} = 0 \tag{41}$$

$$\boldsymbol{\lambda} = \begin{Bmatrix} \lambda_1 \\ \lambda_2 \\ \vdots \\ \lambda_{6N} \end{Bmatrix} \quad ; \quad \underline{\boldsymbol{\Phi}} = \begin{bmatrix} \alpha_1^{(1)} & \alpha_1^{(2)} & \dots & \alpha_1^{(6N)} \\ \alpha_2^{(1)} & \alpha_2^{(2)} & \dots & \alpha_2^{(6N)} \\ \vdots & \vdots & \dots & \vdots \\ \alpha_{6N}^{(1)} & \alpha_{6N}^{(2)} & \dots & \alpha_{6N}^{(6N)} \end{bmatrix} = [\boldsymbol{\alpha}^{(1)} \;\; \boldsymbol{\alpha}^{(2)} \;\; \cdots \;\; \boldsymbol{\alpha}^{(6\mathrm{N})}] \tag{42}$$

This equation is identical to (39) as long as the eigenvalue λ is equal to zero. To approximate this case, the eigenvalue problem (40) was solved and the smallest eigenvalue and corresponding eigenvector solution were considered. As long as this minimum eigenvalue is close to zero, the solution is a good approximation of equation (39) and thus (40) as well. Thus the complex amplitude vector for each resonant frequency is the eigenvector associated with the minimum eigenvalue, as shown in equations (43) and (44).

$$\lambda^{\min} = \min(\boldsymbol{\lambda}) \approx 0 \tag{43}$$

$$\boldsymbol{\alpha} = \boldsymbol{\alpha}^{(\lambda_{\min})} = \begin{Bmatrix} \alpha_1 \\ \alpha_2 \\ \alpha_3 \\ \vdots \\ \alpha_{6N} \end{Bmatrix} \tag{44}$$

These solutions were then used to reconstruct the full stress or displacement vibration fields associated with each resonant frequency according to equations (45) and (46), respectively.

$$\boldsymbol{\sigma}(x,z) = \sum_{\mu=1}^{3N} \alpha_\mu \bar{\boldsymbol{\sigma}}_\mu(z) e^{i(k_\mu x - \omega t)} + \sum_{\mu=3N+1}^{6N} \alpha_\mu \bar{\boldsymbol{\sigma}}_\mu(z) e^{i(k_\mu (x-L) - \omega t)} \tag{45}$$

$$\boldsymbol{u}(x,z) = \sum_{\mu=1}^{3N} \alpha_\mu \bar{\boldsymbol{u}}_\mu(z) e^{i(k_\mu x - \omega t)} + \sum_{\mu=3N+1}^{6N} \alpha_\mu \bar{\boldsymbol{u}}_\mu(z) e^{i(k_\mu (x-L) - \omega t)} \tag{46}$$

The 1D Semi-Analytical Finite Element Method (1D SAFE)

The dispersion analysis method known as the semi-analytical finite element (SAFE) method was utilized for the guided wave vibration formulation. The details of this method are given here.

Some waveguide problems lend themselves to reasonable analytical solutions, including the Lamb and Rayleigh problems, as well as simple geometries such as pipes and multi-layered isotropic structures. However, for structure with a complex cross-section and/or anisotropic material properties, analytical solutions can become cumbersome and very difficult to formulate, let alone solve. Thus several techniques exist for solving guided wave problems in such waveguides, one of which is the semi-analytical finite element (SAFE) method.

The SAFE method takes advantage of the known exponential harmonic wave solution in the wave propagation direction,[19-22] as shown in equation (47).

$$\vec{\boldsymbol{u}}(x,z) = \vec{\boldsymbol{U}}(z) e^{i(kx - \omega t)} \tag{47}$$

If we consider guided waves to be traveling waves in the wave propagation direction coupled with transverse resonance, or standing waves, in the waveguide thickness direction(s), then we only need to solve for the latter. To do this, the waveguide must first be discretized into a number of elements. For the case of a plate-like structure in which we assume plane wave solutions (i.e. the structure is infinite in the in-plane direction perpendicular to the wave propagation vector), this entails simple 1-D discretization through the thickness. For this research, 3-node (quadratic) elements were used. As in traditional finite element analysis, the shape functions of these elements can be described in local coordinates by equation (48).

$$[\boldsymbol{N}] = [N_1 \quad N_2 \quad N_3]$$

$$N_1 = \frac{1}{2}\xi(\xi - 1) \qquad N_2 = 1 - \xi^2 \qquad N_3 = \frac{1}{2}\xi(\xi + 1) \tag{48}$$

Therefore the displacements for any element can be written as in equation (49) based on the shape functions **[N]** and nodal displacement vectors $\vec{\boldsymbol{d}}$, combined with the assumed harmonic solution in the wave propagation direction.

$$\{\vec{\boldsymbol{u}}\} = [\boldsymbol{N}(\xi)]\{\vec{\boldsymbol{d}}\}e^{i(kx-\omega t)} \tag{49}$$

Additionally, we can determine the strain and stress relations from the displacement vector from equations (15) and (16).

$$\{\vec{\boldsymbol{\varepsilon}}\} = \left[c\frac{\partial}{\partial x} + \boldsymbol{L}_y\frac{\partial}{\partial y} + \boldsymbol{L}_z\frac{\partial}{\partial z}\right]\{\vec{\boldsymbol{u}}\} \tag{50}$$

$$\{\vec{\boldsymbol{\sigma}}\} = [\boldsymbol{C}]\{\vec{\boldsymbol{\varepsilon}}\} \tag{51}$$

Here $[\boldsymbol{C}]$ for is the material stiffness matrix for each element and $[\boldsymbol{L}_i]$ are the gather matrices in equation (52).

$$\boldsymbol{L}_x = \begin{bmatrix} 1 & 0 & 0 \\ 0 & 0 & 0 \\ 0 & 0 & 0 \\ 0 & 0 & 0 \\ 0 & 0 & 1 \\ 0 & 1 & 0 \end{bmatrix} \qquad \boldsymbol{L}_y = \begin{bmatrix} 0 & 0 & 0 \\ 0 & 1 & 0 \\ 0 & 0 & 0 \\ 0 & 0 & 1 \\ 0 & 0 & 0 \\ 1 & 0 & 0 \end{bmatrix} \qquad \boldsymbol{L}_z = \begin{bmatrix} 0 & 0 & 0 \\ 0 & 0 & 0 \\ 0 & 0 & 1 \\ 0 & 1 & 0 \\ 1 & 0 & 0 \\ 0 & 0 & 0 \end{bmatrix} \tag{52}$$

By substituting the displacement expression in equation (49) into the strain expression in equation (50), we can formulate the strain in terms of the shape functions, gather matrices, and nodal displacements.

$$\{\vec{\boldsymbol{\varepsilon}}\} = (\boldsymbol{B}_1 + ik\boldsymbol{B}_2)\{\vec{\boldsymbol{d}}\}e^{i(kx-\omega t)} \tag{53}$$

in which

$$[\boldsymbol{B}_1] = [\boldsymbol{L}_y]\,\frac{\partial[\mathbf{N}]}{\partial y} + [\boldsymbol{L}_z]\,\frac{\partial[\mathbf{N}]}{\partial z} \qquad \text{and} \qquad [\boldsymbol{B}_2] = [\boldsymbol{L}_x][\mathbf{N}] \tag{54}$$

We can also describe any external traction $\{\vec{t}\}$ in terms of the nodal external traction vector $\{\vec{\boldsymbol{T}}\}$.

$$\{\vec{t}\} = [\mathbf{N}]\{\vec{\boldsymbol{T}}\}e^{i(kx-\omega t)} \tag{55}$$

We now have expressions for all necessary variables in the principle of virtual work, as written in equation (21), in which the δ operator denotes the variation.

$$\int_{\Gamma} \delta\{\vec{\boldsymbol{u}}\}^T\{\vec{t}\}\,d\Gamma = \int_{\mathrm{V}} \delta\{\vec{\boldsymbol{u}}\}^T\rho\,\frac{\partial^2\{\vec{\boldsymbol{u}}\}}{\partial t^2}\,d\mathrm{V} + \int_{\mathrm{V}} \delta\{\vec{\boldsymbol{\varepsilon}}\}^T\{\vec{\boldsymbol{\sigma}}\}\,d\mathrm{V} \tag{56}$$

The substitution of these expressions into the governing equation (56) yields equation (57).

$$\begin{aligned}\int_{\Gamma} \delta\{\vec{\boldsymbol{d}}\}^T[\boldsymbol{N}]^T[\mathbf{N}]\{\vec{\boldsymbol{T}}\}\,d\Gamma \\ &= \int_{\mathrm{V}} \delta\{\vec{\boldsymbol{d}}\}^T[\boldsymbol{N}]^T\left(-k^2\rho[\boldsymbol{N}]\{\vec{\boldsymbol{d}}\}\right)d\mathrm{V} \\ &+ \int_{\mathrm{V}} \delta\{\vec{\boldsymbol{d}}\}^T(\boldsymbol{B}_1 + ik\boldsymbol{B}_2)^T[\boldsymbol{C}](\boldsymbol{B}_1 \\ &+ ik\boldsymbol{B}_2)\,d\mathrm{V}\end{aligned} \tag{57}$$

By removing the arbitrary virtual nodal displacements and simplifying, we find the following relation.

$$\{\vec{\boldsymbol{F}}\} = ([\boldsymbol{K}_1] + ik[\boldsymbol{K}_2] + k^2[\boldsymbol{K}_3])\{\vec{\boldsymbol{d}}\} - \omega^2[\boldsymbol{M}]\{\vec{\boldsymbol{d}}\} \tag{58}$$

In which the following force, mass, and stiffness matrices are used, similarly to conventional finite element analysis.[19-22]

$$\{\vec{\boldsymbol{F}}\} = \int_{-1}^{1}[\boldsymbol{N}]^T[\boldsymbol{N}]\,\{\vec{\boldsymbol{T}}\}\,d\xi$$

$$[\boldsymbol{K}_1] = \int_{-1}^{1}[\boldsymbol{B}_1]^T[\boldsymbol{C}]\,[\boldsymbol{B}_1]\,d\xi$$

$$[\boldsymbol{K}_2] = \int_{-1}^{1} \left([\boldsymbol{B}_1]^T [\boldsymbol{C}][\boldsymbol{B}_2] - [\boldsymbol{B}_2]^T [\boldsymbol{C}][\boldsymbol{B}_1]\right) \, d\xi \tag{59}$$

$$[\boldsymbol{K}_3] = \int_{-1}^{1} [\boldsymbol{B}_2]^T [\boldsymbol{C}] [\boldsymbol{B}_2] \, d\xi$$

$$[\boldsymbol{M}] = \int_{-1}^{1} \rho [\boldsymbol{N}]^T [\boldsymbol{N}] \, d\xi$$

By applying the traction-free boundary conditions on the top and bottom surfaces, an eigenvalue problem can be formed.

$$([\boldsymbol{A}] - k[\boldsymbol{B}])\{\vec{\boldsymbol{Q}}\} = \{\vec{\boldsymbol{p}}\} \tag{60}$$

in which

$$[\boldsymbol{A}] = \begin{bmatrix} 0 & [\boldsymbol{K}_1] - i\omega^2[\boldsymbol{M}] \\ [\boldsymbol{K}_1] - i\omega^2[\boldsymbol{M}] & i[\boldsymbol{K}_2] \end{bmatrix} \qquad [\boldsymbol{B}] = \begin{bmatrix} [\boldsymbol{K}_1] - i\omega^2[\boldsymbol{M}] & 0 \\ 0 & -[\boldsymbol{K}_3] \end{bmatrix}$$

$$\{\vec{\boldsymbol{Q}}\} = \begin{bmatrix} \{\vec{\boldsymbol{d}}\} \\ k\{\vec{\boldsymbol{d}}\} \end{bmatrix} \qquad \{\vec{\boldsymbol{p}}\} = \begin{bmatrix} 0 \\ \{\vec{\boldsymbol{F}}\} \end{bmatrix} \tag{61}$$

For an unloaded plate, $\{\vec{\boldsymbol{F}}\} = \{\vec{\boldsymbol{p}}\} = 0$, and thus equation (60) can be solved by the following determinant.

$$|[\boldsymbol{A}] - k[\boldsymbol{B}]| = 0 \tag{62}$$

The eigenvalue solutions to (62) are the wavenumber k values as a function of ω. From these values, the phase and group velocity dispersion curves can be generated for the structure. The eigenvectors correspond to the wavestructure of each guided wave k-ω solution. A total of $6N$ eigenvalues will result from this system, where N is the total number of nodes in the SAFE model. These eigenvalues may be complex, with real values corresponding to propagating guided wave modes and complex or imaginary values corresponding to evanescent modes (for an elastic material). Half of these solutions correspond to propagation in the $+x$-direction and the other half are the conjugates in the $-x$-direction.

Numerical Analysis and Results

The approach developed in the theory section was coded in MATLAB and a number of cases were analyzed over various frequency ranges. For all cases, a homogeneous isotropic aluminum semi-infinite plate with thickness of 1 mm and length of 100 mm was considered. The material properties of the plate were Young's modulus of 70 GPa, Poisson's ratio of 0.35, and mass density of 2700 kg/m^3. All six possible unique combinations of free, simply-supported, and clamped boundary conditions were used. Initially, the frequencies of interest were limited to those below 60 kHz, but to understand the effect of modes beyond the first guided wave cutoff frequency, a higher frequency range of 2.50 – 2.55 MHz was analyzed.

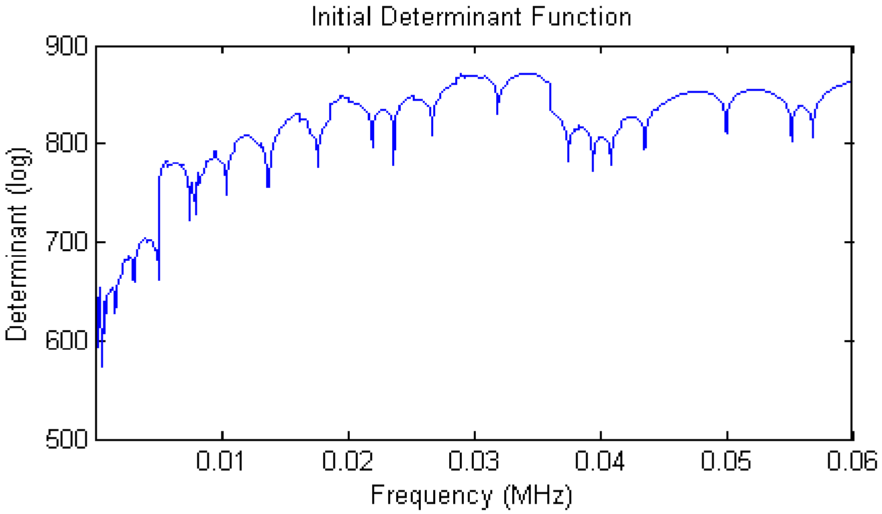

Fig. 2.46 The determinant curve generated by the guided wave vibration formulation for a 1-mm thick by 100-mm long aluminum semi-infinite plate with free-clamped boundary conditions for frequencies ranging from 0-60 kHz.

For the lower frequency range, a typical example of a determinant curve as a function of frequency is given in Fig. 2.46. The natural frequencies of the structure occur at the minima of this curve. The results from the guided wave approach described here are compared to results using a standard finite element (FE) eigenvalue solver in Abaqus Standard with equivalent discretization in the thickness direction. The results of this comparison are shown in Table 2.V.

Table 2.V Comparison of the natural resonant frequency results for a 1-mm thick by 100-mm long aluminum semi-infinite plate with free-clamped boundary conditions, calculated by the guided wave method developed here as well as a FE solver in Abaqus Standard, both with 21 nodes through the thickness.

Mode Type	FEM Freq.	GW Freq.	% Diff
Flexural 1	550	551	0.18%
Flexural 2	1539	1541	0.13%
Flexural 3	3012	3017	0.17%
Flexural 4	4972	4979	0.14%
Flexural 5	7412	7424	0.16%
Shear 1	N/A	7883	N/A
Flexural 6	10329	10345	0.15%
Compressional 1	13594	13613	0.14%
Flexural 7	13716	13738	0.16%
Flexural 8	17565	17594	0.17%
Flexural 9	21869	21906	0.17%
Shear 2	N/A	23649	N/A
Flexural 10	26618	26666	0.18%
Flexural 11	31805	31864	0.19%
Flexural 12	37418	37491	0.20%
Shear 3	N/A	39416	N/A
Compressional 2	40781	40837	0.14%
Flexural 13	43447	43536	0.20%
Flexural 14	49882	49989	0.21%
Shear 4	N/A	55182	N/A
Flexural 15	56712	56839	0.22%

Note that the values of the determinant in Fig. 2.46, even at the minima, are extremely large and cannot be approximated as zero. This is due to the fact that the determinant is that of a 126 x 126 matrix comprised of stress values on the order of 10^6 to 10^9 as well as displacement values on the order of 10^{-6} to 10^{-9}. If clamped-clamped boundary conditions (all displacement) are used, the determinant values are closer to the order of 10^{-300}, while if free-free boundary conditions (all stress) are used, they are on the order of 10^{5000}. Regardless of the explicit values of the determinant, the matrix can be normalized if desired, and the roots are found to be the minima. As is shown in Table 2.V, the fact that the determinant values do not approach zero does not negate the accuracy of the method, as the % error for all frequencies is less than 0.25%.

For the purposes of this research, the guided wave modes that comprise each resonance are of equal importance as the frequencies at which those resonances occur. To analyze the relative significance of each guided wave mode with regard to each structural vibration mode, the complex amplitude vector α can be analyzed at each resonant frequency. Recall that this amplitude vector is determined by equations (41)-(44). The amplitude vectors were normalized and the relative amplitudes of the propagating guided wave modes were plotted for each resonant frequency, as in Fig. 3. Note that in this lower frequency range only three propagating guided wave modes exist: SH0, S0, and A0. It is apparent from these bar plots that each resonance is associated with a single propagating guided wave mode in the frequency range below the first cutoff. This will not be the case at higher frequencies, in which vibration modes corresponding to coupled guided wave modes can exist.

Although frequencies as high as 60 kHz may be considered quite high for traditional structural modal analysis, these are relatively low in the guided wave domain. To ensure that this method accurately calculates resonant frequencies in higher frequency ranges, as well as to investigate the relationship between guided waves above the first cutoff and steady-state vibration, analyses were performed in the range of 2.50-2.55 MHz. The results of such an analysis for the free-free case are shown in Fig. 4 and 5. Note that a single vibration mode may be associated with multiple guided wave modes in this frequency range. This agrees well with the mode conversion behavior of a normally incident guided wave below the first cutoff, for which mode conversion does not occur.

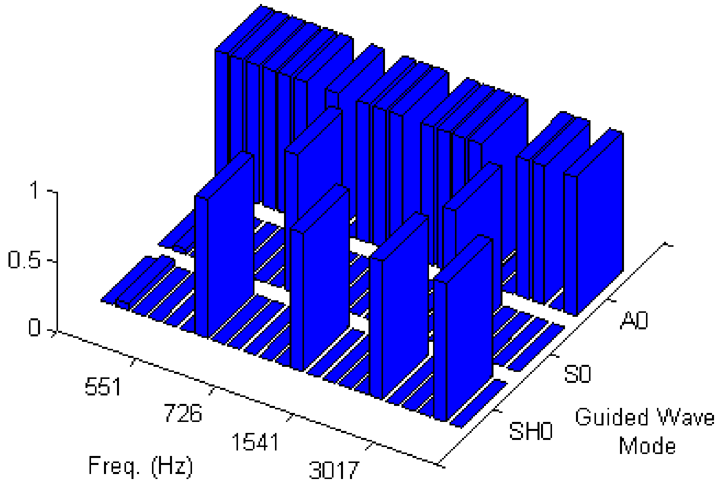

Fig. 2.47 The relative guided wave mode amplitudes corresponding to the resonant frequencies from 0-60 kHz for a 1-mm thick by 100-mm long aluminum semi-infinite plate with free-clamped boundary conditions. Note that no mode coupling occurs and each resonance can be attributed to a single propagating guided wave mode.

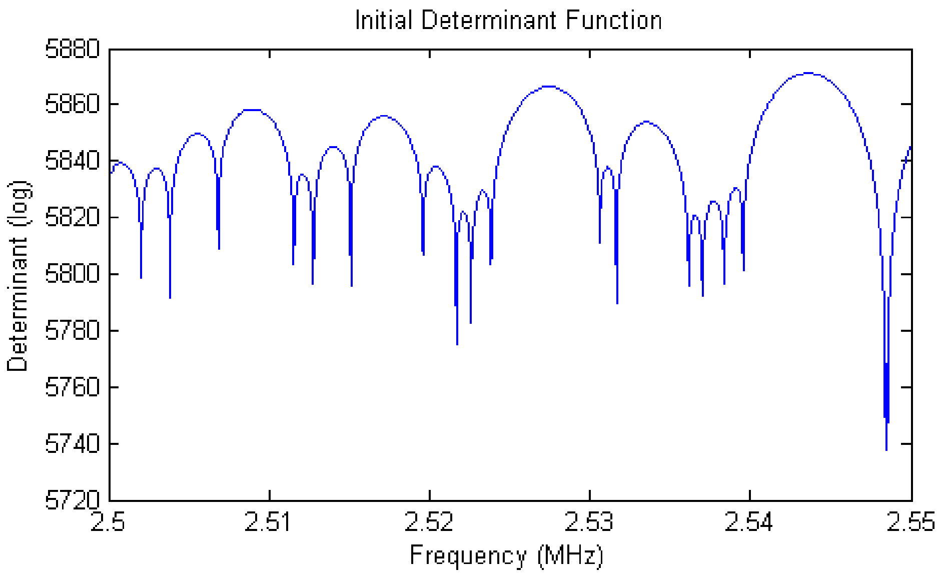

Fig. 2.48 Determinant curve for free-free semi-infinite plate in the frequency range of 2.50-2.55 MHz.

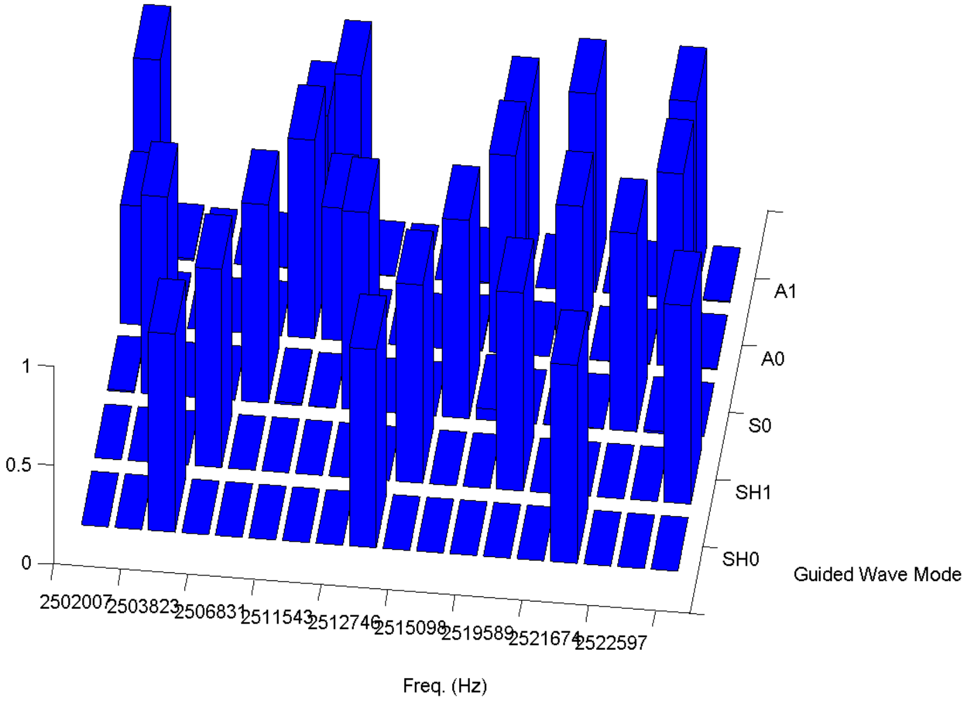

Fig. 2.49 The relative guided wave mode amplitudes corresponding to the resonant frequencies from 2.50-2.55 MHz for a free-free plate. Note that mode coupling does occur above the first cutoff frequency.

In addition to the analysis of resonant frequencies and guided wave mode amplitudes, the full elastic field associated with each resonance (i.e. the mode shape) can also be determined. This is done by combining the guided wave modes with respect to the amplitude vector α according to equations (45) or (46). One example of such a reconstruction is shown in Fig. 2.50 for the in-plane and out-of-plate displacement fields associated with the 3rd vibration mode at 3017 Hz for the aluminum semi-infinite plate previously described. The fields shown here, as well as the other fields calculated using the guided wave method, are in excellent agreement with the standard FE mode shapes. Note that although only the propagating guided wave mode amplitudes are shown in Fig. 2.47 and 2.49, the evanescent modes are critical in order to satisfy the boundary conditions and must be included during the field reconstruction to achieve an accurate result.

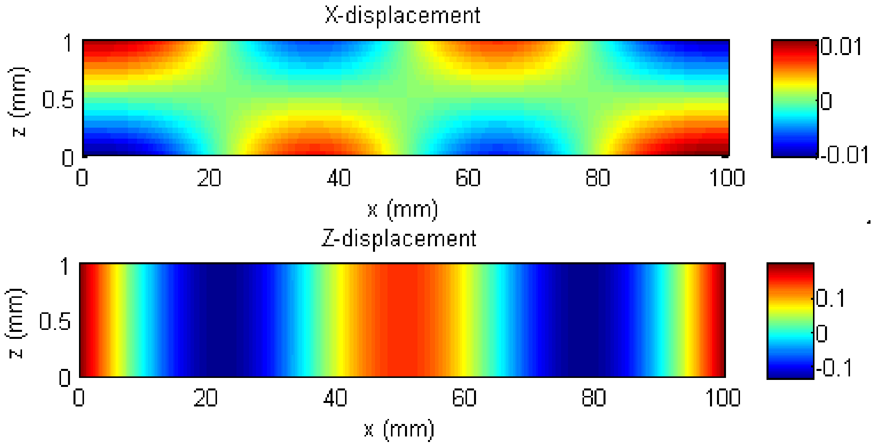

Fig. 2.50 The reconstructed displacement fields for the 3rd vibration mode of the semi-infinite plate at 3017 Hz.

2.2.3 Guided Wave Vibrations for Cylindrical Structures with Arbitrary Cross-Section

Beyond the semi-infinite plate structures initially investigated to determine the validity of the guided wave vibration theory, more complex finite structures were also examined using a similar approach. These are cylindrical structures with arbitrary cross-section, which could include any bars or beams with any cross-section (i.e. circular, rectangular, or of any complex 2D shape).

Theoretical Development

The guided wave vibration formulation for semi-infinite plate like structures provided a significant amount of insight into the link between transient waves and steady-state vibration. However, the direct applicability of the results is limited by the semi-infinite nature of the structure analyzed in the problem. In order to apply the results to more realistic finite three-dimensional structures, the method was expanded to cylindrical objects with arbitrary cross-section. This would include bars, beams, rails, and many other structures.

In order to realize this expansion, a two-dimensional semi-analytical finite element (2D SAFE) approach was utilized to develop the dispersion and wavestructure solutions for the structure. The 2D SAFE method is formulated along the same lines as the 1D SAFE method detailed above, with changes to accommodate the additional dimensionality of the problem. For the case shown in Figure 2.51, a 1 meter long bar with a rectangular cross-section of 4 x 8 cm was considered. A linear 8 x 8 element mesh was used for the analysis, as detailed in Figures 2.52 and 2.53.

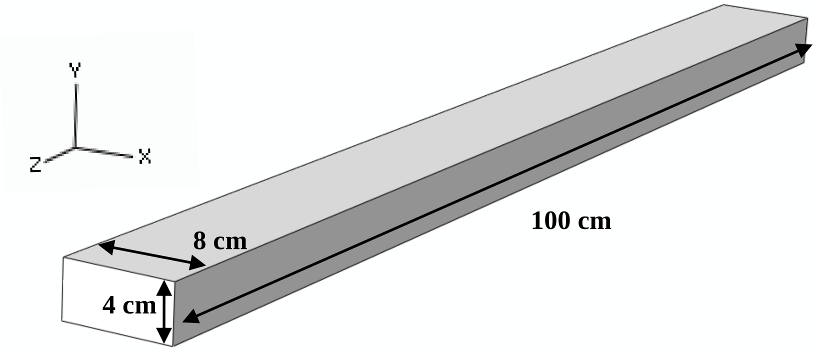

Fig. 2.51 Diagram of the 4 cm x 8 cm x 1 m beam

Mathematically, the guided wave vibration formulation for the three-dimensional cylindrical problem is very similar to that for the semi-infinite plate problem, with the exception of the 2D SAFE instead of the 1D SAFE dispersion analysis. However, instead of applying the boundary conditions to each node through the thickness, they must be applied to all nodes across the cross-section of the ends of the structure. For the case of the rectangular beam with 8 x 8 elements detailed here, this approach yields 243 left- and right-traveling power-normalized guided wave dispersion and wavestructure solutions and thus the full system of equations must contain 486 homogeneous boundary conditions equations. This leads to a characteristic matrix $\mathbf{\Lambda}$(f) with dimensions 486 x 486.

The 2D Semi-Analytical Finite Element Method (2D SAFE)

The SAFE method takes advantage of the known exponential harmonic wave solution in the wave propagation direction, as shown in equation (63).

$$\vec{u}(x,y,z) = \vec{U}(y,z)e^{i(kx-\omega t)} \qquad (63)$$

If we consider guided waves to be traveling waves in the wave propagation direction coupled with transverse resonance, or standing waves, in the waveguide thickness direction(s), then we only need to solve for the latter. To do this, the waveguide must first be discretized into a number of elements. For the case of a cylindrical object with arbitrary cross-section, this entails 2D discretization of the cross-section, as shown in Figure 2.52. For this research, 4-node (linear) elements were used, as shown in Figure 2.53. As in traditional finite element analysis, the shape functions of these elements can be described in local coordinates by equations (64) and (65).

$$[\boldsymbol{N}(\xi,\eta)] = \begin{bmatrix} N_1 & 0 & 0 & N_2 & 0 & 0 & N_3 & 0 & 0 & N_4 & 0 & 0 \\ 0 & N_1 & 0 & 0 & N_2 & 0 & 0 & N_3 & 0 & 0 & N_4 & 0 \\ 0 & 0 & N_1 & 0 & 0 & N_2 & 0 & 0 & N_3 & 0 & 0 & N_4 \end{bmatrix} \tag{64}$$

$$N_1 = \frac{1}{4}(1-\xi)(1-\eta) \qquad N_2 = \frac{1}{4}(1+\xi)(1-\eta)$$

$$N_3 = \frac{1}{4}(1+\xi)(1+\eta) \qquad N_3 = \frac{1}{4}(1-\xi)(1+\eta) \tag{65}$$

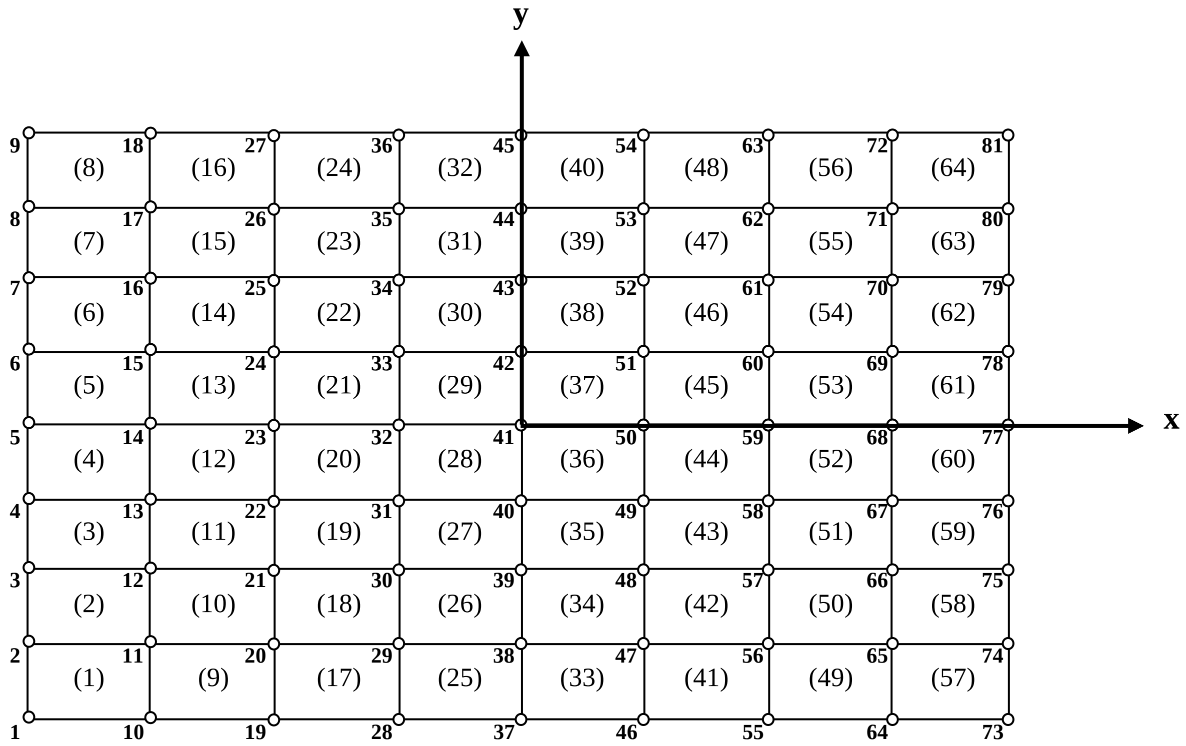

Fig. 2.52 Mesh for the beam cross-section

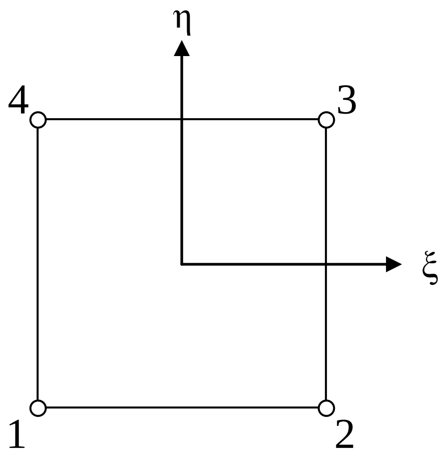

Fig. 2.53 Local coordinate system for linear elements

Therefore the displacements for any element can be written as in equation (66) based on the shape functions **[N]** and nodal displacement vectors $\vec{\boldsymbol{d}}$, combined with the assumed harmonic solution in the wave propagation direction.

$$\{\vec{\boldsymbol{u}}\} = [\boldsymbol{N}(\xi,\eta)]\{\vec{\boldsymbol{d}}\}e^{i(kx-\omega t)} \tag{66}$$

Additionally, we can determine the strain and stress relations from the displacement vector from equations (67) and (68).

$$\{\vec{\boldsymbol{\varepsilon}}\} = \left[\boldsymbol{L}_x\frac{\partial}{\partial x} + \boldsymbol{L}_y\frac{\partial}{\partial v} + \boldsymbol{L}_z\frac{\partial}{\partial z}\right][\boldsymbol{N}(\xi,\eta)]\{\vec{\boldsymbol{u}}\}e^{i(kx-\omega t)} \tag{67}$$

$$\{\vec{\boldsymbol{\sigma}}\} = [\boldsymbol{C}]\{\vec{\boldsymbol{\varepsilon}}\} \tag{68}$$

Here $[\boldsymbol{C}]$ for is the material stiffness matrix for each element and $[\boldsymbol{L}_i]$ are the gather matrices in equation (69).

$$\boldsymbol{L}_x = \begin{bmatrix} 1 & 0 & 0 \\ 0 & 0 & 0 \\ 0 & 0 & 0 \\ 0 & 0 & 0 \\ 0 & 0 & 1 \\ 0 & 1 & 0 \end{bmatrix} \qquad \boldsymbol{L}_y = \begin{bmatrix} 0 & 0 & 0 \\ 0 & 1 & 0 \\ 0 & 0 & 0 \\ 0 & 0 & 1 \\ 0 & 0 & 0 \\ 1 & 0 & 0 \end{bmatrix} \qquad \boldsymbol{L}_z = \begin{bmatrix} 0 & 0 & 0 \\ 0 & 0 & 0 \\ 0 & 0 & 1 \\ 0 & 1 & 0 \\ 1 & 0 & 0 \\ 0 & 0 & 0 \end{bmatrix} \tag{69}$$

By substituting the displacement expression in equation (66) into the strain expression in equation (67), we can formulate the strain in terms of the shape functions, gather matrices, and nodal displacements.

$$\{\vec{\boldsymbol{\varepsilon}}\} = (\boldsymbol{B}_1 + ik\boldsymbol{B}_2)\{\vec{\boldsymbol{d}}\}e^{i(kx-\omega t)} \tag{70}$$

in which

$$[\boldsymbol{B}_1] = [\boldsymbol{L}_y]\frac{\partial[\mathbf{N}]}{\partial y} + [\boldsymbol{L}_z]\frac{\partial[\mathbf{N}]}{\partial z} \qquad \text{and} \qquad [\boldsymbol{B}_2] = [\boldsymbol{L}_x][\mathbf{N}] \tag{71}$$

We can also describe any external traction $\{\vec{\boldsymbol{t}}\}$ in terms of the nodal external traction vector $\{\vec{\boldsymbol{T}}\}$.

$$\{\vec{\boldsymbol{t}}\} = [\mathbf{N}]\{\vec{\boldsymbol{T}}\}e^{i(kx-\omega t)} \tag{72}$$

We now have expressions for all necessary variables in the principle of virtual work, as written in equation (73), in which the δ operator denotes the variation.

$$\int_{\Gamma} \delta\{\vec{\boldsymbol{u}}\}^T\{\vec{\boldsymbol{t}}\}\,d\Gamma = \int_{V} \delta\{\vec{\boldsymbol{u}}\}^T\rho\frac{\partial^2\{\vec{\boldsymbol{u}}\}}{\partial t^2}\,dV + \int_{V} \delta\{\vec{\boldsymbol{\varepsilon}}\}^T\{\vec{\boldsymbol{\sigma}}\}\,dV \tag{73}$$

The substitution of these expressions into the governing equation (38) yields equation (74).

$$\begin{aligned}
&\int_{\Gamma} \delta\{\vec{\boldsymbol{d}}\}^T[\boldsymbol{N}]^T[\mathbf{N}]\{\vec{\boldsymbol{T}}\}\,d\Gamma \\
&\qquad = \int_{V} \delta\{\vec{\boldsymbol{d}}\}^T[\boldsymbol{N}]^T(-k^2\rho[\boldsymbol{N}]\{\vec{\boldsymbol{d}}\})\,dV \\
&\qquad + \int_{V} \delta\{\vec{\boldsymbol{d}}\}^T(\boldsymbol{B}_1 + ik\boldsymbol{B}_2)^T[\boldsymbol{C}](\boldsymbol{B}_1 \\
&\qquad + ik\boldsymbol{B}_2)\,dV
\end{aligned} \tag{74}$$

By removing the arbitrary virtual nodal displacements and simplifying, we find the following relation.

$$\{\vec{\boldsymbol{F}}\} = ([\boldsymbol{K}_1] + ik[\boldsymbol{K}_2] + k^2[\boldsymbol{K}_3])\{\vec{\boldsymbol{d}}\} - \omega^2[\boldsymbol{M}]\{\vec{\boldsymbol{d}}\} \tag{75}$$

In which the following force, mass, and stiffness matrices are used, similarly to conventional finite element analysis.

$$\{\vec{\boldsymbol{F}}\} = \int_{-1}^{1}\int_{-1}^{1}[\boldsymbol{N}]^T[\boldsymbol{N}]\{\vec{\boldsymbol{T}}\}\,d\xi\,d\eta$$

$$[\boldsymbol{K}_1] = \int_{-1}^{1}\int_{-1}^{1}[\boldsymbol{B}_1]^T[\boldsymbol{C}][\boldsymbol{B}_1]\,d\xi\,d\eta$$

$$[\boldsymbol{K}_2] = \int_{-1}^{1}\int_{-1}^{1}([\boldsymbol{B}_1]^T[\boldsymbol{C}][\boldsymbol{B}_2] - [\boldsymbol{B}_2]^T[\boldsymbol{C}][\boldsymbol{B}_1])\,d\xi\,d\eta \tag{76}$$

$$[\boldsymbol{K}_3] = \int_{-1}^{1}\int_{-1}^{1} [\boldsymbol{B}_2]^T [\boldsymbol{C}]\, [\boldsymbol{B}_2]\; d\xi\, d\eta$$

$$[\boldsymbol{M}] = \int_{-1}^{1}\int_{-1}^{1} \rho [\boldsymbol{N}]^T [\boldsymbol{N}]\;\; d\xi\, d\eta$$

By applying the traction-free boundary conditions on the top and bottom surfaces, an eigenvalue problem can be formed.

$$([\boldsymbol{A}] - k[\boldsymbol{B}])\{\vec{\boldsymbol{Q}}\} = \{\vec{\boldsymbol{p}}\} \tag{77}$$

in which

$$[\boldsymbol{A}] = \begin{bmatrix} 0 & [\boldsymbol{K}_1] - i\omega^2[\boldsymbol{M}] \\ [\boldsymbol{K}_1] - i\omega^2[\boldsymbol{M}] & i[\boldsymbol{K}_2] \end{bmatrix} \qquad [\boldsymbol{B}] = \begin{bmatrix} [\boldsymbol{K}_1] - i\omega^2[\boldsymbol{M}] & 0 \\ 0 & -[\boldsymbol{K}_3] \end{bmatrix}$$

$$\{\vec{\boldsymbol{Q}}\} = \begin{bmatrix} \{\vec{\boldsymbol{d}}\} \\ k\{\vec{\boldsymbol{d}}\} \end{bmatrix} \qquad \{\vec{\boldsymbol{p}}\} = \begin{bmatrix} 0 \\ \{\vec{\boldsymbol{F}}\} \end{bmatrix} \tag{78}$$

For an unloaded plate, $\{\vec{\boldsymbol{F}}\} = \{\vec{\boldsymbol{p}}\} = 0$, and thus equation (77) can be solved by the following determinant.

$$|[\boldsymbol{A}] - k[\boldsymbol{B}]| = 0 \tag{79}$$

Just as in the 1D SAFE solution, the eigenvalue solutions to (79) are the wavenumber k values as a function of ω. From these values, the phase and group velocity dispersion curves can be generated for the structure. The eigenvectors correspond to the wavestructure of each guided wave k-ω solution. A total of $6N$ eigenvalues will result from this system, where N is the total number of nodes in the SAFE model. These eigenvalues may be complex, with real values corresponding to propagating guided wave modes and complex or imaginary values corresponding to evanescent modes (for an elastic material). Half of these solutions correspond to propagation in the $+x$-direction and the other half are the conjugates in the $-x$-direction.

Numerical Analysis and Results

For the case discussed here, a frequency range of 0-5000 Hz was selected for consideration, because it contains a number of flexural, compressional, and torsional natural modes, as determined by a traditional eigenvalue analysis in Abaqus 6.9 commercial finite element software. Direct calculation of the determinant of this characteristic matrix leads to exceedance of the real max and real min values of MATLAB in double precision, so the condition value of the matrix was used instead to determine the frequencies for which the matrix is approximately singular.

The dispersion curves for the structure, which were extracted from the 2D SAFE solutions, are shown in Figure 2.54. The mode with the highest phase velocity is the fundamental symmetric-type mode, the mode with the second-highest phase velocity is the fundamental shear-type mode, and the other two modes are the fundamental anti-symmetric-type modes corresponding to the x- and y-dimensions of the cross-section.

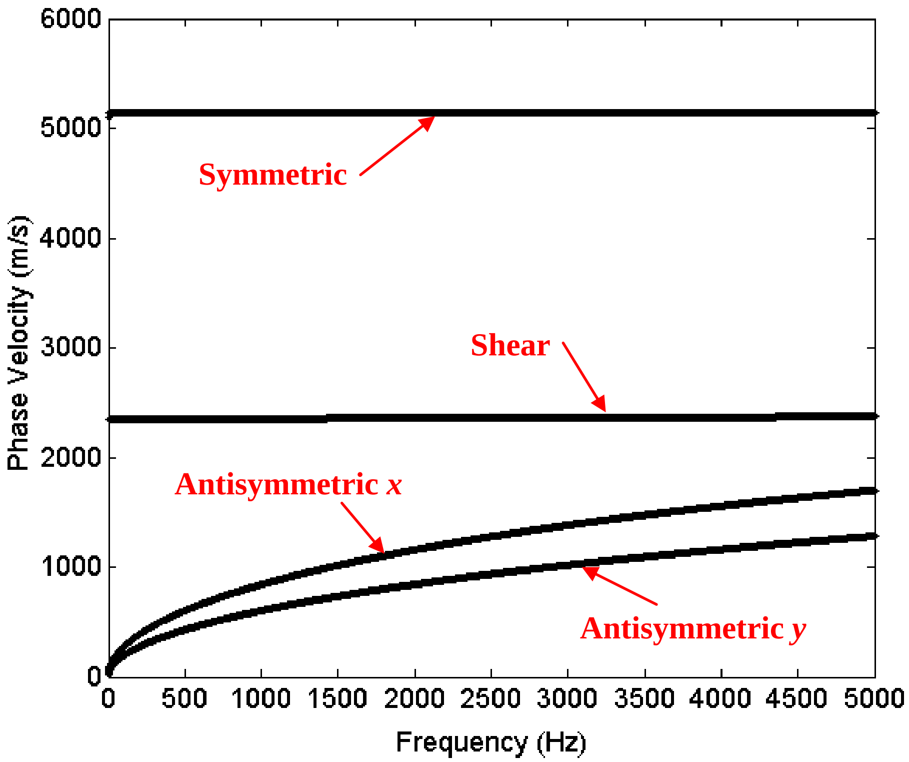

Fig. 2.54 Dispersion curves for the 4 cm x 8 cm rectangular cross section

The resonant frequencies are visible as spikes in the condition value curve for the characteristic matrix. The values of these resonant frequencies were compared to those obtained by a traditional eigenvalue analysis in Abaqus 6.9 for the same structure. A finer mesh was used in the eigenvalue analysis to ensure convergence. The results are compared in Table 2.VI.

In addition to the calculation of the resonant frequencies of each vibration mode, the amplitude factors of different guided wave modes in the expanded vibration fields at vibration resonances were calculated. Figure 2.55 shows the amplitude factors of four guided wave modes for the first several resonant frequencies of a bar with an 80 mm by 40 mm by 1 m dimension. The mode 1, mode 2, mode 3 are the three fundamental guided wave modes for the beam. The amplitude factors were normalized in a way that the summation of all amplitude factors for all the guided wave modes equals 1. Since the upper limit of the frequency range shown in the figure is below the first cut-off frequency of the beam, the vibration resonances are all strongly associated with a single guided wave mode, i.e., for each vibration resonance, one of the four guided wave modes has an amplitude factor very close to 1. This is fully expected from our previous work on mode conversion studies for guided wave reflections at straight edges, in which we have shown that there are no mode conversions under the first cut-off frequencies for the plane wave normal incident cases. As a validation for the amplitude calculations of the guided wave mode expansion method, the amplitude factors for the first 17 vibration modes are given in Table 2.VI. The parameters used in the calculations and the calculation errors are also given. Notice that the errors are all lower than 1%. The calculated amplitude factors were also used with the mode expansion formula to calculate the vibration mode shapes. Very good agreements between the mode shapes calculated using the amplitude factors and the ones predicted by FEM. The mode expansion method is therefore further validated.

Table 2.VI Summary of amplitude factor calculation results for the validation of the guided wave mode expansion method

Steady State Vibration		**Resonant Frequencies**				**Guided Wave Amplitudes**				
Vib. Mode Type	*Vib. Mode Order*	*FEM_lim*	*FEM_mesh*	*GW Vib*	*% error*	*GW 1 (A_y)*	*GW 2 (A_x)*	*GW 3 (SH)*	*GW 4 (S)*	*Match?*
Flexural	1_y	**211**	209	212	0.47%	1	0.01	0.01	0	✓
Flexural	1_x	**408**	405	409	0.25%	0	1	0	0	✓
Flexural	2_y	**573**	569	575	0.35%	1	0	0	0	✓
Flexural	2_x	**1069**	1062	1071	0.19%	0.01	1	0	0	✓
Flexural	3_y	**1103**	1097	1107	0.36%	1	0	0.01	0	✓
Torsional	1	**1189**	1167	1197	0.67%	0	0.02	1	0	✓
Flexural	4_y	**1785**	1774	1792	0.39%	1	0.03	0.01	0	✓
Flexural	3_x	**1976**	1965	1981	0.25%	0	1	0	0	✓
Torsional	2	**2382**	2337	2398	0.67%	0.01	0.01	1	0.01	✓
Compressional	1	**2583**	2583	2584	0.04%	0	0	0	1	✓
Flexural	5_y	**2602**	2586	2611	0.35%	1	0	0	0	✓
Flexural	4_x	**3063**	3047	3071	0.26%	0	1	0	0	✓
Flexural	6_y	**3536**	3513	3550	0.40%	1	0	0	0	✓
Torsional	3	**3581**	3516	3605	0.67%	0.01	0.01	1	0	✓
Flexural	5_x	**4281**	4260	4294	0.30%	0.01	1	0.01	0.01	✓
Flexural	7_y	**4573**	4548	4590	0.37%	1	0	0	0	✓
Torsional	4	**4788**	4694	4821	0.69%	0	0.01	1	0	✓

For conceptual understanding, the deformed mode shapes of the beam with superimposed von Mises stress distributions from the Abaqus eigenvalue analysis are shown in Figures 2.56 through 2.59.

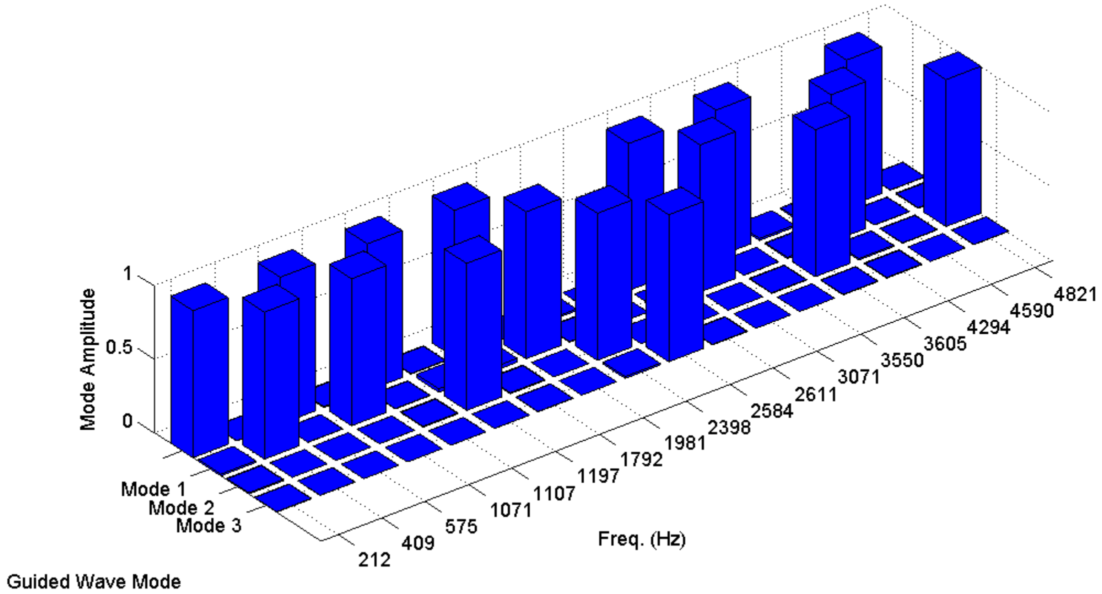

Fig. 2.55 Guided wave amplitude factors for the vibration modes of a rectangular beam.

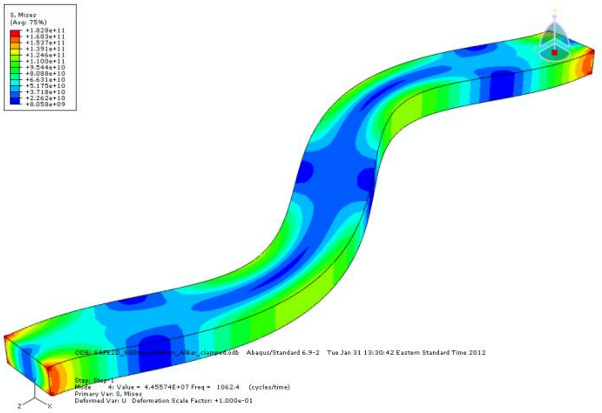

Fig. 2.56 Flexural mode 2_x

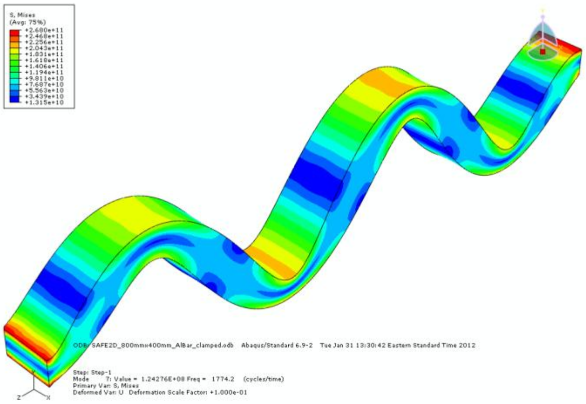

Fig. 2.57 Flexural mode 4_y

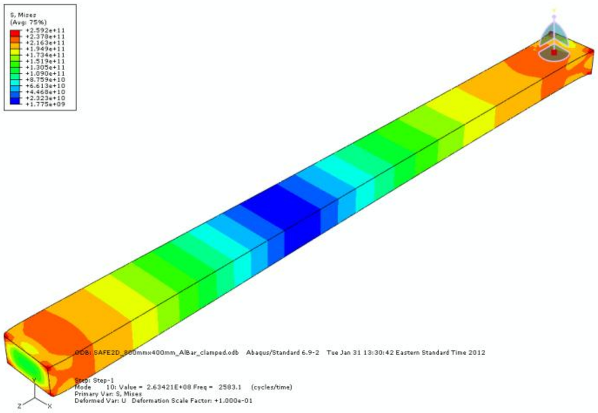

Fig. 2.58 Compressional mode 1

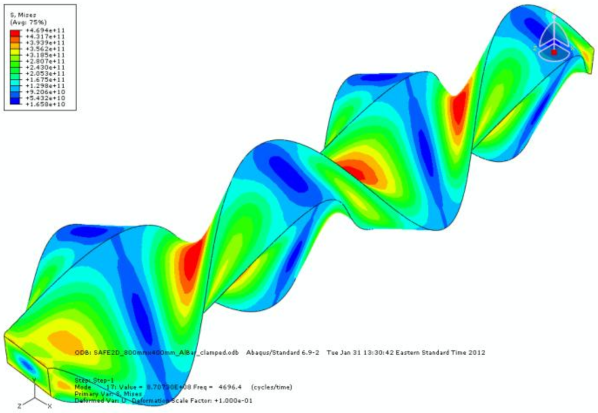

Fig. 2.59 Torsional mode 4

2.2.4 Significance and Interpretation of the Guided Wave Theory

The development of guided wave vibration theory for various structures provides significant new insight into the connection between transient guided wave propagation and steady-state structural vibration. Not only does this work successfully demonstrate that the resonant frequencies and mode shapes of various structures (across a broad range of frequencies) can be calculated based on guided wave theory, but it also allows us to associate known structural resonance frequencies and mode shapes with specific propagating guided wave modes. This understanding could be utilized to selectively design appropriate actuators to excite guided wave modes with desired properties and have a transducer resonance at the resonant frequency of the structure associated with that desired guided wave mode. Additionally, based on the known sensitivity properties of different guided wave modes, these properties could be extended to the structural resonance(s) that are comprised primarily of that mode. All the possibilities of applying this knowledge to the UMAT concept are yet to be investigated.

3. Finite Element Simulation

Throughout this project, finite element simulations were used extensively to serve as powerful numerical experimentation to validate theoretical developments and also to assist in actuator design.

3.1 FE Validation of Annular Array Theory

3.1.1 Waveform Predictions for Phased Annular Array Transducers

To verify the theoretical development established for phased annular array transducers during this project, several finite element (FE) simulations were performed in Abaqus/Explicit commercial finite element software.

Finite Element Model Design

The finite element model chosen to test the waveform predictions for annular arrays is a 1-mm-thick isotropic aluminum disk with material properties: Young's modulus = 70 GPa, Poisson's ratio = 0.35, and density = 2700 kg/m^3. Normal pressure loading was applied evenly across the area of the transducer elements at a pressure of 1000 N/m^3. The time-domain signal applied to the elements was a 5-cycle Hanning-windowed tone burst centered at 300 kHz. The annular array parameters were as follows: N = 4, s = 3 mm, WSR = ½, and r_0 = 1.5 mm. Linear time delays of 833 ns were applied to the elements. Measurement output was taken as in-plane and out-of-plane displacement on the top and bottom surfaces at a distance of 30 cm from the center of the array. Sampling frequency used for data collection was 25MHz. The model was constructed using axisymmetric stress elements and the model discretization was done with a mesh size on the order of 50 µm. A picture of the model near the transducer is given in Figure 3.1. Figures 3.2 and 3.3 show the in-plane displacement fields of the A0 and S0 modes, respectively.

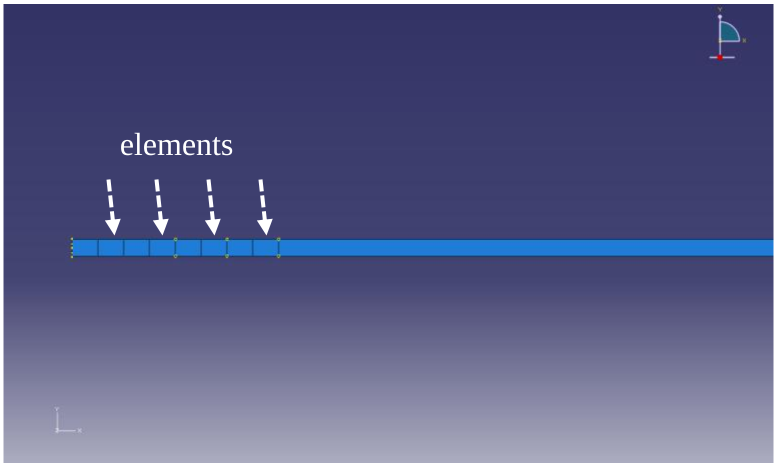

Fig. 3.1 Finite element model of 1-mm aluminum plate and N=4 annular array transducer elements.

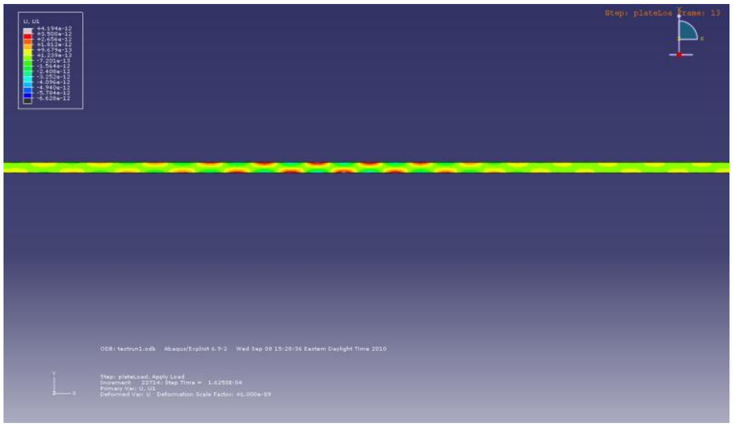

Fig. 3.2 In-plane displacement field of the A0 mode propagating in the FE simulation.

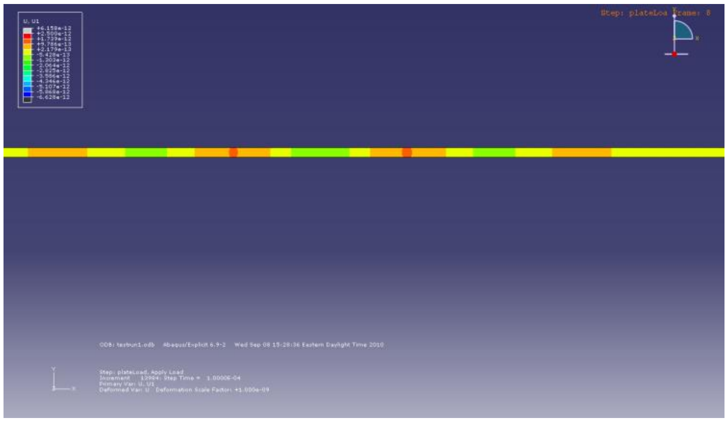

Fig. 3.3 In-plane displacement field of the S0 mode propagating in the FE simulation.

Analytical Waveform Expressions

Recall that the displacements **u** associated with a propagating guided wave mode ν generated at a distance *x* and depth *z* due to a point source surface traction **t** on domain ζ is described by equation (80).

$$\mathbf{u}_\nu(x,z) = \left[\frac{\mathbf{v}_\nu^*(d/2)}{4P_{\nu\nu}} \cdot \int_{-\infty}^{\infty} \mathbf{t}(\zeta)e^{-ik_\nu^*\zeta}\; d\zeta\right]\bar{\mathbf{u}}_\nu(z)e^{i(k_\nu^* x-\omega t)} \qquad (80)$$

By applying this point source solution to the geometry of the phased annular arrays studied here, an expression for the displacements generated by such arrays for particular guided wave mode ν is described in equations (81), in which $\mathbf{E}_\nu$ is the excitability matrix for the mode.

$$u_{r\nu} \approx \sqrt{\frac{2\pi}{ik_\nu r}}E_{xz_\nu}\rho_{Tr}\left[\sum_{n=0}^{N-1}\{R_{2_n}J_1[R_{2_n}k]-R_{1_n}J_1[R_{1_n}k]\}\right]e^{i(k_\nu r-n\omega\Delta t)} \qquad (81a)$$

$$u_{zv} \approx \sqrt{\frac{2\pi}{ik_v r}} E_{zz_v} \rho_{Tr} \left[\sum_{n=0}^{N-1} \{R_{2_n} J_1[R_{2_n} k] - R_{1_n} J_1[R_{1_n} k]\} \right] e^{i(k_v r - n\omega \Delta t)} \qquad (81b)$$

By calculating the values of the excitability matrix and the wavenumber-frequency relations for the plate waveguide modeled in the FE simulation, and then calculating the displacement field as a function of time based on the time-domain annular array forcing in the model, the expected guided wave displacements can be predicted at a given distance from the transducer.

Comparison of Predictions and FE Results

The output data from the FE model was compared to the analytical predictions for both the in-plane and out-of plane displacements for the A0 and S0 modes. A comparison of the results is given in Figures 3.4 and 3.5. It can be seen that the predicted results match well with the finite element results, thus verifying the analytical calculations for the phased annular array excitation spectrum.

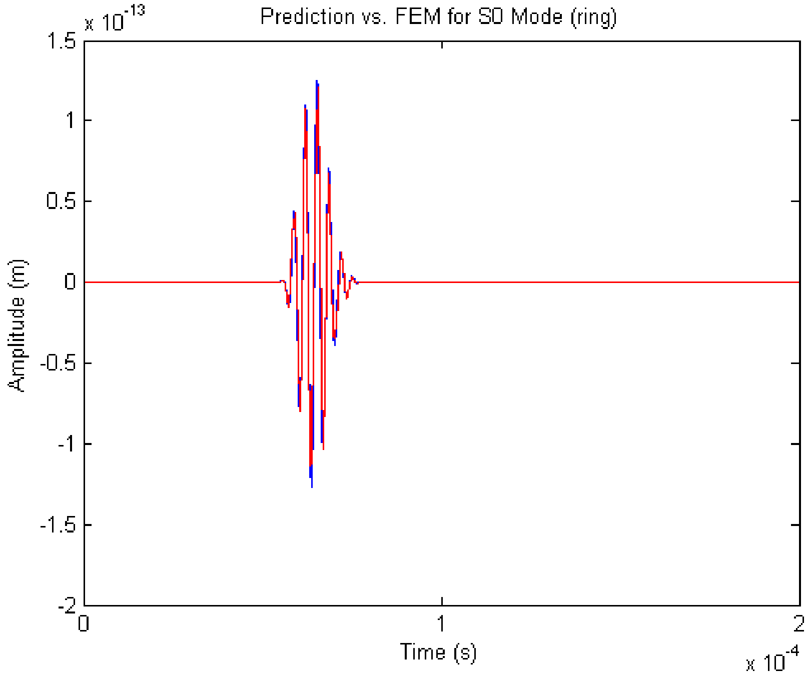

Fig. 3.4 In-plane displacement signal of the S0 mode from the FE simulation (red) compared to the analytical prediction (blue).

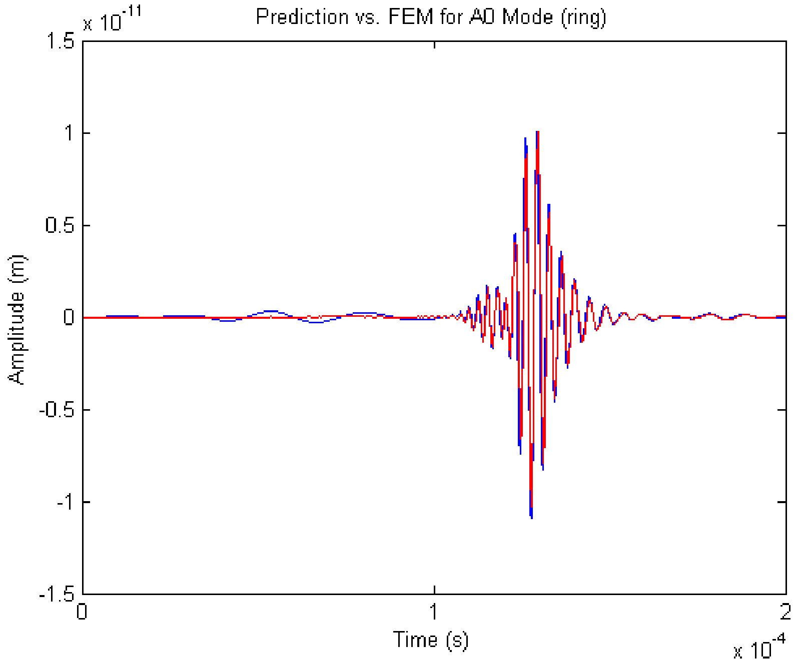

Fig. 3.5 In-plane displacement signal of the A0 mode from the FE simulation (red) compared to the analytical prediction (blue).

It should be explained that in the time-domain waveforms above, the S0 and A0 modes were separated by adding or subtracting the displacements measured on the top and bottom surfaces of the plate in the FE simulation. The symmetric (S) modes have symmetric in-plane displacements and antisymmetric out-of-plane displacements about the midplane, while the antisymmetric (A) modes have the opposite symmetry configuration. This can be used to decouple the symmetric and antisymmetric modes from the time-domain results. The following equations were used to perform this separation.

$$\begin{aligned} u^{S}_{top}(x,t) &= \frac{1}{2}\left(u^{FE}_{top}(x,t) + u^{FE}_{bottom}(x,t)\right) \\ u^{A}_{top}(x,t) &= \frac{1}{2}\left(u^{FE}_{top}(x,t) - u^{FE}_{bottom}(x,t)\right) \\ w^{S}_{top}(x,t) &= \frac{1}{2}\left(w^{FE}_{top}(x,t) - w^{FE}_{bottom}(x,t)\right) \\ w^{A}_{top}(x,t) &= \frac{1}{2}\left(w^{FE}_{top}(x,t) + w^{FE}_{bottom}(x,t)\right) \end{aligned} \tag{82}$$

Here *u* and *w* refer to the in-plane and out-of-plane displacements, while *A* and *S* superscripts refer to the symmetric and anti-symmetric modes, respectively. The superscript *FE* refers to the measured displacements from the FE simulation.

3.1.2 Inward- and Outward-Propagating Annular Array Waveforms

By creating an annular array model with a very large center radius, it is possible to clearly separate the wave packets from the near and far sides of the array, which correspond to the outward- and inward- propagating waves, respectively. For this FE case, the parameters of the annular array are kept identical to the previous model, except for the inner radius r_0, which is increased from 1.5 mm to 30 mm. The results from the simulation are compared to the analytical predictions in Figures 3.6 and 3.7. Here it can be seen that the outward and inward wave packets are mostly separated and that the wavenumber-domain excitation spectra correctly predicted the waveform for both. This shows that the calculations for annular arrays contain information regarding the combination of the inward and outward propagating waves.

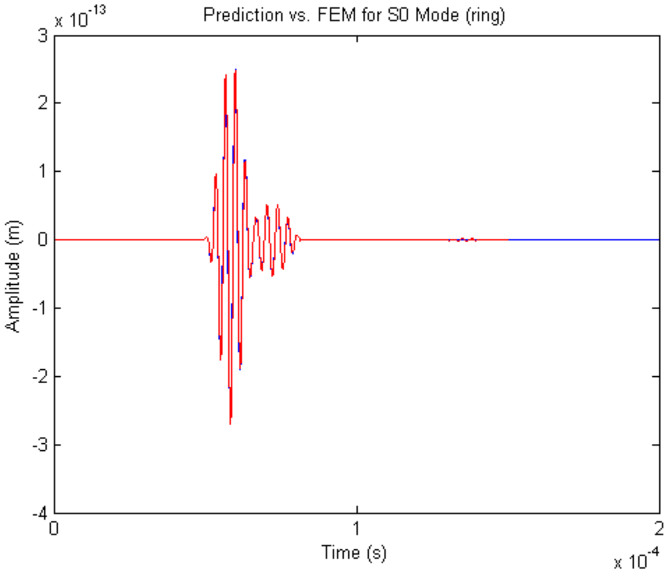

Fig. 3.6 In-plane displacement signal of the S0 mode from the FE simulation (red) compared to the analytical prediction (blue).

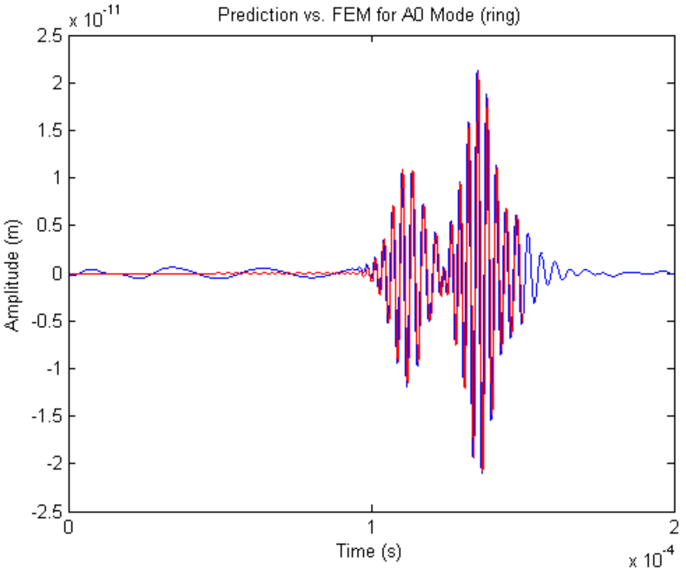

Fig. 3.7 In-plane displacement signal of the A0 mode from the FE simulation (red) compared to the analytical prediction (blue).

However, our calculations regarding the separation of the excitation spectra for the inward- and outward- propagating waves should be able to accurately predict the individual FE waveforms as well. Such an analysis should allow us to view the inward and outward waves separately. This analysis was performed and compared to the finite element results, as shown below, for which the Fourier expansion was summed over 201 terms (m = -100 to m = +100).

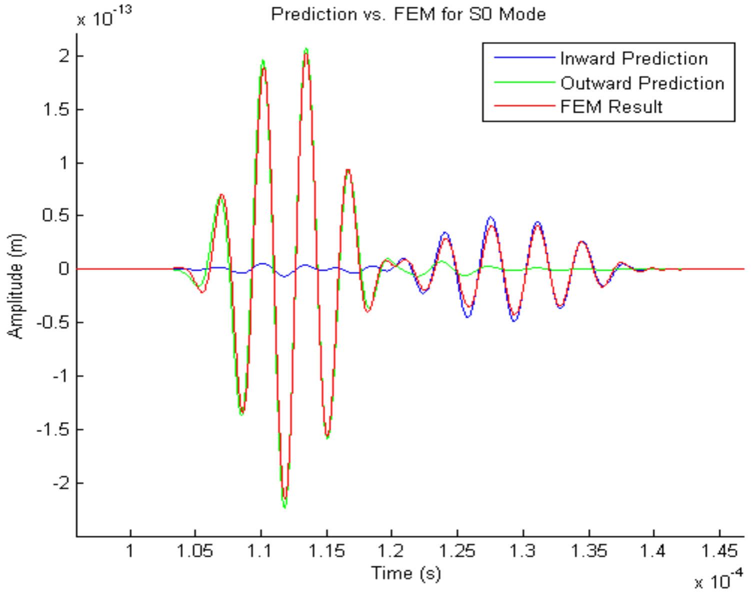

Fig. 3.8 In-plane displacement signal of the S0 mode from the FE simulation (red) compared to the sum of the predicted inward and outward waves

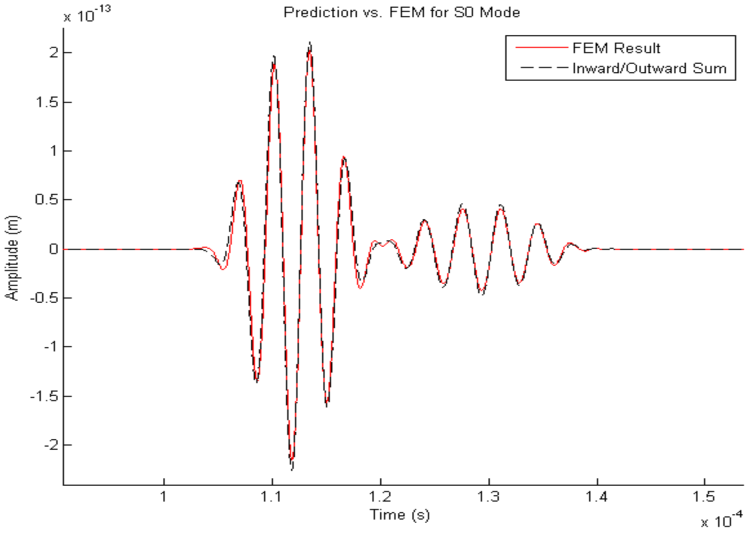

Fig. 3.9 In-plane displacement signal of the S0 mode from the FE simulation (red) compared to the inward (blue) and outward (green) waves

Note that the sum of the inward and outward waves agrees very well with the finite element results for the S0 mode. For the A0 mode, there is a general agreement, but a small phase shift is apparent throughout the results, as was also present in the full annular array prediction results for the A0 mode (see Figure 3.6). The source of this phase disagreement has not been identified, but it could be due to a small error in the predicted phase velocities of the A0 mode. Of primary importance is that the calculations of the separated inward- and outward-wave excitation spectra are verified and the individual inward and outward wave pulses are accurately predicted as compared to the FE results.

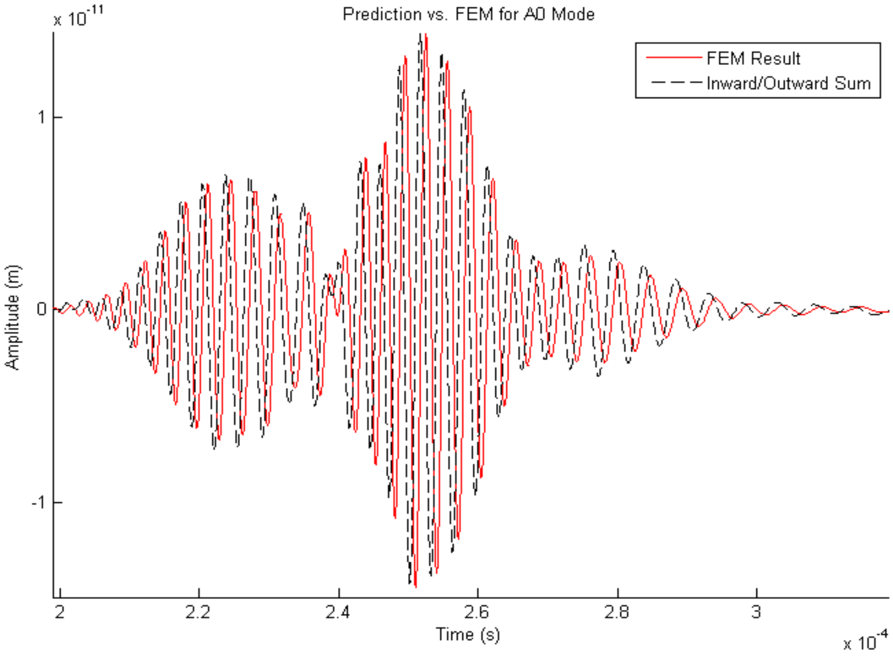

Fig. 3.10 In-plane displacement signal of the A0 mode from the FE simulation (red) compared to the sum of the predicted inward and outward waves (dashed black).

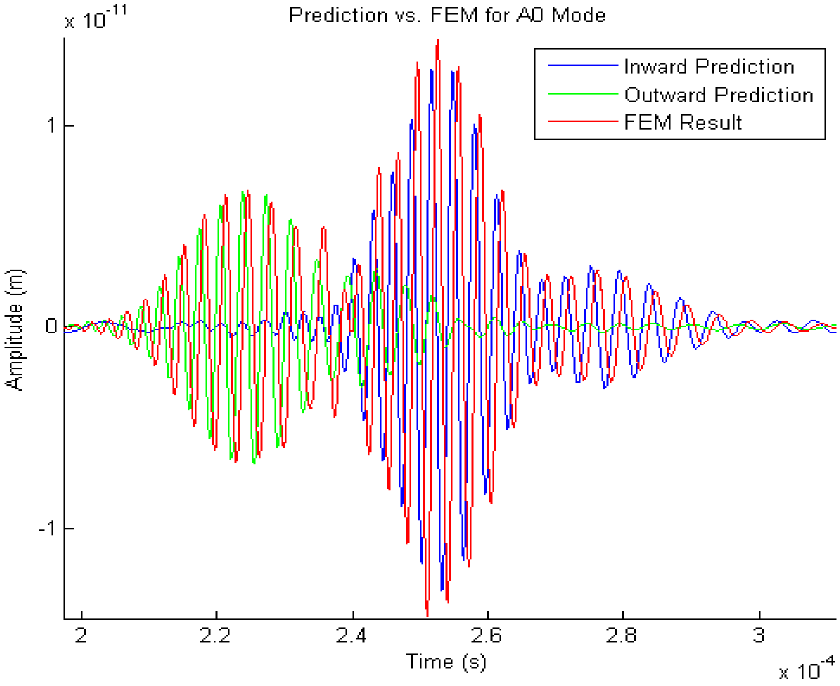

Fig. 3.11 In-plane displacement signal of the A0 mode from the FE simulation (red) compared to the inward (blue) and outward (green) waves individually.

3.1.3. Correction Factor FE Results

The correction factor, α, is the ratio between a desired wavelength and the annular or comb array spacing required to optimally excite that wavelength without the need for phasing. This factor is dependent on the number of elements in a comb or annular array, as well as the inner radius for an annular array, as described in the annular array theory section. To verify these predictions, several finite element models were created to simulate different annular array designs taking into account the predicted correction factors. Each array was tested for its ability to excite the A0 mode in a 1mm aluminum plate at 300 kHz, for which the wavelength is 5.167 mm. The first annular array was a 4-element array with inner radius 0.5*s*, while the second array also had 4 elements, but had an inner radius or 0.7*s*. The specifications for these arrays with and without taking the correction factor into consideration are given in Table 3.I.

Annular Array Transducer Dimensions for Correction Factor FE			
[Inner Radius 0.5s]		[Inner Radius 0.7s]	
no correction factor	α = 0.9526	no correction factor	α = 0.8939
$s = 5.167$ mm	$s = 4.922$ mm	$s = 5.167$ mm	$s = 4.6188$ mm
$w = 2.5835$ mm	$w = 2.461$ mm	$w = 2.5835$ mm	$w = 2.3094$ mm
$r_0 = 2.5835$ mm	$r_0 = 2.461$ mm	$r_0 = 3.6169$ mm	$r_0 = 3.233$ mm
$A = 754.99\ mm^2$	$A = 685.0\ mm^2$	$A = 822.0\ mm^2$	$A = 656.8\ mm^2$

Table 3.I Dimensions for corrected and uncorrected annular arrays with inner radii 0.5*s* and 0.7*s* used for correction factor FE verification.

The models were run and the out-of-plane displacement was recorded at a distance 50 cm from the center of the array. The A0 mode was extracted from the signals for the corrected and uncorrected array designs, and they were plotted and compared, as shown in Figures 3.12 and 3.13. To compensate for the unequal size of the arrays (due to different geometries), the pressure load applied to the transducer in the model was scaled to yield equivalent excitation for both corrected and uncorrected arrays. The results show that the arrays with the correction factor taken into account produce "cleaner" and higher amplitude wave packets. To estimate the total energy in each wave packet, the sum of the squares of the amplitude were taken for each time-domain signal. This resulted in an estimated increase in energy of 25.7% for the 0.5*s* inner radius array and an increase in energy of 12.8% for the 0.7*s* inner radius array when the spacing correction factor was taken into account during transducer design.

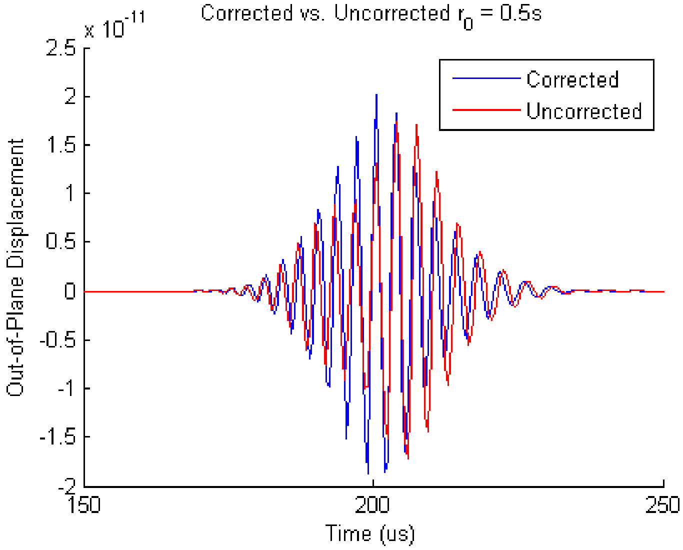

Fig. 3.12 A0 mode generation from 0.5s inner radius annular arrays with uncorrected spacing (red) and corrected spacing (blue).

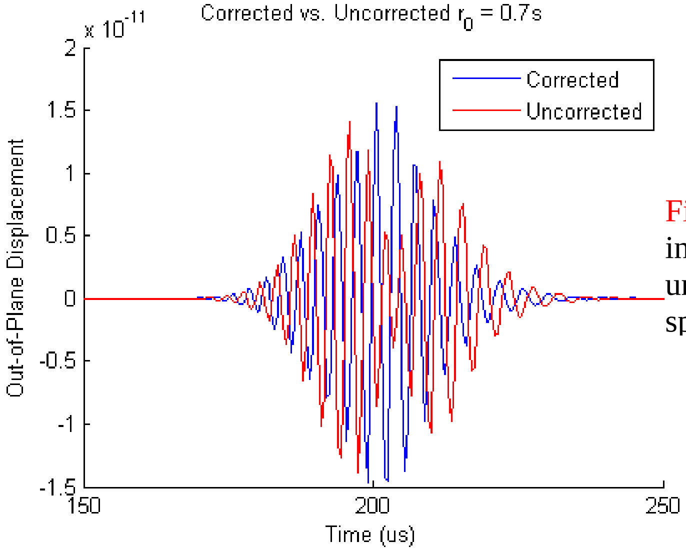

Fig. 3.13 A0 mode generation from 0.7s inner radius annular arrays with uncorrected spacing (red) and corrected spacing (blue).

Perhaps a better method to analyze the energy existing at the mode and frequency of interest (A0 mode at 300 kHz in this case) is to compare the power-spectral density time-frequency plots of the excited guided waves. The time-frequency PSD can be generated with a short-time FFT transform method. The time-frequency plots for $r_0 = 0.5s$ and $r_0 = 0.7s$ are shown in Figures 3.14 and 3.15. It can be seen that the annular arrays without the correction factor are not exciting the A0 mode at 300 kHz. In fact, they are exciting the A0 mode in a weaker manner than the corrected array, and at a different frequency than was desired. This is due to the fact that the primary wavelengths being excited by the uncorrected arrays are not equal to the wavelength of the A0 mode at 300 kHz, but they are equal to the wavelength of the A0 mode at higher or lower frequencies. Thus not only are we receiving less total energy in the A0 mode, as shown in the time-domain plots in Figures 3.12 and 3.13, but much of the energy is not even in the mode and frequency that we desired. To analyze the total energy at the mode and frequency, we can take a cross-section of the time-frequency PSD plots at 300 kHz. Doing so generates the time-PSD plots shown in Figures 3.16 and 3.17.

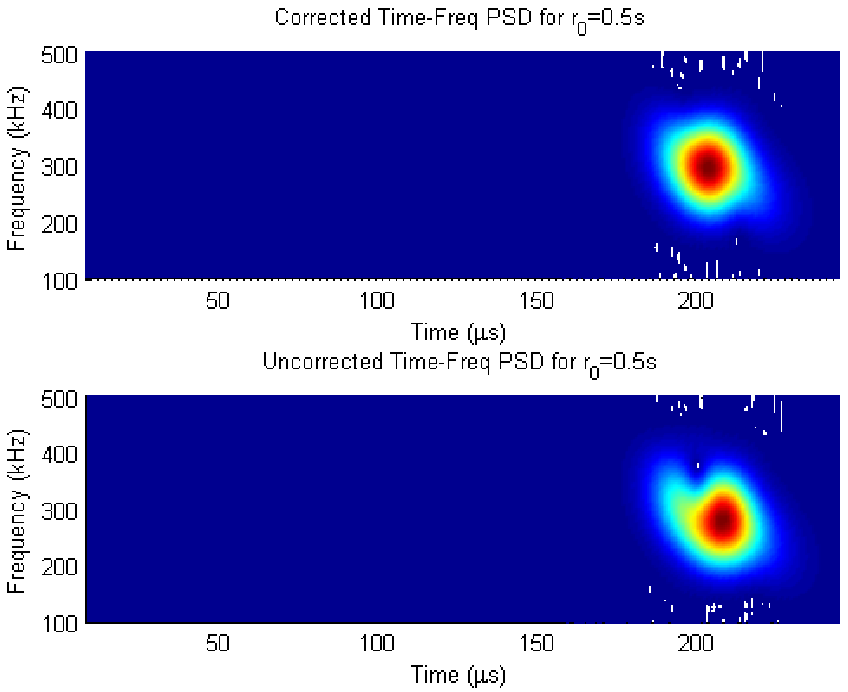

Fig. 3.14 Time-frequency power-spectral density plot of the corrected (top) and uncorrected (bottom) arrays, r_0=0.5s

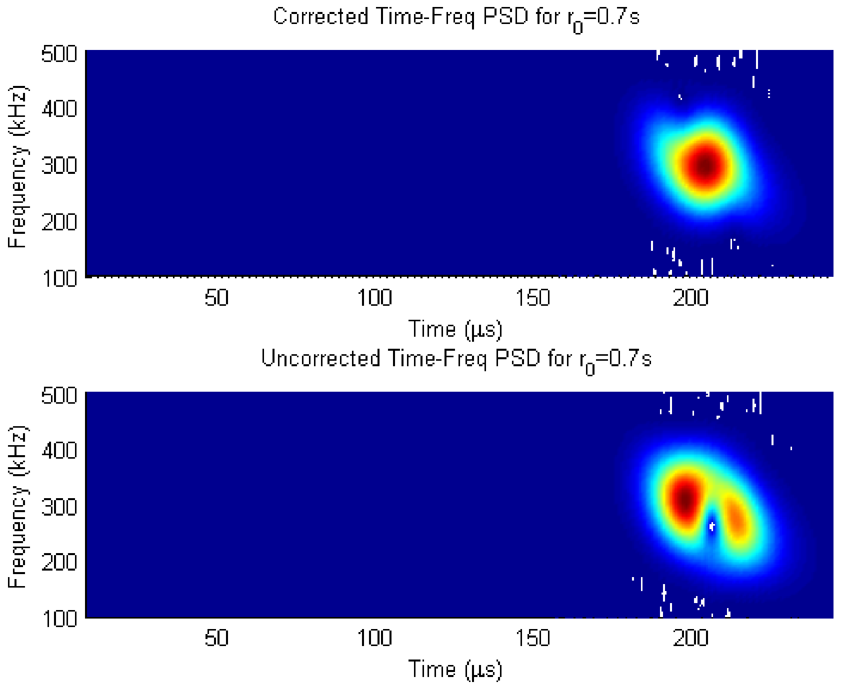

Fig. 3.15 Time-frequency power-spectral density plot of the corrected (top) and uncorrected (bottom) arrays, r_0=0.7s

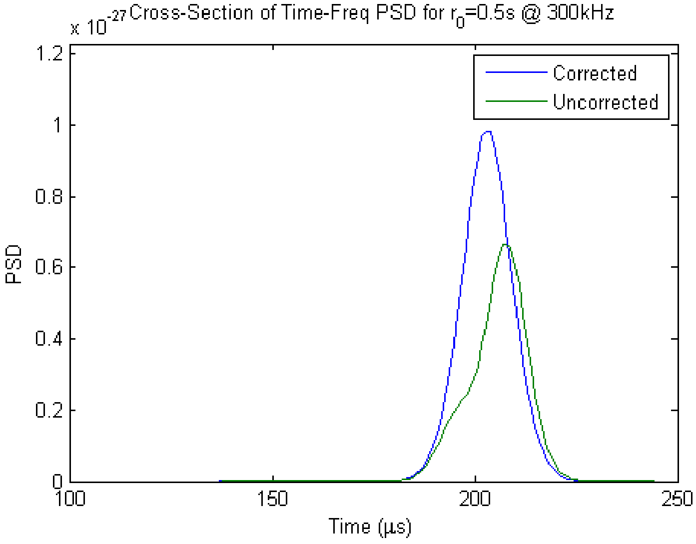

Fig. 3.16 Cross-section of the time-frequency power-spectral density plot of the corrected (blue) and uncorrected (green) arrays, $r_0 = 0.5s$, at 300 kHz.

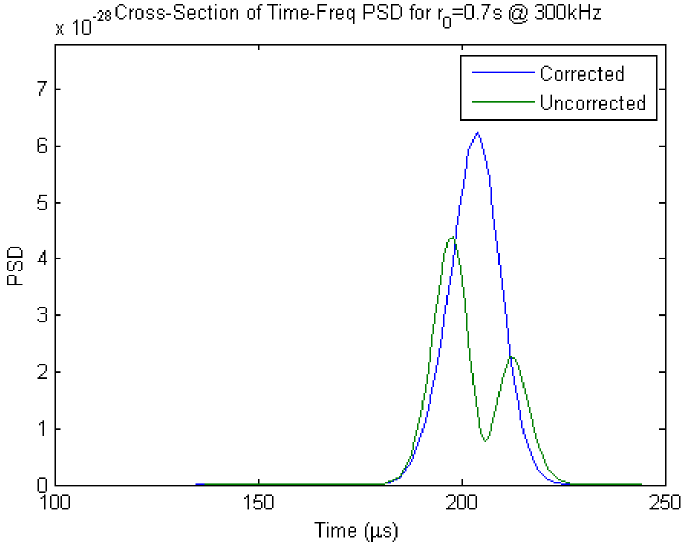

Fig. 3.17 Cross-section of the time-frequency power-spectral density plot of the corrected (blue) and uncorrected (green) arrays, $r_0 = 0.7s$, at 300 kHz.

Here we can see that the corrected arrays are putting much more energy into the desired mode and frequency. Integrating under these curves yields the total energy excited. Through this analysis, we see that the arrays which were designed with the correction factor in mind actually produce 45.2% and 38.7% more energy in the desired mode and frequency than the uncorrected arrays with inner radii of 0.5*s* and 0.7*s* respectively. In addition to the increased energy with the corrected array, we can also see that the wave packets are much cleaner in both the time and frequency domains.

3.1.4. Mode Selection Based on Excitation Spectrum Analysis Mode Excitability

The previous sections have verified the calculations to predict guided wave mode excitation in a plate with a phased annular array transducer. To show that the mode selection predictions for phased annular arrays (including considerations of mode excitability) are accurate, two modes at a single frequency were chosen to verify the effect of phasing on mode selection. To simplify the finite element simulation and analysis, a frequency below the first cutoff was chosen, 1.139 MHz. Based on the phasing map shown in Figure 3.18, it can be seen that the A0 mode has very little energy for a 0° phase delay and much more energy for a 135° phase delay. A FE simulation was conducted to verify the mode selection capabilities of the specified annular array (see Table II below) on a 1-mm Al plate. The time-domain waveforms were extracted at a distance 0.5 m away from the center of the array; these are given in Figures 3.19 and 3.20.

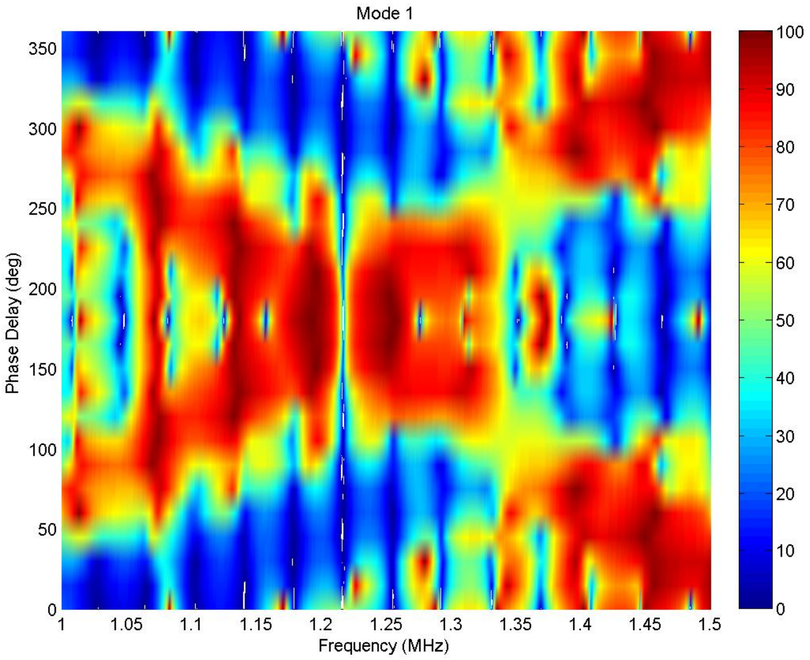

Fig. 3.18 Contour map in the region of excitation used for the FE simulation to test time delay parameters for mode control of the A0 (mode 1) and S0 modes in a 1-mm Al plate.

Annular Array Transducer Dimensions
N=8
$r_0 = 2.5$ mm
w = 2.5 mm
s = 5.0 mm

Table 3.II Annular array dimensions used for mode excitation calculations.

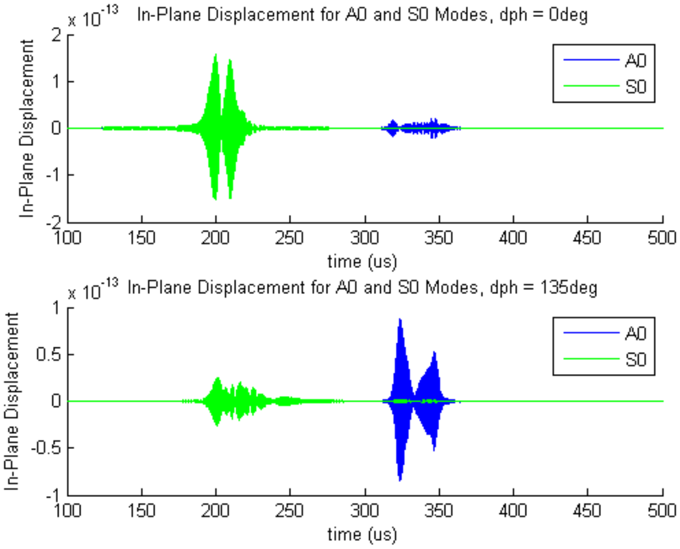

Fig. 3.19 In-plane surface displacements measured for the A0 and S0 modes in a 1-mm Al plate. The excitation source was an annular array with dimensions given in Table II. Phase delays of 0° and 135° were used to selectively excite the S0 and A0 modes, respectively.

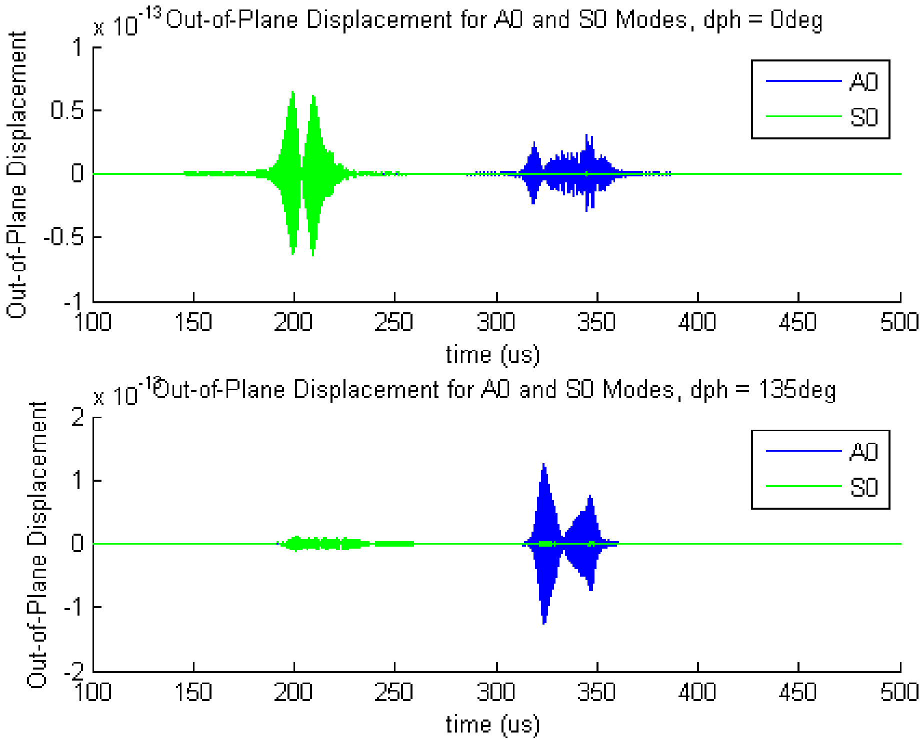

Fig. 3.20 Out-of-plane surface displacements measured for the A0 and S0 modes in a 1-mm Al plate. The excitation source was an annular array with dimensions given in Table II. Phase delays of 0° and 135° were used to selectively excite the S0 and A0 modes, respectively.

It is clear from the waveform plots that the predicted mode was preferentially excited with the selected phase delays. Note that these are simply the surface displacements and do not relate directly to the mode energies used to select these phase delays. The mode energy plot for the selected mode is shown in Figure 3.18. To directly compare the excited energy in each mode, we can analyze the power spectral density time-frequency functions, as was done for the correction factor FE analysis. In doing this, we obtain the PSD cross-sections shown in Figures 3.21 and 3.22. The predicted and measured relative mode energies are given in Table 3.III.

Percent Mode Energies from Mode Excitation FE Analysis				
		Predicted	**In-Plane Measured**	**Out-of-Plane Measured**
0° phase delay	***A0***	0.87 %	3.03 %	24.65 %
	S0	99.13 %	96.97 %	75.35 %
135° phase delay	***A0***	95.91 %	91.01 %	98.73 %
	S0	4.09 %	8.99 %	1.27 %

Table 3.III Predicted and measured mode energy for the A0 and S0 modes for two phase delays at 1.139 MHz.

Here we can see that the results agree well with the predictions, with the exception of the out-of-plane displacement measurement of A0 mode at 0° phase delay. However, we must take into account the fact that these mode energy predictions are with respect to the energy distributed through the entire thickness of the waveguide, while our measurements in this FE model are only of the surface displacements. Thus the through-thickness distribution of power for each mode also comes into play. Perhaps a better way to compare predictions and results is to consider only the in-plane and out-of-plane power flow at the surface for each mode, frequency, and time delay. Following this approach, the results are shown in Table 3.IV below. These values do match slightly better than the general predicted mode energy values in Table 3.III above.

Percent Mode Energies from Mode Excitation FE Analysis					
		Predicted In-Plane Surface Power Flow	**In-Plane Measured**	**Predicted Out-of-Plane Surface Power Flow**	**Out-of-Plane Measured**
0° phase delay	***A0***	1.29 %	3.03 %	11.46 %	24.65 %
	S0	98.71 %	96.97 %	88.54 %	75.35 %
135° phase delay	***A0***	97.22 %	91.01 %	99.71 %	98.73 %
	S0	1.27 %	8.99 %	0.29 %	1.27 %

Table 3.IV Predicted and measured surface power flow values for the A0 and S0 modes for two phase delays at 1.139 MHz.

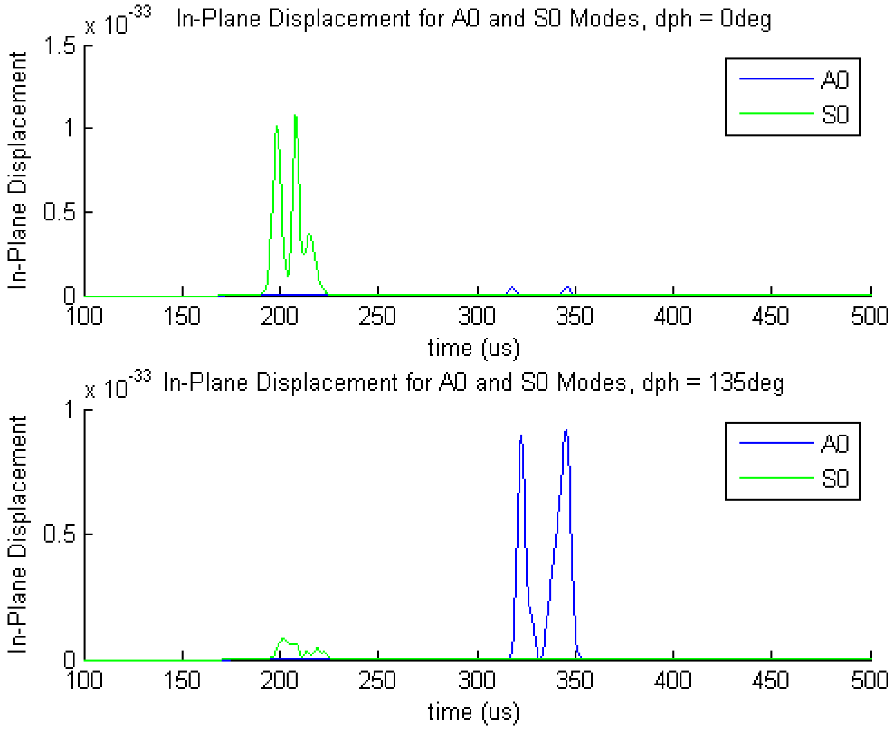

Fig. 3.21 Mode PSD as a function of time generated from in-plane surface displacements measured for the A0 and S0 modes in a 1-mm Al plate.

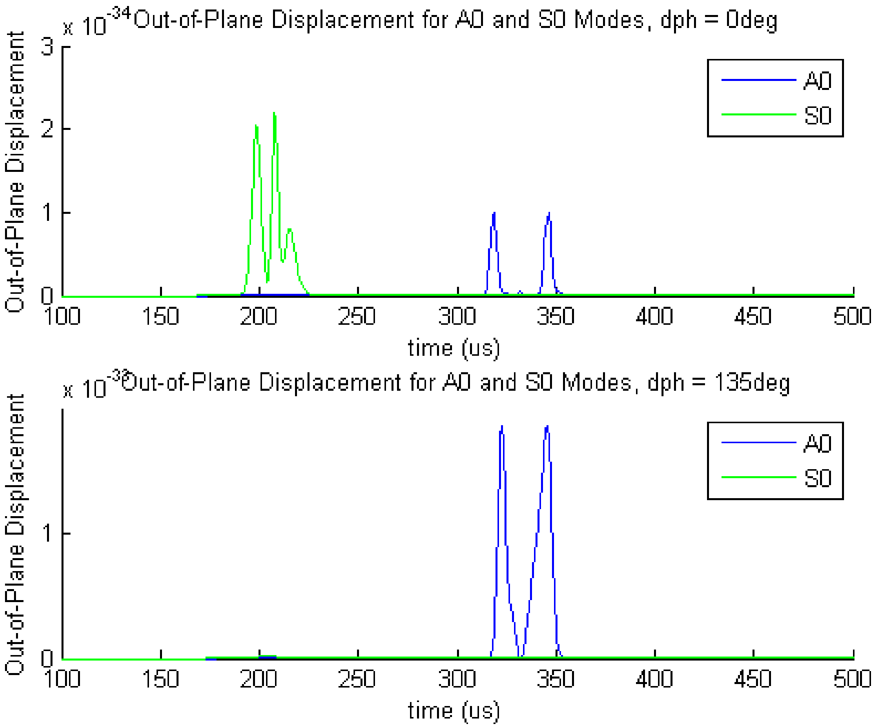

Fig. 3.22 Mode PSD as a function of time generated from out-of-plane surface displacements measured for the A0 and S0 modes in a 1-mm Al plate.

3.2 Plate Vibrations Introduced by Guided Waves

The free vibration of a 2D plate was analyzed using ABAQUS. As in Figure 3.23, the model was based on a plane strain aluminum plate with clamped ends. The length was 0.2m and the thickness was 0.01m. The natural frequencies between 50kHz to 150kHz were extracted and listed in Table 3.V.

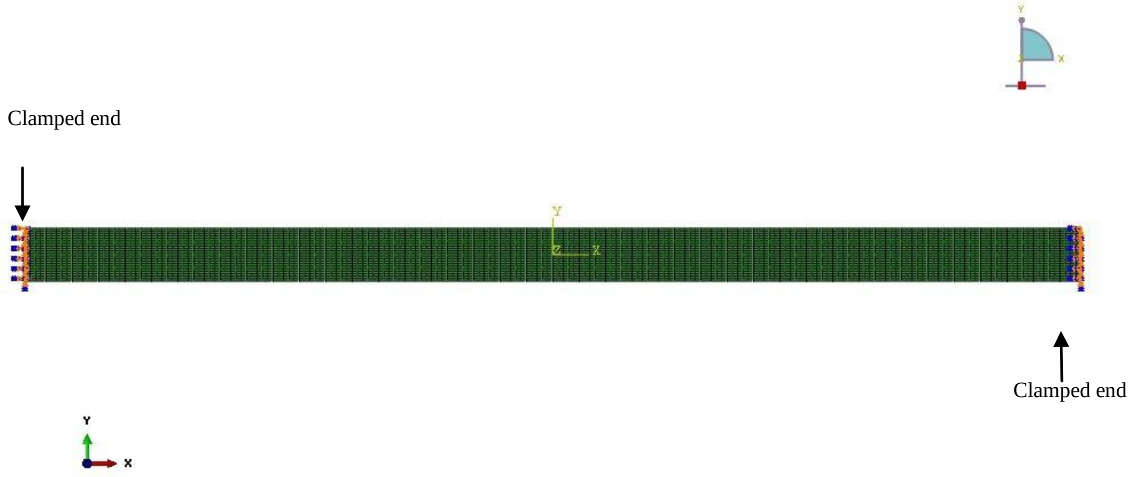

Figure 3.23. Model setup for free vibration in ABAQUS

No.	natural frequency (Hz)	sym/antisym
1	54355.3	S
2	54973.3	A
3	62296.9	A
4	67783.8	S
5	69750.9	A
6	77309.5	A
7	81096.1	S
8	84951.5	A
9	92659.3	A
10	94258.8	S
11	100419	A
12	107232	S
13	108217	A
14	116045	A
15	119969	S
16	123893	A
17	131755	A
18	132411	S
19	139621	A
20	144490	S
21	147483	A

Table 3.V. Natural frequencies of 2D plate in the range 50kHz to 150kHz.

Two typical modes associated with the natural modes are symmetric mode and antisymmetric mode. Symmetric modes are the modes with symmetric in-plane displacements but antisymmetric out-of-plane displacements. They are also viewed as compressional modes as shown in Figure 3.24a. In contrast, antisymmetric modes, which are also known as flexure modes, have antisymmetric in-plane displacement but symmetric out-of-plane displacement. An example of antisymmetric modes can be found in Figure 3.24b.

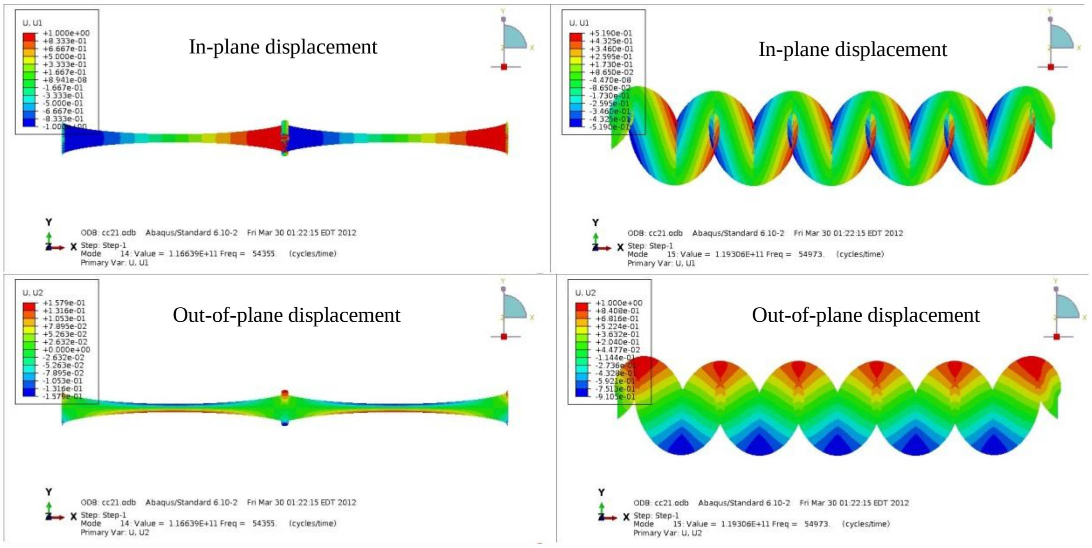

(a) Symmetric mode (b) Antisymmetric mode

Figure 3.24. Displacement fields of natural modes: (a) symmetric (compressional) mode at 54355.3Hz; (b)antisymmetric (flexure) mode at 54973.3Hz.

Models concerning 2D plate vibration under guided wave loadings were then performed. The geometry of the model can be referred to Figure 3.25. It was a plain strain model with the dimension of 0.2m by 0.01m. The material is aluminum and material damping is modeled as Rayleigh damping with α being set to 0 and β equating to 7.96E-009. In order to study the effect of guided wave loadings to structural vibration, the guided wave inputs were added on the left end of the plate. Clamped boundary condition was also created at the right end of the plate. ABAQUS STANDARD software package was adopted to simulate the forced vibration response under guided wave excitation. The loading frequency was tuned in order to record the structural response within an interested loading frequency range. For more precise study of the responses, two receiving points were selected in the middle of the top and bottom surfaces. The displacement values of the two points were recorded in addition to the full displacement field of the plate.

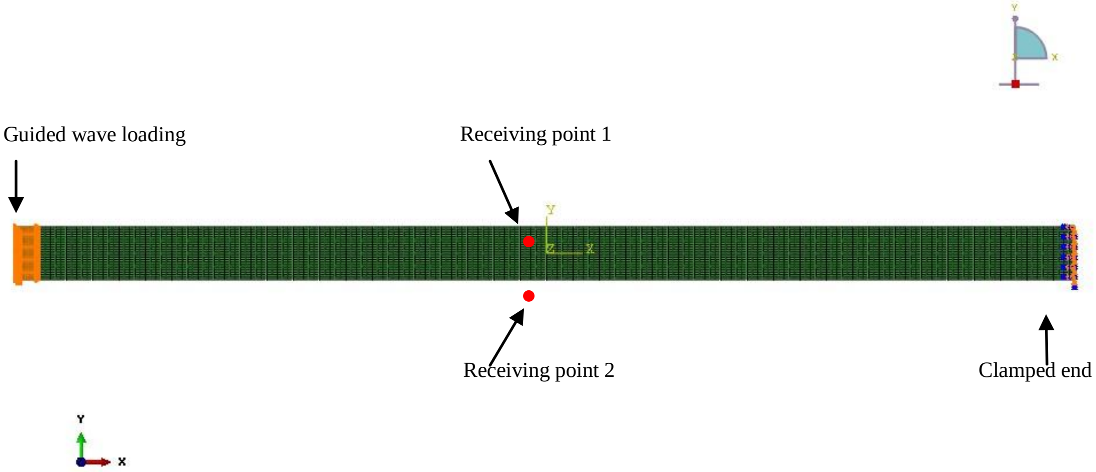

Figure 3.25. Model setup of forced vibration in ABAQUS

The guided wave loadings were introduced by setting the nodal displacements in the loading region. To impinging a guided wave mode into the plate, the distribution of nodal displacements in the left end should follow the wave structure of the typical guided wave mode. In this numerical experiment, A0 and S0 were selected as two guided wave loading cases. The frequency range in this analysis was from 50k to 150k. In such low frequency range, the wave structures of A0 and S0 will not vary too much. Figure 3.26 gives the wave structures of the two modes at 100kHz as well as the details of loading areas.

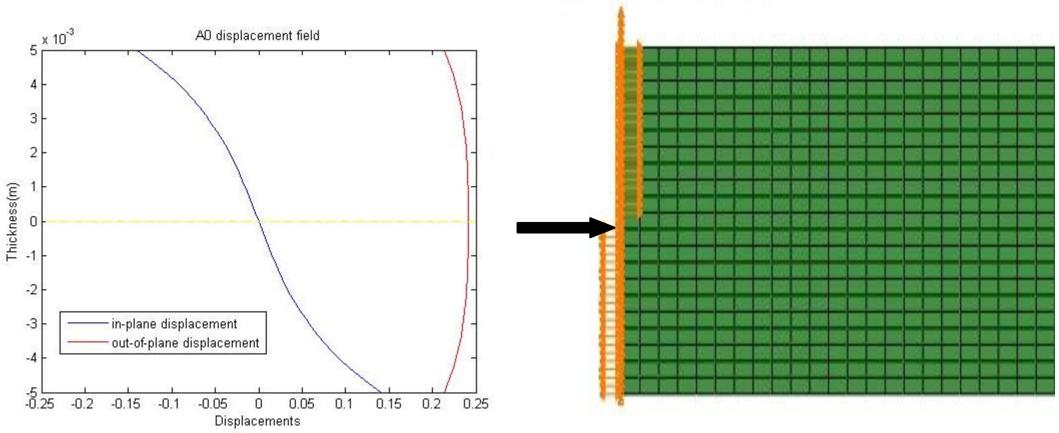

(a1) Displacement field of A0 mode at 100kHz (a2) A0 mode loaded on the plate

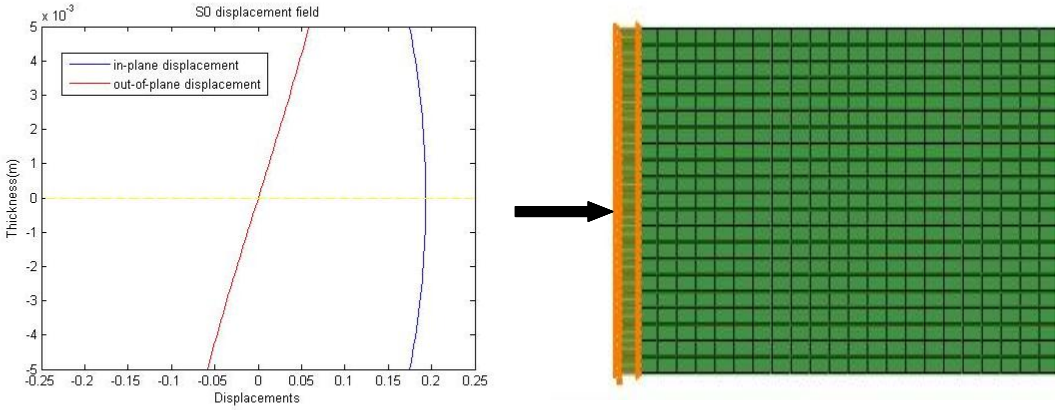

(b1) Displacement field of S0 mode at 100kHz (b2) S0 mode loaded on the plate

Figure 3.26. Guided wave structures of A0 and S0 and their loading on the plate.

The structural responses under A0 loading were obtained from 50kHz to 150kHz with 100Hz increments. The in-plane displacements of the two receiving points, which are the middle points on the top and bottom surfaces as illustrated in Figure 3.25, are plotted in Figure 3.27. All the displacement values were recorded from the operational deflection shape, which has the same phase as the guided wave loading. Figure 6 depicts the out-of-plane displacements of the two points. Figures 3.27 and Figure 3.28 demonstrate clearly that the in-plane displacements of the two receiving locations are opposite, while out-of-plane displacements in the responses are identical. More specific presentation is shown in Figure 3.29. Note the y axis of Figure 3.29 (a) and (b) has the order of -9, this implies that the summation of in-plane displacements and the subtraction of out-of-plane displacement are trivial.

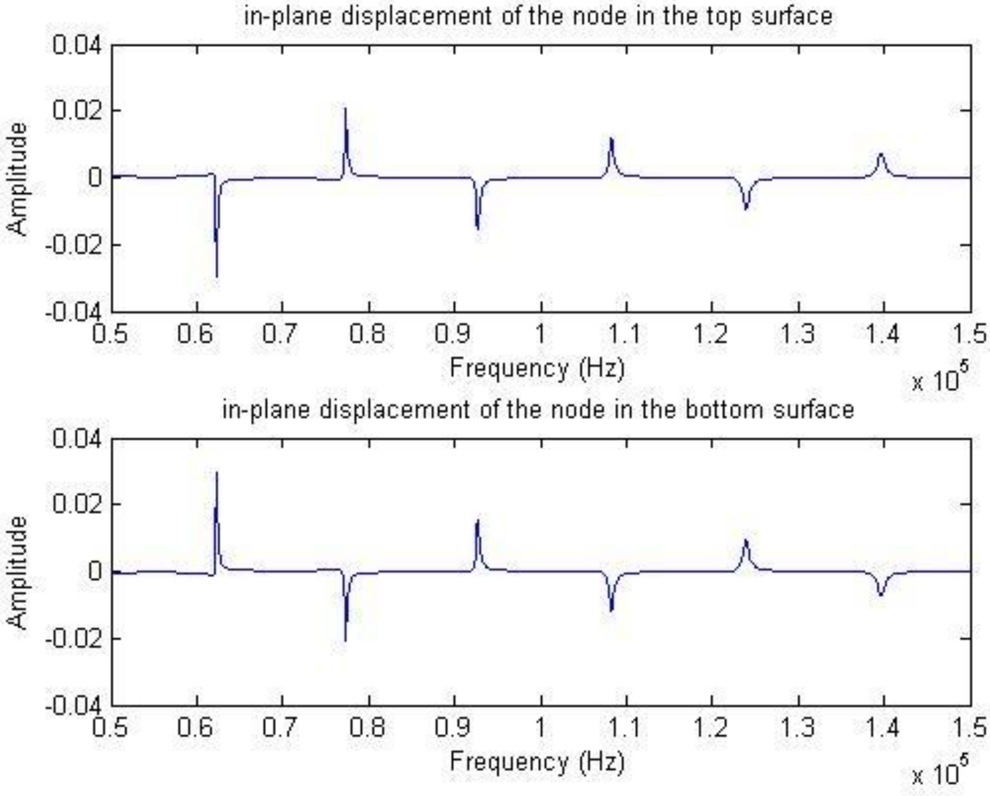

Figure 3.27. In-plane displacements of the nodes in the top surface (top figure) and bottom surface (bottom figure).

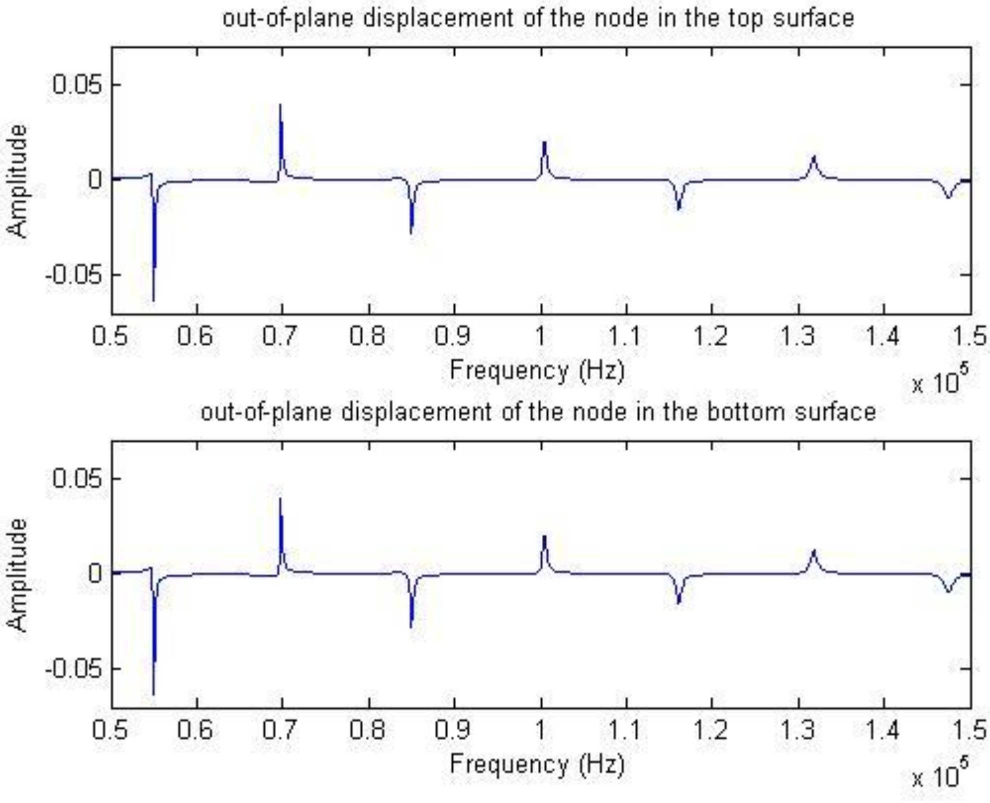

Figure 3.28. Out-of-plane displacements of the nodes in the top surface (top figure) and bottom surface (bottom figure).

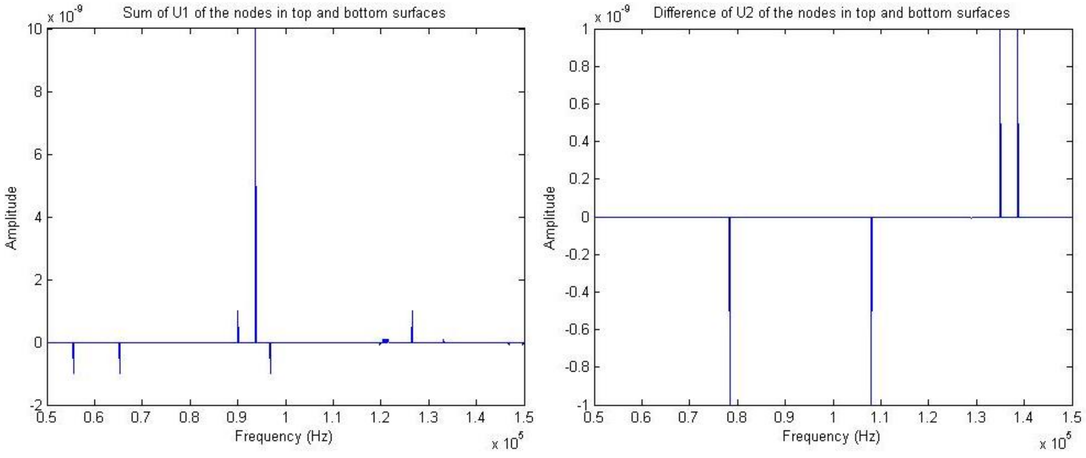

(a) (b)

Figure 3.29. Identification of antisymmetric mode: (a) the summation of in-plane displacements of top and bottom nodes is very close to zero; (b) the subtraction of out-of-plane displacements almost equals to zero.

A0 guided wave loading can successfully excite the antisymmetric vibration modes and suppress the symmetric modes. The peaks of the displacement responses correspond to the natural frequencies that can be generated by A0 loadings (see Figure 3.30). Table 3.VI gives a summary of the peak frequencies and natural frequencies of the 2D plate.

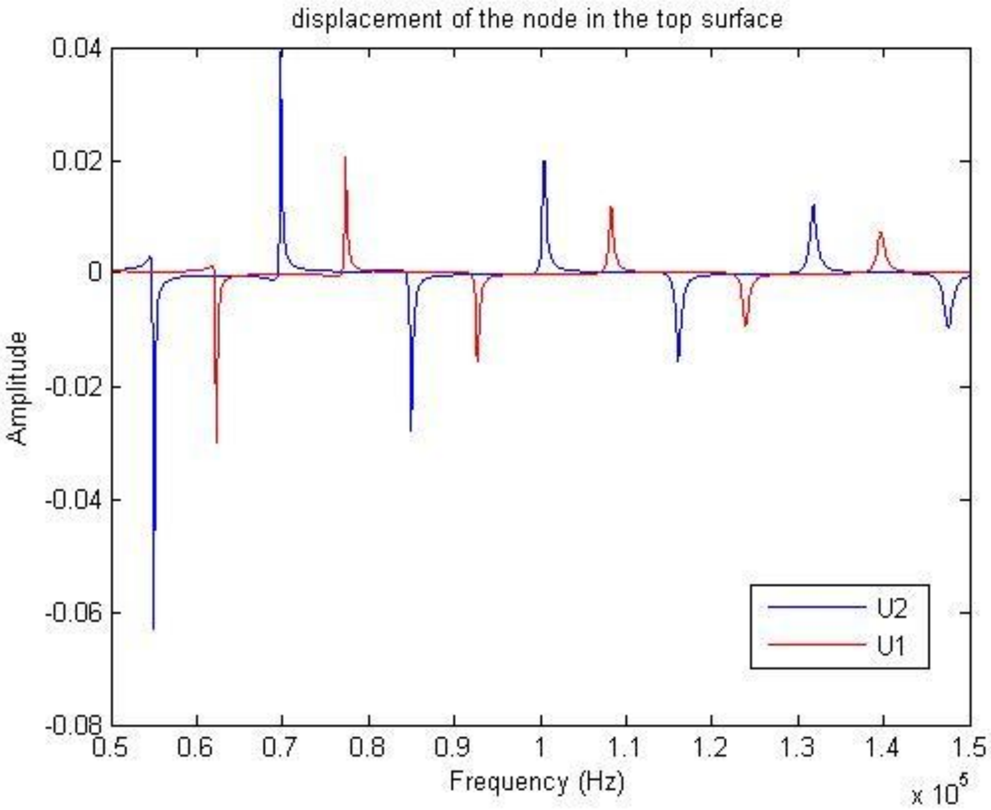

Figure 3.30. In-plane and out-of-plane displacement of the node in the top surface. Peaks give the natural frequencies of antisymmetric modes.

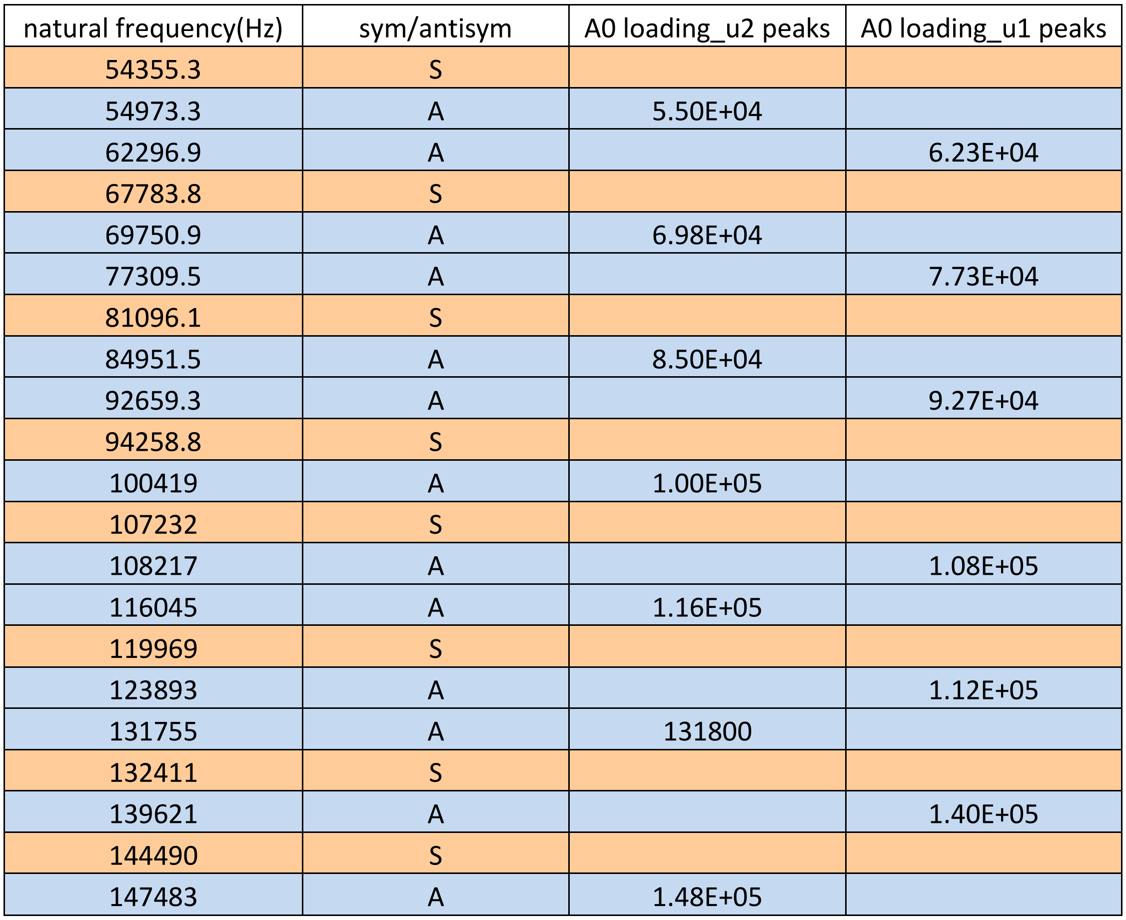

natural frequency(Hz)	sym/antisym	A0 loading_u2 peaks	A0 loading_u1 peaks
54355.3	S		
54973.3	A	5.50E+04	
62296.9	A		6.23E+04
67783.8	S		
69750.9	A	6.98E+04	
77309.5	A		7.73E+04
81096.1	S		
84951.5	A	8.50E+04	
92659.3	A		9.27E+04
94258.8	S		
100419	A	1.00E+05	
107232	S		
108217	A		1.08E+05
116045	A	1.16E+05	
119969	S		
123893	A		1.12E+05
131755	A	131800	
132411	S		
139621	A		1.40E+05
144490	S		
147483	A	1.48E+05	

Table 3.VI. Antisymmetric vibration modes generated by the A0 loadings.

Operational deflection shapes of A0 input around natural frequency 54973.3Hz are illustrated in Figures 3.31 and 3.32, which plot the in-plane displacements and out-of-plane displacements respectively. It is obvious that when the loading frequency hit a natural frequency, the plate vibrates more intensively.

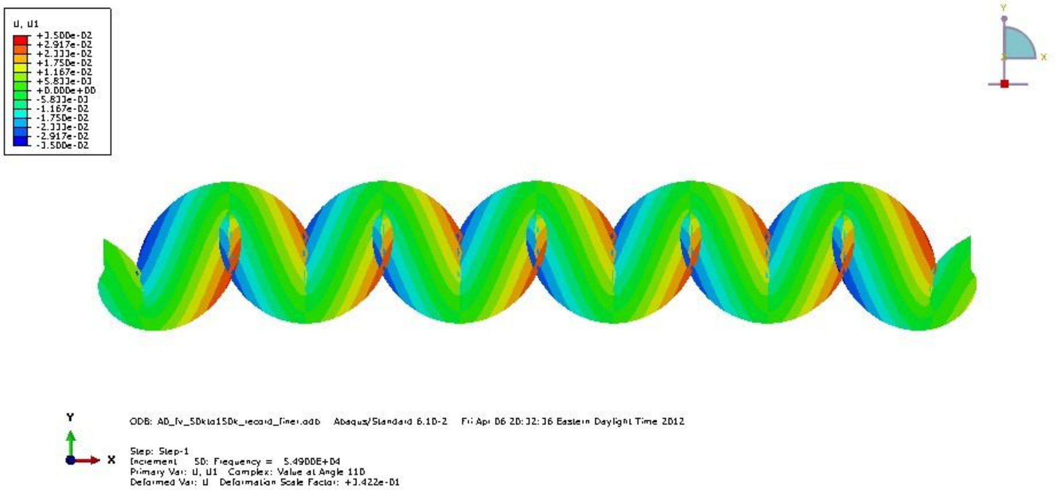

(a) In-plane displacement field under A0 loading at 54900Hz

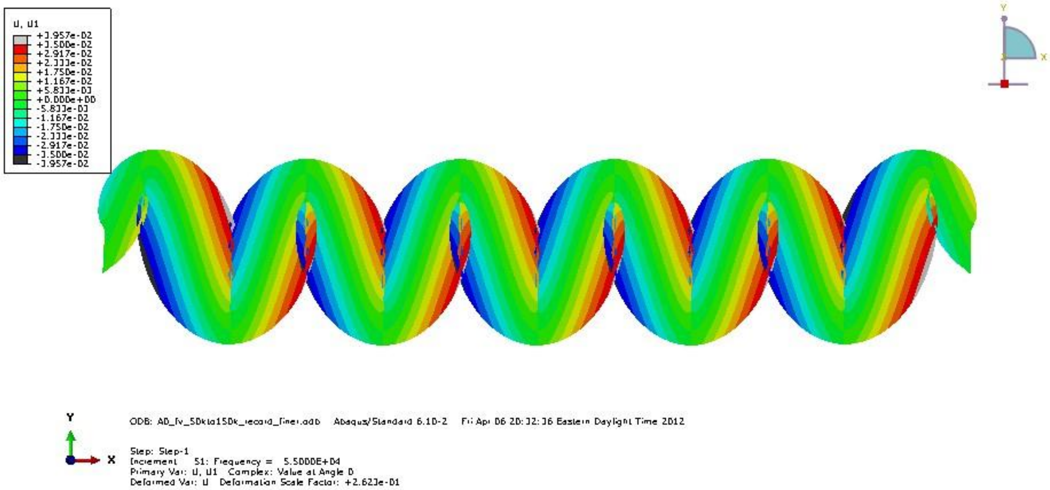

(b) In-plane displacement field under A0 loading at 55000Hz

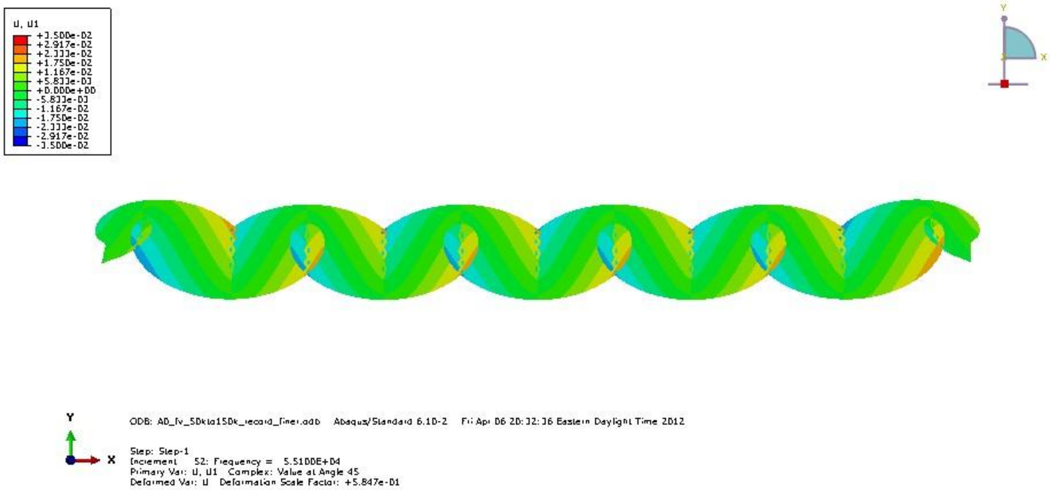

(c) In-plane displacement field under A0 loading at 55100Hz

Figure 3.31. In-plane displacement under A0 input at (a) 54900Hz; (b) 55000Hz; (c) 55100Hz.

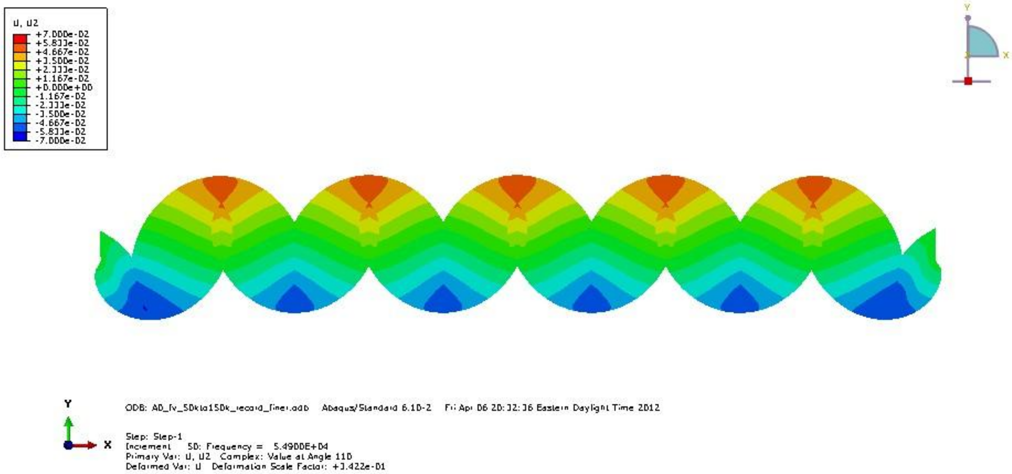

(a) Out-of-plane displacement field under A0 loading at 54900Hz

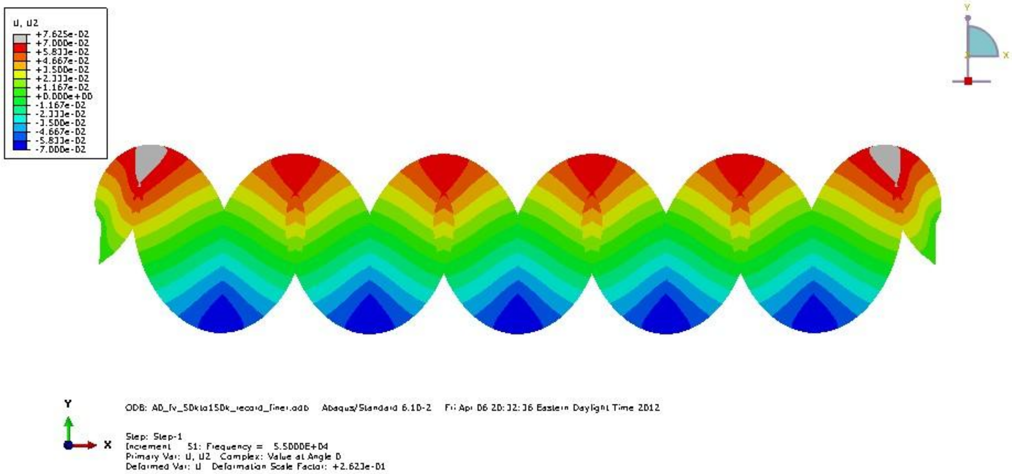

(b) Out-of-plane displacement field under A0 loading at 55000Hz

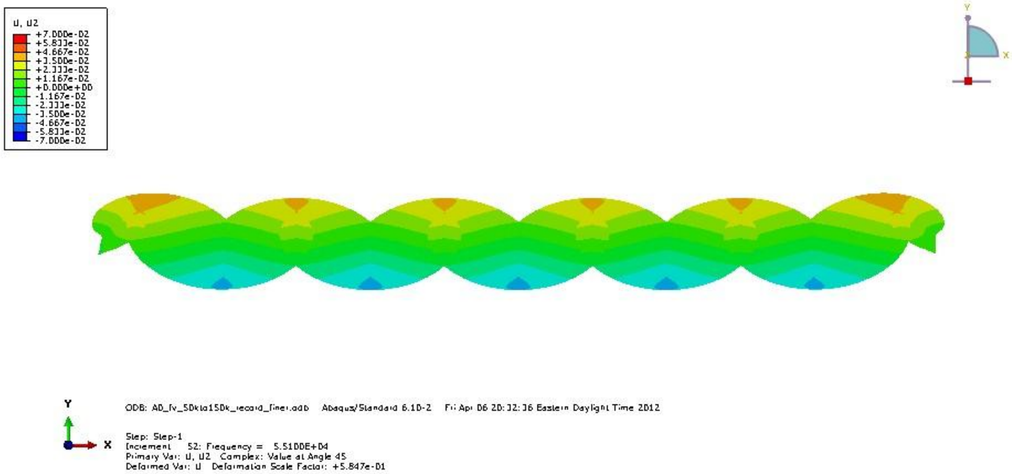

(c) Out-of-plane displacement field under A0 loading at 55100Hz

Figure 3.32. Out-of-plane displacement under A0 input at (a) 54900Hz; (b) 55000Hz; (c) 55100Hz.

The scenarios of S0 loading were also studied. The in-plane displacement and out-of-plane displacement of the node in the top and bottom surfaces are given in Figures 3.33 and Figure 3.34, respectively. The symmetry of in-plane displacement and the antisymmetry of the out-of-plane displacement fully demonstrates that the generated ODS are symmetry. Unlike the A0 case, the natural frequencies here are obtained at the points where the phase shifts. A comparison of phase shifting frequencies and the natural frequencies of the 2D plate can be referred to Table 3.VII.

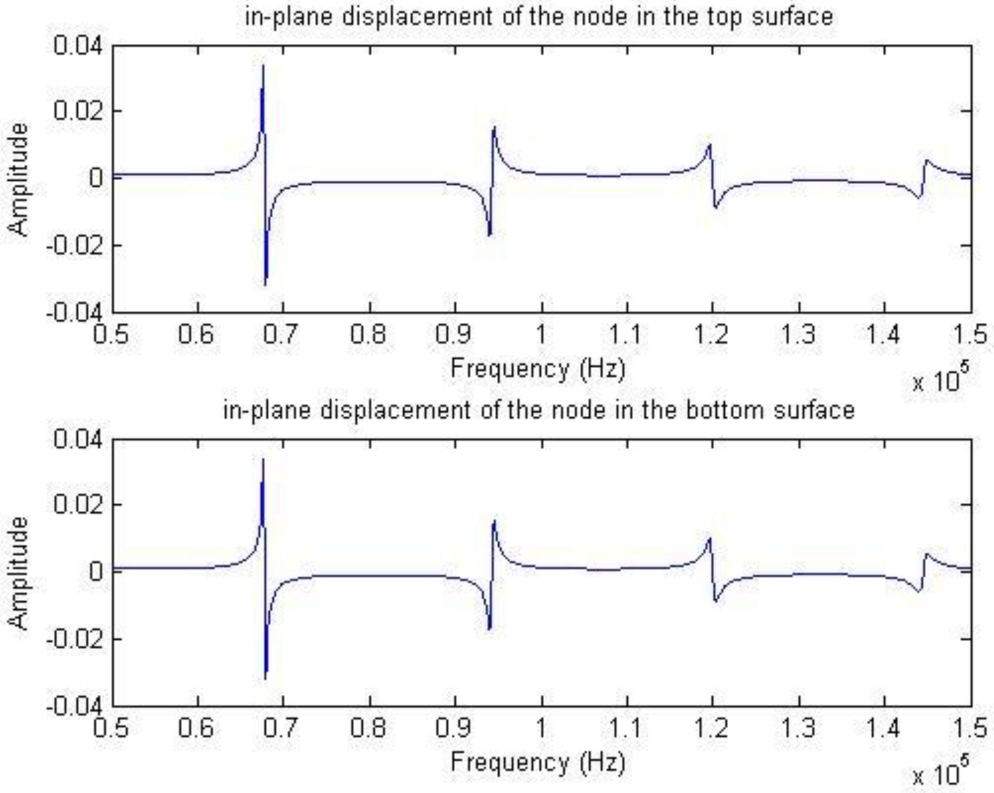

Figure 3.33. In-plane displacements of the nodes in the top surface (top figure) and bottom surface (bottom figure).

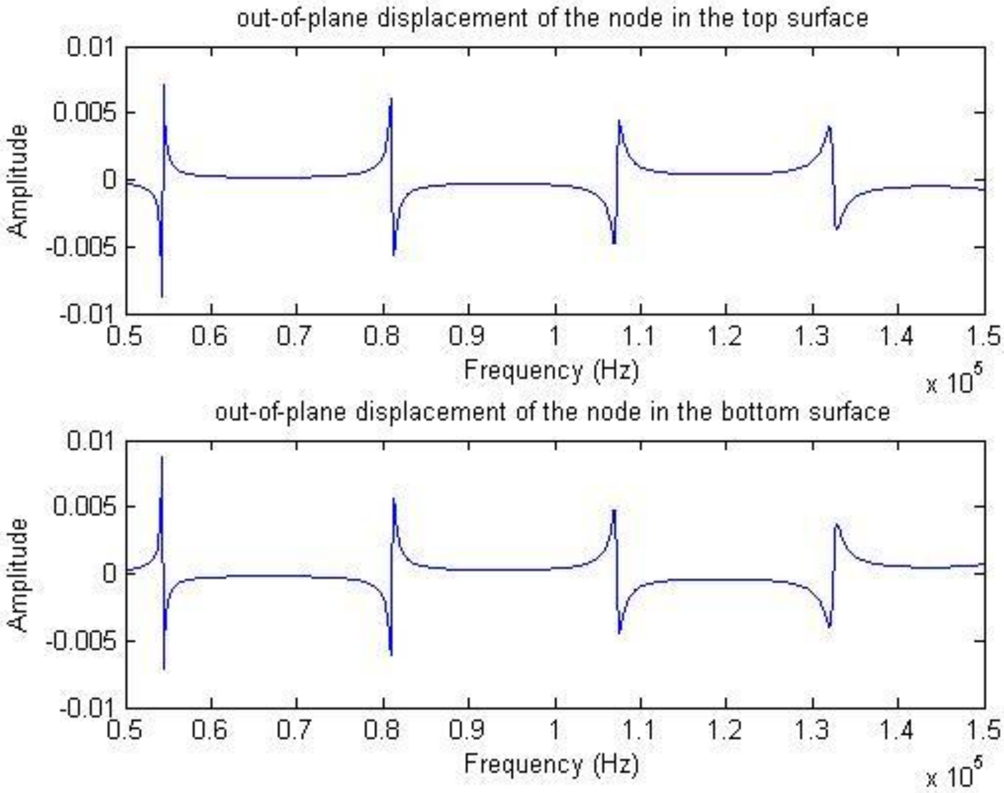

Figure 3.34. In-plane displacements of the nodes in the top surface (top figure) and bottom surface (bottom figure).

natural frequency	sym/antisym	S0 loading_u1 shifts	S0 loading_u2 shifts
54355.3	S		5.44E+04
54973.3	A		
62296.9	A		
67783.8	S	6.78E+04	
69750.9	A		
77309.5	A		
81096.1	S		8.11E+04
84951.5	A		
92659.3	A		
94258.8	S	9.43E+04	
100419	A		
107232	S		1.07E+05
108217	A		
116045	A		
119969	S	1.20E+05	
123893	A		
131755	A		
132411	S		1.33E+05
139621	A		
144490	S	1.45E+05	
147483	A		

Table 3.VII. Symmetric vibration modes generated by the S0 loadings.

Operational deflection shapes of S0 input around the natural frequency of 67783.8Hz are illustrated in Figures 3.35 and 3.36, which plot the in-plane displacements and out-of-plane displacements respectively. It is not hard to notice that when the loading frequency hits a natural frequency, the plate vibrates more intensively.

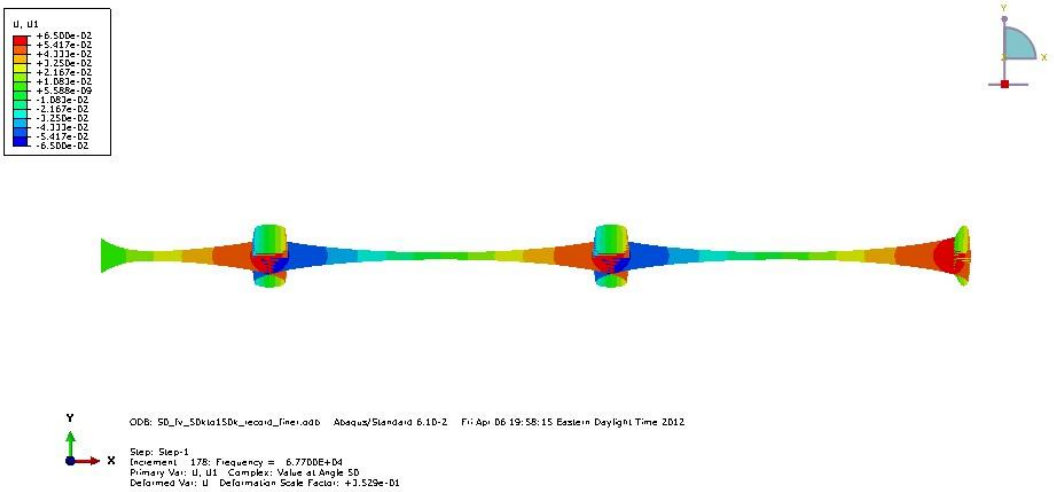

(a) In-plane displacement field under S0 loading at 67700Hz

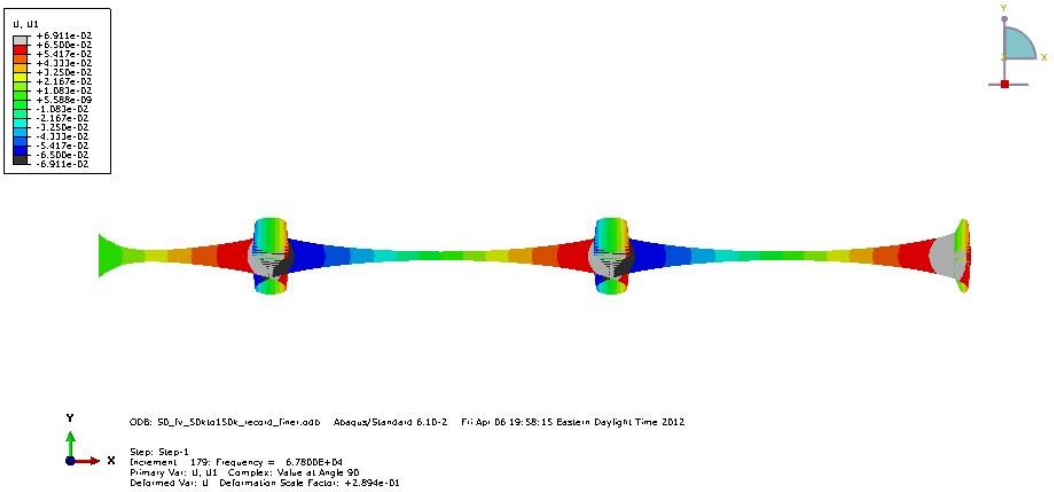

(b) In-plane displacement field under S0 loading at 67800Hz

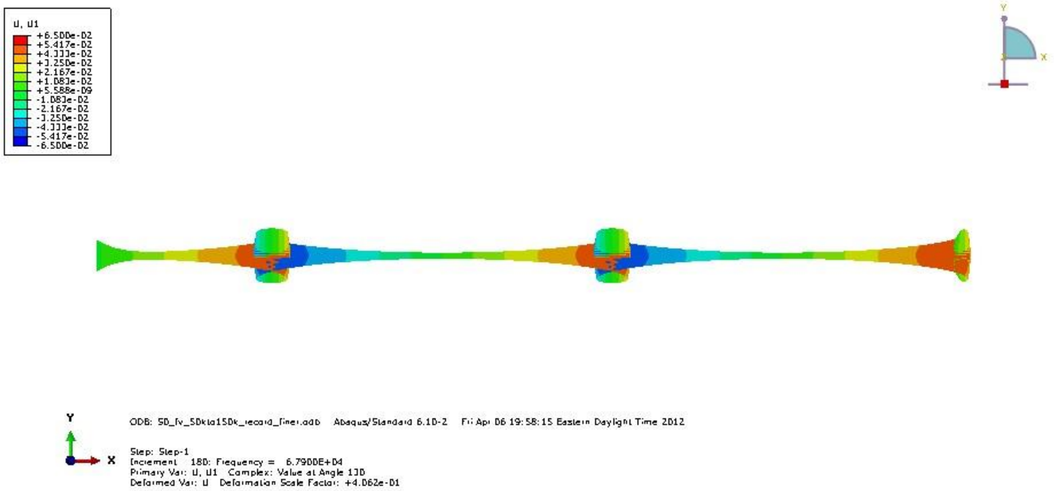

(c) In-plane displacement field under S0 loading at 67900Hz

Figure 3.35. In-plane displacement under S0 input at (a) 67700Hz; (b) 678000Hz; (c) 67900Hz.

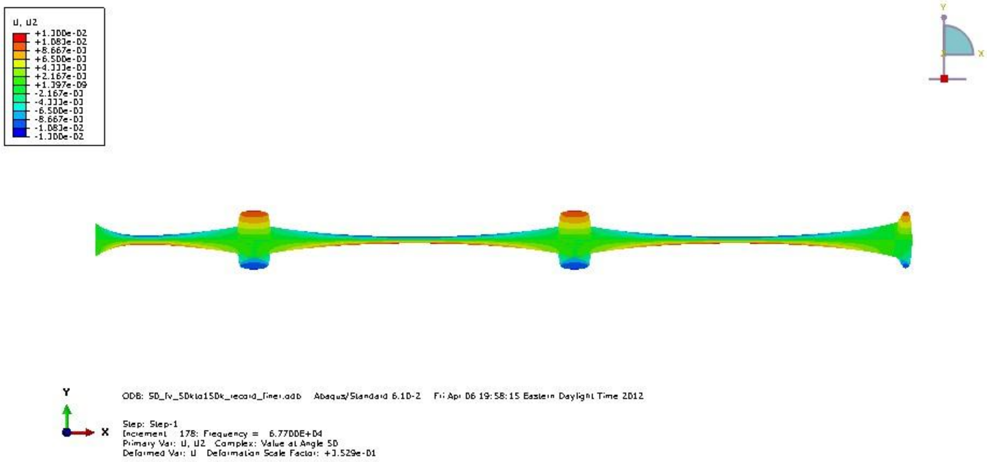

(a) Out-of-plane displacement field under S0 loading at 67700Hz

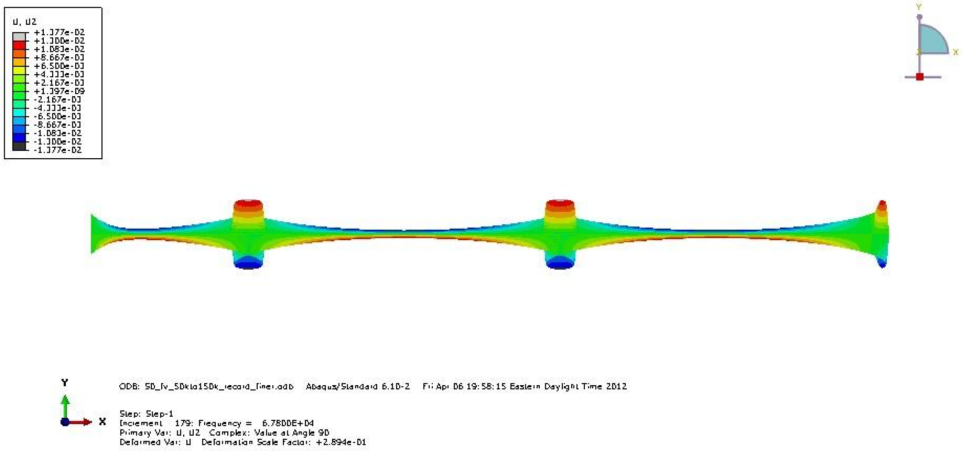

(b) Out-of-plane displacement field under S0 loading at 67800Hz

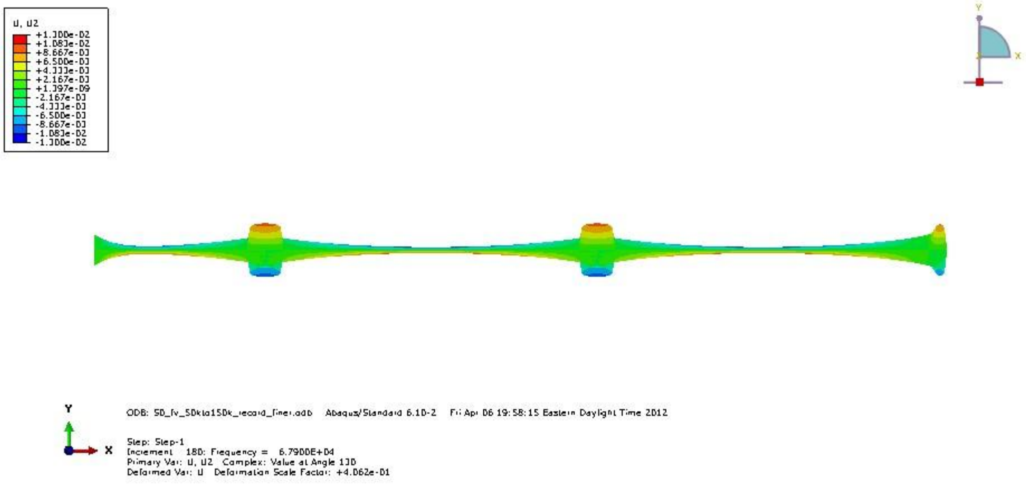

(c) Out-of-plane displacement field under S0 loading at 67900Hz

Figure 3.36. Out-of-plane displacement under S0 input at (a) 67700Hz; (b) 678000Hz; (c) 67900Hz.

A summary of the ODS modes generated through A0 and S0 guided wave loading is presented in Table 3.VIII. By optimally generate guided wave modes, the structural vibration, hence the stress and displacement fields can be controlled.

natural frequency	sym/antisym	A0 loading	S0 loading
54355.3	S		5.44E+04
54973.3	A	5.50E+04	
62296.9	A	6.23E+04	
67783.8	S		6.78E+04
69750.9	A	6.98E+04	
77309.5	A	7.73E+04	
81096.1	S		8.11E+04
84951.5	A	8.50E+04	
92659.3	A	9.27E+04	
94258.8	S		9.43E+04
100419	A	1.00E+05	
107232	S		1.07E+05
108217	A	1.08E+05	
116045	A	1.16E+05	
119969	S		1.20E+05
123893	A	1.12E+05	
131755	A	1.32E+05	
132411	S		1.33E+05
139621	A	1.40E+05	
144490	S		1.45E+05
147483	A	1.48E+05	

Table 3.VIII. Natural frequencies can be excited by A0 and S0 modes

As indicated in the previous study, the guided wave loading can successfully control the ODSs of the structure. Symmetric guided wave modes can only generate symmetric (compressional) vibration modes. Similarly, antisymmetric guided wave modes can only excite antisymmtric (flexure) modes. In the frequency range inspected in this simulation, the steady state vibration fields are only comprise the contribution of A0 mode or S0 mode. Therefore, when the loading function has the wave structures of A0 or S0 mode, the natural frequencies of antisymetric or symmetric modes can be identified respectively from the frequency response functions. This study, in another way, demonstrates the relation between the guided wave modes and vibration modals.

3.3 Defect Sensitivity Difference Due to Different Guided Wave Loading Functions

Finite element simulations were also carried out to demonstrate the differences in defect detection sensitivity when applying different guided wave loading functions in both transient guided wave tests and ultrasonic vibration tests. It was shown that high sensitivity to different types of defects can be achieved by using phased comb or annular array transducers to selectively apply different guided wave loading functions.

3.3.1 Transient guided wave tests

The sample used for sensitivity study for transient guided wave tests was a 16 layer quasi-isotropic plate made from AS4/8552-2 carbon epoxy prepregs. The layup sequence: was $[(0/45/90/-45)_S]_2$ as illustrated in Figure 3.37. Each layer had the thickness of 0.145 mm and the material density was 1.6 g/cm^3. The elastic material property is listed in Table 3.IX.

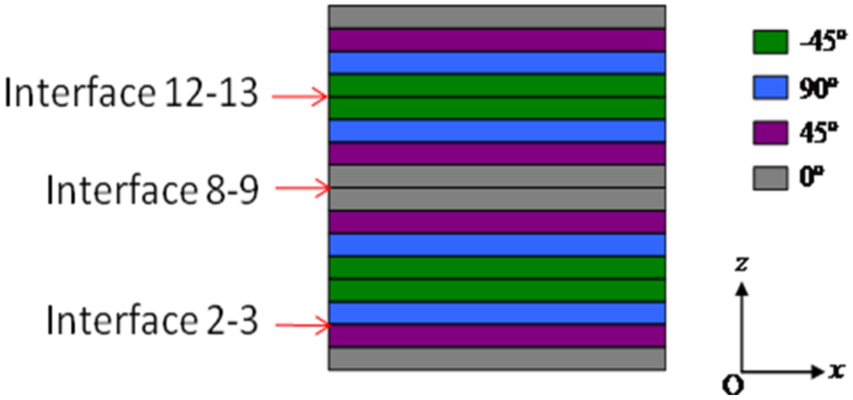

Figure 3.37. Layup sequence of a 16 layer composite laminates

C_{11}	143.8582
C_{12}	4.1803
C_{13}	4.1803
C_{22}	10.6533
C_{23}	3.281
C_{33}	10.6533
C_{44}	3.674
C_{55}	4.895
C_{66}	4.895

Table 3.IX. Elastic modulus of AS4/8552-2 material (GPa)

Dispersion curves for this plate can be calculated following the SAFE method just introduced. Because of its anisotropy, the shape of the dispersion curves depends on the direction of wave launching. Wave behaviors are quite different if sending it in different directions. Figure 3.38 presents the dispersion curves for several wave launching directions.

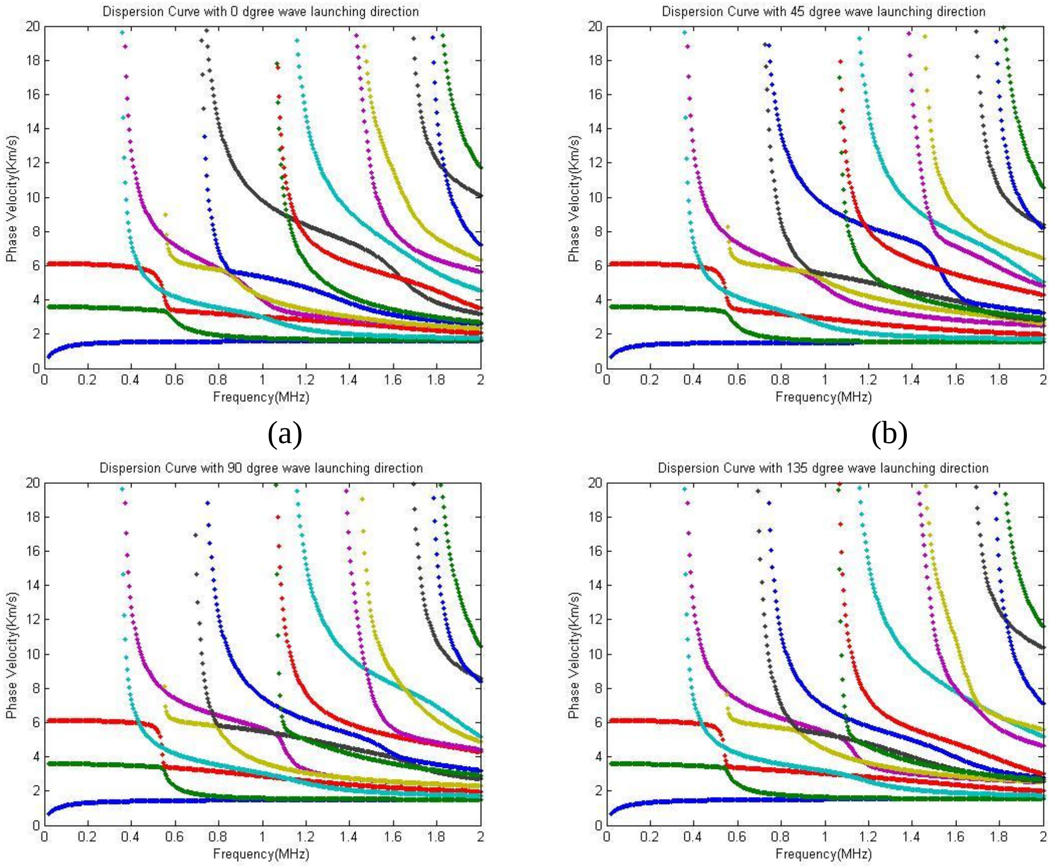

(a) (b)

(c) (d)

Figure 3.38. Variation of the dispersion curves with respect to the wave launching directions. (a), (b), (c) and (d) correspond to wave launching directions 0, 45, 90 and 135 degrees, respectively.

Delamination is the most common defect in composite panels. However, they are usually hidden in the structure and cannot be observed directly. The multiple choices of guided wave modes with different wave structures make the detection of the locations of the delamination possible. In order to detect delamination located at a specific ply interface, it is desired to find an optimal wave impinging into the composite laminates by choosing an appropriate loading frequency and guided wave mode. At the area of the delamination, shear displacements become discontinued, while out-of-plane displacements may still have a chance of passing this defected region by the contact of upper and lower interfaces of the delamination. In other words, ultrasonic guided waves with significant shear displacements at the interface where the delamination defect is located would not travel across this region hence leading to a defect alarms.

In composite structures, guided waves cannot be simply separated into Lamb waves and shear horizontal waves. In fact, those two groups of waves are coupled together when they propagate. However, the layup sequence of this sample plate makes it close to an isotropic plate. In this case, the guided waves can be roughly divided into semi-lamb wave with trivial shear horizontal displacement and semi-shear horizontal wave with dominant shear horizontal displacement. For the semi-Lamb wave, a sensitivity parameter characterized by the significance of the in-plane displacement within the total guided wave displacement field is defined as:

$$S_I = \frac{\overline{U}_x(z_I)\Delta h}{\sum\limits_{j=x,y,z}\int_0^h \overline{U}_j(z)dz} \quad . \tag{83}$$

Here, $\overline{U}_i(i = x, y, z)$ are normalized particle displacements, Δh is the mesh size for calculating displacement distributions across the plate thickness, $\overline{U}_x(z_I)$ is the in-plane displacement at the selected interface and x, y, z are the indices of the system coordinates, where x denotes the wave propagation direction, y refers to the wave front direction, and z is in the plate thickness direction. The sensitivity factor of the semi-Lamb wave for three delaminations, which is located between layers 2 and 3, layers 8 and 9, as well as layers 12 and 13 individually, are displayed in Figures 3.39 to 3.41.

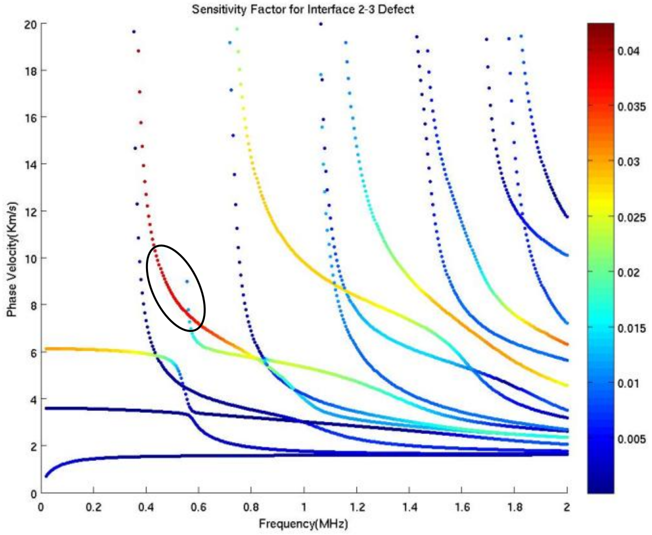

Figure 3.39. Sensitivity factors of semi-Lamb waves on a dispersion curve for detecting delamination between layers 2 and 3. Wave launching direction is 0 degree. The region circled indicates good loading function choices for delamination along interface 2-3.

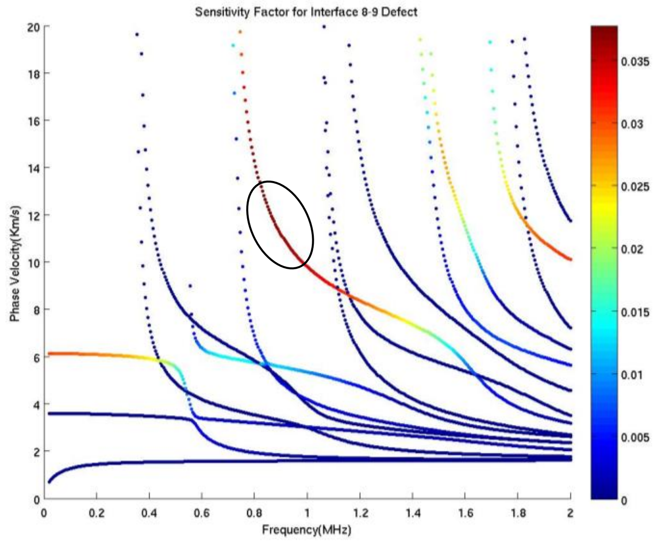

Figure 3.40. Sensitivity factor of semi-Lambs wave on a dispersion curve for detecting delaminations between layers 8 and 9. Wave launching direction is 0 degree. The region circled indicates good loading function choices for delamination along interface 8-9.

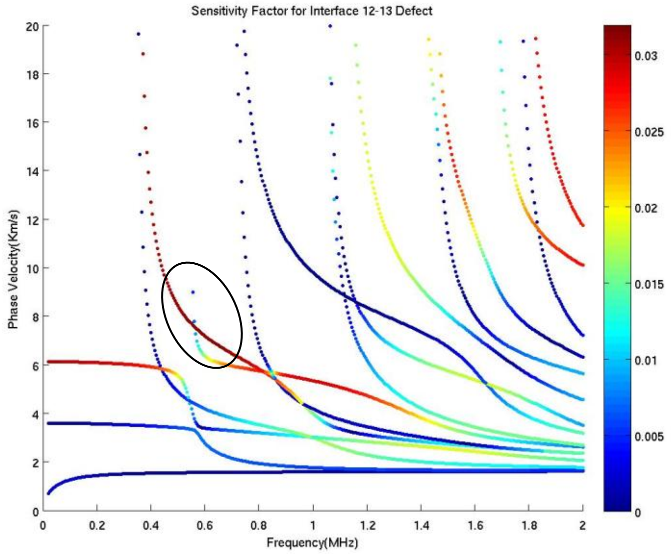

Figure 3.41. Sensitivity factor of semi-Lamb waves on a dispersion curve for detecting delaminations between layers 12 and 13. Wave launching direction is 0 degree. The region circled indicates good loading function choices for delamination along interface 12-13.

Dispersion curves highlighted with the red color in the above figures are the loading regions most sensitive to a typical delamination. In other words, in order to successfully investigate the delamination defect at a specific interface, the loading function should be established in the red region.

Following the same fashion, the sensitivity factor for semi-shear horizontal wave is defined as:

$$S_I = \frac{\bar{U}_y\left(z_I\right)\Delta h}{\sum_{j=x,y,z}\int_0^h \bar{U}_j\left(z\right)dz} \qquad (84)$$

Different from equation (84), the shear horizontal displacement is used to replace the in-plane displacement at the appropriate interface. The sensitivity factor of semi-shear horizontal waves for the three delamination, located between layers 2 and 3, layers 8 and 9 as well as layers 12 and 13 individually, are displayed in Figures 3.42 to 3.44. The red region on the dispersion curves denotes the effective loading functions to such delamination.

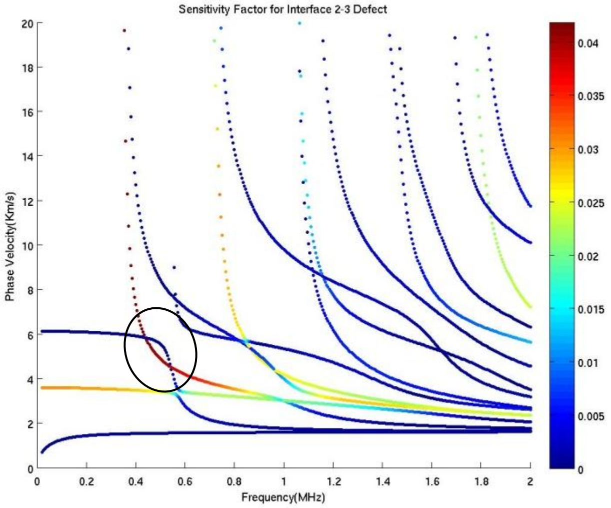

Figure 3.42. Sensitivity factor of semi-shear horizontal waves on a dispersion curve for detecting delaminations between layers 2 and 3. Wave launching direction is 0 degree. The region circled indicates good loading function choices for delamination along interface 2-3.

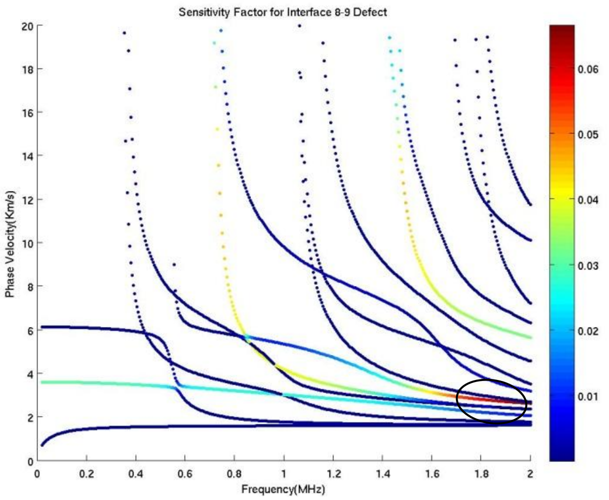

Figure 3.43. Sensitivity factor of semi-shear horizontal waves on a dispersion curve for detecting delaminations between layers 8 and 9. Wave launching direction is 0 degree. The region circled indicates good loading function choices for delamination along interface 8-9.

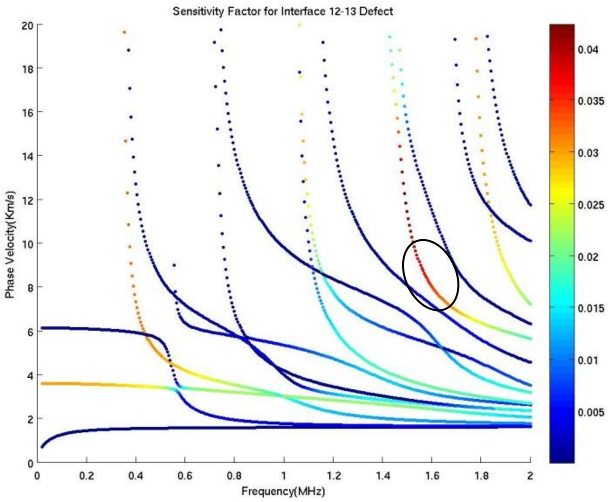

Figure 3.44. Sensitivity factor of semi-shear horizontal waves on a dispersion curve for detecting delaminations between layers 12 and 13. Wave launching direction is 0 degree. . The region circled indicates good loading function choices for delamination along interface 12-13.

To verify the effectiveness of the sensitivity factor proposed in the last chapter, finite element modeling was conducted using the commercial FEM software ABAQUS. Explicit analysis in ABAQUS can model the wave propagation process and the interaction with defects. The geometry of the model is shown in Figure 3.45. Transmitter and receiver are comb type array transducers. The spacing for adjacent fingers is 4.22 mm, which corresponds with the ones used in experiments. Time delay is applied to each finger of the transmitter when necessary, which enhances the mode selection capability of the transducer (Yan and Rose 2009). Delamination, as seen in the middle of the plate, is simulated in different interfaces in several models.

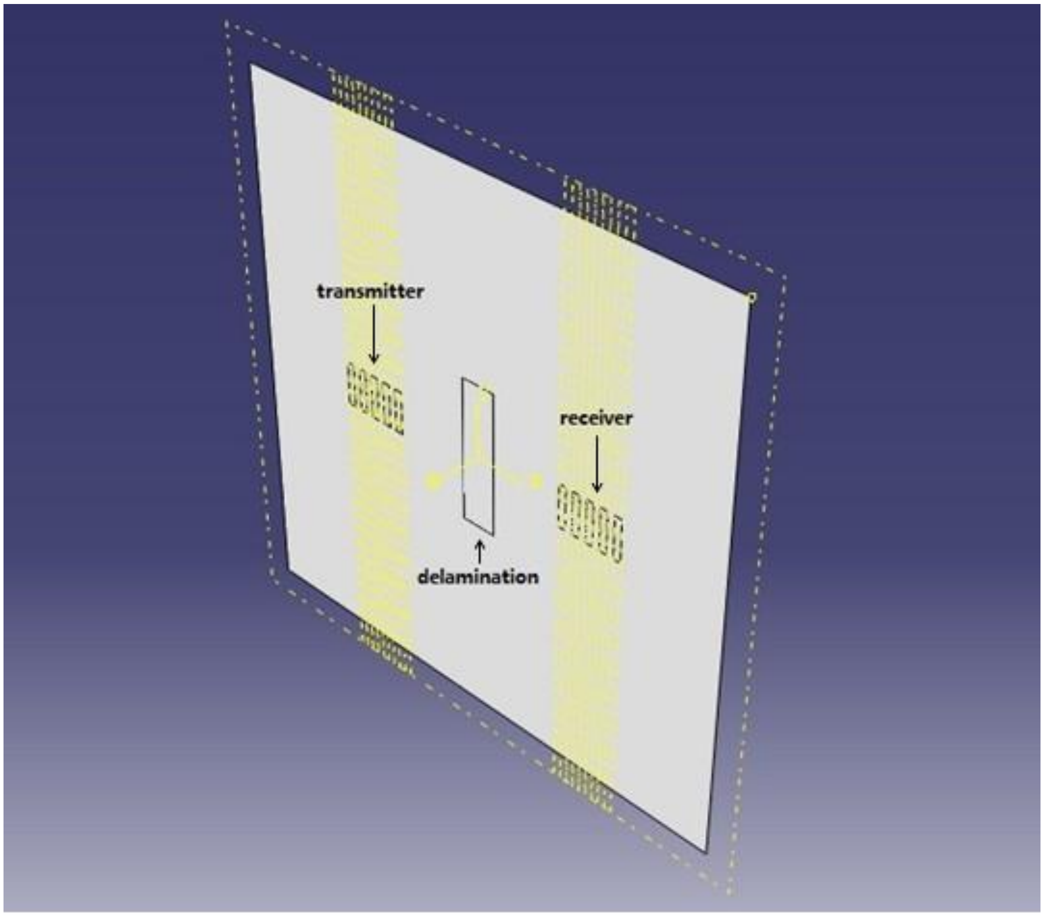

Figure 3.45. Geometry of finite element model in ABAQUS.

The first loading choice is mode 5 at 500 kHz, which is marked with a cross in Figure 3.46. It is obvious that such a guided wave is sensitive to delamination located in the interface between layers 2 and 3, and layers 12 and 13, while it is not a good candidate for inspecting delaminations embedded between layers 8 and 9.

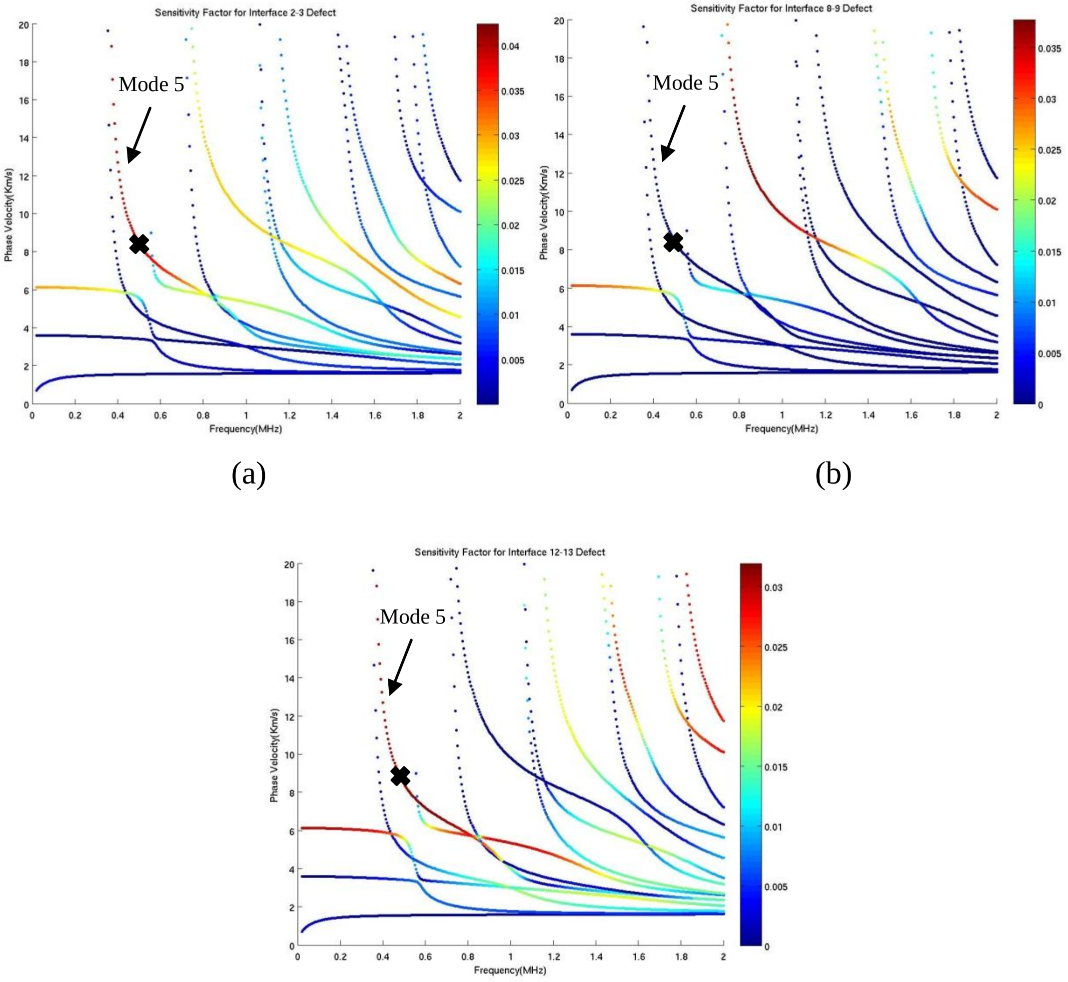

(a)

(b)

(c)

Figure 3.46. Selected guided wave loading function: mode 5 at 500 kHz on sensitivity curves. (a) Sensitivity curve for interface 2-3 defects; (b) Sensitivity curve for interface 8-9 defects; (c) Sensitivity curve for interface 12-13 defects.

The wave structure of mode 5 at 500 kHz is illustrated in Figure 3.47. This is a semi-Lamb type wave since the shear horizontal displacement U_y is very small. As can be seen, the in-plane displacement U_x has very high value at interface 2-3 and 12-13, which corresponds to the sensitivity factor calculation.

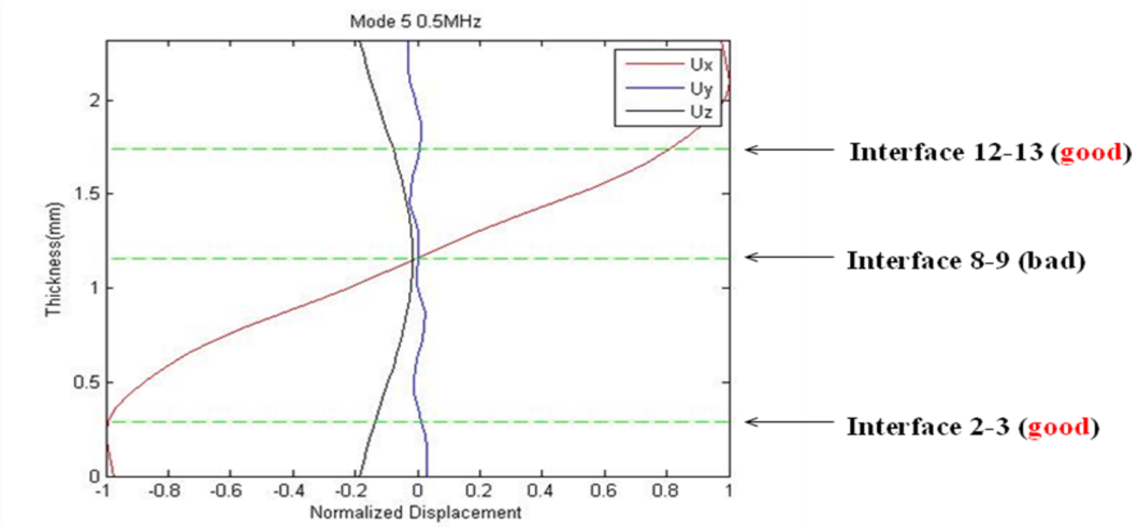

Figure 3.47. Wave structure of mode 5 at 500 kHz. Displacement components vary with the plate thickness. Red curve is the in-plane displacement (U_x); blue curve is the shear horizontal displacement (U_y); black curve is the out-of-plane displacement (U_z).

Finite element models were developed for this loading function. In order to excite mode 5 at 500 kHz, a 1us time delay was applied to the comb transducer. Four cases were studied in the simulations: baseline and delaminations inserted in three different interfaces individually. The finite element results can refer to Figure 3.48. The Von-Misses stress field can be visualized.

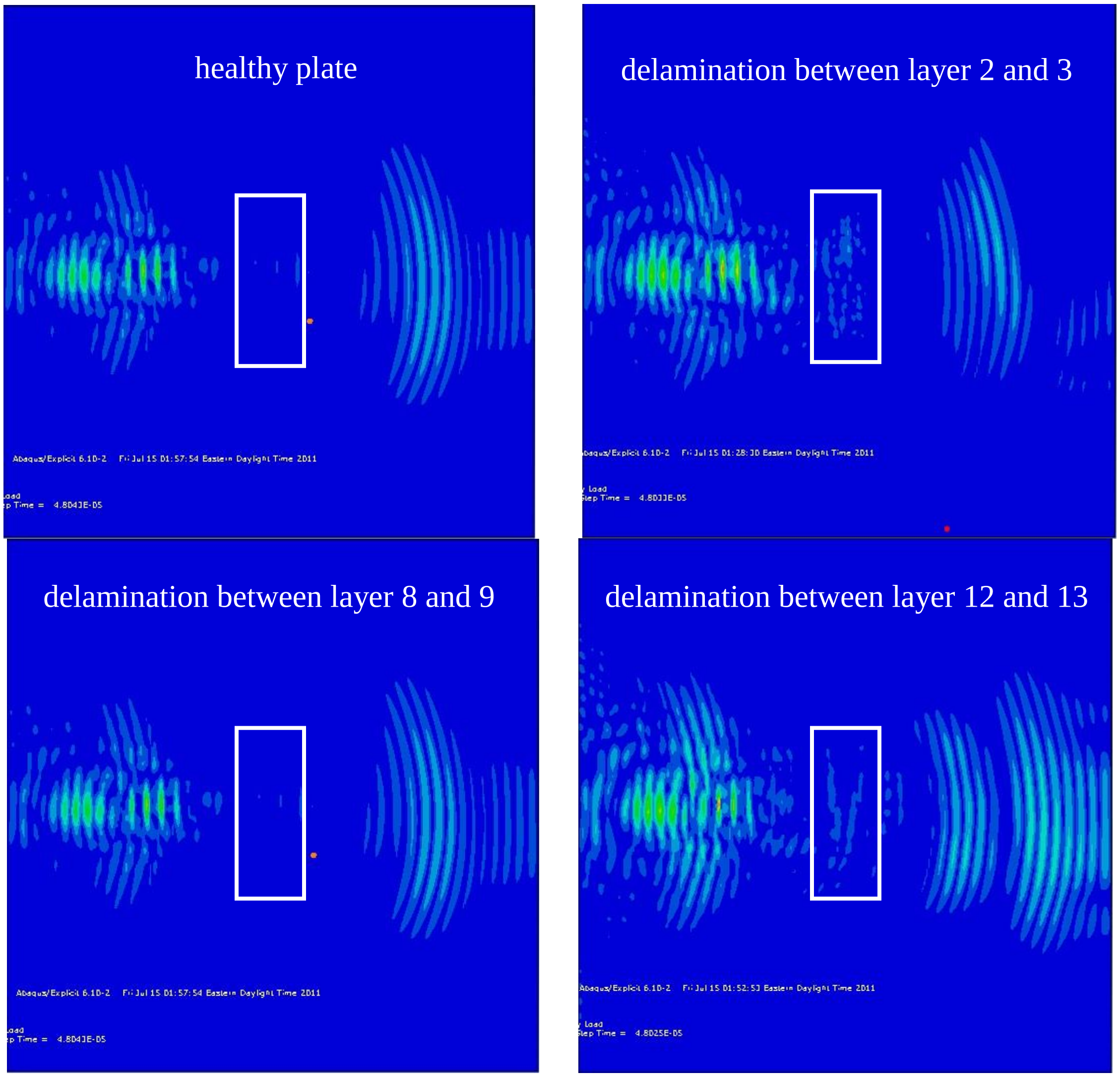

Figure 3.48. Finite element simulations for guided wave loading mode 5 at 500 kHz. Damage states are labeled in each picture. Delamination regions are enclosed by a rectangular.

As indicated in the finite element result, some wave energy is trapped in the damaged region when the delamination was embedded between layers 2 and 3 or layers 12 and 13. Moreover, under those two delamination cases, mode conversion occurs, which can be clearly observed from the wave passing through the defect region. However, when delamination is in the interface between layers 8 and 9, the wave behavior is exactly the same as that in a healthy plate: no energy trapped inside the damaged region and no mode conversion. Therefore, a delamination in layers 8 and 9 cannot be detected using this guided wave mode. The finite element simulation strongly supports the guided wave sensitivity assumption.

Another loading considered is mode 4 at 520 kHz, which is marked by a cross in the sensitivity curves in Figure 3.49. The sensitivity curve indicates that this wave is only sensitive to delamination located in the interface between layers 2 and 3 and layers 12 and 13.

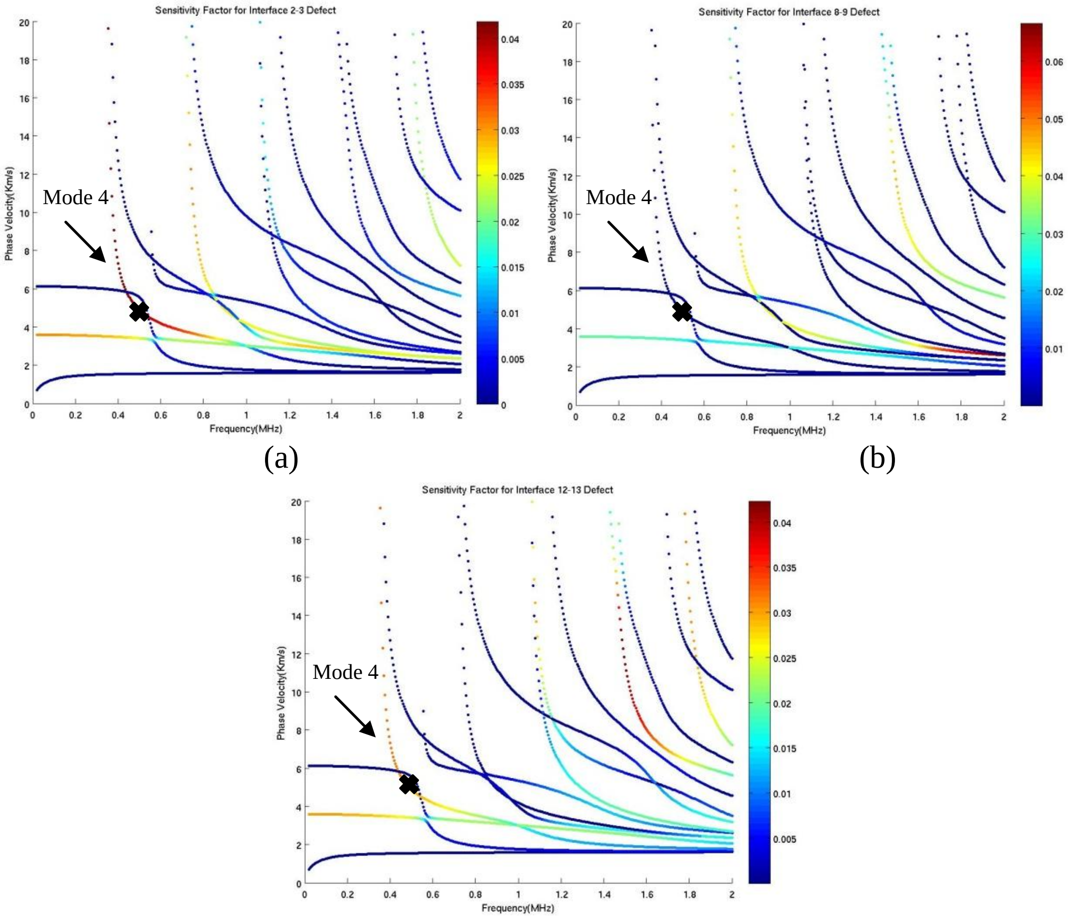

(a) (b)

(c)

Figure 3.49. Selected guided wave loading function: mode 4 at 520 kHz on sensitivity curves. (a), (b), (c) are sensitivity curves for defects in interface 2-3, interface 8-9, and interface 12-13 respectively.

The wave structure of mode 4 at 520 kHz is illustrated in Figure 3.50. With the dominant shear horizontal displacement U_y, it is classified as a semi-shear horizontal wave. Figure 3.47 shows that U_y has a very high value at interface 2-3 and 12-13, which agrees well with the sensitivity factor calculation in Figure 3.49.

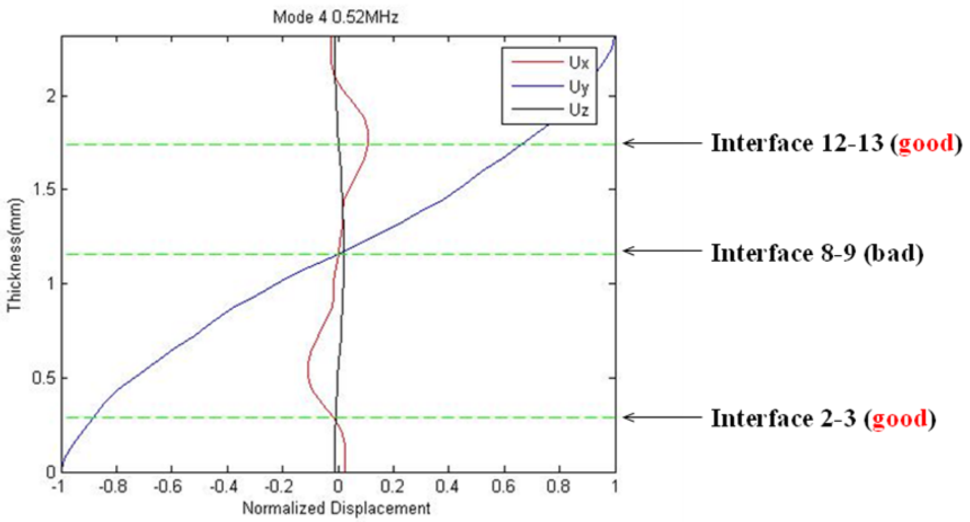

Figure 3.50. Wave structure of mode 4 at 520 kHz. Displacement components vary with the plate thickness. Red curve is the in-plane displacement (U_x); blue curve is the shear horizontal displacement (U_y); black curve is the out-of-plane displacement (U_z).

Finite element models were developed as well. 0.1262 us time delay was added to the transmitter to excite mode 4 at 520 kHz. Four cases were studied in the simulations: baseline and delaminations inserted in three different interfaces individually. The finite element results with Von-Misses stress contour plots are shown in Figure 3.51.

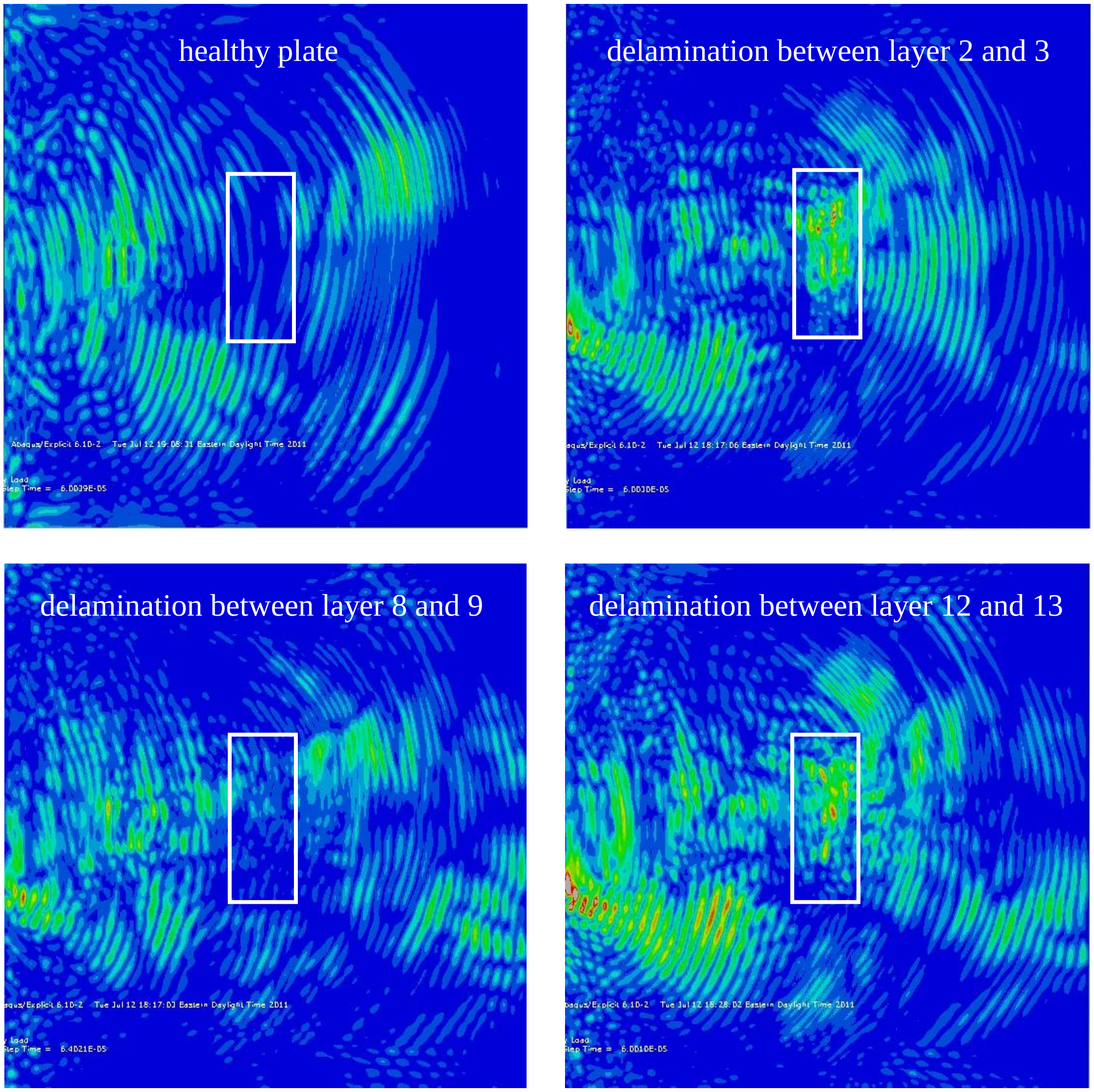

Figure 3.51. Finite element simulations for guided wave loading mode 4 at 520 kHz. Damage states are labeled in each picture. Delamination regions are enclosed by a rectangular.

Figure 3.51 indicates that when a delamination is presented between layers 2 and 3 or layers 12 and 13, much wave energy is trapped in the damaged region. However, a delamination in the interface between layers 8 and 9 has little interference with the wave field. Thus, a delamination in layers 8 and 9 is invisible for this kind of wave mode, which agrees with the theoretic study.

A detailed view of wave propagation process in the plate with delamination between layers 12 and 13 is in Figure 3.52. As can be seen, some part of wave is reflected back by the defect and therefore provides the defect information.

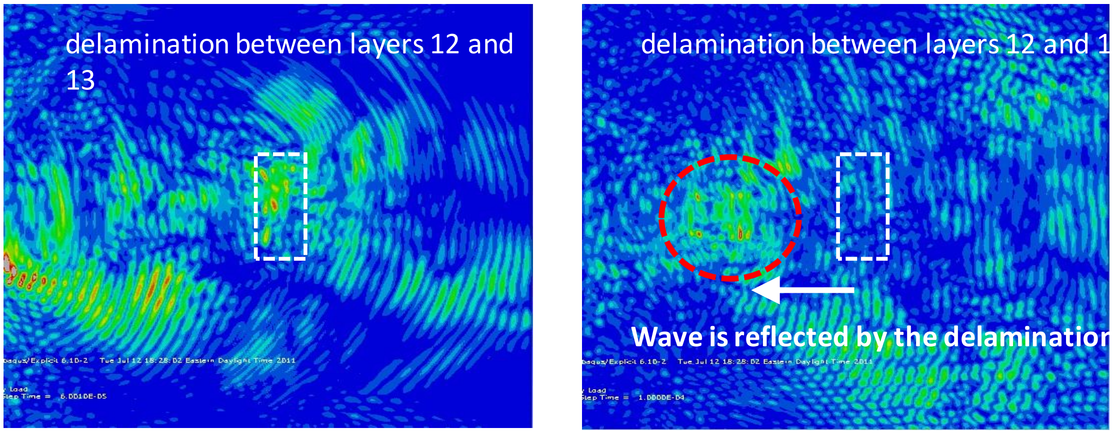

(a) (b)

Figure 3.52. Wave propagation in the plate with a delamination between layers 12 and 13. (a) and (b) are snap shots after the wave propagates 50 us and 100 us, respectively.

The finite element simulation results clearly demonstrate that by choosing different guided wave modes and frequencies, high defect detection sensitivity can be achieved in transient guided wave tests for different defects.

3.3.2 Defect Detection Sensitivity in Ultrasonic Vibration Tests

Finite element simulations were also conducted to observe the defect detection sensitivity in ultrasonic vibration tests under different guided wave loading functions. The commercial software package ABAQUS Standard was adopted in the FEM calculation. The geometry of the model is shown in Figure 3.53. A four-ring annular array in the lower right corner served as the actuator. The plate studied in the simulation was a 0.15 m by 0.15 m by 0.003 m aluminum plate. Several points were marked on the plate to record the vibration amplitude under different guided wave loading functions. The locations of the points selected for the vibration amplitude study are all given in Figure 3.53. As also shown in Figure 3.53, a square shaped surface defect with a 0.008 m by 0.008 m area and a 33% depth of the plate thickness was included in the model for the defect sensitivity study. Vibration amplitudes were calculated in ABAQUS for different guided wave loading functions provided by different frequency and phase delays that are applied to the 4 elements of the annular array actuator. Example vibration amplitudes for different phased delays under a 180 kHz driving frequency are given in Figures 5.54 to 5.57. Amplitudes measured from both the healthy plate without the defect and the plate with the surface defect are plotted.

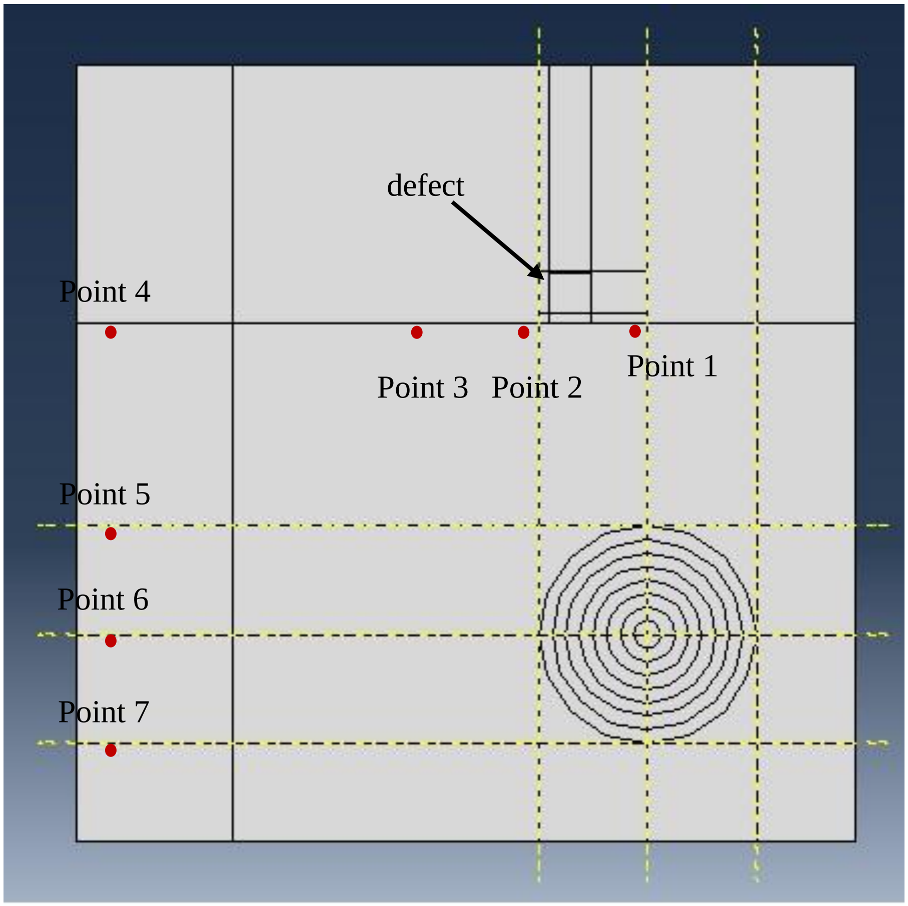

Figure 3.53. Geometry of the FEM model for a defect sensitivity study for ultrasonic vibration tests. Seven points were selected to study the vibration amplitudes under different guided wave loading functions. The location and dimension of the defect used in the defect sensitivity study is also marked in the figure.

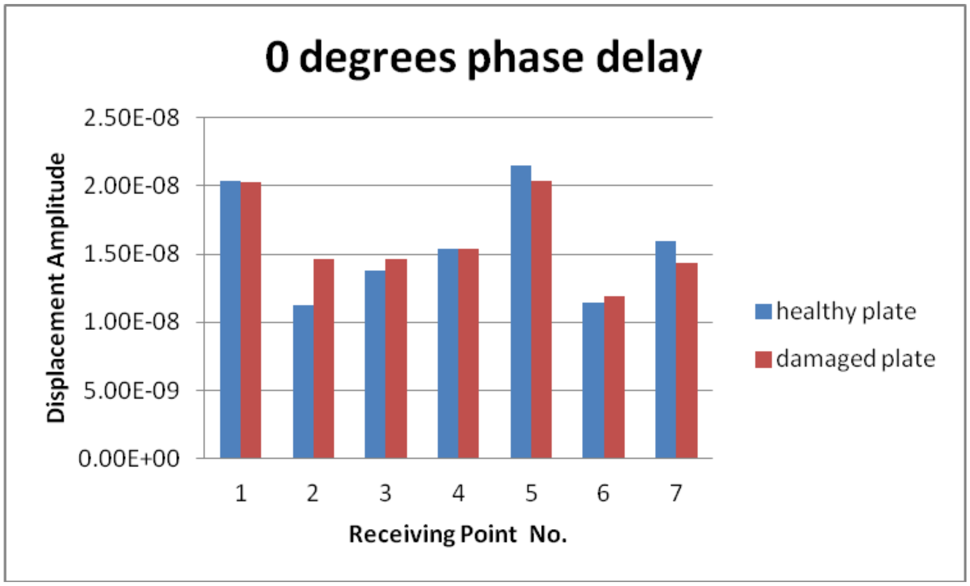

Figure 3.54. Displacement amplitude comparison of seven sensors in the healthy plate and damaged plate when the loading frequency is 180 kHz and phase delay 0 degrees.

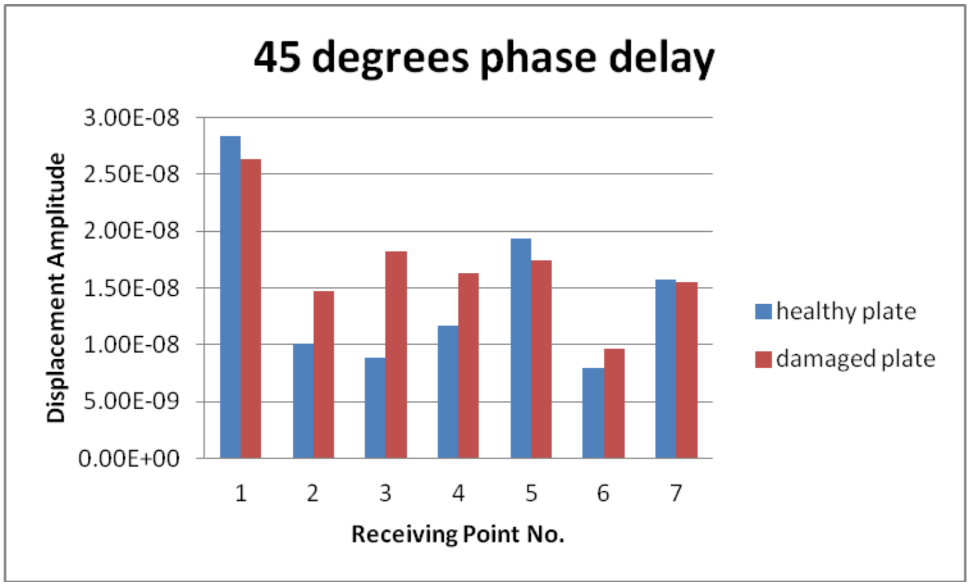

Figure 3.55. Displacement amplitude comparison of seven sensors in the healthy plate and damaged plate when the loading frequency is 180 kHz and phase delay 45 degrees.

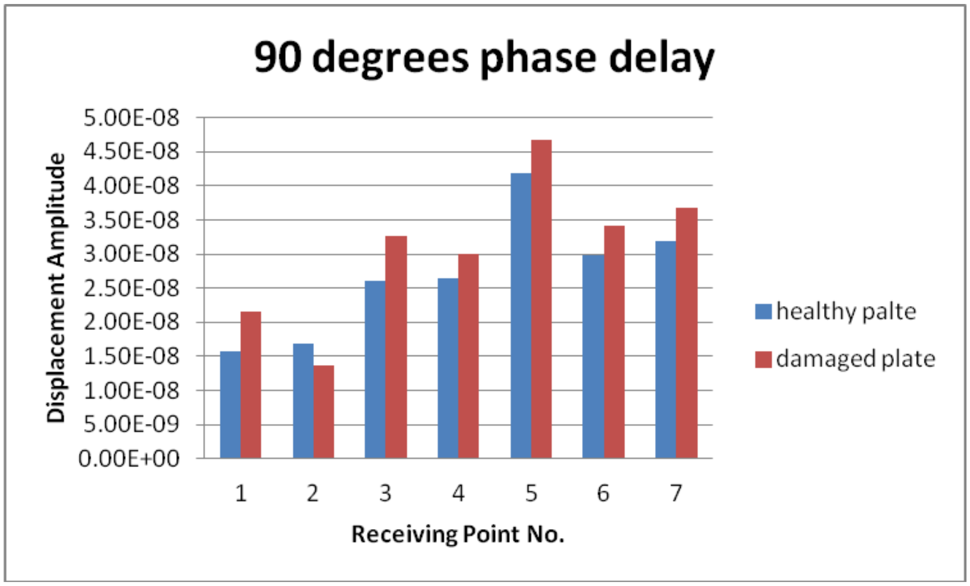

Figure 3.56. Displacement amplitude comparison of seven sensors in the healthy plate and damaged plate when the loading frequency is 180 kHz and phase delay 90 degrees.

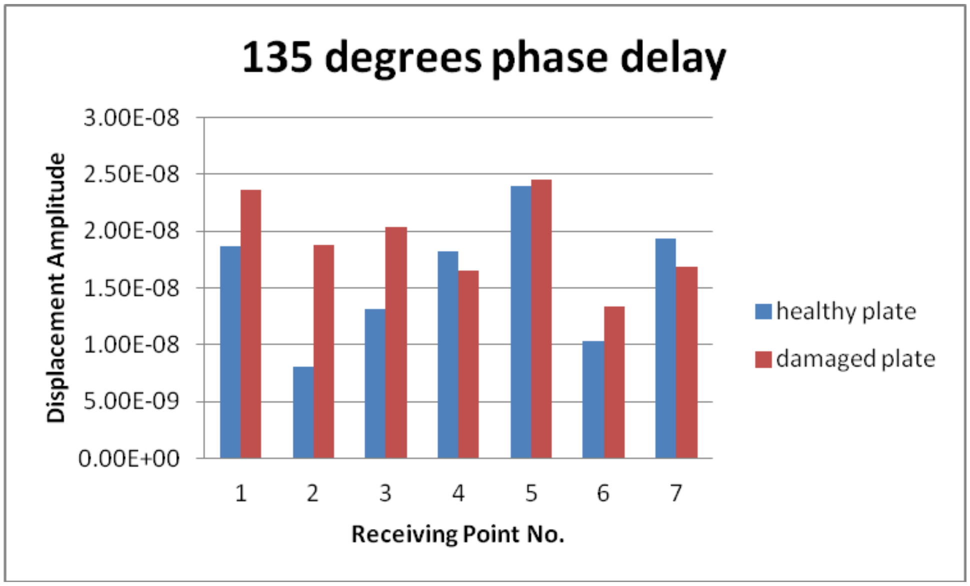

Figure 3.57. Displacement amplitude comparison of seven sensors in the healthy plate and damaged plate when the loading frequency is 180 kHz and phase delay 135 degrees.

From Figures 3.54 to Figure 3.57, it can observed that, after the defect was introduced, the 45 degrees and the 135 degrees phase delays yield more significant amplitude variations than the 0 degrees and the 90 degrees phase delays do. More quantitatively, the relative changes of the amplitudes for each sensor in each phase delay scenario are listed in Table 3.X.

The last row of Table 3.X shows that the total changing ratio of 45 degrees and 135 degrees were higher than 0 degrees and 90 degrees, so they were more sensitive to this defect.

The amplitude difference ratios of each sensor under each phase delay loading are plotted in Figure 3.58. Also shown is that the 45 degrees and 90 degrees phase delay at 180 kHz has a strong ability to detect this defect. Especially when the sensor location are close to the defect, which are sensor 2 and 3 in this model, these sensors are more likely to set a defect alarm.

Table -3.X. Displacement amplitude changing ratio after introducing the defect.

Displacement amplitude changing ratio after introducing the defect				
	0 degrees	45 degrees	90 degrees	135degrees
sensor 1	0.004447875	0.072216563	0.3652262	0.268181185
sensor 2	0.299842791	0.452441077	0.18844905	1.326151915
sensor 3	0.061044051	1.060629288	0.24816654	0.555879326
sensor 4	0.001226183	0.402192608	0.13450815	0.092596793
sensor 5	0.050337354	0.096638765	0.11450048	0.021777744
sensor 6	0.04147545	0.225973426	0.14562303	0.298123094
sensor 7	0.09960291	0.01157649	0.1531298	0.12471986
sum of all sensors	0.557976615	2.321668216	1.34960326	2.687429917

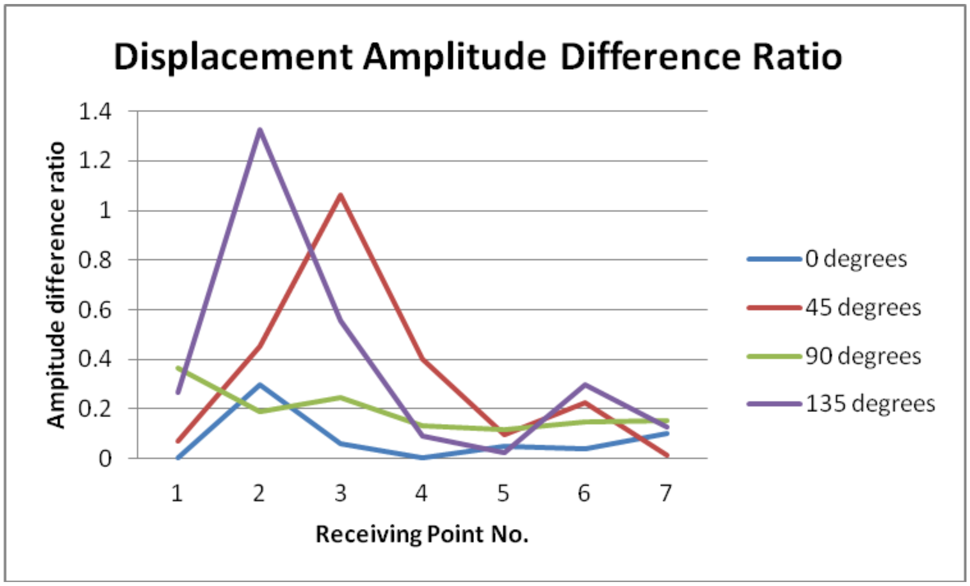

Figure 3.58. The displacement amplitude difference ratios showing high defect detection sensitivity from 45 and 135 degree phase delays.

4. Annular Array Design and Fabrication

Five different annular array patterns were designed. The designed annular array patterns are shown in Figure 4.1, with r denoting the diameter of the arrays, s being the element spacing, and N representing the number of elements. Among the five designs, one is for a segmented annular array in which each element of the array is separated into 4 segments. The segmented annular array is more suitable for UMAT applications on structures with strong material anisotropy. It is also applicable in transient guided wave tests to gain defect circumferential location information in defect detection. The annular arrays were designed based on a consideration of high flexibility in guided wave mode and frequency control. The center frequencies of the annular arrays will all be around 400 kHz, except for the largest array, whose center frequency will be at 200 kHz.

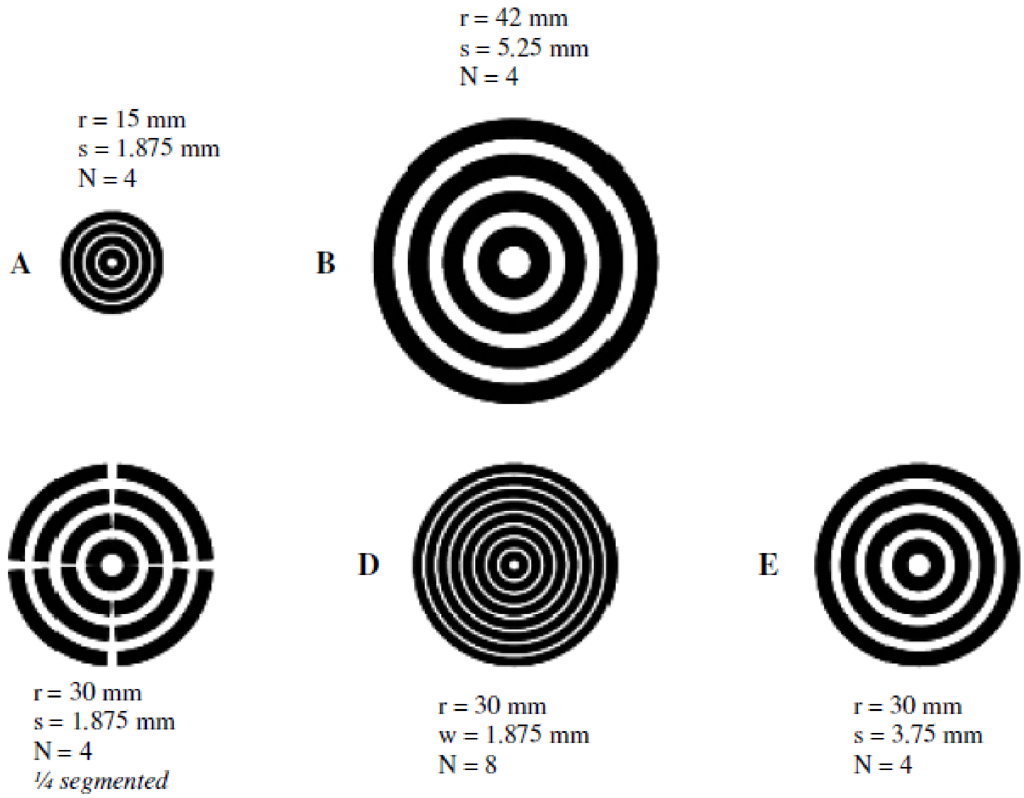

Figure 4.1. Designs of the annular array patterns

The designed annular array patterns were applied to the piezo-composite disks acquired from Smart Material using the photolithography technique. The finished electrodes are shown in Figure 4.2. Two 42 mm diameter disks and two 30 mm diameter disks were used in the fabrication. The electrode patterns applied to the two large disks are 4 equally spaced co-axial circular rings. A pattern with 8 equally spaced co-axial rings was created on one small disk. The other small disk has 4 segments with each segment having 4 fan-shaped electrodes. All individual electrode elements of the 4 disks will be wired. The wired disks will then be packaged into a copper housing with epoxy applied to the back of the disks as the backing material. Minor electrode material loss due to scratching during the fabrication process can be observed in Figure 4.2. Silver conductive epoxy will be used to repair the electrode material loss prior to wiring the electrode elements.

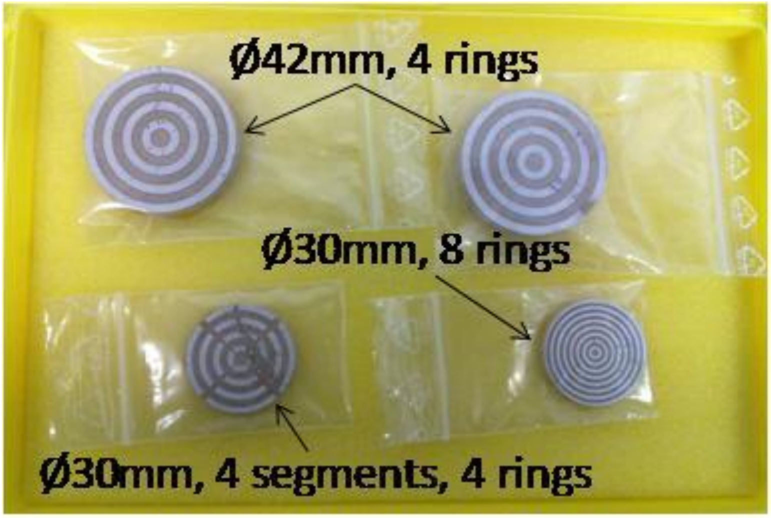

Figure 4.2. Piezo-composite disks with designed electrode patterns etched through photolithography.

For ease of connecting the multi-element annular array to the output channels of the ultrasonic vibration test system developed for this project, we prepared SMB and LEMO connectors with multiple pins. Figure 4.3 shows a cable with two female SMB connectors, one female 10 pin male LEMO connector, and one 10 pin female LEMO connector. For the annular array actuators with 4 individual elements, a 5 pin male LEMO connector can be wired to the elements with the extra pin being the shared ground of the 4 elements. To connect the actuator to the testing system, another cable with 4 female SMB connectors at one end and a 5 pin female LEMO connector at the other end can be made to match both the SMB connectors on the testing system and the LEMO connector of the actuator. The connection can then be done by pushing the SMB connectors into the 4 output channel SMB connectors and simply pushing the two LEMO connectors together. For 8 element array actuators, at least two 5 pin LEMO connectors may be used. Each connector can be wired to 4 elements of the actuator. If a testing system with more output channels is used, LEMO connectors with more pins can be used. Such a design of connectors for the actuators is expected to greatly reduce wiring problems for UMAT testing which always involves multiple channels.

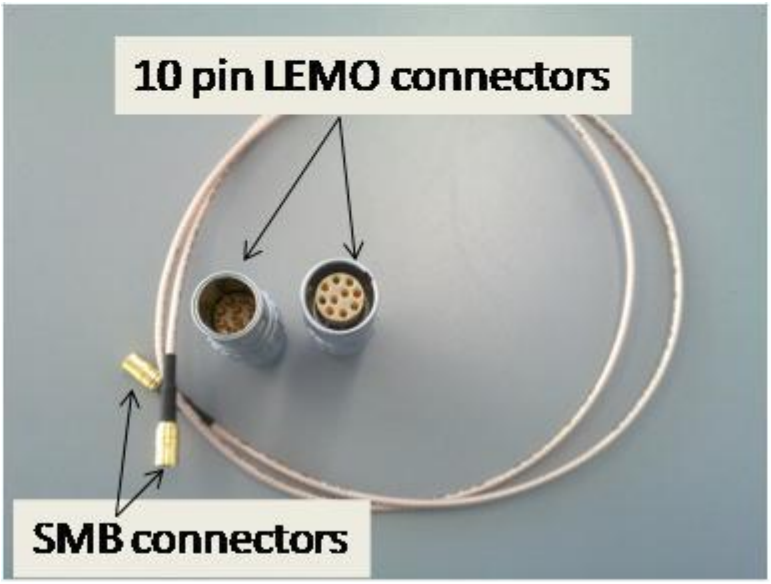

Figure 4.3: SMB and LEMO connectors.

UMAT actuator fabrication was carried out at Penn State University. A finished prototype actuator is shown in Figure 4.4. The actuator has a 42 mm diameter piezo-composite disk with 4 individual electrode rings. The disk is housed in a copper tube with an aluminum wear plate attached to the bottom of the tube. The ground of the piezo-composite disk is wired to the copper housing and the aluminum wear plate. Epoxy is filled back to the back of the piezo-composite to serve as the backing material. A 5 pin LEMO connector is used to provide electrical connections to the 4 hot electrodes and the ground electrode.

Figure 4.4. A prototype UMAT actuator.

5. Ultrasonic Vibration System Design and Development

5.1 Hardware System Design and Development

In Phase I of this project, it was demonstrated that a key to success of the UMAT tests was the selection of appropriate guided wave modes and frequencies as the ultrasonic loading functions. Time delay annular array transducers, due to their excellent capability of guided wave mode and frequency selections, were developed in Phase II of this project as the UMAT actuators to provide the desired ultrasonic loading functions. To use the time delay annular array actuators for UMAT tests, however, a unique hardware system is needed to excite the actuators as well as to acquire the UMAT signals for defect detection purposes. It is required that the system is able to output multi-channel sine wave signals. Controllable phase shifts among different output channels are also required as the phase shifts (time delays) play an important role in the guided wave mode selections. The frequency range of the system needs to cover a typical guided wave application range, say 20 kHz – 1 MHz. To achieve steady state vibration stages under the ultrasonic loading functions, it is necessary to have up to 3000 cycles of sine wave inputs. The hardware system, therefore, should be capable of outputting sine waves with large numbers of cycles. For the phase shifts among different output channels, it is obvious that smaller phase shift resolution is better as the guided wave mode control can be more accurate. As shown before, a multi-channel receiver is beneficial in a UMAT test as different test points may be responsible for defects at different locations or different types of defects. Relatively high sampling frequency for the receiving channels, for example, 100 times the actuator operating frequency, is necessary for further improving signal-to-noise ratio through signal averaging in a potential noisy environment. The on-board memory of the receiving channels needs to be sufficient for receiving long signals with relatively high sampling frequencies.

FBS and Penn State designed such a hardware system to meet the aforementioned system requirements. We found out that no ready-to-use systems are available in the market to meet all the requirements. To build a custom system, we contacted several hardware manufacturers including U.S. Ultratek, Physical Acoustic NDT (PACNDT), and National Instruments (NI). The most applicable system solution we obtained is from NI. We were able to design a NI hardware system that offers 4 channel phase shift controllable sine wave function generators and an 8 channel receiving card with the sampling frequency up to 60 MHz and a total of 128 MB onboard memory. As comparison, the multi-channel phase array card offered by U.S. Ultratek only outputs square waves and is also limited in tone burst signals with small numbers of cycles. There is a power consumption issue for the U.S. Ultratek card for outputting long signals with large numbers of cycles. There is a function generator card offered by PACNDT that can produce long sine wave output signals. However, there is only a single channel version of the card and no easy-to-implement solutions for controllable phase shifts among different cards are available.

The initial system designed by FBS and Penn State using NI hardware consists of 4 NI PXI-5402 function generator cards, 1 NI PXI-5105, 8 channel A/D card, and a NI PXI-

1033, 5 slots PXI Chassis with integrated MXI-Express Controller. Four slots of the PXI Chassis will be occupied by the function generator cards. With the integrated MXI-Express Controller, it is straightforward to apply phase shifts among different function generator channels. The additional slot in the Chassis is for the 8 channel A/D card. The trigger of the A/D card is offered by the MXI-Express Controller. The onboard memory for each A/D channel is 16 MB which is sufficient for more than 0.1 second of a receiving signal with a 10 MHz sampling frequency. The longest time duration for receiving signals that we used in the past experiments was less than 20 ms.

The hardware system was further upgraded to include more channels. As demonstrated in the theoretical study of guided wave excitation by annular array and comb transducers, the capability of guided wave mode and frequency control can be greatly improved with more transducer elements and more output channels to separately drive the transducer elements. A NI PXIe 1065 chassis with 18 slots and four new function generator cards PXI 5412 were purchased to upgrade the hardware system with an extended number of output channels.

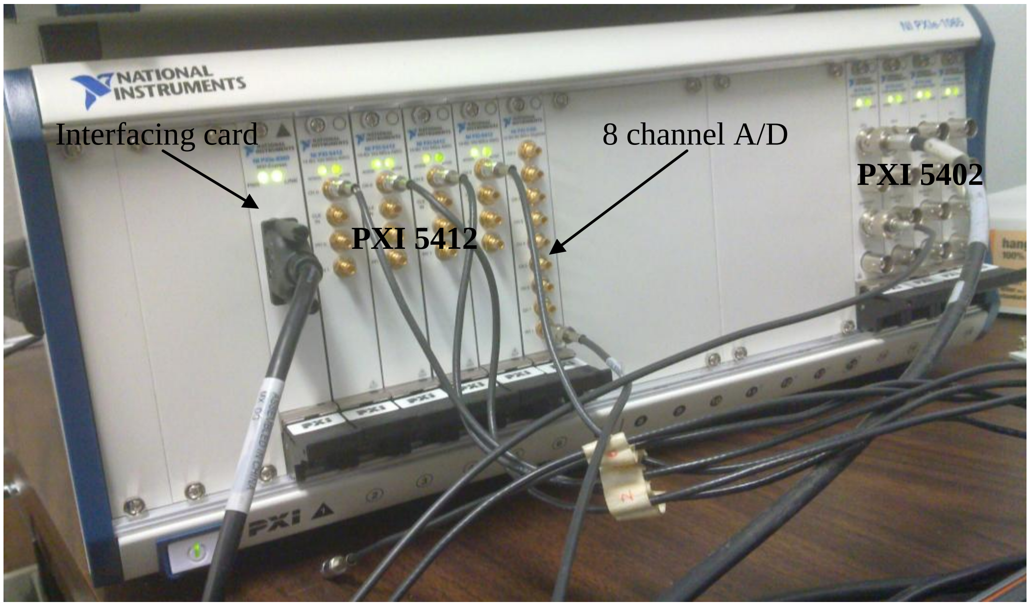

Figure 5.1. Updated system having the new PXI chassis with 8 output channels and 8 receiving channels.

Figure 5.1 shows the new chassis with 8 function generator cards, one interface card, and one A/D card with 8 channels. Figure 5.2 shows four of the eight output signals from the updated hardware system. The driving frequency was 500 kHz and the phase delay was 45 degrees among each adjacent channels. The correct frequency and phase delay can be seen in the display of the oscilloscope. Since the oscilloscope only has 4 display channels, only the signals from 3 of the 4 PXI 5412 cards and 1 of the 4 PXI 5402 cards are shown. Just from Figure 5.2, it is clear that the two types of function generator cards can now work together with correct frequency and phase delays. The upgraded system can threfore be used to drive two actuators each with 4 elements or one 8 element actuator.

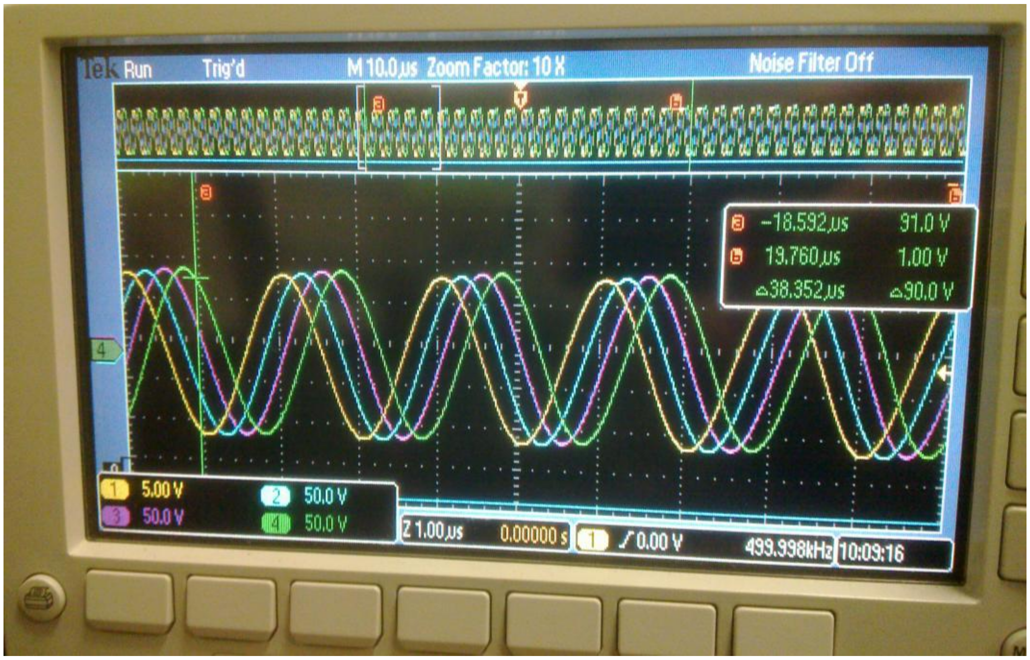

Figure 5.2. Sample phase delayed sine signals outputted from the new chassis with 8 output channels. The oscilloscope has only 4 channels to display 4 of the output signals. The frequency and phase delays match with what was defined in the software interface.

5.2 Software Design and Development

Besides the hardware system development, FBS also developed a custom software package for controlling the hardware system for ultrasonic vibration data acquisition and for processing the vibration data for damage detection. Wave mechanics calculation software was also developed. The software was all programmed in Labview. The Labview State Machine programming architectures were used to develop the software. State Machine architecture is an efficient way to handle complex decision-making algorithms in Labview. The use of State Machine makes it easy to maintain and to upgrade the source codes.

The software interface is tab-based. In the current version, 5 tabs are included in the interface: Setup, Transient Test, Continuous Sine, Data Analysis, and Report. The order of the tabs was arranged to accommodate a complete UMAT test. Figure 5.3 presents the Setup interface. Within this interface, the system operator can define the geometry of the annular array actuator and also the structure under the UMAT inspection as a waveguide. The driving signals for a transient guided wave test can also be defined in this interface. Based on the actuator geometry, the waveguide, and the driving signals, the excitation spectrum together with the dispersion curves can be calculated and displayed in this interface. The driving signals can be adjusted based on the output to identify the optimum setup in terms of frequency and time delay for guided wave mode selection.

Figure 5.4 shows the interface of the Transient Test tab, in which the frequency and time delay selected from the setup interface can be input here for transient guided wave tests. Frequency tuning and time delay tuning options are also available at this interface. The goal of the transient guided wave tests is to verify the time delay and frequency input for the selection of the guided wave loading function. Multiple signal gates based on the group velocities can be defined at the interface to capture the amplitude variations of different guided wave modes and frequencies for different time delays. The optimal time delay and frequency for the excitation of a certain guided wave mode can then be analyzed from the amplitude variations.

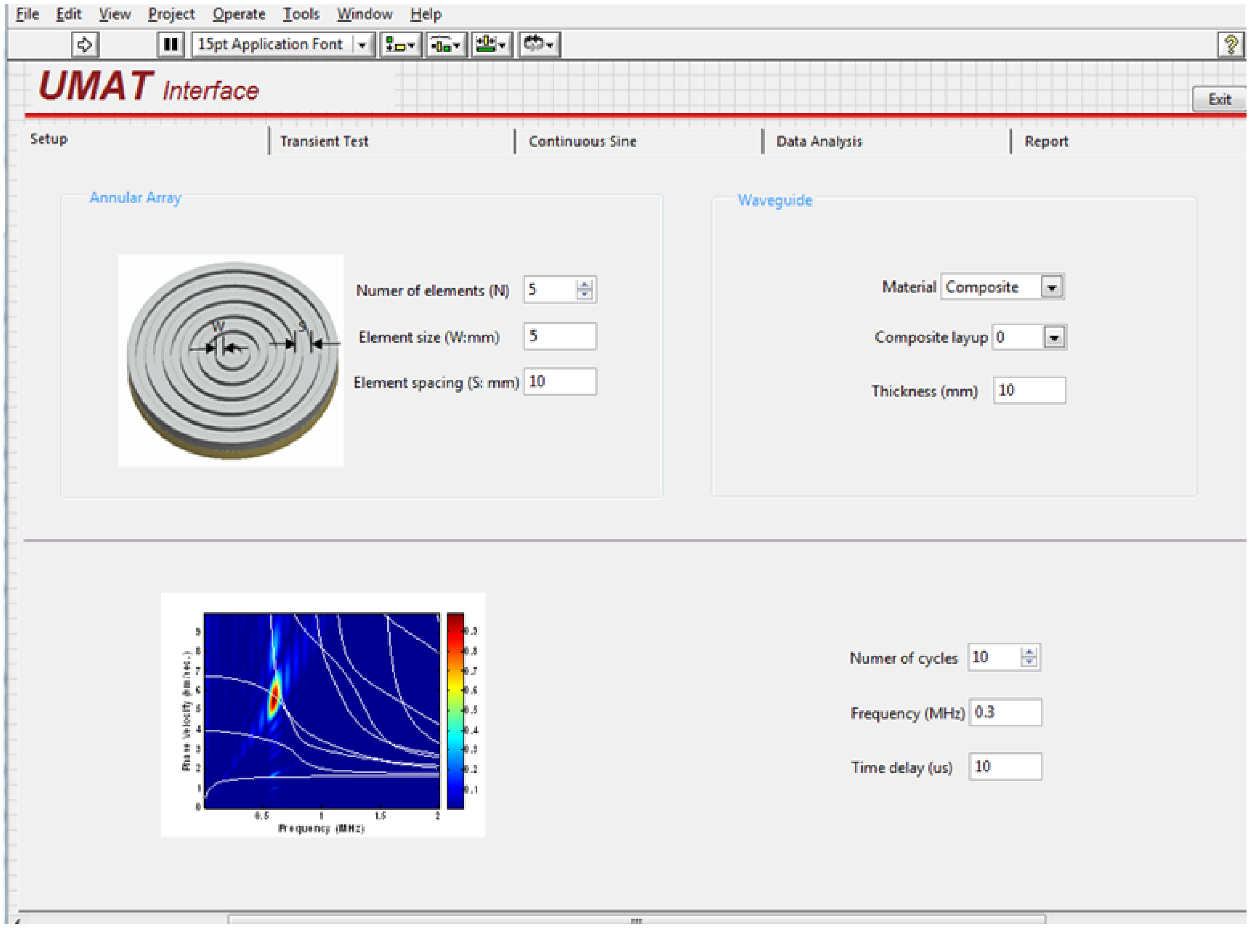

Numer of elements (N) 5

Element size (W:mm) 5

Element spacing (S: mm) 10

Material Composite

Composite layup 0

Thickness (mm) 10

Numer of cycles 10

Frequency (MHz) 0.3

Time delay (us) 10

Figure 5.3. *New UMAT software interface. The Setup tab is shown.*

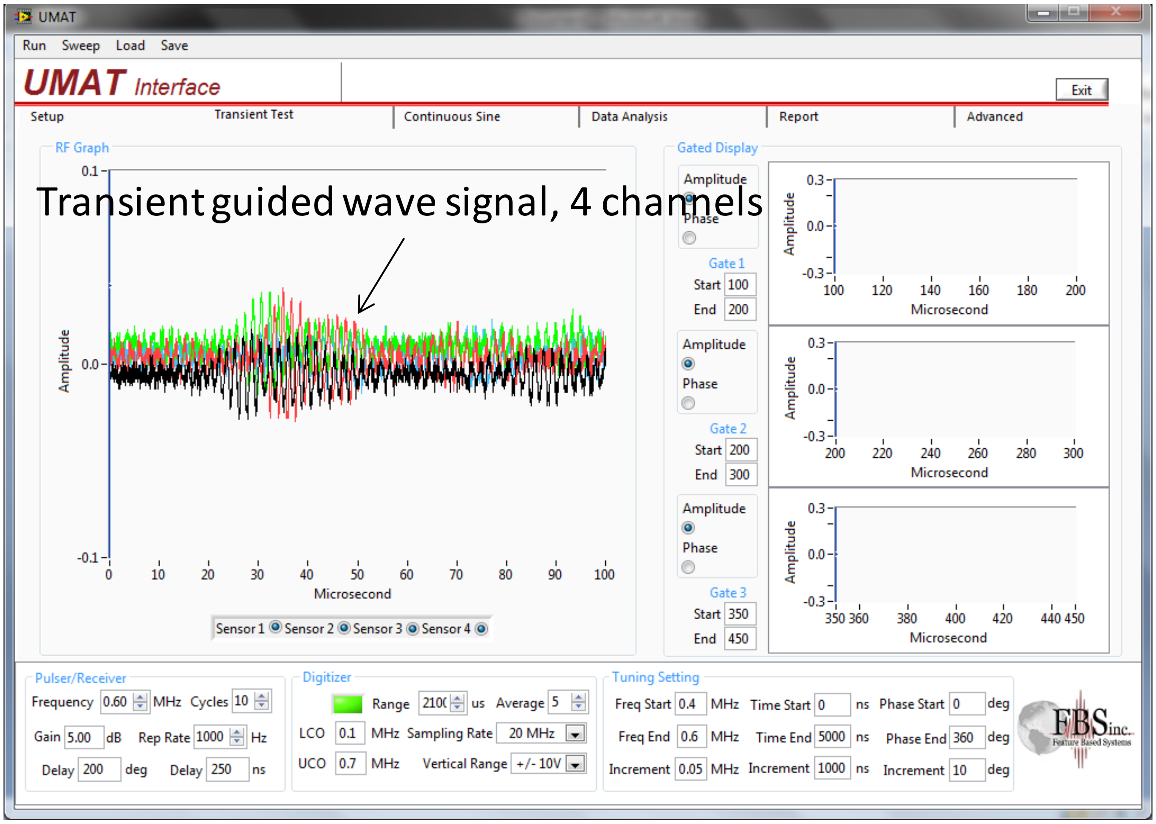

Transient guided wave signal, 4 channels

Gate 1: Start 100, End 200
Gate 2: Start 200, End 300
Gate 3: Start 350, End 450

Pulser/Receiver
Frequency 0.60 MHz
Cycles 10
Gain 5.00 dB
Rep Rate 1000 Hz
Delay 200 deg
Delay 250 ns

Digitizer
Range 210(us
Average 5
LCO 0.1 MHz
Sampling Rate 20 MHz
UCO 0.7 MHz
Vertical Range +/- 10V

Tuning Setting
Freq Start 0.4 MHz
Time Start 0 ns
Phase Start 0 deg
Freq End 0.6 MHz
Time End 5000 ns
Phase End 360 deg
Increment 0.05 MHz
Increment 1000 ns
Increment 10 deg

Figure 5.4. *The interface of the Transient Test tab in the UMAT software interface showing 4 signals collected by 4 sensors attached to a test sample..*

A screen shot of the automatic UMAT frequency and time delay tuning interface (Continuous Sine Tab) is shown in Figure 5.5. Continous sine waves were applied to drive an annular array. The vibration signals were received by 4 disc sensors distributed in the test structure. After an automatic frequency and phase delay tuning is finished, the frequency and phase slides in the interface can be used to select the test data associated with a specific frequency and phase delay combination. The test data are displayed in waveforms and also with bar presentations of amplitudes and phase angles. All the test data for the whole tuning process can be saved into ASCII files for post-processing.

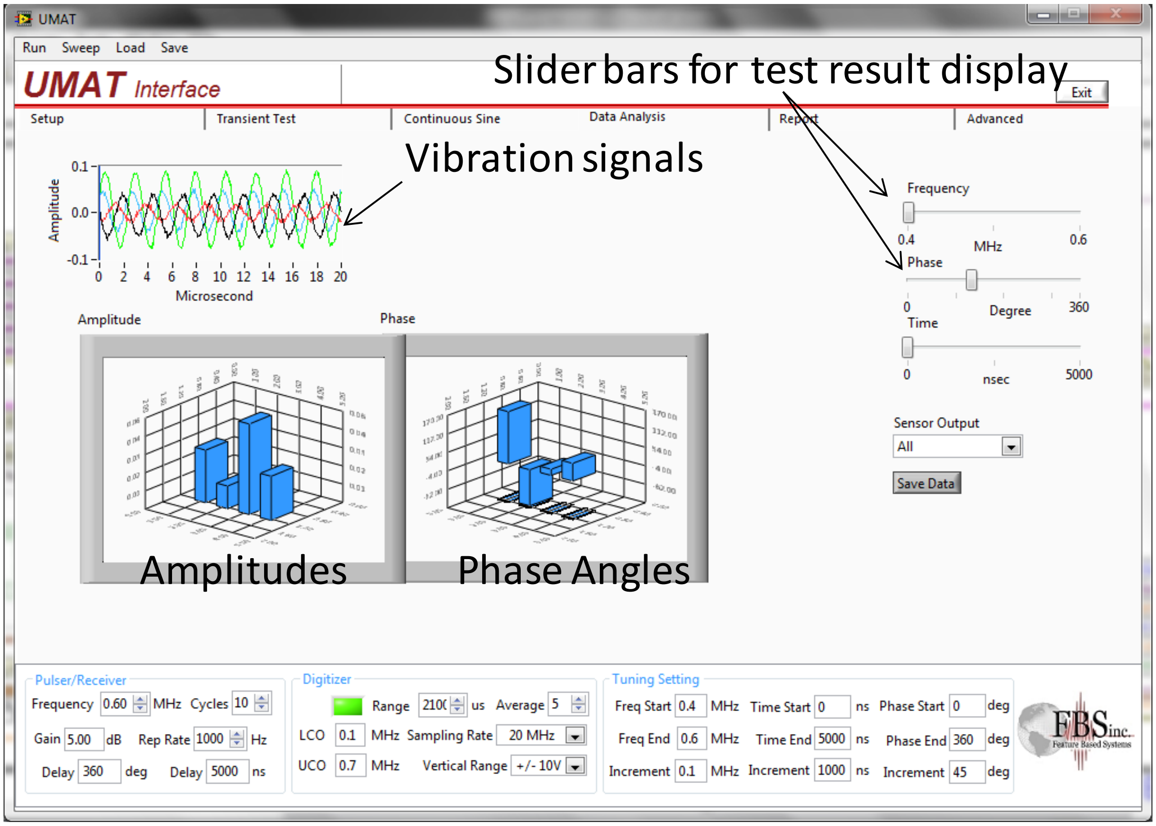

Sensor Output: All

Pulser/Receiver

Frequency 0.60 MHz Cycles 10

Gain 5.00 dB Rep Rate 1000 Hz

Delay 360 deg Delay 5000 ns

Digitizer

Range 210(us Average 5

LCO 0.1 MHz Sampling Rate 20 MHz

UCO 0.7 MHz Vertical Range +/- 10V

Tuning Setting

Freq Start 0.4 MHz Time Start 0 ns Phase Start 0 deg

Freq End 0.6 MHz Time End 5000 ns Phase End 360 deg

Increment 0.1 MHz Increment 1000 ns Increment 45 deg

Figure 5.5. *Screen shot of the software interface for automatic frequency and delay tuning, UMAT mode.*

Figure 5.6 shows the interface of the software for a loading function study (Data Analysis Tab). The two color maps shown in the interface are plotted based on the ultrasonic vibration amplitudes obtained at two different UMAT tests. The vibration amplitudes are plotted with respect to different frequencies and phase delays on the annular array elements. Different combinations of frequencies and phase delays correspond to different loading functions. After the ‘Process’ button shown to the center of the interface in Figure 5.6 is pressed, a number of loading functions that provide the most changes from the UMAT test 1 (left color map) to the UMAT test 2 (right color map) will be identified. The associated vibration amplitude change ratios will then be plotted to the lower-right graph within the interface. The ‘No of Max Value’ input on the interface can be changed to select how many good loading function choices to display. The drop off box below that input can be used to select among the displayed loading functions. After a loading function is selected, the frequency and phase delay of the loading function are displayed. The corresponding amplitude change ratios introduced by that loading function are also highlighted in red. Same options are availabe in the updated software to study the loading functions with poor sensitivity. The loading function study is essential for our UMAT concept, as different loading functions can be identified for the detection of different damage types.

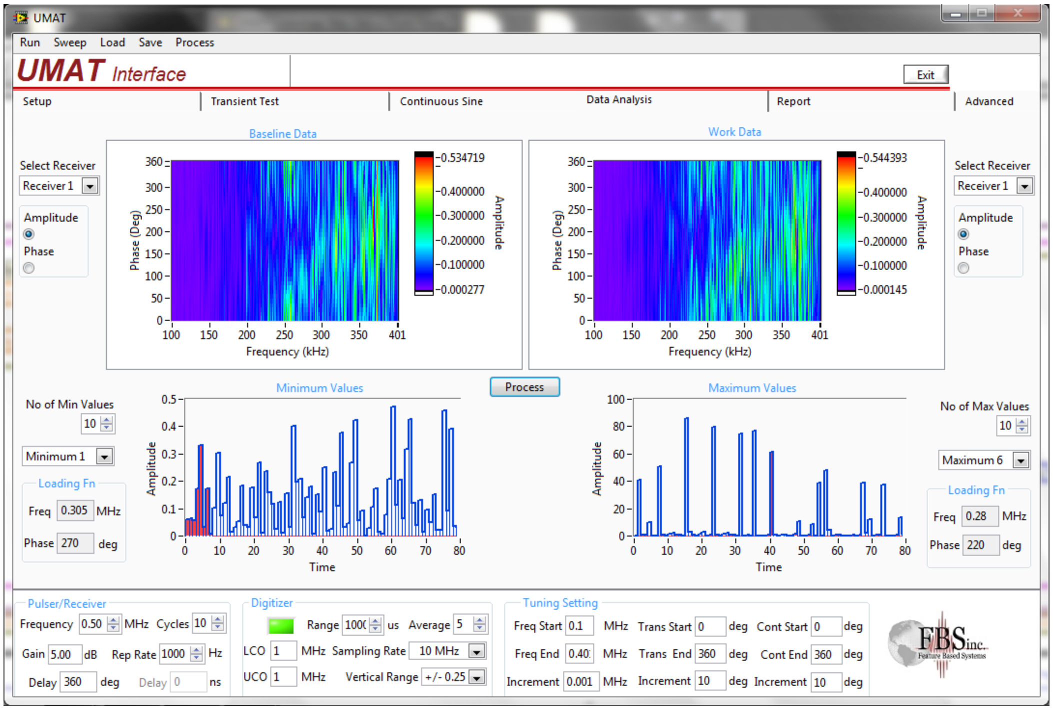

Select Receiver: Receiver 1
Amplitude ●
Phase ○

Select Receiver: Receiver 1
Amplitude ●
Phase ○

No of Min Values: 10
Minimum 1
Loading Fn
Freq 0.305 MHz
Phase 270 deg

No of Max Values: 10
Maximum 6
Loading Fn
Freq 0.28 MHz
Phase 220 deg

Pulser/Receiver
Frequency 0.50 MHz Cycles 10
Gain 5.00 dB Rep Rate 1000 Hz
Delay 360 deg Delay 0 ns

Digitizer
Range 100(us Average 5
LCO 1 MHz Sampling Rate 10 MHz
UCO 1 MHz Vertical Range +/- 0.25

Tuning Setting
Freq Start 0.1 MHz Trans Start 0 deg Cont Start 0 deg
Freq End 0.40 MHz Trans End 360 deg Cont End 360 deg
Increment 0.001 MHz Increment 10 deg Increment 10 deg

Figure 5.6. Updated software interface for loading function study.

Wave mechanics based vibration loading function selections provide us with a key innovation of the UMAT approach. FBS and Penn State have developed various computer programs for wave mechanics studies of guided waves in multilayer anisotropic composite plate structures. Most of the computer programs are written in Matlab. Matlab is a powerful research tool. However, it is not suitable for industrial field applications and product developments. In contrast, LabVIEW is a widely accepted programming language for industrial applications. The extremely strong hardware control capability of LabVIEW is greatly suitable for product development. In this project, MATLAB codes for obtaining dispersion curves for multilayer anisotropic composite plate structures via a Semi-Analytical Finite Element (SAFE) method were converted into LabVIEW. A user-interface was designed for defining the structure for which the dispersion curves were being generated. The user-interface allows the user to first select the number of layers in the plate structure, and then define the properties of the material layer-by-layer. The material parameters include the layer material, layer thickness, and layer lay-up angle.

The layer material control allows the user to simply select from a library of existing materials or to define a new material. Selecting an existing material from the material library will gather the appropriate material parameters for the given layer (namely the stiffness matrix and density). Defining a new material will access a pop-up window that will guide the user through the process of entering the parameters for the new material. This process is outlined in Figure 5.7. As shown in this figure, the user can select from different varieties of material inputs depending on the material parameters available.

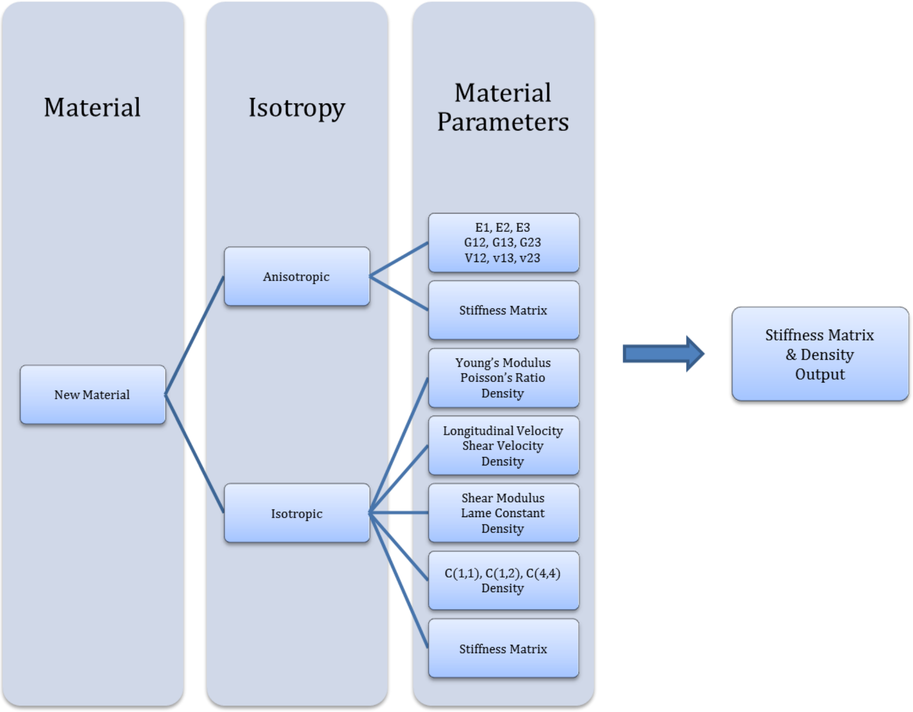

***Figure 5.7**: Entering new materials in software.*

After the material layers and their properties have been defined, the software displays a cross-sectional representation of the plate structure for which the dispersion curves will be generated, shown in Figure 5.8.

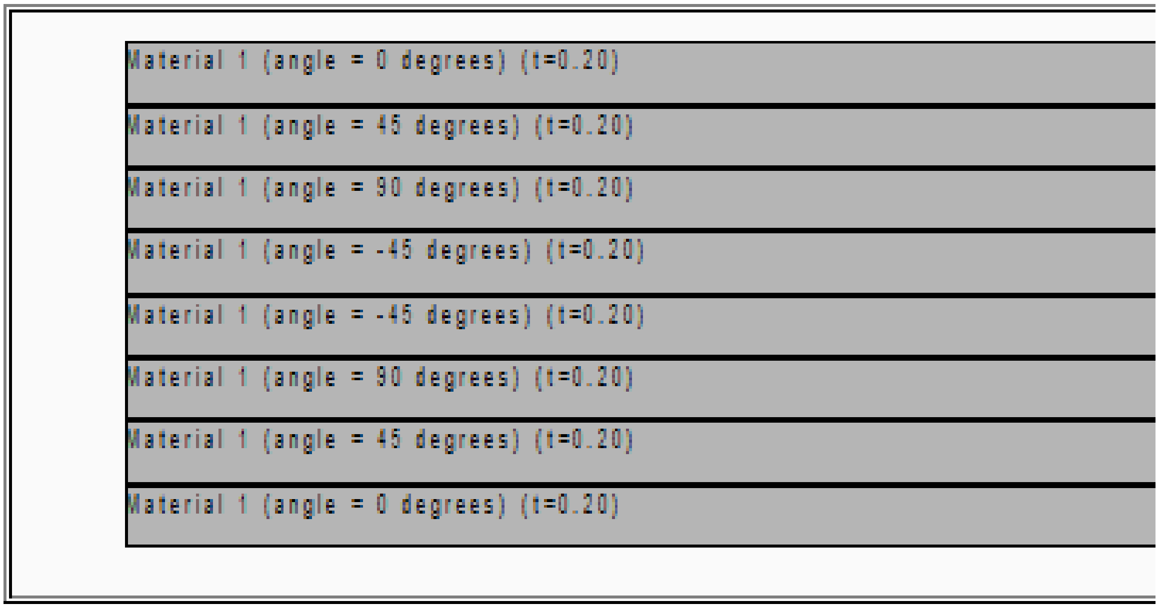

```
Material 1 (angle = 0 degrees) (t=0.20)
Material 1 (angle = 45 degrees) (t=0.20)
Material 1 (angle = 90 degrees) (t=0.20)
Material 1 (angle = -45 degrees) (t=0.20)
Material 1 (angle = -45 degrees) (t=0.20)
Material 1 (angle = 90 degrees) (t=0.20)
Material 1 (angle = 45 degrees) (t=0.20)
Material 1 (angle = 0 degrees) (t=0.20)
```

***Figure 5.8**: Software representation of plate structure generated from user-input.*

At this point, the material and structure have been completely defined. The user can select the control to generate the dispersion curves for the structure. The SAFE software routine will execute; assembling the appropriate matrices, finding eigenvalues and eigenvectors, and plotting the eigenvalues that produce the phase velocity dispersion curves. The group velocity dispersion curves are calculated simultaneously.

The user-interface was designed for the convenience of the user with regard to generating and viewing dispersion curves and related information. The process of defining the structure and generating its dispersion curves is as follows:

1. Create a new project and input a project name.
2. Add a structure and input the structure name.
3. Define the material parameters and confirm the structure from the picture.
4. Press the control for generating dispersion curves.

Shown below are screenshots of the software that demonstrate its ease-of-use.

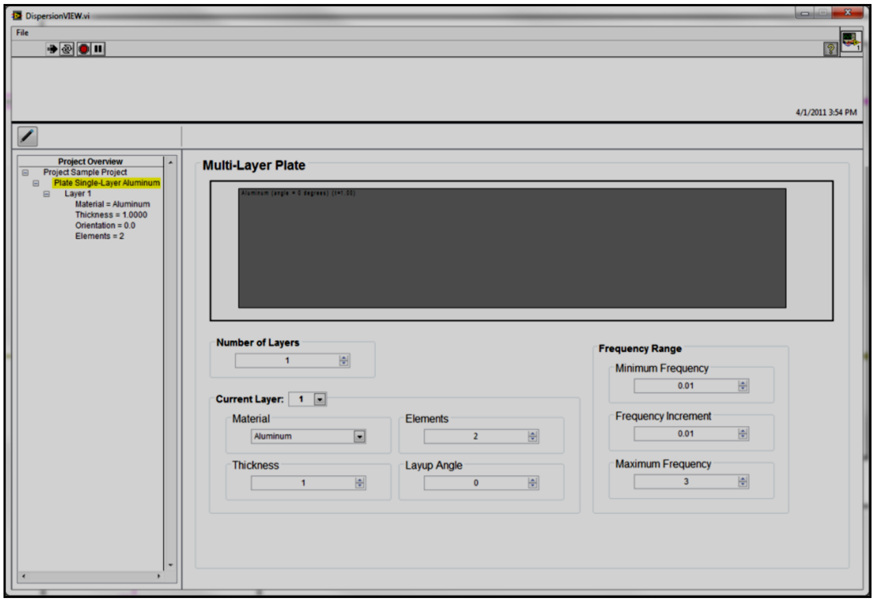

Project Overview
- Project Sample Project
  - Plate Single-Layer Aluminum
    - Layer 1
      - Material = Aluminum
      - Thickness = 1.0000
      - Orientation = 0.0
      - Elements = 2

Number of Layers: 1

Current Layer: 1
Material: Aluminum
Elements: 2
Thickness: 1
Layup Angle: 0

Frequency Range
Minimum Frequency: 0.01
Frequency Increment: 0.01
Maximum Frequency: 3

Figure 5.9*: Interface for specifying material parameters and viewing structure schematic.*

Figure 5.9 shows the interface that is used for defining the structure for which the dispersion curves will be generated. As shown, only a few user-defined parameters must be specified in order to generate the dispersion curves.

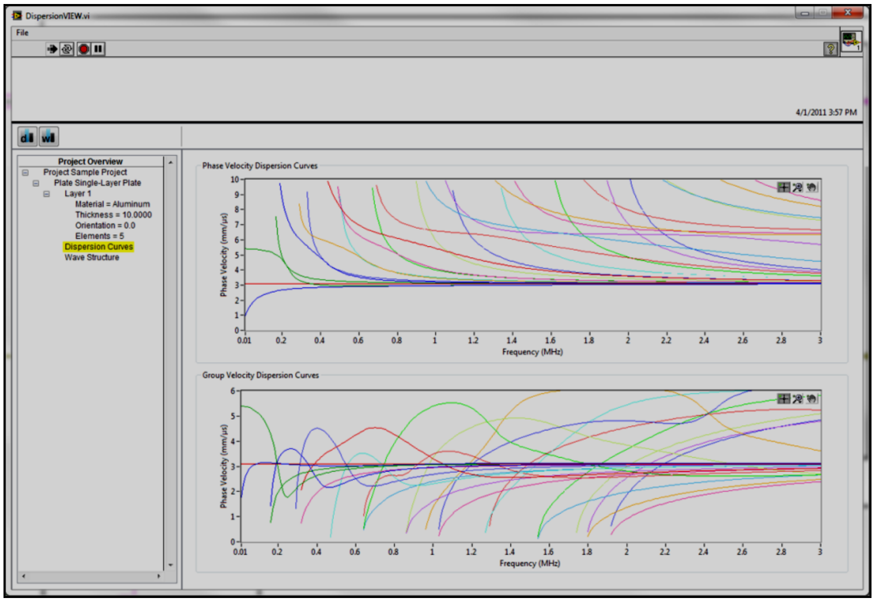

Project Overview
- Project Sample Project
  - Plate Single-Layer Plate
    - Layer 1
      - Material = Aluminum
      - Thickness = 10.0000
      - Orientation = 0.0
      - Elements = 5
    - Dispersion Curves
    - Wave Structure

Figure 5.10: *Interface for viewing the dispersion curves.*

Figure 5.10 shows the interface for viewing the dispersion curves. Note that the dispersion curves shown in this figure have been traced using the orthogonality-based mode-sorting algorithm. The user may use the control buttons located at the top left of the window for switching between a view of the phase/group velocity dispersion curves and the wave structures. The user may also simply select the window they would like to view from the Project Overview tree control located at the left-hand side of the screen. For example, selecting "Dispersion Curves" will display the group/phase velocity dispersion curves window, while selecting "Wave Structure" will display the phase velocity/wave structure window.

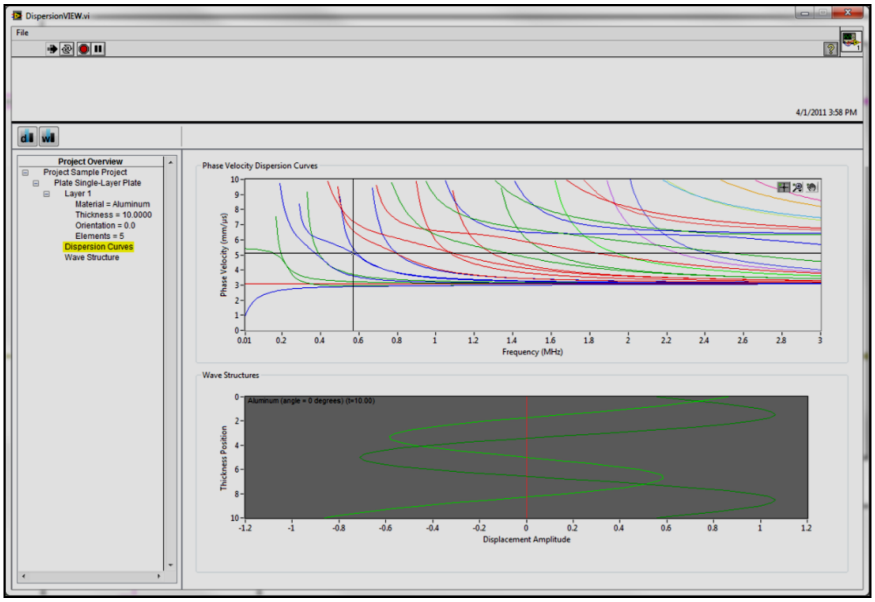

Material = Aluminum
Thickness = 10.0000
Orientation = 0.0
Elements = 5

***Figure 5.11**: Interface for viewing wave structures.*

Figure 5.11 shows the interface for viewing wave structures. The wave structure (x, y, and z displacements) for any mode-frequency combination may be viewed by simply moving the black cursor on the phase velocity dispersion curves graph to the point for which the user would like to view the wave structure. The three displacement components are depicted by the three colored plots.

The saving and loading routines automatically save all input parameters and generated data to a pre-defined path on the computer. Project data can be recalled, modified, and augmented by choosing to open an existing project when starting the software (as opposed to creating a new project).

With the wave mechanics study subroutines, users of the UMAT system can self define optimal loading functions based on wave mechanics studies. Automatic loading function selections can also be conducted based on the knowledge of the test sample. This is particularly useful for test objectives with simple plate-like geometries. For test samples with complex geometry, especially samples with different materials and thicknesses for different regions, a training process through frequency and phase delay tuning can be carried out to identify the good loading functions for different defects.

6. Composite Test Sample Fabrication and Acquisition

To carry out experimental demonstration of the UMAT technology developed in this project a number of composite test samples were fabricated or acquired.

A batch of composite panels was fabricated using facilities available at Penn State. Hexcel AS4/8552 unidirectional carbon/epoxy prepregs were used in the fabrication as raw materials. The prepregs were cut in pieces with different fiber orientations and stacked together following different stacking sequences. The stacked prepregs then went into a vacuum bagged autoclave process to have the epoxy cured.

In total, 7 panels were fabricated including one 23” by 23” 16 layer large cross-ply plate, two 12” by 12” 16 layer small cross-ply plates, two 12”by 12” 16 layer quasi-isotropic plate, and two 12” by 12” quasi-isotropic plates with center bonded doublers. The bonded doublers are of a 2” by 12” dimension. Delamination defects simulated using thin Teflon tapes were inserted into the large cross-ply plate, one small cross-ply plate, and a bonding specimen.

FBS also purchased composite parts including composite spoilers used for cars and composite propellers designed for air-boats. Figure 6.1 shows two composite spoiler samples, each with 8 sensors attached for UMAT tests. The composite spoiler samples are with a 3-D shape of side wings. The samples are made of carbon fiber reinforced materials and therefore are inhomogenous and anisotropic structures.

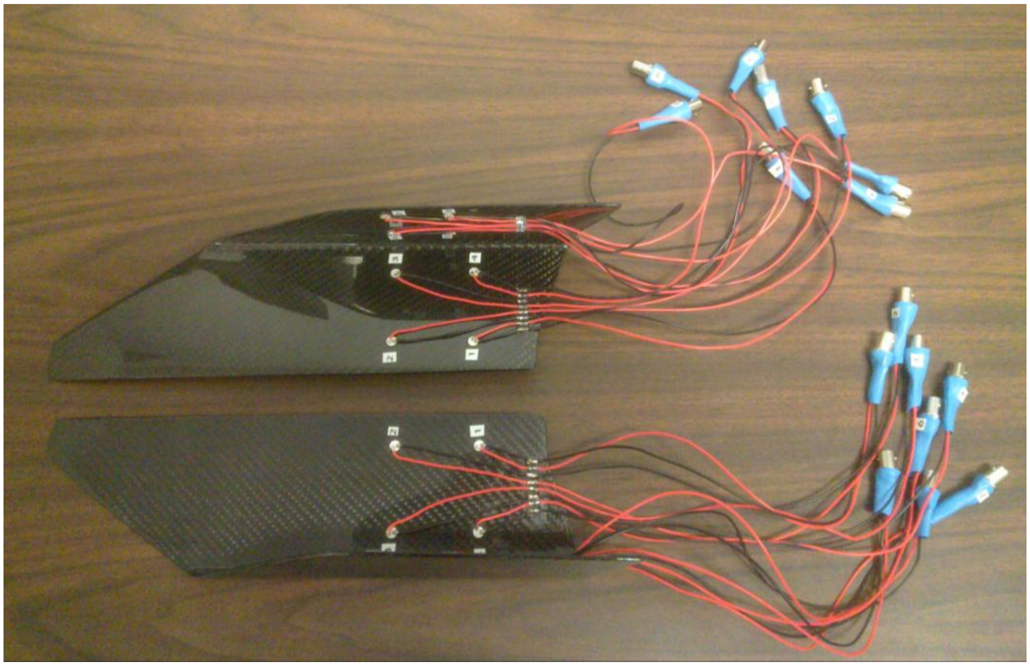

Figure 6.1. *Two composite test samples with 8 sensors attached to each sample.*

Figure 6.2 shows a picture of one carbon composite propeller. The composite propeller was purchased at the www.warpdriveprops.com website.

Figure 6.2. *A composite propeller purchased by FBS as a UMAT test sample.*

FBS also contacted Kail Neiman and Bill Heaner from Hill AFB for getting some Air Force materials. With the project manager Dr. David Stargel's help, Hill AFB agreed to send FBS some retired composite parts from an F-16 fighter jet. A package from Hill AFB arrived at FBS on July 22, 2011. The package includes five pieces of composite panels cut from a scrap piece from an F-16 and a never in service composite panel with an existing delamination defect. A picture of the scrap piece from the F-16 is presented in Figure 6.3. The picture was provided by Karl Nieman at Hill AFB. Figure 6.4 shows the panels included in the package from Hill AFB. A picture of the never in service composite panel and a side view of the panel showing the delamination defect located at a corner of the panel are given in Figure 6.5.

Figure 6.3. *A picture of the scrap F-16 composite part before being cut. Five of the cut pieces were sent to FBS as test samples for demonstrating UMAT applications on realistic composite aircraft structures.*

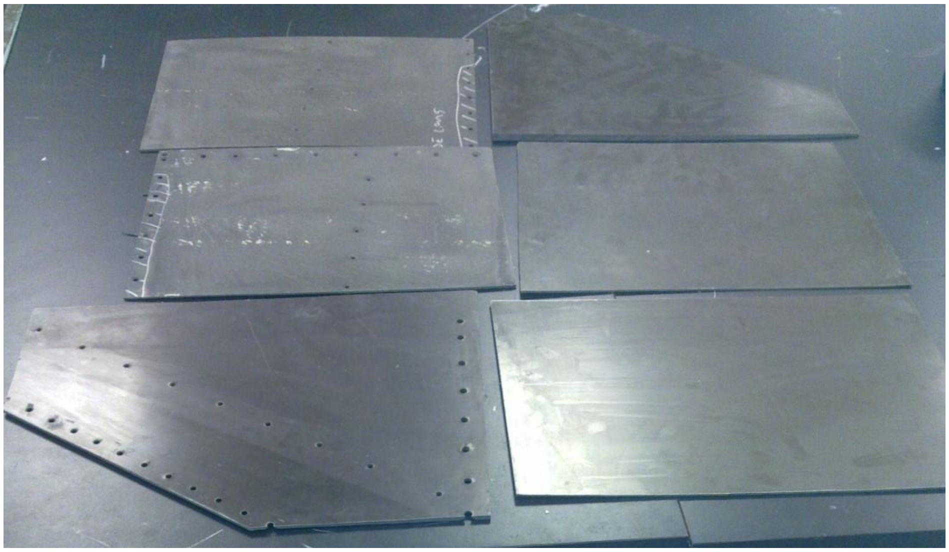

Figure 6.4. The six composite panels out of the package from Hill AFB.

Figure 6.5. An Air Force composite panel with a delamination defect located at one corner of the panel.

Although not clearly shown in the pictures, all Air Force panels have ply drops throughout the body which yield thickness variations from one boundary to the other. The thicknesses of the composite panels range from 0.066” to 0.32”. Guided wave inspection of structures with changing thicknesses is sometimes challenging due to the fact that mode conversions may occur when guided waves travel from one thickness to another. There are holes in some test samples which may introduce a further challenge to transient guided wave tests.

7. Transient Guided Wave Experiments

Transient guided wave tests were carried out to demonstrate that sensitivity to different defects can be achieved by applying different guided wave modes and frequencies. Phase delay comb type transducers were used in the experiments to prove that phased comb type transducers are an effective means of providing different guided wave loading functions.

In Section 3.3 of this project, we showed that different guided wave mode and frequency combinations provide high sensitivity to delamination defects located at different interfaces of a composite plate. To verify the sensitivity study, we conducted transient guided wave scans of the composite plate with 3 embedded delamination defects, by using different mode and frequency combinations selected by two time delay comb transducers. Based on the bulk wave C-scan result of the plate, the locations of three delaminations are marked with crosses in Figure 7.1. The delamination defects were simulated by embedding Telfon tapes in the interfaces of composite prepreg layers. Delamination defect 1 shown in Figure 7.1 was embedded to the interface 2-3. Delamination 2 was inserted between the layers 8 and 9, and delamination 3 was between the layer 12 and 13.

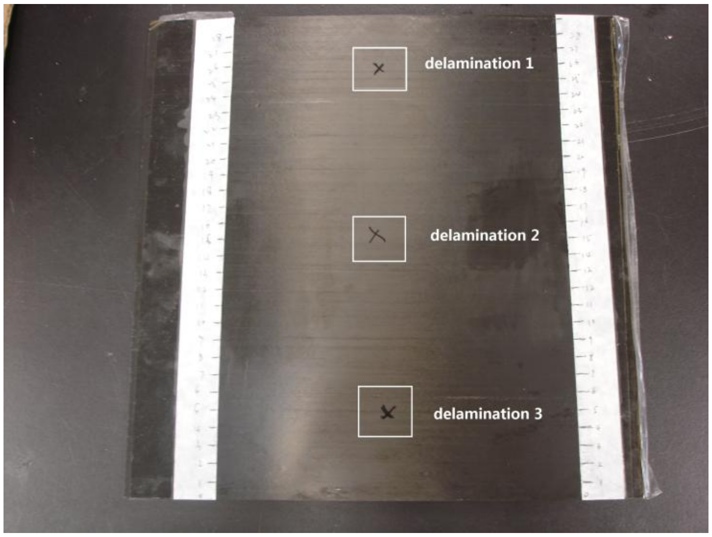

Figure 7.1. *A picture of the test composite plate with the delamination locations marked.*

Two comb transducers were used to detect the defects. Figure 7.2 shows the experimental setup. The pitch of the comb transducer was 0.332 inch.

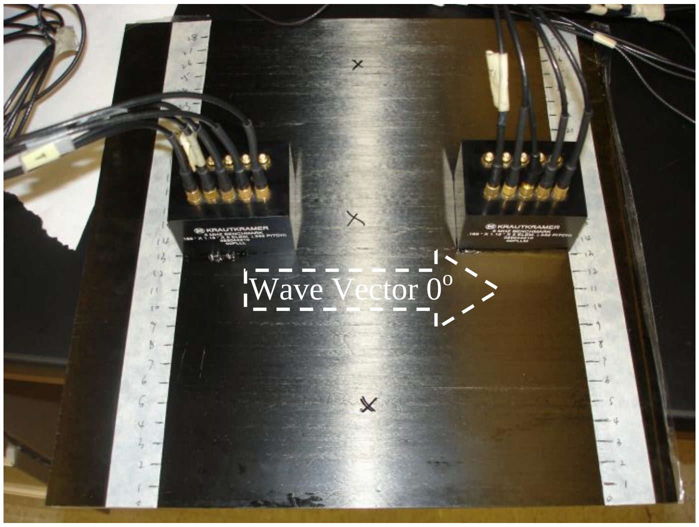

Figure 7.2. *Experimental setup for the transient short distance guided wave scan*

Based on a sensitivity study of the delamination defect, as given in Section 3.3, two wave modes were selected in the test. One was mode 8 at 1.03MHz, and the other was mode 5 at 700 kHz. To select the first mode and frequency combination, a time delay of 91.5 μs was applied to any adjacent comb elements. As shown in Figure 6, the two comb transducers were placed face-to-face at the 0^o direction. For the transient guided wave scan, the two transducers were moved step by step together at the 90^o direction. Through-transmission signals were taken for each of the steps. For all signals, the wave vector direction was 0^o. The magnitudes of the signals were plotted together into a signal magnitude map with the x coordinate of the map being time sampling points of the signals, the y coordinate being the scanning steps, and the color intensity representing the magnitudes.

Figure 7.3 shows the signal magnitude map obtained using the mode 5 at 700 kHz. It is demonstrated that the signal magnitudes dropped when the wave propagation pass across a defect. As a result, the blue low intensity color regions along the scan direction predicted the locations of the delamination defects. As discussed previously, mode 5 at the frequency range from 500 kHz to 800 kHz is sensitive to the delamination defects 1 and 3, but not defect 2 in the center of the plate. In Figure 7.3, we can see clear magnitude drops of the through transmission guided wave signals at the locations of the delamination defects 1 and 3. For the delamination defect 2, however, the magnitude of the guided wave signal did not change as significantly as for the other two defects. This validated that the selected mode 5 at 700 kHz were sensitive to the defects 1 and 3, but not sensitive to the defect 2.

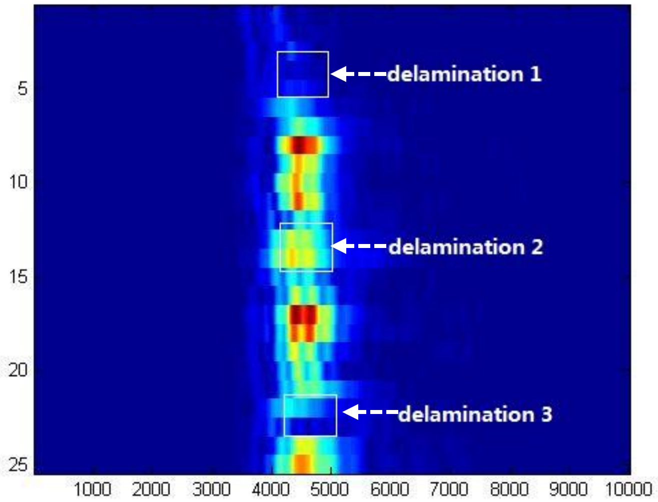

Figure 7.3 *Guided wave scan image using mode 5 at 700 kHz showing good sensitivity to delamination 1 and delamination 3 but lower sensitivity to delamination 2.*

The operating frequency and time delays were also adjusted to select mode 8 at 1.03 MHz for another guided wave scan. The corresponding signal magnitude map is shown in Figure 7.4. From the magnitude map, signal amplitude deceases can be observed for all three defects. It appeared that the decrease in amplitude was the least for the delamination defect 3 and the most for the center delamination: defect 2. This also agrees with the sensitivity calculations. The differences in signal magnitude drops for the three defects were not as large as predicted by the calculations, though, especially for delamination 2. The sensitivity calculations showed a quite low sensitivity value of the selected mode and frequency for delaminations located at interface 12-13. The appearance of the delamination defect 3 in Figure 7.4 was due to the fact that the simulated delamination defect was rather thick such that the out-of-plane displacements also play a role for the wave propagation discontinuity at the delamination. Nevertheless, the transient guided wave scan experiments reported here demonstrated the value of sensitivity calculations and also the possibility of using different guided wave inputs to differentiate delamination defects located at different interfaces inside a composite plate.

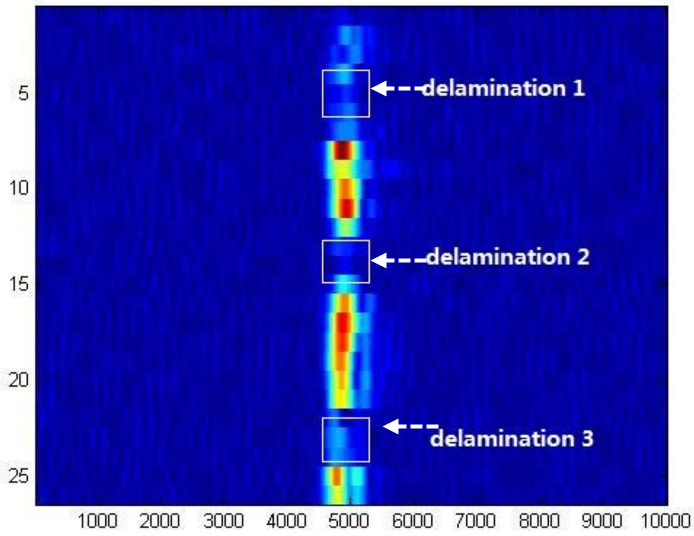

Figure 7.4 *Guided wave scan image using mode 8 at 1.03MHz, showing good sensitivity to all three defects. It appeared that the decrease in amplitude was the least for the delamination defect 3 and the most for the center delamination which agreed with the sensitivity calculation results:*

Through transient guided wave scans using two time delay comb transducers, we clearly demonstrated that different guided wave inputs can be selected using time delay comb transducers to detect various delamination defects at different interfaces and also possibly differentiate them from each other.

8. Ultrasonic Vibration Experiments

Ultrasonic vibration experiments have been carried out on various structures using the system developed in this project. Some experiments were conducted to further verify the theories of ultrasonic vibrations. Others were carried out to demonstrate the defect detection and characterization capability of the new UMAT approach.

8.1 Plate with Symmetric/Anti-symmetric Loadings

An experiment was designed to test the theory that the initial excitation of a particular guided wave mode into a structure can determine the final steady-state modal vibration characteristics that are excited into the structure. The premise of the experiment was to utilize two PZT discs mounted directly opposite each other on an aluminum plate. The discs could then be driven in-phase or out-of-phase with each other in order to predominantly excite the S0 and A0 guided wave modes, respectively, in the plate. The frequency response of the plate to such excitation could then be measured and compared. Additionally, a boundary condition change and defect were introduced and the frequency response of the structure due to each excitation was again recorded and compared to the healthy state. Based on the ultrasonic vibrations theory, it would be expected that the two different types of excitation would excite primarily compressional and flexural vibration modes, respectively, in the structure. This would manifest itself as differences in the frequency response of the structure. The effects of boundary condition changes and damage would also show up in the frequency spectrum and the severity of their effect on the frequency response would be dependent on the type of excitation used.

Although many different propagating guided wave modes can exist in a particular structure at any given frequency, it is possible to preferentially excite one or more modes over the others. The relative excitation of a mode at a particular frequency is governed by two factors, as was discussed in the section on annular array theory and design: 1) the wavenumber-domain excitation spectrum of the source and 2) the excitability of the mode by the applied force of the source. Since the loading distribution of the opposing discs is identical for both symmetric and antisymmetric activation, the factor that will determine the relative excitation of multiple guided wave modes is the compatibility of the force applied by the actuators with the wavestructure (in this case the velocity field) of the guided wave modes. This compatibility is more simply referred to as the wave mode excitability.

The derivation of guided wave excitabilities can be found in reference [4]. According to the equations for excitability calculations, for perfectly symmetric and antisymmetric in-plane loading, only S and A guided wave modes, respectively, would be excited in the waveguide. For the radial mode excitation of the PZT discs, in-plane loading is a good approximation. Note that for out-of-plane loading, the opposite case would be true, in which symmetric excitation would generate A modes and antisymmetric excitation would generate S modes.

8.1.1. Chirp Experiments

Besides using forced vibrations introduced by controlled guided wave inputs for defect detection, frequency response functions (FRFs) that can be measured through chirp guided wave inputs are considered as an alternative means of UMAT defect detection. Experimental work has been continued to seek the connections between excitations of resonant frequencies and guided wave chirp inputs, and also to define an appropriate FRF analysis approach for defect detections using chirp guided wave inputs based UMAT.

Experimental Setup

Figure 8.1 shows the test sample used in our initial experiments. Two PZT disk actuators were symmetrically attached to the two surfaces of the test sample which is a 12”x12” aluminum plate. The idea of using two symmetrically mounted actuators was to gain control on the guided wave inputs. When the two actuators are driven in-phase, symmetric guided wave modes will be generated into the test sample. To input antisymmetric guided wave modes, out-of-phase driving signals can be used for the two actuators. To obtain the out-of-phase driving signals, we made a voltage transformer to reverse the phase of an alternating input voltage signal.

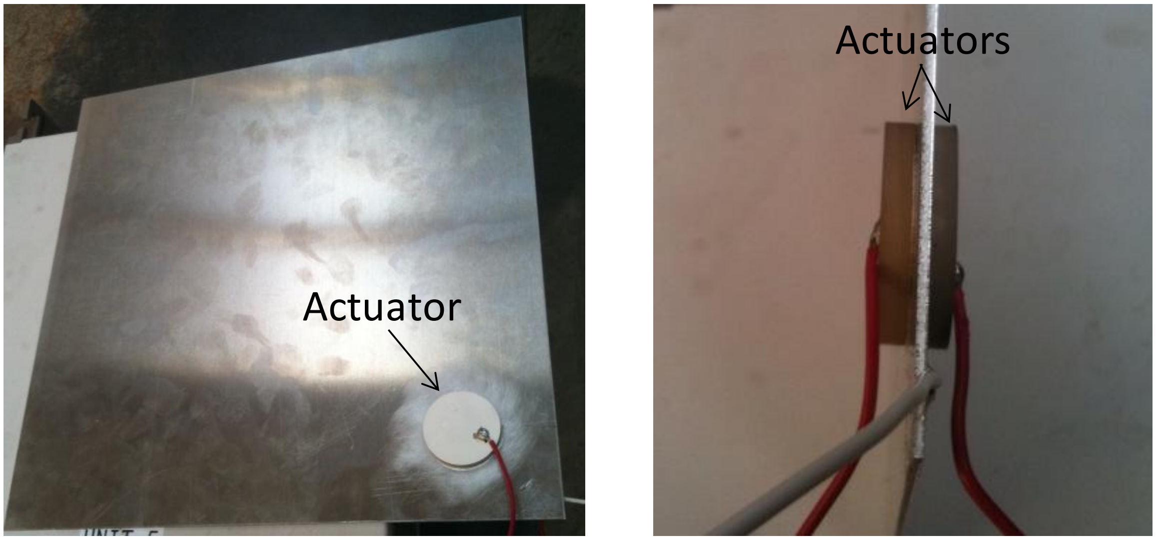

Fig. 8.1. Test sample and actuators for chirp guided wave vibration tests. (Left) Top view of the plate showing that the actuator was attached close to one corner of the aluminum plate. (Right) Side view of the plate showing the symmetry of the actuator attachments on both surfaces of the plate.

The natural resonant frequency response of the plate was tested with a chirp excitation signal with a frequency range of 40-80 kHz over a 1 ms duration. The response of the plate was measured at the three marked positions with acoustic emission (AE) sensors, and the input spectrum was measured with an AE sensor bonded directly to one of the actuators. The response was measured *after* the excitation signal was complete, thus the results pertain to the free vibration response as opposed to the forced vibration response of the plate. These measurements were done with both symmetric and anti-symmetric excitations, for a defect-free case, a BC-change case, and a defect case. The transfer function, H(f), was calculated using the following approach. The time domain signals for both the input, x(t), and output, y(t), were recorded and processed by applying the Fast-Fourier Transform (FFT) to yield X(f) and Y(f), respectively. These were used to calculate the auto-power spectrum, $G_{xx}(f)$, and cross-power spectrum, $G_{xy}(f)$. The transfer function was then calculated as $H(f) = G_{xy}/G_{xx}$. The results for the defect-free case for each measurement position are shown in Figure 8.2.

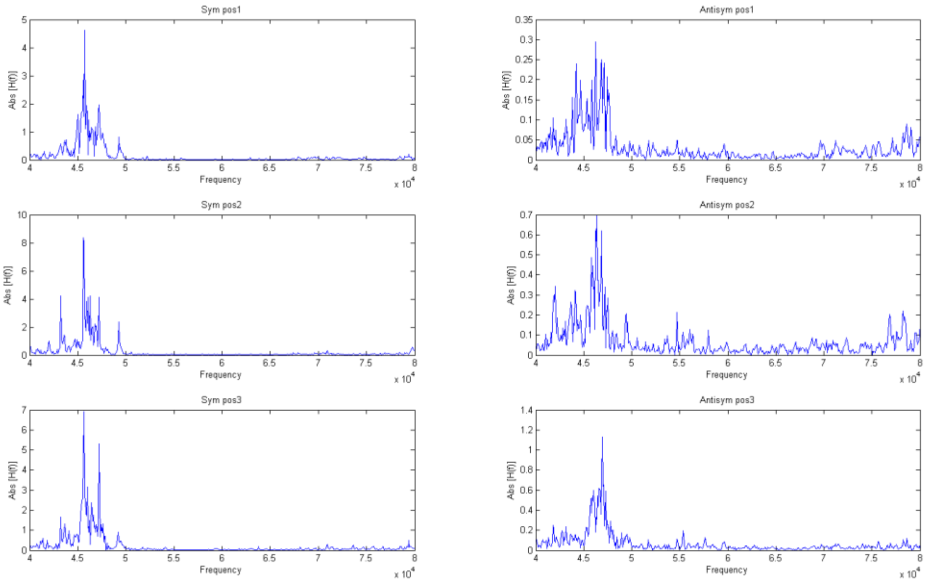

Fig. 8.2 Transfer function results measured from 3 different measurement positions for the defect-free case with symmetric excitation (left) and anti-symmetric excitation (right), showing some resonant peaks for all measurement positions

There are some resonant peaks that are present at each measurement position, but the overall correlation is still questionable. This is most likely due to the measurement of the input signal, because the AE sensor was placed directly on the PWAS transducer. An examination of the input time-domain signal, $x(t)$, shows that significant content is present *after* the excitation was shut off. This is because the transducer reacts to the vibrations in the plate and thus the input signal measured is corrupted by the response of the plate. This phenomenon, in addition to interference from the out-of-phase transducer (mounted on the opposite side of the plate), is most likely to blame for the poor coherence and large amount of noise present in the anti-symmetric activation results (as compared to the symmetric activation results).

Results and Analysis

The results for the case involving a change in boundary conditions (by rotating the plate 90º CW in the mounting bracket) are shown in Figure 8.3. Results for the case involving the introduction of a simulated corrosion defect are shown in Figure 8.4. The defect was a 0.5” x 0.5” approximately 20% CSA defect introduced with a Dremel tool. It is located as shown in Figure 8.5. Note that the response of the plates is different for symmetric vs. anti-symmetric excitation, even though the actuators were not being activated during the response measurement. This shows that the excited resonances in the plate are affected by the guided waves used to initially induce the vibration.

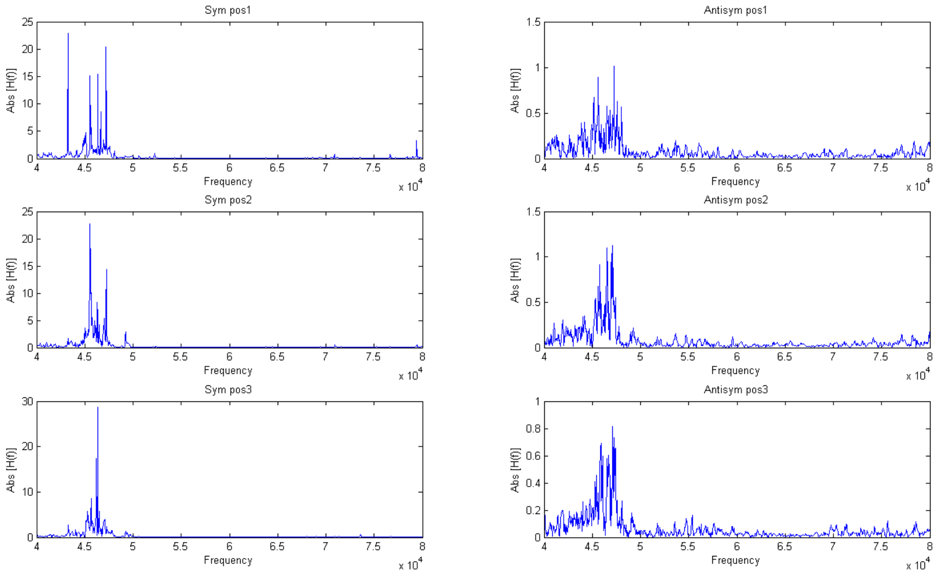

Fig. 8.3 Transfer function results measured at 3 positions for the change in boundary conditions. (Left) Transfer functions under symmetric excitations, (Right) Transfer functions under anti-symmetric excitations, showing different changes in transfer functions due to different excitations.

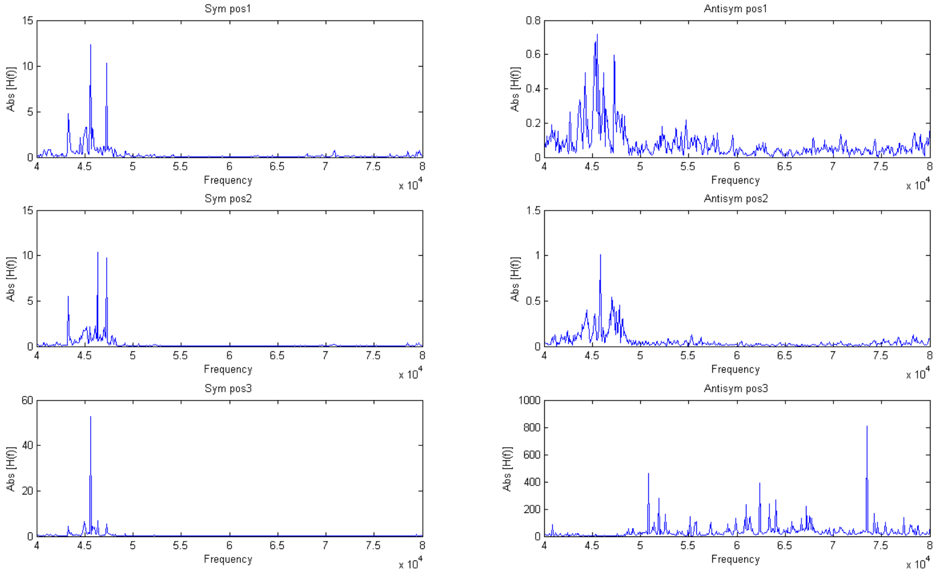

Fig. 8.4 Transfer function results measured at 3 positions for the defect case. (Left) Transfer functions under symmetric excitations, (Right) Transfer functions under anti-symmetric excitations, showing different changes in transfer functions due to different excitations.

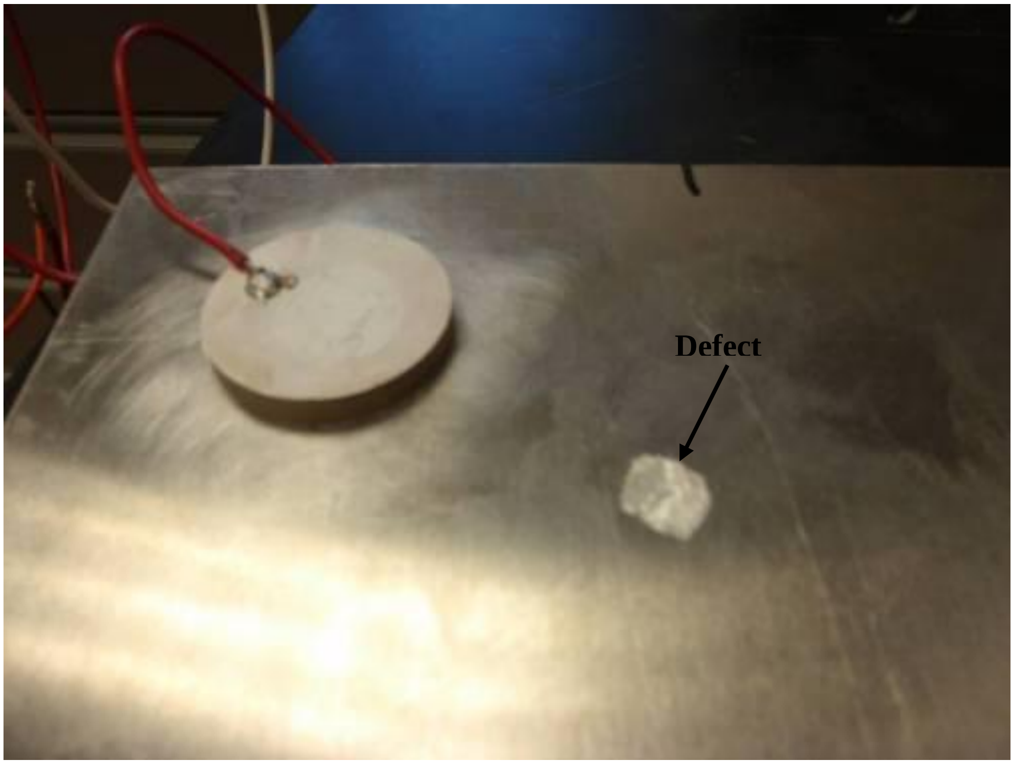

Fig. 8.5 Aluminum plate with simulated corrosion defect; defect size is approximately 0.5” x 0.5” and 20% cross-sectional area.

8.1.2. Forced Vibration Experiments

In addition to utilizing a chirp input to estimate the transfer function of the structure, the National Instruments multi-channel phased array system was used to measure the forced vibration response spectrum in a similar experiment.

Experimental Setup

In this experiment, two transducers were also mounted on opposite sides of an aluminum plate. Four small PWAS receivers were used to measure the vibration at different points on the plate, and the NI system was used to drive the actuators (both in- and out-of-phase) and to record the vibration magnitude at for each receiver. Figure 8.7 shows the test sample used in our initial experiments. Two PZT disk actuators were symmetrically attached to the two surfaces of the test sample which is a 12” x 12” x ¼”-thick aluminum plate, as shown in Figure 8.6. The actuators were excited with a sinusoidal continuous wave signal at frequencies from 10 kHz to 30 kHz at 10 Hz increments. At each frequency, symmetric excitation was achieved by using in-phase actuation and anti-symmetric excitation was achieved by using out-of-phase actuation.

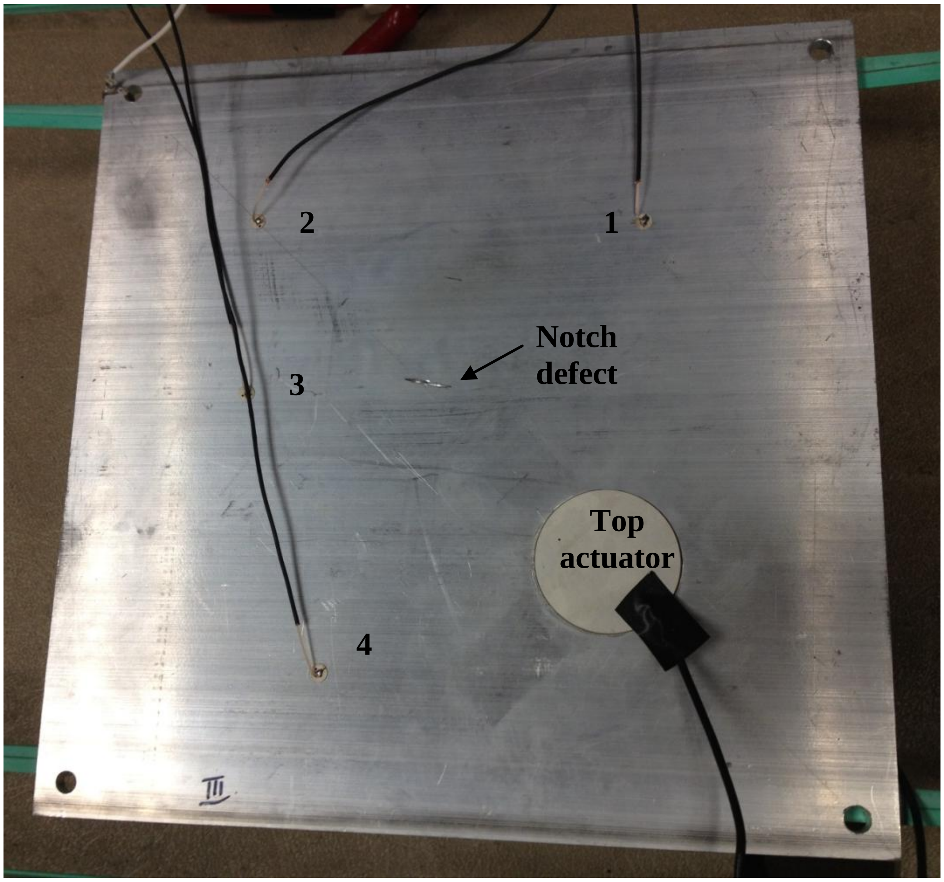

Fig. 8.6 The 12” x 12” x ¼”-thick aluminum plate with oppositely mounted PZT disc actuators and four receiver PWAS. Note that the notch defect was not introduced until after the initial “healthy” data was collected.

Results and Comparison to FE Predictions

To extract frequency response data from this sine dwell test, the normalized maximum vibration amplitude (over all four receiving channels) was calculated for each frequency and for each driving condition (sym. and antisym.). The results of this test for the healthy plate are shown in Figure 8.7. Several features of the plot are immediately apparent. The antisymmetric excitation clearly excites a much larger number of modes over the given frequency range. Also, for many (but not all) of the peaks, they are more dominant in one of the two spectra.

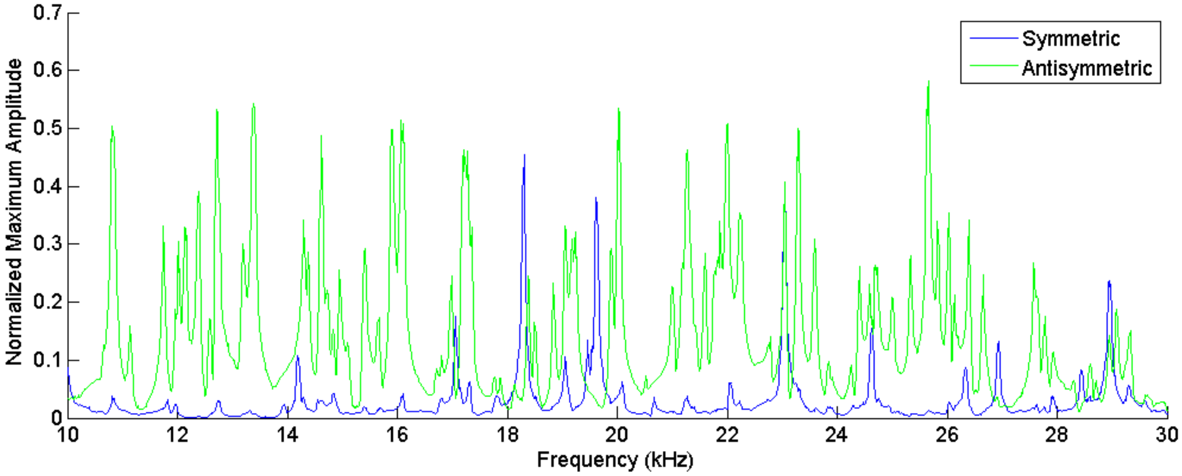

Fig. 8.7 Frequency response for symmetric (blue) and antisymmetric (green) actuation of the healthy plate.

To further analyze the response spectra and how they may be connected to transient guided waves according to our ultrasonic vibration theory, a finite element (FE) eigenvalue analysis was performed on a model of the aluminum plate specimen to determine the resonant frequencies and mode shapes of the plate in the frequency range of interest (10-30 kHz). The analysis resulted in a total of 163 natural modes, 39 of which were dominantly in-plane (compressional) modes, and the remainder of which were dominantly out-of-plane (flexural) modes. Since this frequency range is well below the first cutoff frequency in the plate (near 300 kHz), the flexural plate modes should be associated with the A type guided wave mode and the compressional plate modes should be associated with the S type guided wave mode. In order to analyze this concept, the FE resonant frequencies for the in-plane and out-of-plane modes were plotted against the measured frequency response curves for the symmetric and antisymmetric loading, respectively. The results are shown in Figures 8.8 and 8.9. Note that in order to accommodate for possible variations in material properties, a frequency scaling factor of 3.25% was utilized to shift the FE results to best match the response curves. This is not to say that this adjustment is necessarily accurate, but it does yield a relatively good match to the data and is well within the reasonable range of material properties for 6061 aluminum.

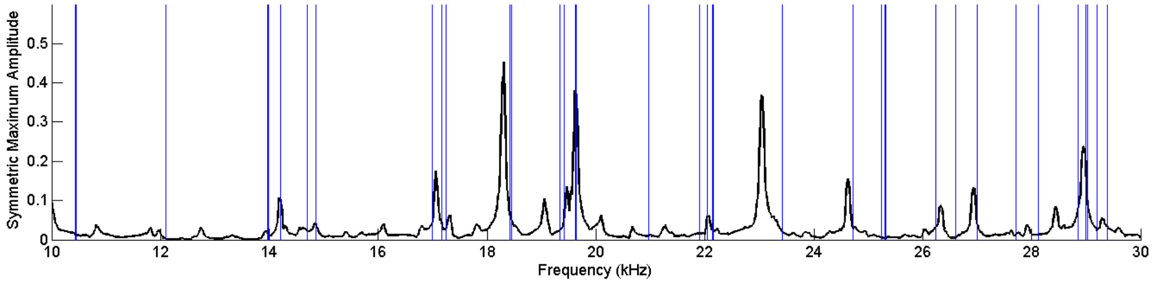

Fig. 8.8 Frequency response for symmetric actuation and in-plane FE resonances.

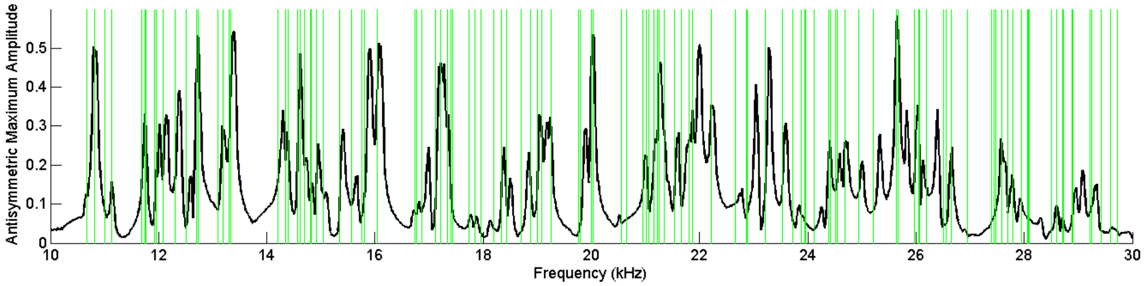

Fig. 8.9 Frequency response for antisymmetric actuation and out-of-plane FE resonances.

Notice that in Figure 8.8, the groups of frequency response peaks as well as the predominant single peaks match rather well with the calculated in-plane resonances from the FE analysis. As for Figure 8.9, the far greater number of predicted flexural resonances agrees well with the greater number of peaks in the antisymmetric response as compared to the symmetric response. The general clusters of FE resonances matches rather well with the clusters of peaks in the response spectrum, and the regions of little measured frequency response match with the frequency regions in which no flexural peaks were predicted. These regions are highlighted in Figures 8.10 and 8.11.

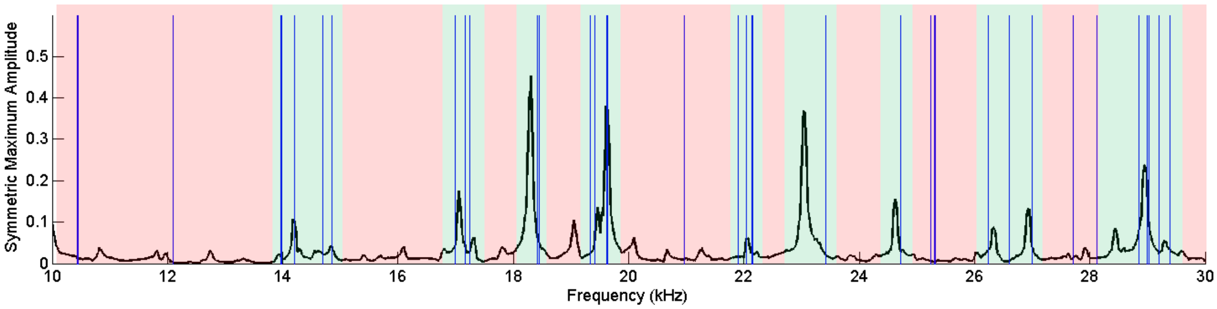

Fig. 8.10 Highlighted regions of the frequency response for symmetric actuation and in-plane FE resonances (from Fig. 8.8).

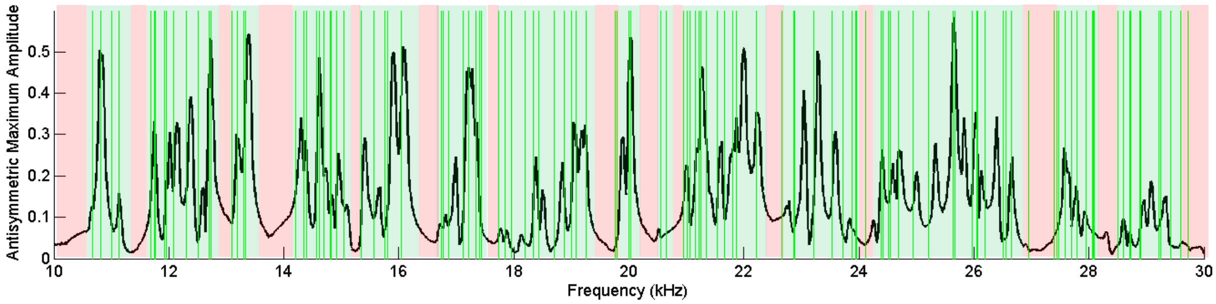

Fig. 8.11 Highlighted regions of the frequency response for symmetric actuation and in-plane FE resonances (from Fig. 8.9).

Defect Results

Although the comparison between the FE resonances and the resonances excited in the plate by symmetric and antisymmetric excitation was the primary goal of this experiment, it was decided to test the effect of a defect on the frequency response related to each of the two types of excitation. This was done by introducing a notch defect, as shown in Figure 8.6. The effect on the frequency response spectrum due to symmetric and antisymmetric loading is shown in Figures 8.12 through 8.15. The "healthy" and "notch" spectra are superimposed over bar plots of the frequency shift and change in magnitude of the peaks in the frequency spectra.

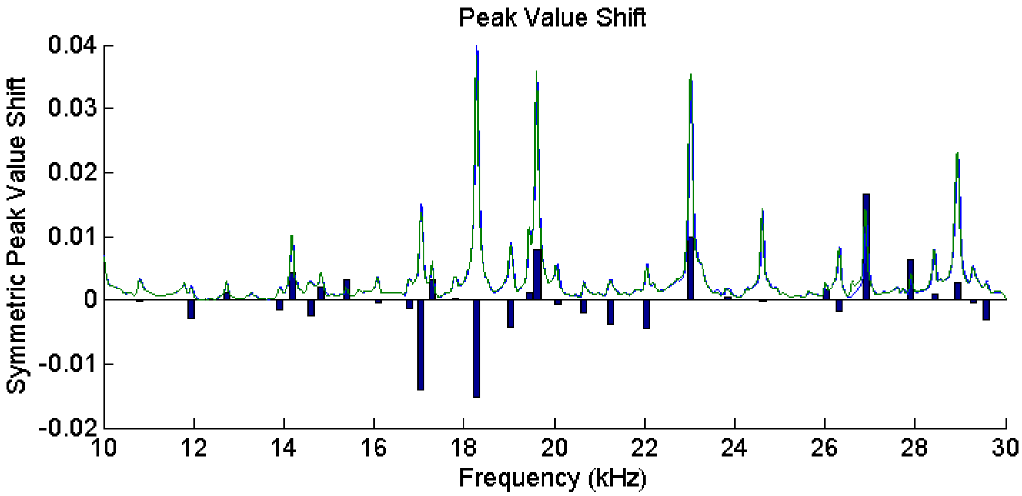

Fig. 8.12 The healthy spectrum (blue line), notch damage spectrum (green line), and shift in peak values (bars) for symmetric excitation.

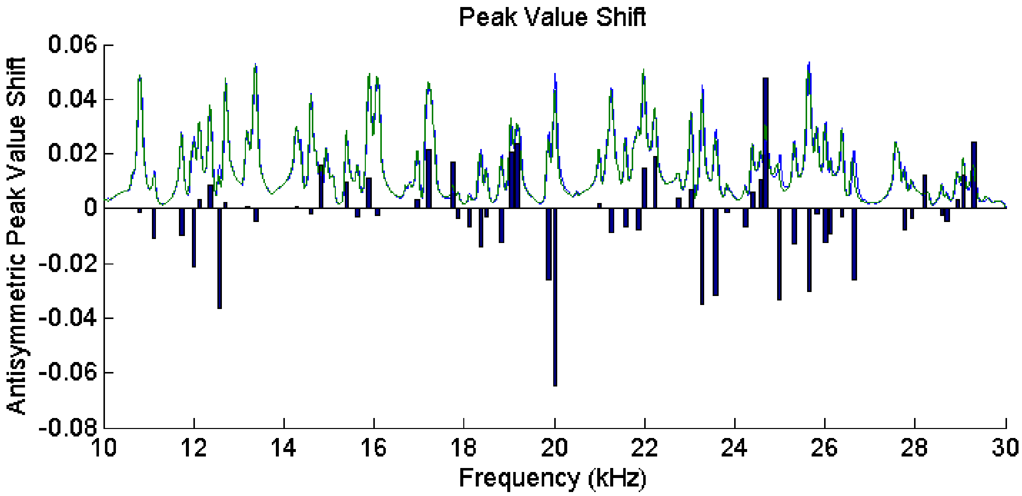

Fig. 8.13 The healthy spectrum (blue line), notch damage spectrum (green line), and shift in peak values (bars) for antisymmetric excitation.

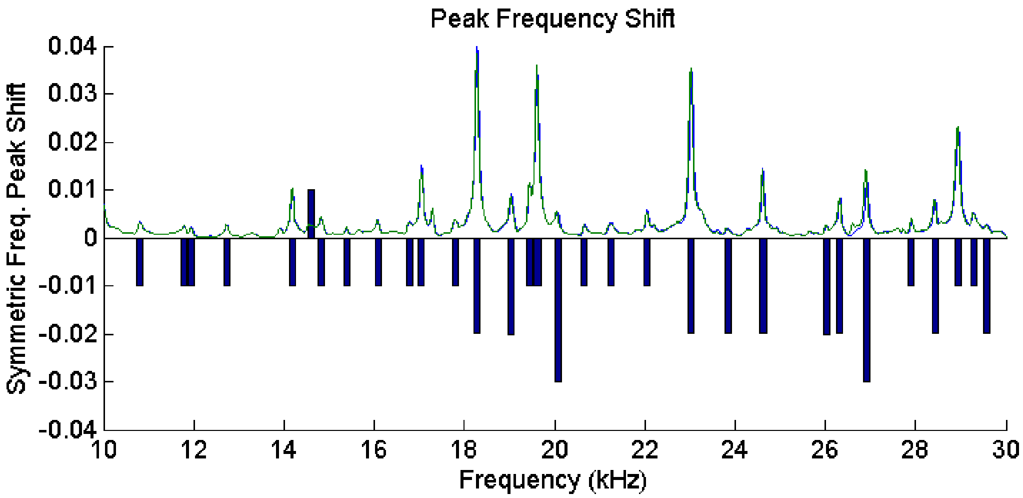

Fig. 8.14 The healthy spectrum (blue line), notch damage spectrum (green line), and shift in peak frequencies (bars) for symmetric excitation.

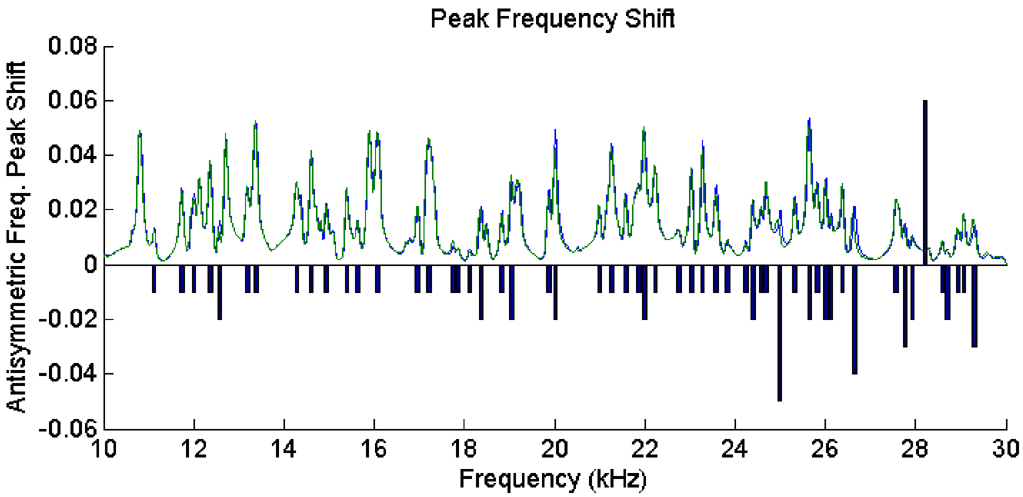

Fig. 8.15 The healthy spectrum (blue line), notch damage spectrum (green line), and shift in peak frequencies (bars) for antisymmetric excitation.

Note that for both the symmetric and antisymmetric excitation, the notch defect only had an appreciable effect on the peak response magnitude at certain frequencies, while others remained essentially unchanged (see Figures 8.12 and 8.13). In general, the resonant frequencies for both excitation types decreased. It is of interest that most of the peaks (in the symmetric and antisymmetric excitation spectra) experienced a decrease in frequency of 10 Hz, while particular peaks experienced increases in frequency or decreases greater than 10 Hz. The uniform 10 Hz decrease could possibly be attributed to temperature variation between the healthy and defect states, but the clearly non-uniform variation in the peak response magnitude and in the peak frequency shift for many of the resonances indicates a substantive change in the system (i.e. the notch damage).

8.1.3. Conclusions

The comparison of the measured frequency response spectra to symmetric and antisymmetric loading with predicted FE natural resonances, in conjunction with the guided wave excitability analysis, tends to support the ultrasonic vibration theory that structural vibrations are due to the superposition of propagating guided wave modes in the structure and that the compressional and flexural plate modes are associated with the S and A type guided wave modes, respectively. The experimental results also support the idea that the source influence of the transducer (in terms of guided wave excitability) has some influence on the excitation of the resonant modes in the structure.

8.2 UMAT Mode Sensitivity Test

The experimental setup of an UMAT mode sensitivity test is shown in Figure 8.16. A 6.35 mm thick 305 mm by 305 mm aluminum plate was used in the experiments. A 4 element annular array transducer was used in the experiment to selectively excite 200 kHz A0 and S0 modes as two different ultrasonic loading functions. In the ultrasonic vibration tests, 12 piezoelectric disk sensors were attached to 12 randomly selected positions on the surface of the aluminum plate using instant adhesives. The annular array actuator was also glued to the surface of the plate. In such a way, the measurement inconsistency due to sensor/actuator coupling conditions can be greatly suppressed. To take a baseline data, the plate was simply placed onto a flat table. Continuous sine wave outputs from the multichannel hardware system were applied to the 4 elements of the annular array actuator. Phase shifts among different elements that were applied to obtain the baseline data for the two different vibration loading functions. The peak-to-peak amplitudes of the forced vibrations under the two loading functions were recorded as the baseline.

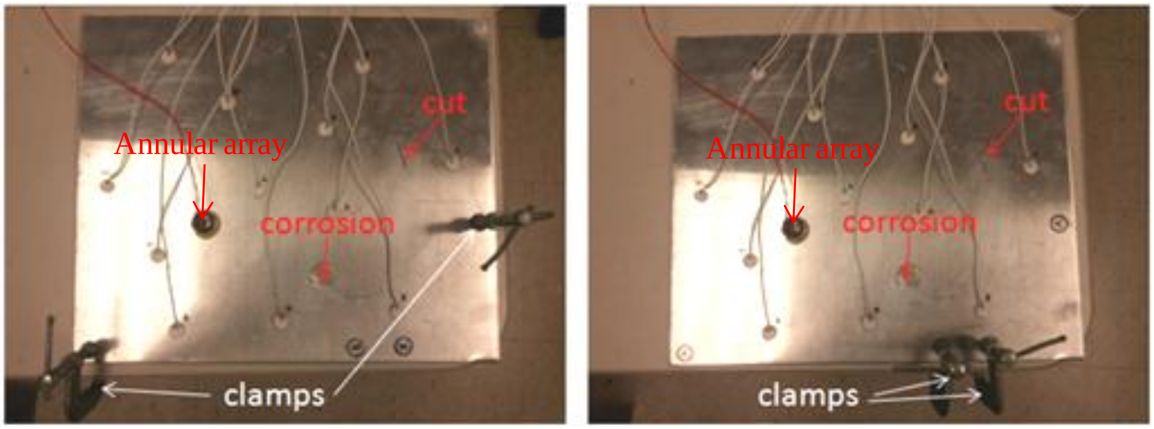

Fig. 8.16 Actuator/sensor setup and demonstration of boundary condition variations used in the experiments. (Left) Boundary condition change A, (Right) Boundary condition change B. Note that the boundary conditions for taking the damage detection data were the same as in the baseline, i.e., no clamping boundary conditions were applied.

Previous to the damage detection tests, boundary condition variations were introduced to the plate by clamping the plate to the table surface at different clamping locations. For each boundary condition change, the forced vibration amplitudes at the 12 disk sensor locations were collected under the two different time delay annular array loading functions. For damage detection, a simulated corrosion area was introduced to the aluminum plate followed by a saw cut defect. Forced vibration data were recorded after each defect was introduced. Fig. 8.16 also demonstrates how the boundary condition variations were introduced.

Figure 8.17 shows the relative changes of the vibration amplitude ratios for the two different loading conditions (two different phase delays). A S0 / A0 ratio was calculated for each sensor position under each test conditions by dividing the vibration amplitude obtained with the phase delay for exciting the S0 mode by the corresponding amplitude obtained with the A0 mode input. The results shown in Figure 8.17 are overall relative changes of the S0 /A0 ratios for the boundary condition changes and the two defects. The results suggest that the S0 / A0 ratio can be a good feature for damage detection as it is very sensitive to the corrosion and cut defects, but minimally reacts to boundary condition changes. The reason for that is because the two guided wave modes react similarly to the boundary condition changes but have quite different responses to defects due to their defect detection sensitivity differences. Phased annular array actuators make it possible to apply different loading functions in the UMAT tests through electronically tuning the guided wave modes and frequencies. Great flexibility in choosing loading functions and the corresponding vibration features can therefore be achieved for different application requirements.

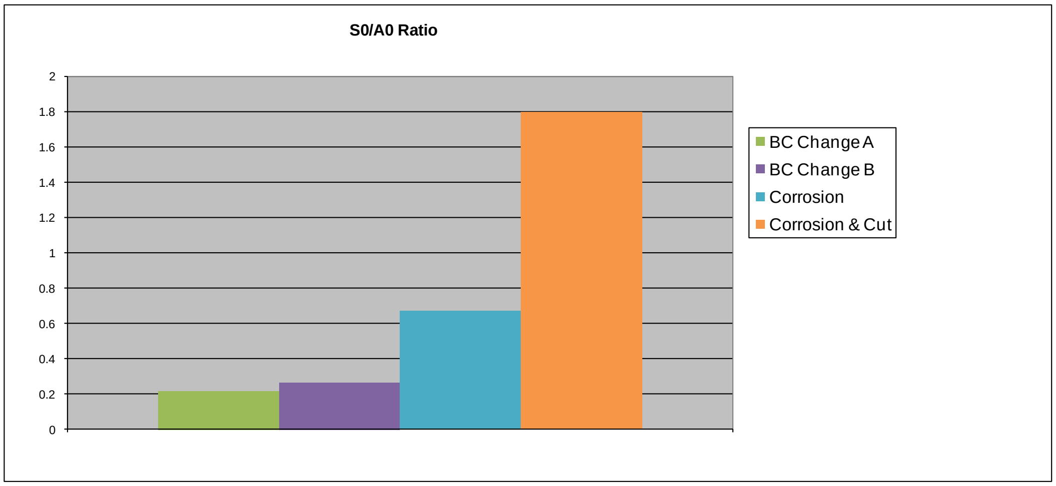

Fig. 8.17 Relative changes in the S0/ A0 vibration amplitude ratios for different test conditions. The S0/A0 ratios were calculated by dividing the vibration amplitudes obtained under the S0 loading function by the corresponding amplitudes obtained under the A0 loading function.

8.3 Aluminum Panels with an Irregular Shape

Prior to UMAT experiments on composite structures, aluminum panels with an irregular shape were used to test the system and to validate the UMAT approach. An aluminum plate sample with an irregular shape was first used for automatic frequency and phase delay tuning tests. As shown in Figure 8.18, an annular array actuator was spring loaded onto the surface of the test sample which was fixed to a test table using 9 screws. The screws were initially tightened by a torque wrench with the same torque limit. Liquid gel coupling was used to couple the annular array to the test sample. Four channel continuous sine waves outputted from the hardware system were used to drive the annular array actuator with 4 elements. Four small disk sensors were attached to the surface of the test sample as the receivers. When collecting the UMAT test data, the automatic tuning was applied to sweep the frequency of the driving signals as well as the phase delays among the output channels. For each frequency and phase delay combination, the high frequency forced vibration signals were collected by the four receivers. The amplitudes and instantaneous phases of the signals were extracted and then saved into an ASCII data file. After one automatic tuning process was finished, the amplitudes and phases of the vibration signals under all the loading functions were saved for all four receivers.

Two baseline data files were generated at different times for the same initial boundary conditions, i.e., all 9 screws were tightened using a same torque level. The actuator coupling condition was not changed when taking the two data sets. The idea was to demonstrate the repeatability of the UMAT test. Figure 1 shows the experimental setup for the baseline data collection. After collecting the baseline data, the actuator was lifted up and the liquid coupling was wiped from both the actuator and the test sample. The actuator was replaced back to the sample after we re-apply some coupling to the test sample. Another automatic tuning process was then carried out to save another data file. This was to test the influence of the coupling condition. Following the coupling condition test, bolt loose conditions were introduced to the test sample by loosing the screws. One screw was loosed at a time, following by an automatic tuning to save a data file. Notice that, each time after one data file was saved, the loosen screw was re-fastened to the same torque level as before being loosened. The next screw was then loosened to simulate the loose bolt condition. In other words, there was only one loose screw for each data file saved under the simulated loose bolt conditions. Three different bolts, labeled #2, #3, and #4 were involved in the tests, one following the other. The second baseline data and the actuator replacement data for the coupling condition test were compared with the first baseline data to show the repeatability of the UMAT test and to study the influence of coupling conditions. The actuator replacement data were then used as the new baseline to compare with the loose bolt data. Since many loading functions were used in the tests, the comparisons can be used to demonstrate the differences in loose bolt detection sensitivity of different loading functions. Optimal loading functions can therefore be suggested based on the comparisons. The test data can also be input into pattern recognition algorithms for further analysis.

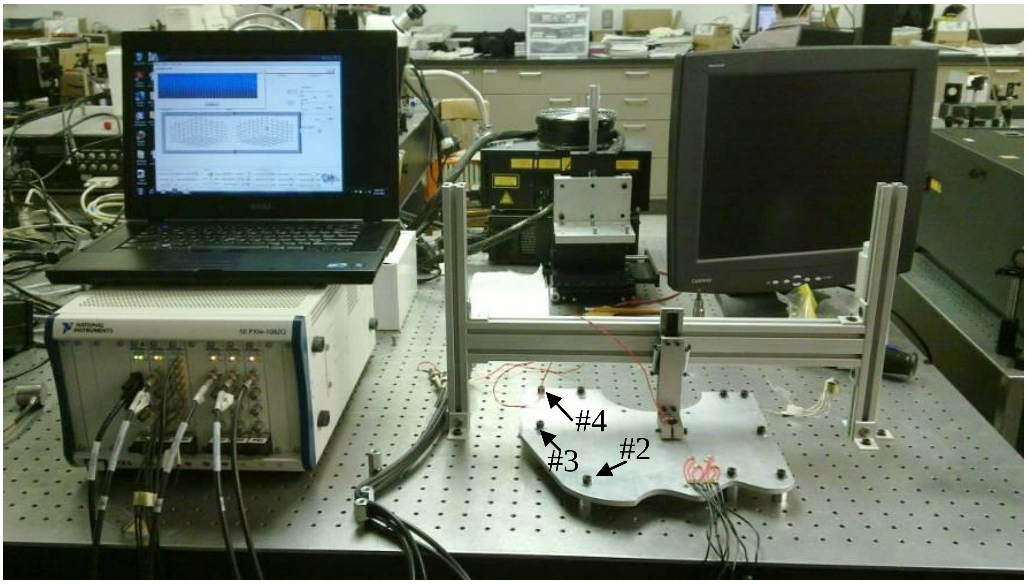

Figure 8.18. Experimental setup

Figure 8.19 shows the example intensity maps of the UMAT vibration amplitudes plotted from the first baseline data. The amplitudes measured by the 4 sensors were plotted in figures (a) to (d) respectively. The x-axis of the intensity maps is the phase shifts among the four output channels, while the y-axis is the driving frequency. As can be seen, the tuning process started from 350 kHz to 460 kHz with a 10 kHz frequency step. For each frequency, a sweep of phase delays was conducted from 0 degree to 360 degrees with a 10 degree increment. Apparently, the vibration amplitudes vary with the change of the loading functions. Based on the intensity maps, one can tell that when using 440 kHz or 450 kHz as the driving frequency and a phase delay of 0 degrees (as circled in the figures), relatively high vibration amplitudes were received by all four receivers.

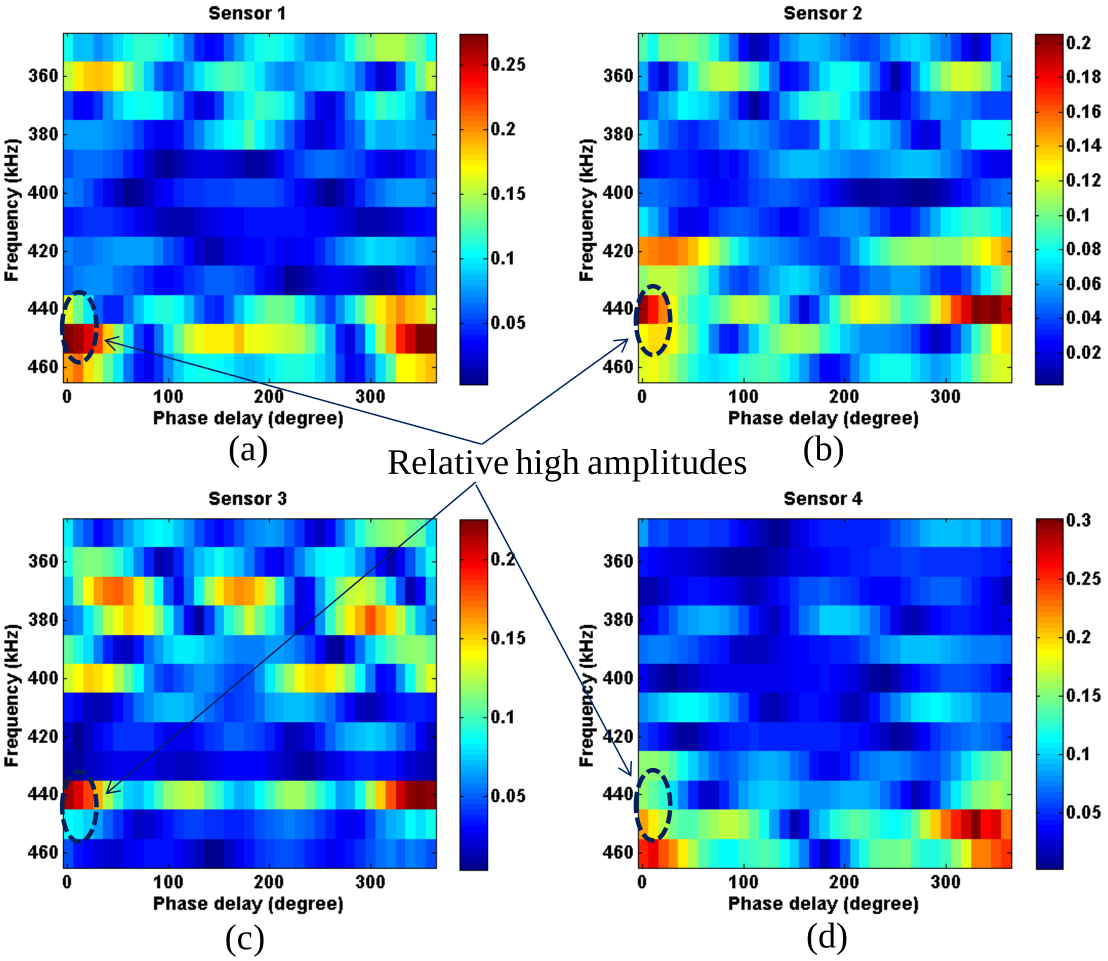

Figure 8.19. *Amplitude intensity maps based on the first baseline data. Relatively high amplitudes for frequencies 440 kHz and 450 kHz and 0 phase delay are circled in the plots.*

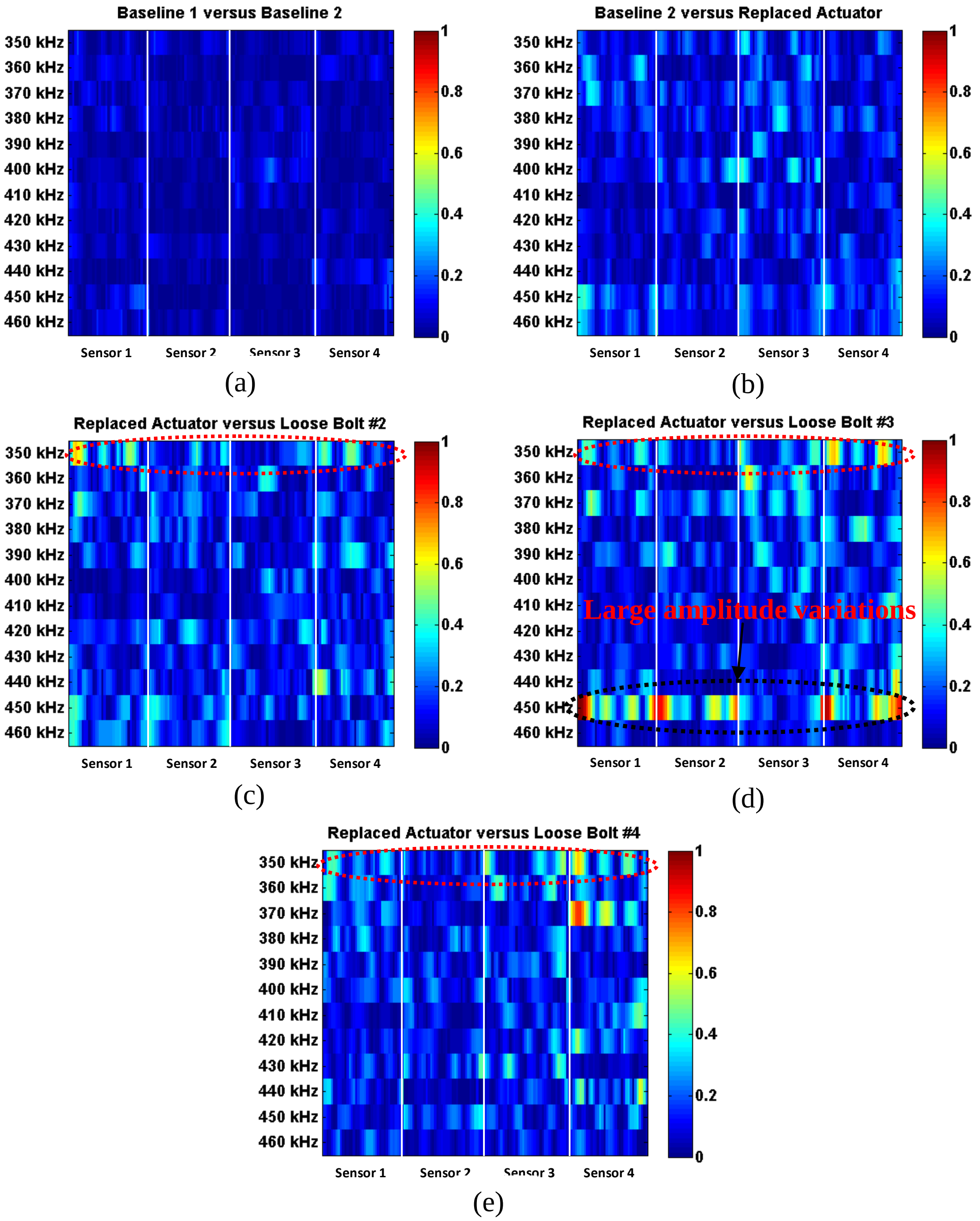

(a) (b) (c) (d) (e)

Figure 8.20. Intensity maps showing the amplitude differences calculated from the data comparisons.

The data comparison results are shown in Figure 8.20 as amplitude difference intensity maps. The intensity maps for all four sensors were combined together. The y-axis is still the driving frequency. The x-axis now includes the phase delays for all 4 sensors, i.e., phase delays from 0 to 360 degrees for sensor 1, the same phase delays for sensor 2, 3, and 4. The intensity maps were also normalized based on the maximum amplitude differences found in all five comparisons. In Figure 8.20(a), it is clear that the two baseline data were very similar which demonstrates the repeatability of the UMAT test. The highest intensity shown in Figure 8.20(b) is also relatively low. This suggested that the baseline data and the data taken after replacing the actuator were fairly similar with each other. The influence of coupling condition was thus reasonably low, especially when comparing to the loose bolt cases.

High intensities can be observed in Figure 8.20 (c), (d), and (e). It is obvious that the UMAT amplitudes can be used for detecting bolt loose conditions when appropriate loading functions are applied. As for the optimal loading functions, very good indications of the loose condition of bolt #3 can be seen from Figure 8.20 (d), as circled with a black dashed line. More specifically, when the frequency 450 kHz and phase delay 0 degrees was used, a very good sensitivity can be gained from all sensors for the detection of the loose condition of bolt #3. The sensitivity to the looseness of the other two bolts based on such a loading function, however, was not as good. That is due to the specific vibration pattern introduced by the loading function. It is believed that the pattern has strong amplitude at the bolt #3 location. The other two bolts may locate at or close to some vibration nodal points. An alternative loading function for high sensitivity to the conditions of all three bolts is frequency 350 kHz and phase delay at around 30 degrees. The relative amplitude variations for the loose conditions of the three bolts that were observed under this loading function are circled with red dashed lines in the figures. It can be determined that with such a loading function, the data from all 4 sensors can yield good sensitivity to the conditions of all three bolts. Such a conclusion will be further tested with more experiment runs.

Three identical test samples were also prepared and used for loading function tuning tests. A picture showing all three samples is given in Figure 8.21. Each sample has 9 disk sensors attached to the surface in a 3x3 grid. During the tests, only the first 8 sensors were used to record the vibration data due to the channel limit of the current hardware system. The frequency tuning for each test had a start frequency of 300 kHz and an end frequency of 500 kHz. The frequency increment was 20 kHz. The phase delay sweep was the same as that used for the test described in the previous section. As a result, each test generated 16x101x37 data points, with 16 being the number of amplitudes and phases obtained by 8 channels, 101 being the number of frequencies, and 37 being the number of phase delays. Baseline data and loose bolt data were collected for all three samples. Only bolt #2 was involved for the first set of tests.

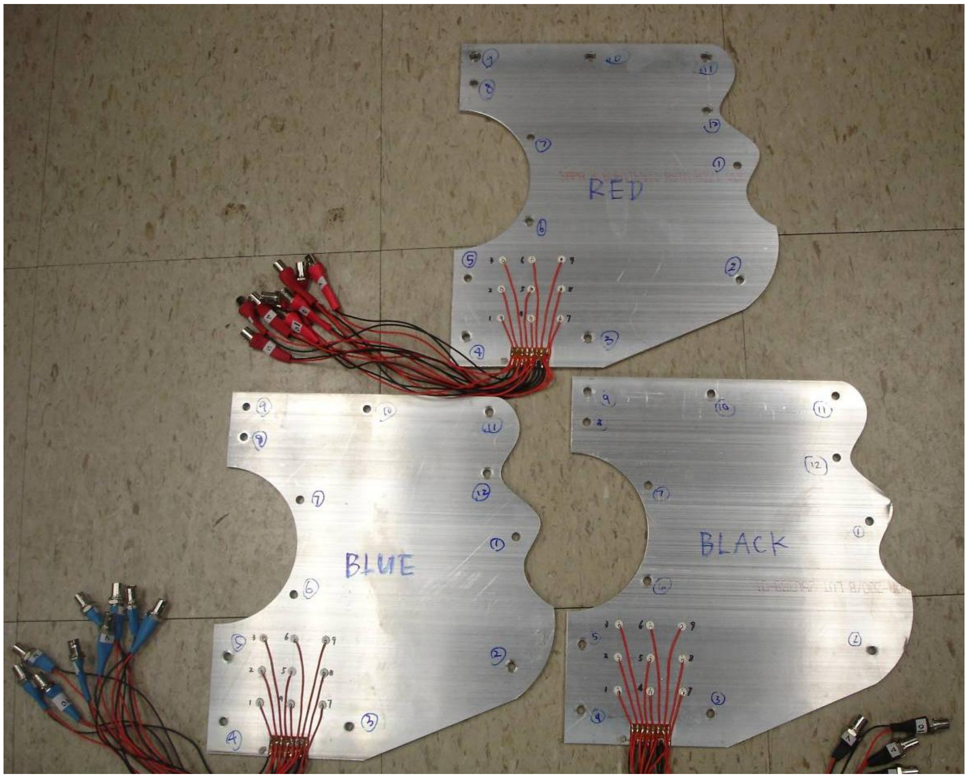

***Figure 8.21**. Three identical test samples, each with 9 sensors attached in a 3x3 grid.*

The experimental setup is shown in Figure 8.22. In total, 5 screws were used to bolt the test sample to an optical breadboard. The torque limit applied to tighten the screws was 40 in-lbs. The screws were numbered as Bolt 2, 4, 6, 8, and 10, respectively. The test sample was placed underneath the test stand with an annular array spring loaded to the surface. Liquid gel couplant was applied to couple the annular array to the test sample. During the UMAT test, 4 sine wave driving signals with controlled frequency and phase delays were applied to the 4 elements of the annular array. A frequency and phase delay tuning was carried out for each test. The frequency was varied from 300 kHz to 350 kHz with a 5 kHz step. For the phase delay tuning, the range was from 0 degrees to 360 degrees and the tuning step was 12 degrees. To study the variations in UMAT responses to loosened bolt conditions, 7 tests were performed. The tests were numbered from I to VII. The test condition changes made for every test are given below.

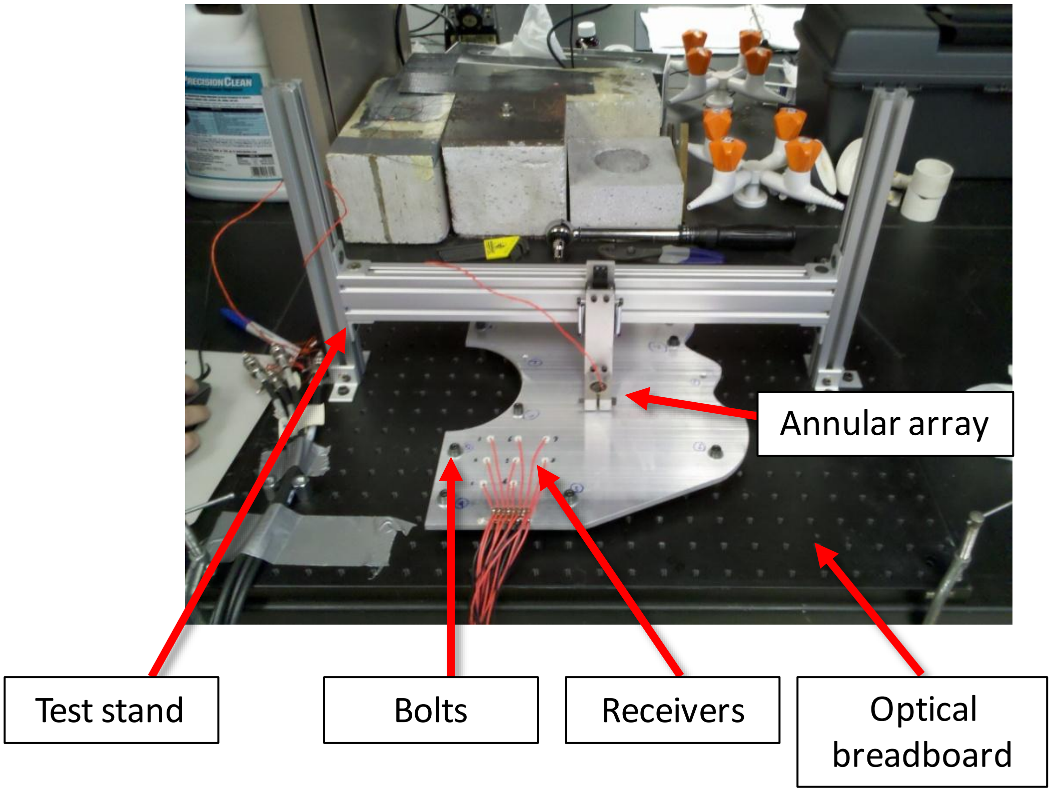

Figure 8.22. Experimental setup

Cumulative Damage States:
I. Baseline
II. Reset transducer and couplant
III. No changes
IV. Bolt 2 loosened from 40 in-lbs to 20 in-lbs (50%)
V. Bolt 4 loosened from 40 in-lbs to 20 in-lbs (50%)
VI. Bolt 10 loosened from 40 in-lbs to 36 in-lbs (10%)
VII. Bolt 10 removed

For each test, 8 out of the total 9 sensors attached to the test sample were used to record the forced vibration amplitudes and relative phases under different loading functions, since the current hardware system has only 8 A/D channels. In each test, a number of 275 amplitude values and corresponding phase measurements were saved to the result file. The objective of the tests was to show the variations in UMAT responses with respect to loosened bolt conditions.

Figures 8.23 and 8.24 show the amplitude maps for test conditions I and IV respectively. The x-axis of each amplitude map is the phase delay tuning step and the y-axis is the frequency tuning step. All amplitude maps were normalized using the maximum amplitude measured at test I. It is obvious that after the torque of Bolt 2 was reduced 50%, obvious amplitude variations were observed by all sensors for the frequency and phase delay tuning.

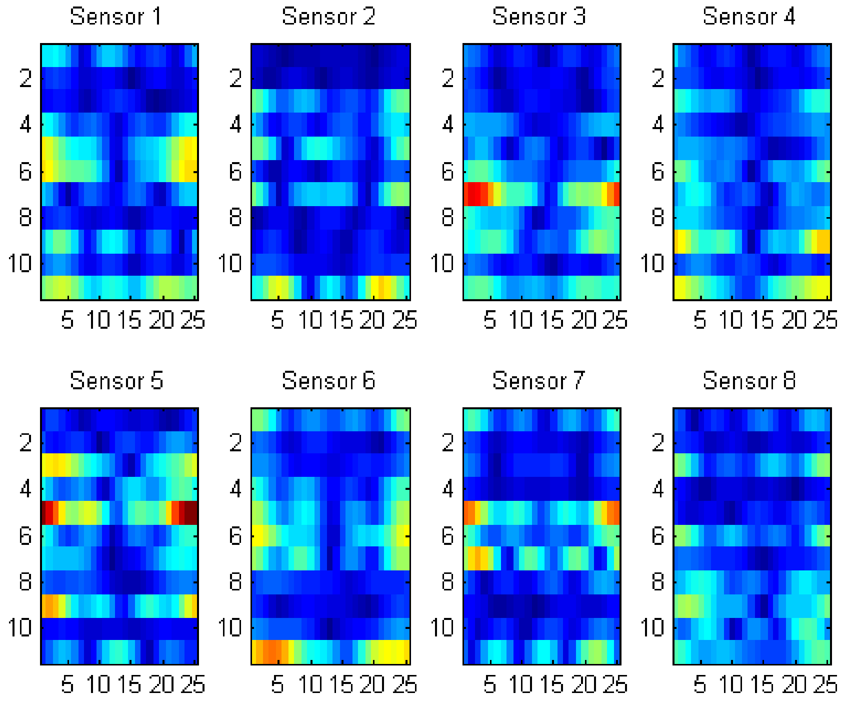

Figure 8.23. *Normalized UMAT amplitude maps for test I, the baseline data.*

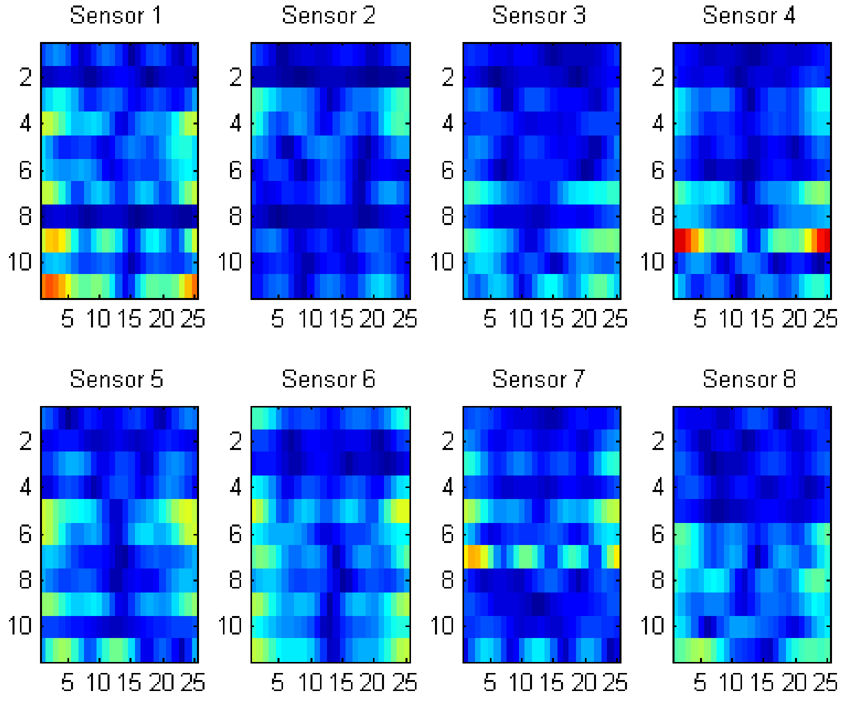

Figure 8.24. *Normalized UMAT amplitude maps for test IV with the torque of Bolt 2 reduced 50%, showing different amplitude variations from the baseline data in Fig. 8.23 for different frequency and phase delay inputs.*

Example amplitude map comparison results are shown in Figures 8.25 to 8.26. Figure 8.25 shows the absolute values of amplitude changes from the baseline data, Test I, to the data taken in Test III. Figure 11 shows the corresponding comparison between Test V and Test I. The comparison between the last test, Test VII, with the first baseline test is shown in Figure 8.27. The amplitude comparison maps were normalized using the maximum found in the last comparison.

As can be seen, the UMAT amplitude variations caused by resetting the transducer and couplant were much less noticeable comparing to the changes due to loosened bolt conditions. There was growth in amplitude variations from Test V to Test VII. Image processing as a feature extraction tool and pattern recognition algorithms can be developed to investigate further the amplitude maps to seek robust UMAT features for loosened bolt condition monitoring. Work efforts are also undertaken to identify the optimum loading functions to reduce the necessary frequency and phase delay tuning steps. The theory on annular array guided wave excitation is applied in this work.

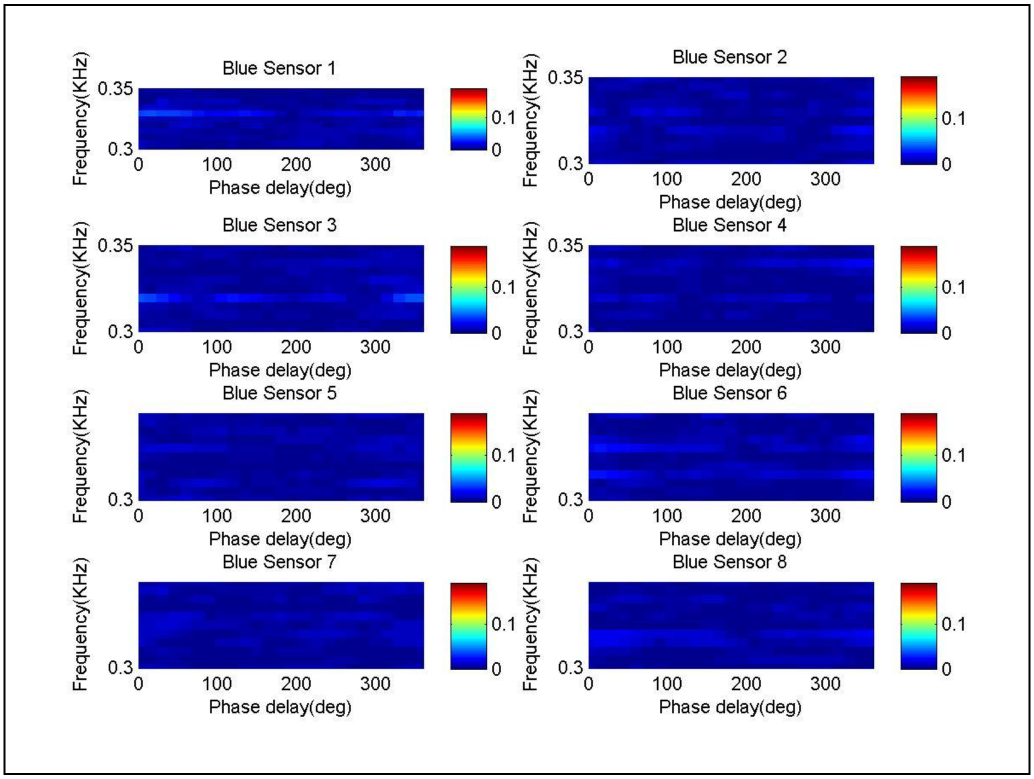

Figure 8.25. Amplitude map comparison between Test III and Test I.

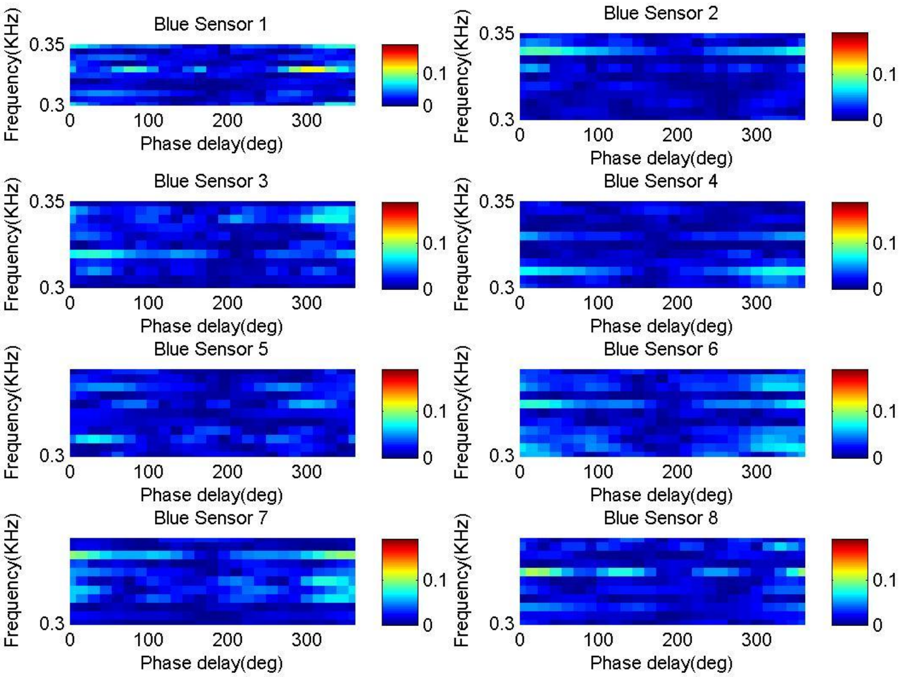

Figure 8.26. Amplitude map comparison between Test IV and Test I.

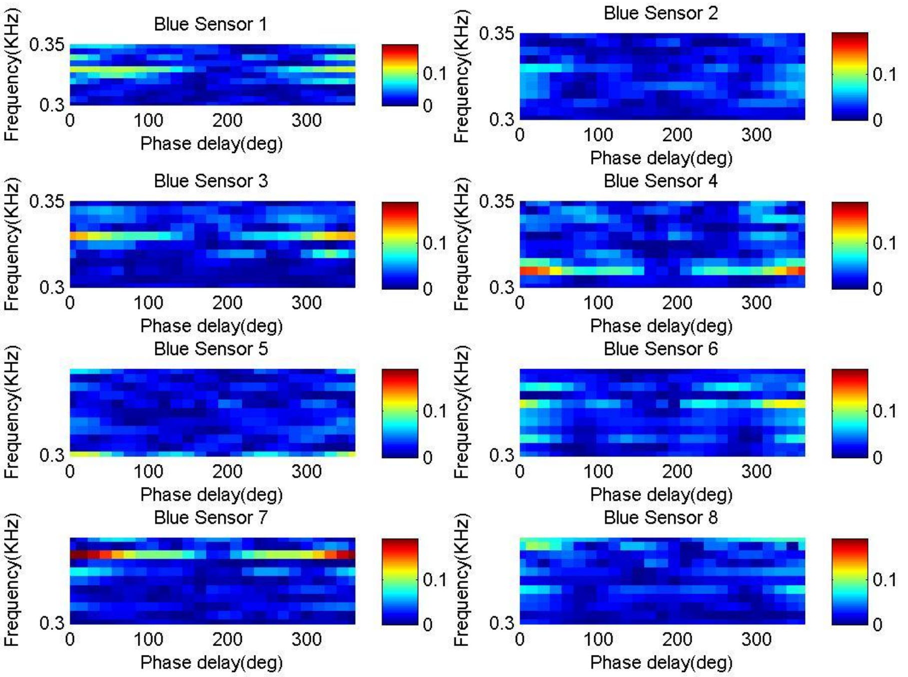

Figure 8.27. Amplitude map comparison between Test VII and Test I.

UMAT experiments were continued using one of the aluminum panels shown in Figure 8.21. Both boundary condition changes and a real defect were introduced to the irregular-shaped aluminum plate sample. The tests were focused on identifying different loading functions that are sensitive to different boundary condition changes and defects. In total, 5 test states were included in the experiment. The condition of each test state is briefly explained below:

State 1 = baseline
State 2 = bolt 10 loosened 50%
State 3 = bolt 10 removed
State 4 = 30% depth corrosion
State 5 = 100% depth corrosion

As can be seen, in addition to the bolt loosening conditions that were studied before, a defect was introduced to the plate in two steps. Figure 8.28 shows a picture of the plate after the 100% depth corrosion defect was introduced. Frequency and phase delay tuning was employed in the test to produce vibration signals under different ultrasonic loading functions. The frequency tuning was conducted with 200 kHz being the starting frequency, 600 kHz being the end frequency, and 5 kHz being the frequency tuning increment. The phase delays were varied from 0 to 360 degrees with 15 degrees as the increment. As a result, for each test state, the number of loading functions as combinations of frequencies and phase delays was 81*25 = 2025. Among the 9 disk sensors attached to the plate, sensors 1 – 8 were used to measure the vibration magnitudes and phases under different loading functions, as only 8 A/D channels were available in the current UMAT testing system. The detections of the bolt loosening conditions and the corrosion defect were based on monitoring the variations in vibration magnitudes and phases among different test states.

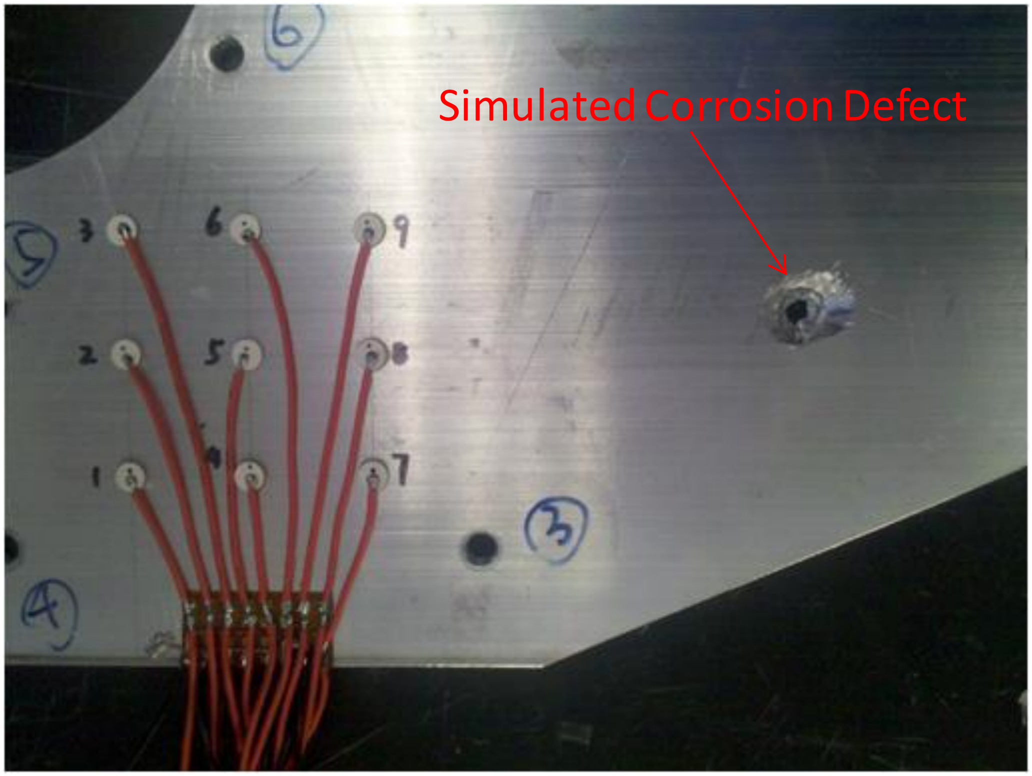

Figure 8.28. *Aluminum plate test sample with the 100% depth corrosion defect.*

One important objective of the experiment was to identify appropriate loading functions for the detections of the bolt loosening conditions and the corrosion defect. By calculating the vibration magnitude changes from test states 2-5 with respect to their immediately previous test states, we evaluated the sensitivity to changes in test conditions under different loading functions. More specifically, the loading function dependent sensitivity was calculated as the summation of the magnitude variation ratios for all 8 measurement sensors. Based on the calculation results, the loading functions were sorted in an order with the summation of magnitude variation ratios descending from the first load function to the last. The first ten loading functions from the sorted results were then defined as the good loading function choices for the detection of the corresponding change in test condition. The last then loading functions, in contrast, were defined as the poor loading function choices. Figures 8.29 – 8.32 present the vibration magnitude changes in percentage obtained through the poor loading function choices and the good loading function choices, respectively for the comparisons between State 2 and State 1, State 3 and State 2, State 4 and State 3, as well as State 5 and State 4. As can be seen, the poor loading function choices yield only very small vibration magnitude changes for the corresponding boundary condition changes or defects. In the plots with the same scale as the plots for the magnitude changes under the good loading function choices, the magnitude changes under the poor loading function choices are too small to be clearly seen. The magnitude changes for the poor loading function choices were then magnified 10 times and plotted as the inserts in the corresponding figures. Even after 10 time magnification, the changes observed under the poor choices were still much smaller than the ones observed under the good choices. Note that for each loading function choice, the magnitude changes in percentage for all 8 sensors are shown in the figures. For the poor choices, the changes in percentage were all lower than 2%. For the good choices, however, at least one sensor among the 8 sensors produced a 45% or higher magnitude change. The maximum magnitude change under the good loading function choices was above 140%. This clearly demonstrated the significance of loading function choices for detecting bolt loosening conditions and corrosion defects.

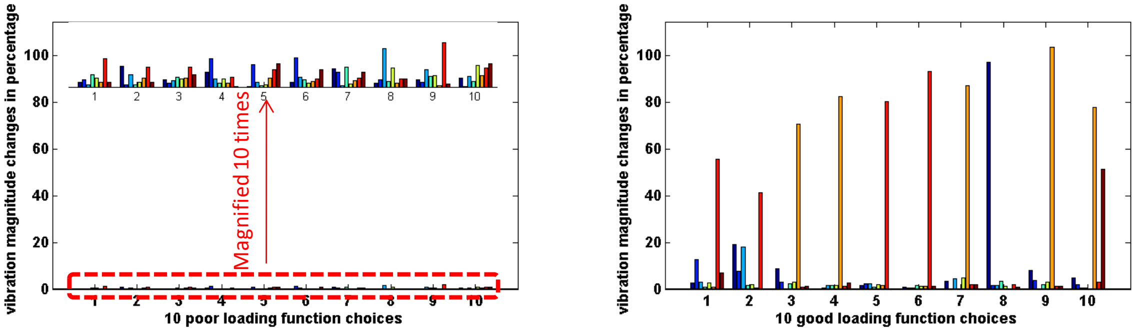

***Figure 8.29**. Vibration magnitude changes in percentage due to 50% torque reduction on bolt 10, under (Left) 10 poor loading function choices and (right) 10 good loading function choices, showing significant differences in vibration amplitude variations due to different loading function choices.*

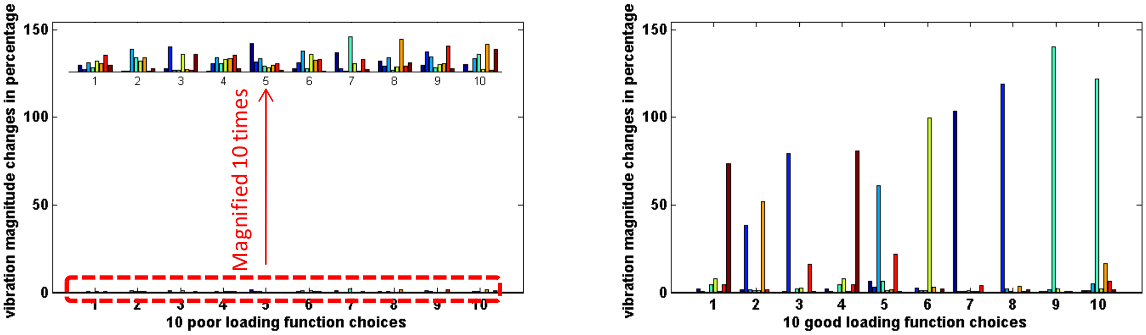

***Figure 8.30**. Vibration magnitude changes in percentage from 50% torque reduction on bolt 10 to bolt 10 removal, under (Left) 10 poor loading function choices and (right) 10 good loading function choices, showing significant differences in vibration amplitude variations due to different loading function choices..*

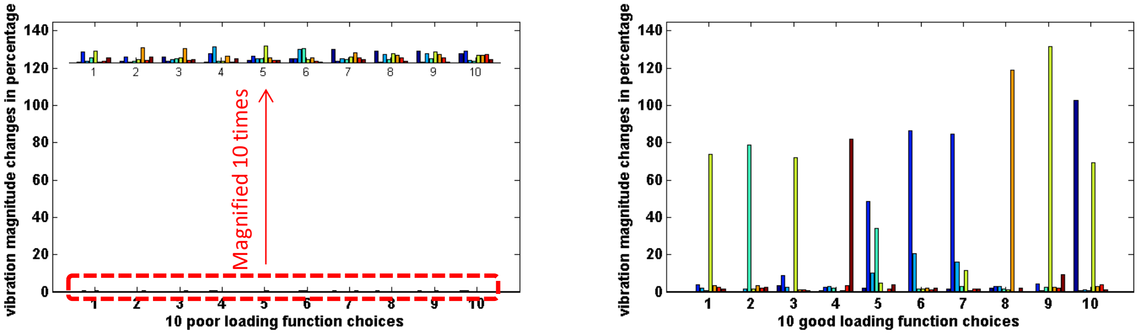

***Figure 8.31**. Vibration magnitude changes in percentage due to the introduction of a 30% depth corrosion, under (Left) 10 poor loading function choices and (right) 10 good loading function choices, showing significant differences in vibration amplitude variations due to different loading function choices.*

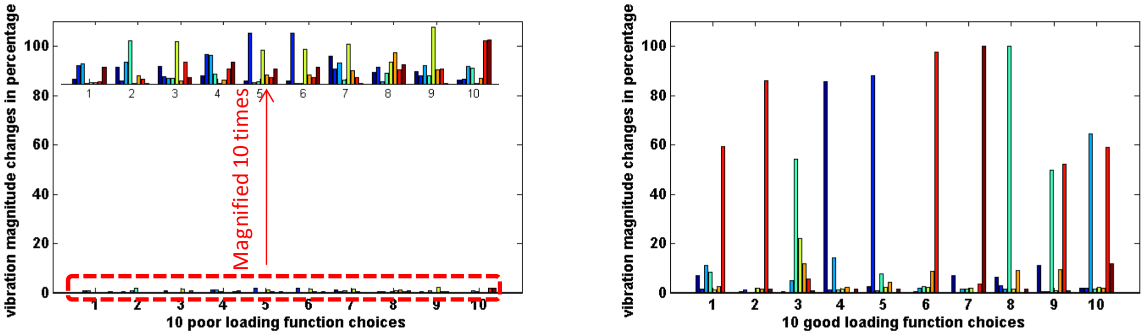

***Figure 8.32**. Vibration magnitude changes in percentage from the 30% depth corrosion to the 100% depth corrosion, under (Left) 10 poor loading function choices and (right) 10 good loading function choices, showing significant differences in vibration amplitude variations due to different loading function choices.*

The poor loading function choices and the good ones that were used to generate Figures 8.29-8.32 were identified based on the vibration magnitude changes themselves. It was therefore not surprising to see the differences in magnitude changes under the two types of loading functions. Another important task was then to investigate what would happen if the good and poor loading functions that were identify for one type of test condition change are applied for the detection of another test condition change. Figure 8.33 shows the magnitude changes in percentage from State 4 to State 3 when the 30% corrosion was introduced, under the loading functions used to generate Figure 8 for the 50% reduction of the torque of bolt 10. It is shown that there were no significant differences in magnitude changes under the 10 poor loading function choices for 50% torque reduction and the 10 corresponding good choices. The plots in Figure 8.33 are with the same scale as the ones in Figure 8.29, since they were under the same loading functions. By comparing Figure 8.33 with Figure Figure 8.29, one can see that the magnitude changes were much smaller in the two Figure 8.33 plots than the results shown in the good loading function choices plot in Figure 8.29, which means that the good loading function choices for 50% torque reduction of bolt 10 was not sensitive to the 30% depth corrosion. The magnitude changes due to the 50% torque reduction under the loading functions for the 30% depth corrosion are shown in Figure 8.34. It was also demonstrated that the good loading functions for detecting the torque reduction were not sensitive to the corrosion defect. It is therefore feasible to use different loading functions to gain good sensitivity to different defects and also differentiate the defects.

Based on our loading function study, we also found that the loading sensitive to 50% bolt loosen condition and 100% bolt loosen condition are very similar. For the 30% through-thickness corrosion and a corrosion region with a through hole, the loading functions that are sensitive to the two defects are almost identical. Those results demonstrated that the loading functions are quit consistency to one kind of defect or boundary change. Table 8.I shows a comparison of the good loading functions to detect the 50% bolt loosen and the ones to detect the 100% bolt loosen conditions. The loading functions that were found sensitive to both two boundary condition changes are highlighted in the figure. The highlighted loading functions are therefore good candidates for detecting bolt loosen conditions.

Similar conclusions on certain loading functions are sensitive to certain damage types or boundary condition changes have also been obtained from the loading function study of the previous UMAT data for both aluminum and composite test samples.

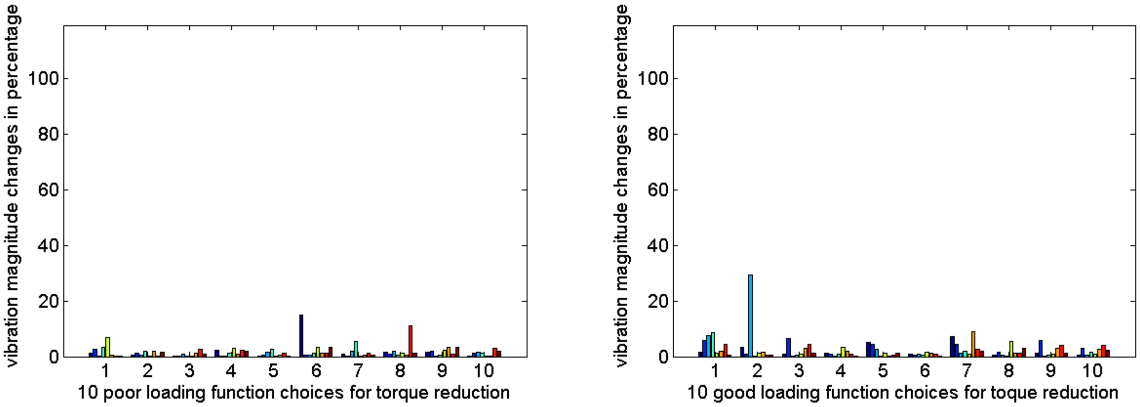

Figure 8.33. *Vibration magnitude changes in percentage from the 30% depth corrosion under the loading functions identified as poor (left) and good (right) choices for detecting 50% torque reduction of bolt 10, both showing small vibration magnitude variations for the 3% depth corrosion. Therefore, the good loading function choices for 50% torque reduction of bolt 10 were not sensitive to the 30% depth corrosion.*

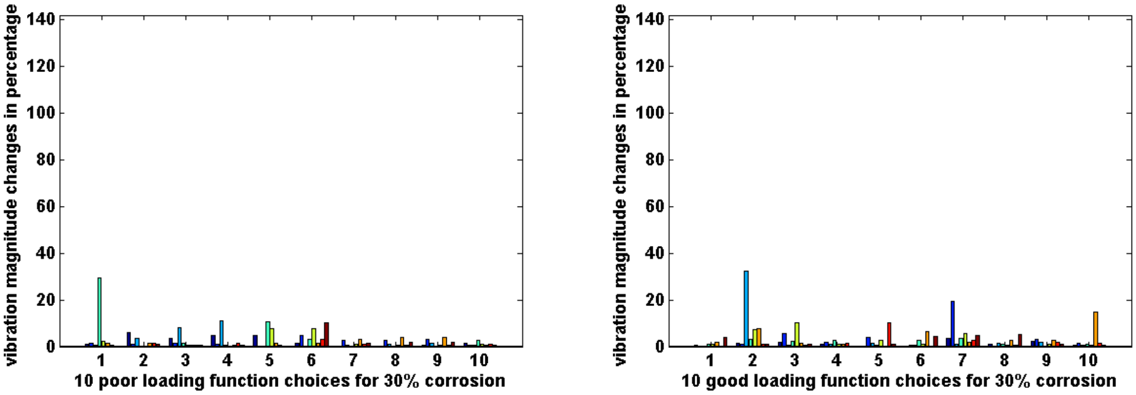

Figure 8.34. *Vibration magnitude changes in percentage from the 50% torque reduction of bolt 10 under the loading functions identified as poor (left) and good (right) choices for detecting 30% depth corrosion, both showing small vibration magnitude variations for the 3% depth corrosion. Therefore, the good loading function choices for the 3% depth corrosion were not sensitive to the 50% torque reduction of bolt 10.*

Baseline VS 50% bolt loose		Baseline VS 100% bolt loose	
Frequency (MHz)	Phase (Degree)	Frequency (MHz)	Phase (Degree)
0.21	135	0.2	285
0.21	120	0.21	120
0.255	270	0.2	75
0.21	45	0.21	135
0.2	285	0.255	270
0.245	240	0.21	45
0.21	30	0.245	240
0.21	0	0.2	105
0.21	15	0.21	30
0.2	75	0.21	0
0.2	105	0.205	75
0.21	105	0.2	90
0.21	360	0.235	315
0.205	75	0.215	60
0.245	15	0.21	15
0.21	150	0.24	90
0.21	225	0.21	360
0.21	90	0.245	270
0.245	270	0.2	300
0.2	90	0.21	255

Table 8.I. Comparison of good loading function choices to detect the bolt loosen condition with 50% torque reduction and the bolt loosen condition with 100% torque reduction.

8.4 Composite Spoiler

Ultrasonic vibration tests were carried out on 3D composite samples as well. The composite test sample is made of woven carbon/epoxy materials. The sample was originally designed for being used as a rear spoiler for a car. The shape of the composite sample is therefore rather irregular. The sample has an 'L' shaped bended area. As can be seen from the experimental setup shown in Figure 8.35, eight sensors were attached to the surface of the composite test sample to receive ultrasonic vibration signals. There were 4 sensors on each side of the bended area. The test sample was simply supported by several cylindrical supporters underneath one surface of the sample. Five other screws were positioned to the test table to hold the sample in a fixed position to ensure good consistency in boundary conditions for the ultrasonic vibration tests. The prototype actuator that was fabricated in the previous month was applied through a spring loading to a flat area of the test sample, as also shown in Figure 8.35. The diameter of the actuator is roughly 1.7". The actuator has four individual annular elements.

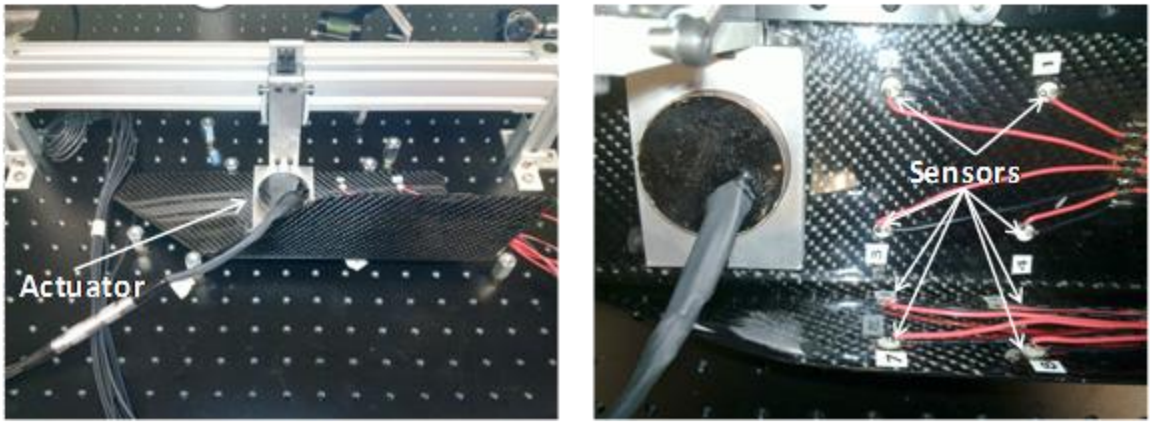

Figure 8.35. Experimental setup.

During the UMAT test, 4 sine wave driving signals with controlled frequency and phase delays were applied to the 4 elements of the annular array. A frequency and phase delay tuning was carried out for each test. The frequency was varied from 200 kHz to 400 kHz with a 1 kHz step. For the phase delay tuning, the range was from 0 degree to 360 degrees and the tuning step was 15 degrees.

To study the variations in UMAT responses to damage, a damaged area was introduced to the composite sample. The damage was created by hitting a steel screw placed to the surface of the sample with a hammer. Figure 8.36 shows a picture of the damage. As can be seen, a through thickness hole was introduced.

Ultrasonic vibration data collections were performed before and after the introduction of the damage. For each test, the 8 sensors attached to the test sample were used to record the forced vibration amplitudes established by different loading functions during the frequency and phase delay tuning process. In each test, a number of 5025 amplitude values were saved to the data file. The objective of the tests was to show the variations in UMAT responses caused by the damage.

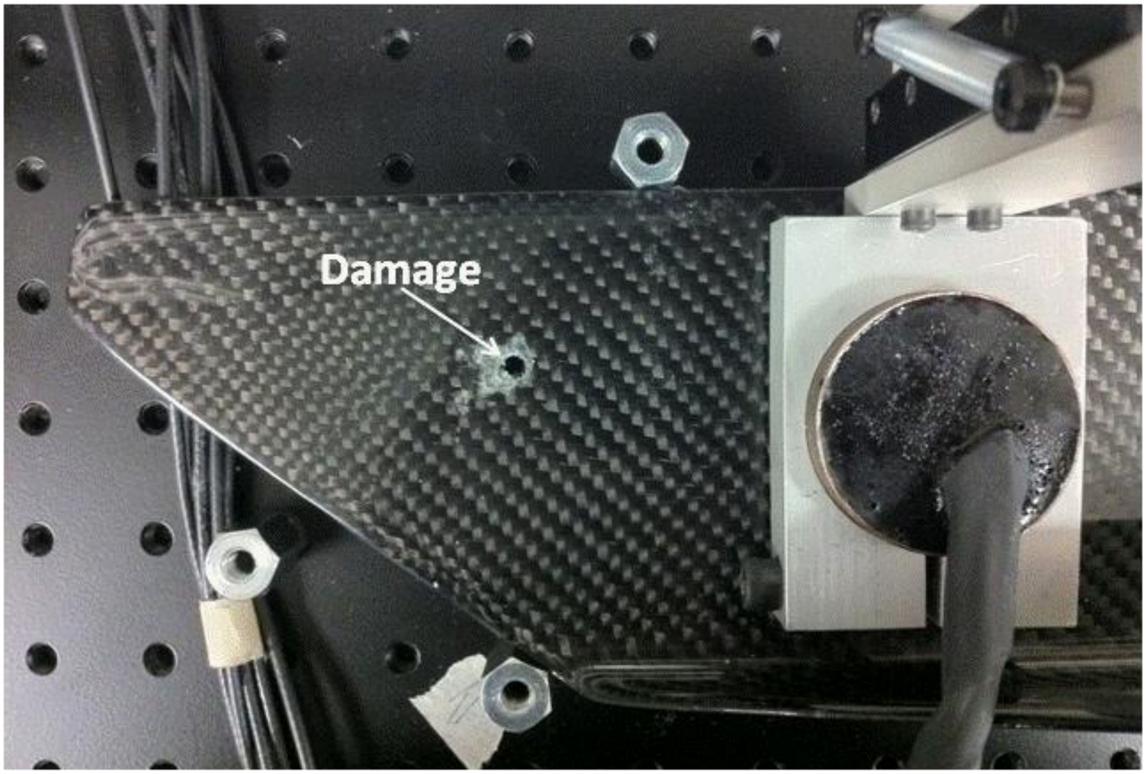

Figure 8.36. Damage introduced to the composite test sample.

Figures 8.37 and 8.38 show the amplitude magnitude maps respectively for the damage free test sample and the damaged test sample.

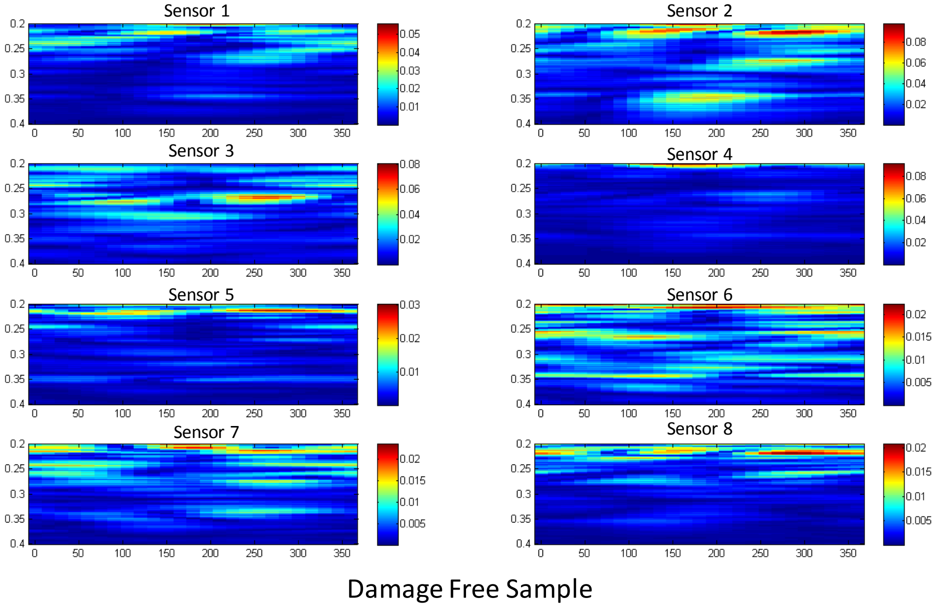

Figure 8.37. UMAT amplitude magnitude maps for the damage free composite test sample.

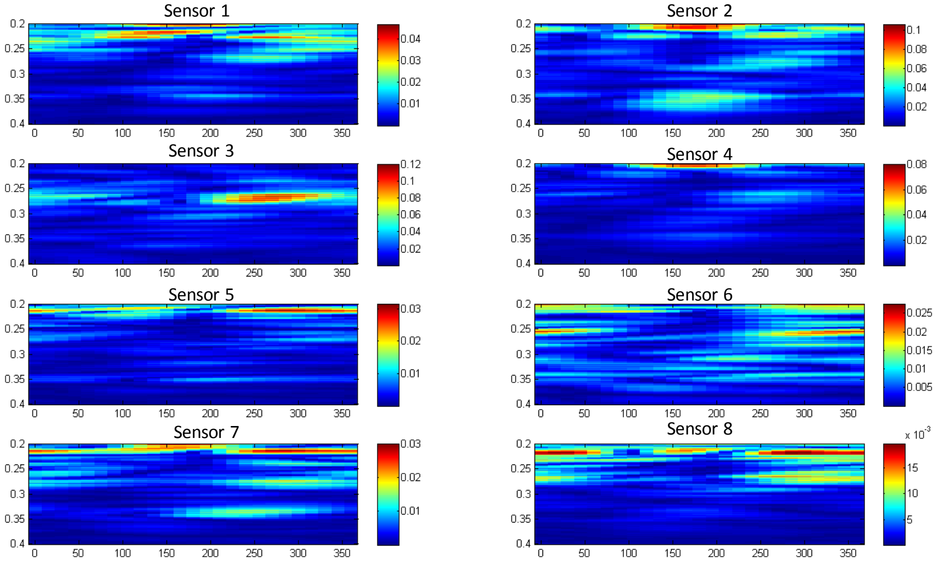

Damaged Sample

Figure 8.38. UMAT amplitude magnitude maps for the damage free composite test sample.

By comparing Figures 8.37 and 8.38, one can clearly observe variations in amplitude magnitude maps for all the sensors. To more quantitatively investigate the amplitude variations, Figure 8.39 presents the summation of the magnitude variation ratios for all 8 sensors. A log scale was used to plot the color intensity map. The blue area in the map that corresponds to a value of -1 indicates equal or less than 10% magnitude variations, while the value 0 in the color bar represents equal or higher than 100% magnitude variations. As clearly shown, most loading functions do not have good sensitivity to the damage to the composite test sample as they only lead to equal or less than 10% vibration magnitude variations. Some loading functions, however, produced some vibration magnitude variations higher than 100%, and thus were very sensitive to the damage.

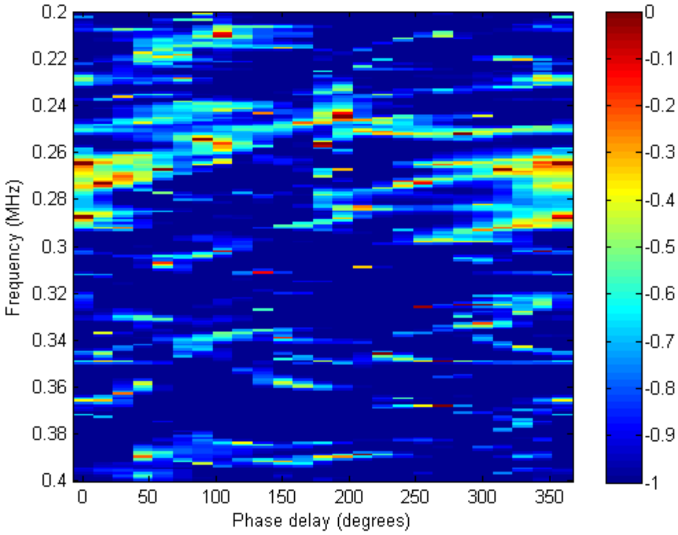

Figure 8.39. Ultrasonic vibration amplitude variation ratios summed from all 8 sensors.

Based on the calculation results shown in Figure 8.39, the loading functions were sorted in an order with the summation of magnitude variation ratios descending from the first load function to the last. The first ten loading functions from the sorted results were then defined as the good loading function choices for the detection of the corresponding change in test condition. The last then loading functions, in contrast, were defined as the poor loading function choices. Figure 8.40 presents the vibration magnitude changes in percentage obtained through the poor loading function choices and the good loading function choices. In the plots with the same scale as the plots for the magnitude changes under the good loading function choices, the magnitude changes under the poor loading function choices are too small to be clearly seen. The magnitude changes for the poor loading function choices were then magnified for 10 times and plotted as the inserts in the corresponding figures. Even after the 10 time magnification, the changes observed under the poor choices were still much smaller than the ones observed under the good choices. This clearly demonstrates the significance of loading function choices for detecting the damage to the composite test sample. By choosing the right loading function, the damage in the composite sample can be very well detected.

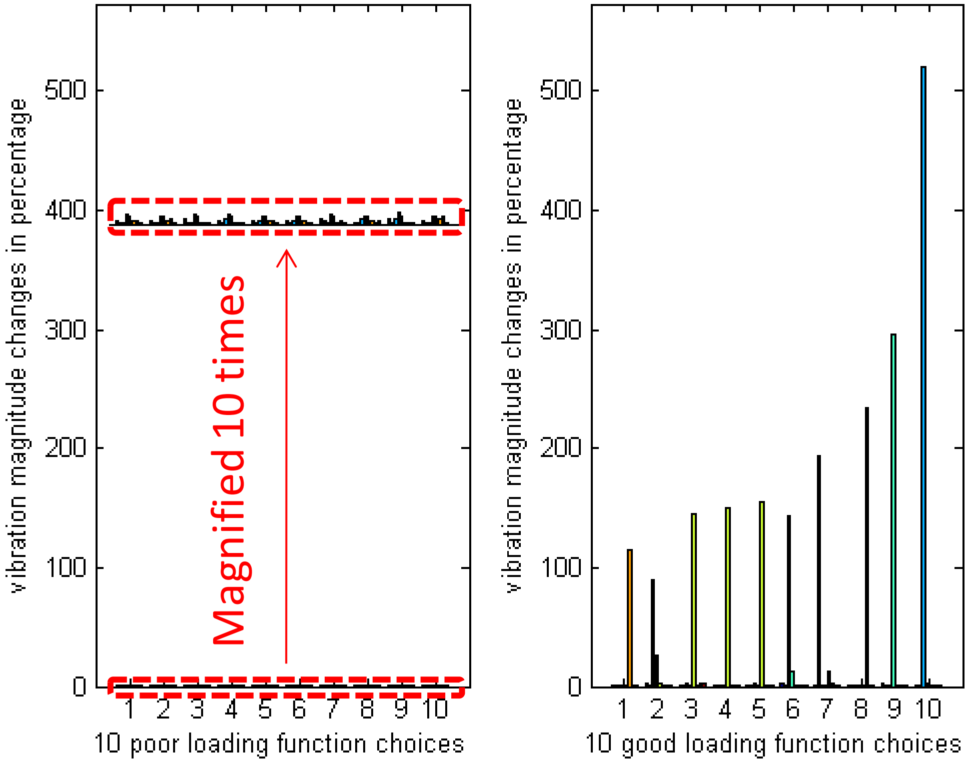

Figure 8.40. Vibration magnitude changes in percentage under (Left) 10 poor loading function choices and (right) 10 good loading function choices.

8.5 Composite Propeller

Figure 8.41 shows the experimental setup for the UMAT tests that have been carried out on an aircraft composite propeller blade. The propeller blade was made from carbon/epoxy composite material. It was an anisotropic structure with a complex 3D geometry. The main purpose of the tests conducted on the propeller blade was to show that the loading functions provided by an annular array actuator can make differences in both the transient guided wave test and the UMAT test results. With appropriate loading functions, high sensitivity to defects or structural condition changes can be achieved in UMAT tests.

The propeller blade was hanged in the air to achieve a rather stable boundary condition for both transient guided wave tests and UMAT tests. An annular array was hot glued close to the center of the blade to serve as the actuator. A broadband transducer was clamped in between the actuator and the tip of the blade to serve as the receiver. Both transient guided wave tests and ultrasonic vibration tests were performed. In the transient guided wave test, clear wave packages were observed. It was also seen that the wave form varied with the frequency and phase delays applied to the annular array elements. In the ultrasonic vibration tests, after continuous sine wave inputs being applied to the actuator, continuous vibration signals were received from the receiver transducer, demonstrating well formed forced vibrations. The vibration amplitudes also varied with the frequency and phase delay loading functions.

After taking baseline data for both transient guided wave and vibration tests, some hot glue was put to the blade surface between the actuator and receiver to test the loading function dependent sensitivity to such a surface condition variation. Figures 8.42 and 8.43 present example results from the transient guided wave tests and the vibration tests respectively. The signals shown in Figure 8.42 were taken with a 250 kHz driving frequency and different phase delays to the annular array elements. Both the baseline signals and the signals collected after the hot glue was introduced to the blade surface are included. The baseline signals were plotted in blue while the new signals were plotted in red. As can be seen, the transient signals varied with the phase delays. There were only very minor changes in transient guided wave signals due to the hot glue. In contrast, the vibration amplitude maps with respect to the phase delays and frequencies of the annular array actuator, as presented in Figure 8.43, did identify good loading function choices that can produce significant vibration amplitude changes. The test results therefore suggested that the UMAT loading functions can be tuned using a phased delayed annular array actuator to yield high sensitivity to a certain type of defect or structural condition changes. The variations in vibration amplitudes can sometimes be more significant than the changes in transient guided wave signals since the vibrations include a very large number of boundary reflections and multiple guided wave interactions with the defect.

Figure 8.41. *Experimental setup for the initial tests on a composite propeller blade.*

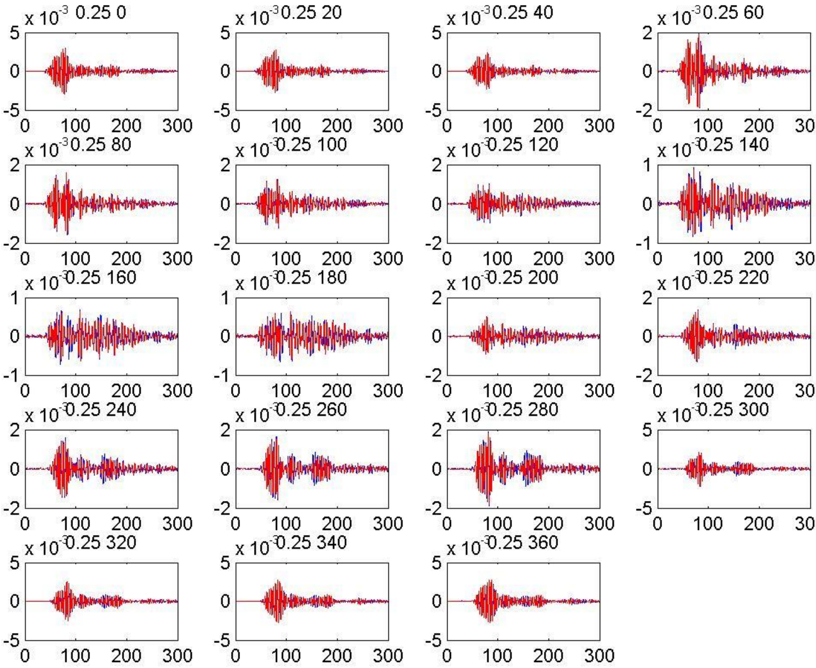

Figure 8.42. *Transient guided wave signals for a 250 kHz driving frequency and different phase delays. Baseline signals are in blue color and new signals taken after the hot glue was introduced are in red.*

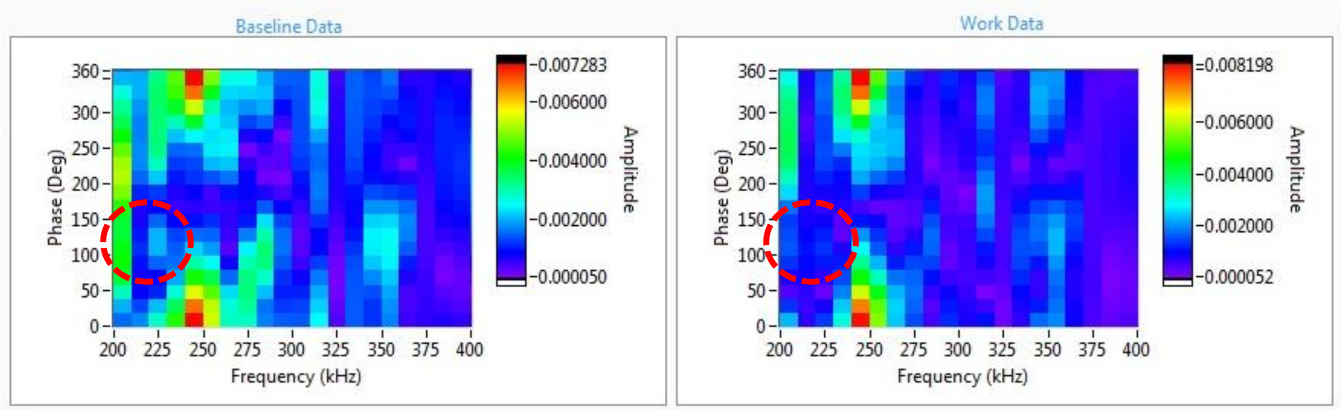

***Figure 8.43**. Vibration amplitude maps with respect to the phase delays and frequencies applied to the annular array actuator: (Left) baseline date, (Right) Data taken after a structural condition change. The circled regions show some significant vibration amplitude changes.*

8.6 Air Force Panels

Initial damage detection experiments on Air Force composite test samples have been carried out in this month. The thickest panel among the retired F-16 panels was selected as the first test sample for the experiments. The selected panel has an irregular shape. There are also rivet holes in the panel. Like all other panels, there are thickness variations caused by ply drops in the selected panel. A four element annular array and a broadband transducer were used in the experiments as the actuator and receiver respectively. Figure 8.44 shows a picture of the test panel with both the actuator and the receiver attached to the surface of the panel using hot glue.

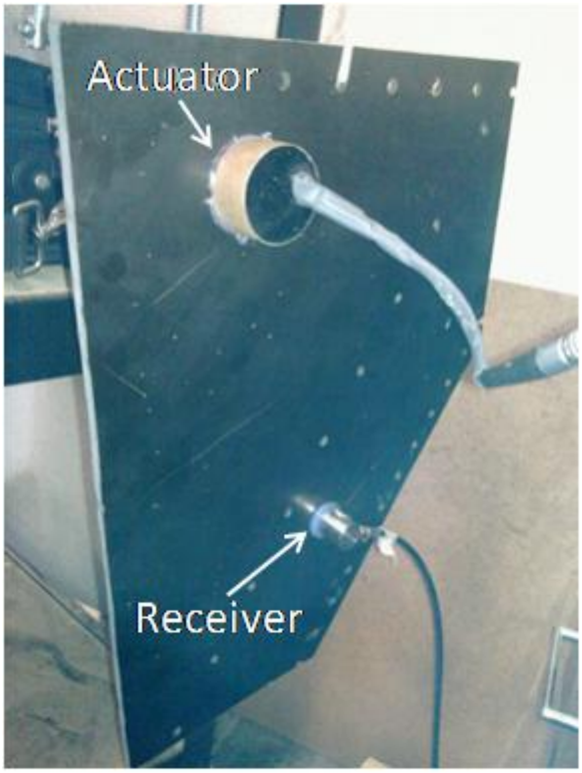

Figure 8.44. *An Air Force composite panel with an actuator and a receiver attached for transient guided wave and UMAT tests.*

To simulate a crack defect, a notch was introduced to an open hole located at the edge of the test panel. Cracks at rivet holes are common defects in aircraft structures as the areas around rivet holes are usually stress concentration regions. The length of the simulated crack was 0.5”. Figure 8.45 shows pictures of the simulated crack defect.

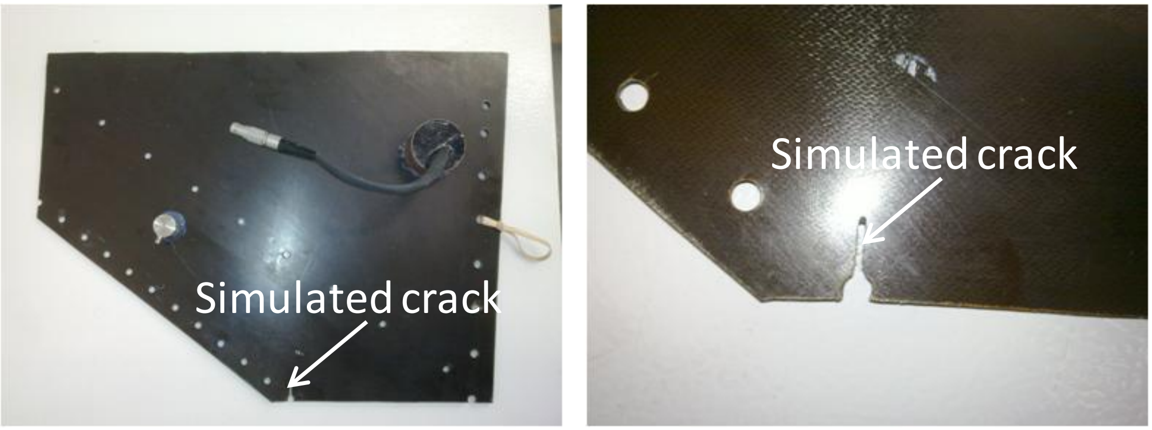

Figure 8.45. *A simulated crack defect introduced to an open hole located at the edge of the test panel. (Left) Complete view of the test panel showing the simulated crack location. (Right) A close view of the simulated crack. The length of the crack was 0.5”.*

Transient guided wave signals and ultrasonic vibration amplitudes were collected before and after the simulated defect was introduced. Different phase delay and driving frequencies were applied to the four element actuator to provide different loading functions. Example transient guided wave signals are shown in Figure 8.46 for 200 kHz tone-burst inputs with different phase delays. The baseline signals taken before the crack was introduced are plotted in blue while the signals taken after the crack was introduced are plotted in red. As can be seen, the transient guided wave signals varied significantly when different phase delay angles were applied to the four elements of the annular array actuator. The baseline signals and the signals taken after the crack was introduced were very similar due to the fact that the crack was far away from the direct wave path between the actuator and the receiver. The signals were rather complicated as well because of the wave scattering at the rivet holes in the panel and also the possible mode conversions for wave traveling across different thicknesses.

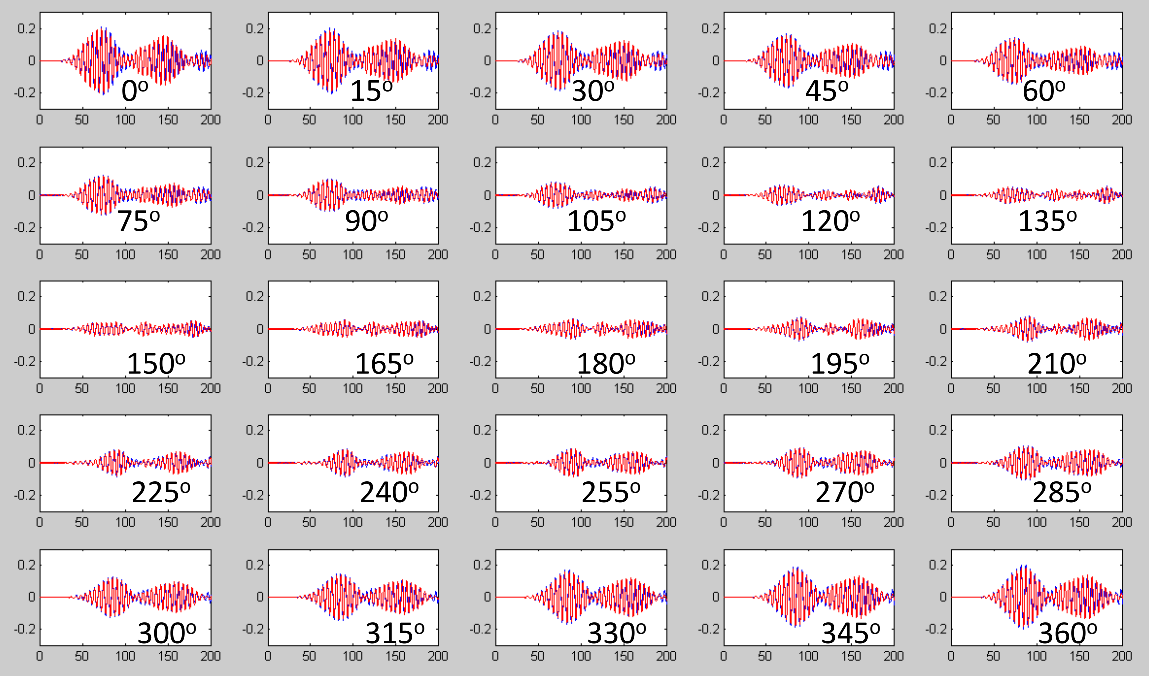

Figure 8.46. Transient guided wave signals for 200 kHz tone burst inputs with different phase delays applied to the four elements of the annular array actuator.

Figure 8.47 shows the color map comparison of the ultrasonic vibration amplitudes between the baseline data and the data taken after the crack was introduced. It was revealed that the vibration amplitudes were quite similar for most of the loading functions except for the 200 kHz ones. A comparison plotted in columns is shown in Figure 8.48 with the columns for the 200 kHz loading functions enlarged in the insert of the figure. In the enlarged view, the x-axis of the plot is for different phase delay angles, increasing from 0 degree to 360 degrees from the left to the right. Significant vibration amplitude changes due to the crack can be observed. For loading functions other than the 200 kHz ones, the vibration amplitude variations were small. That, again, demonstrated the importance of using appropriate loading functions in UMAT tests for high defect sensitivity.

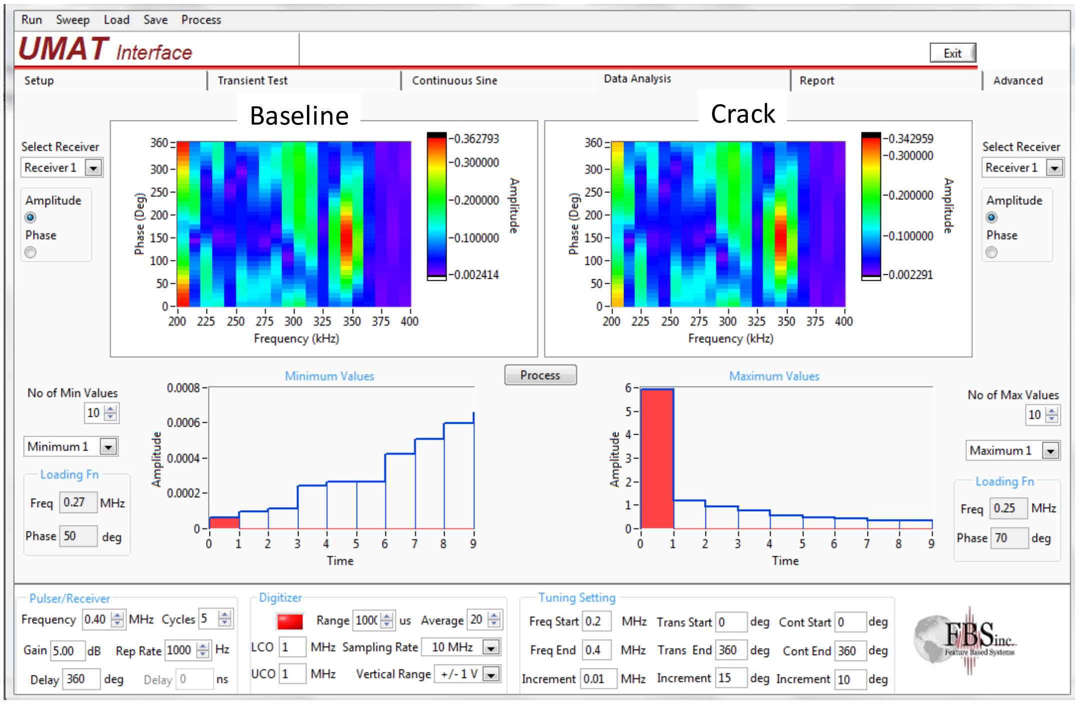

Select Receiver: Receiver 1

Amplitude ●
Phase ○

No of Min Values: 10

Minimum 1

Loading Fn
Freq 0.27 MHz
Phase 50 deg

Select Receiver: Receiver 1

Amplitude ●
Phase ○

No of Max Values: 10

Maximum 1

Loading Fn
Freq 0.25 MHz
Phase 70 deg

Pulser/Receiver
Frequency 0.40 MHz Cycles 5
Gain 5.00 dB Rep Rate 1000 Hz
Delay 360 deg Delay 0 ns

Digitizer
Range 1000 us Average 20
LCO 1 MHz Sampling Rate 10 MHz
UCO 1 MHz Vertical Range +/-1 V

Tuning Setting
Freq Start 0.2 MHz Trans Start 0 deg Cont Start 0 deg
Freq End 0.4 MHz Trans End 360 deg Cont End 360 deg
Increment 0.01 MHz Increment 15 deg Increment 10 deg

Figure 8.47. Color map comparison of the ultrasonic vibration amplitudes under different loading functions. Clear variations can be observed for the 200 kHz loading functions with different phase delay angles.

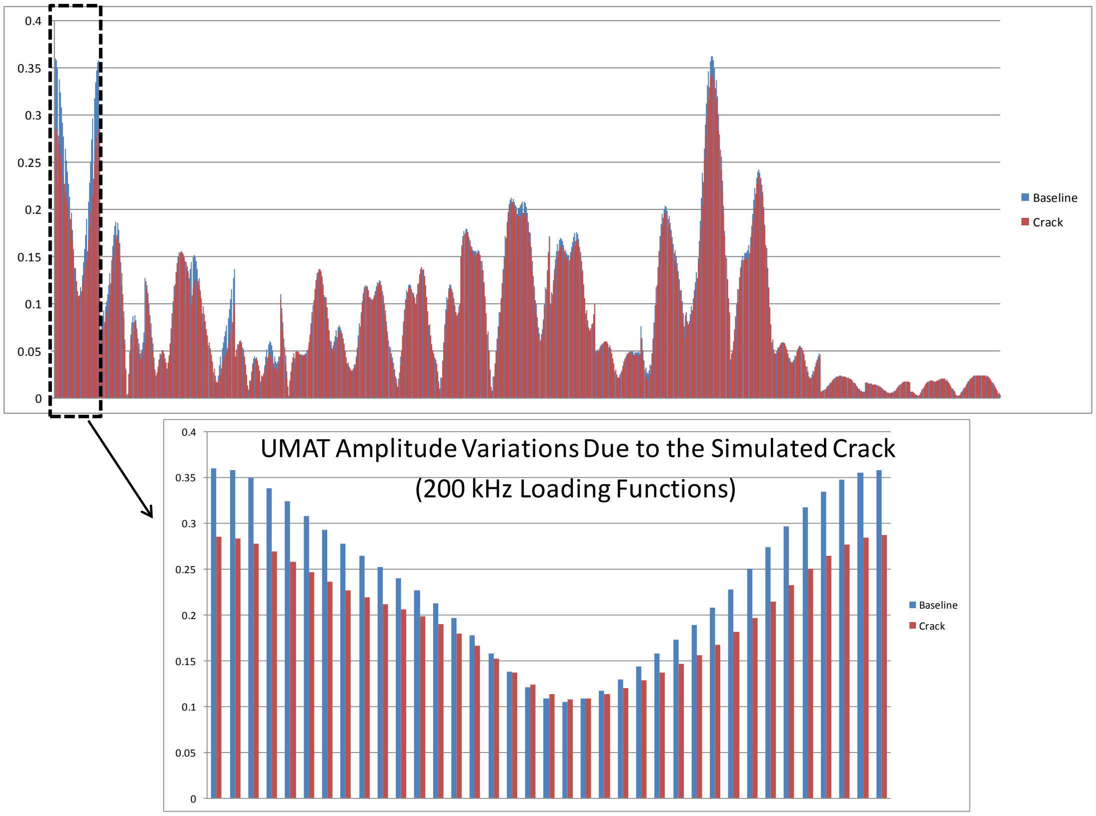

Figure 8.48. Vibration amplitude comparison plotted in column format.

Another defect was introduced to the test sample. This time, the defect was close to the receiver location. It was an objective to learn the difference in testing results with the defect being close to the receiver rather than being far away from the direct wave path between the transmitter and the receiver. A picture of the 2nd defect can be found in Figure 8.49.

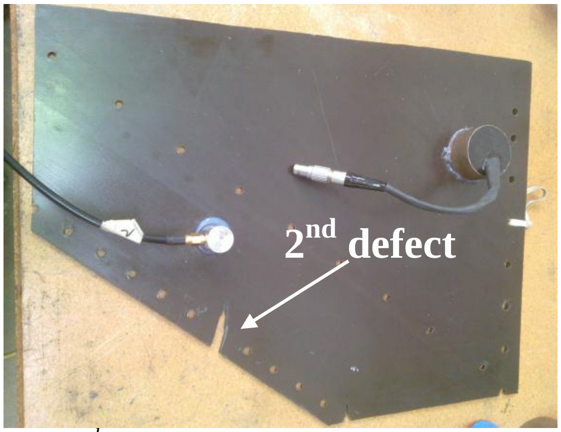

Figure 8.49. Picture of the 2nd defect. The second defect was closer to the receiver than the first defect.

In the transient tests, frequency and phase delay were varied to produce different guided wave loadings. We operated the frequencies from 0.2MHz to 0.4MHz with a step of 10 kHz. The phase delays between adjacent elements varied from 0 degree to 360 degree with an increment of 40 degrees. The signals were first taken with only the first simulated crack in the test sample as a new set of baseline data. After that, another saw cut defect was introduced at the lower right corner of the panel. Due to the fact that the new defect was close to the receiver, defect reflections were clearly observed for some loading frequencies and phase delays. However, there were very small or almost none changes in transient guided wave signals for some frequency and phase delay combinations. Figure 8.50 shows an example. In Figure 8.50, the signal plotted in blue was from the new baseline data and the one plotted in red was taken after the 2nd defect was introduced. The loading frequency was 0.25 MHz and phase delay was 160 degree. As can be seen, no clear changes due to the 2nd defect can be observed. It therefore suggested that 0.25 MHz frequency and 160 degree phase delay was not a good loading to achieve the excitations of the guided waves that are sensitive to the defect.

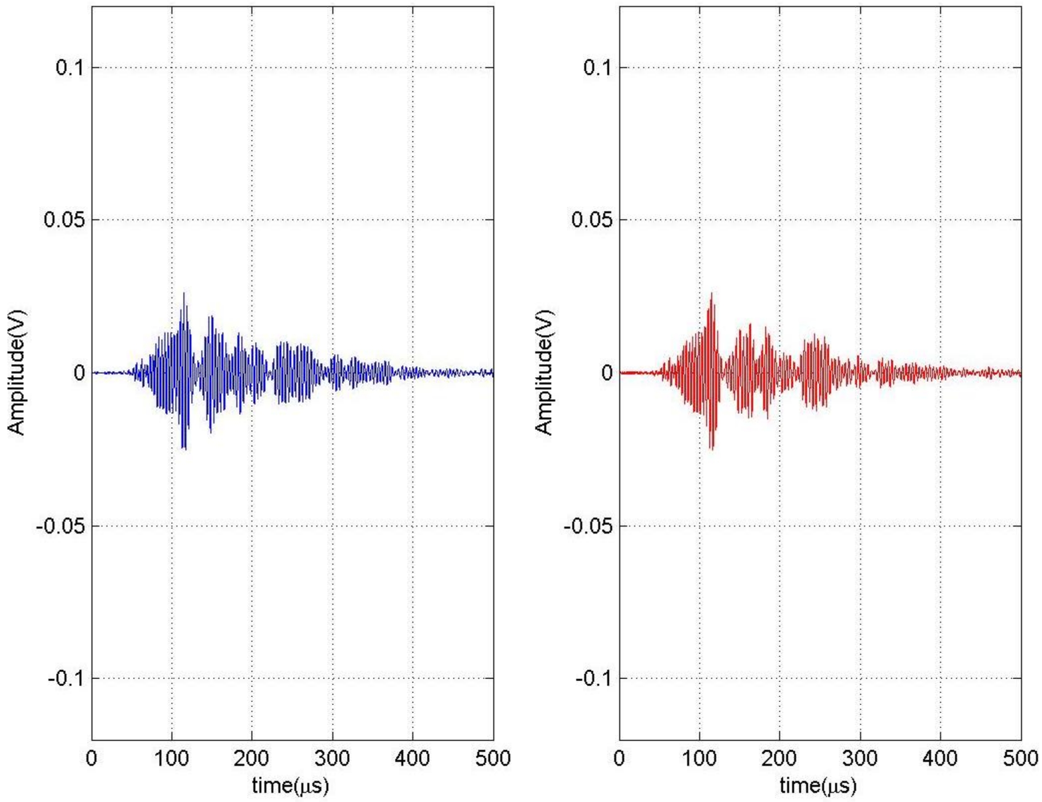

Figure 8.50. Transient guided wave signals for the test sample with only the first defect (left) and the sample with two defects (right). The loading frequency was 0.25MHz and phase delay was 160 degree.

Figure 8.51 shows the signals obtained in another loading case: frequency 0.21 MHz and phase delay 240 degrees. Three strong wave packages can be easily noticed in the signals. The wave package 1 arriving at about 100us in both figures was indentified as the wave directly travels from the actuator to the receiver. This wave package was not affected by the defect, which gives almost identical amplitude in both testing states. Wave package 2 and 3 were noted as reflected signals based on their arrival time and the distance between the transmitter and receiver. In guided wave reflection/scatter problem, mode conversion may occur when the waves hit a boundary or a defect. The reflected/scattered modes and their energy ratio depend on the boundary conditions or the geometry of the defect. Comparing the amplitude of wave package 2 and 3 in two figures of Figure 8.51, it can be seen that the energy of wave package 3 increased while the energy of wave package 2 decreased. This reflected the change of geometry of the boundary and thus gave the defect alarm. Obviously, the loading frequencies and phase delays can be quite critical in transient guided wave tests. The annular array actuator developed in this project for loading function tuning can be a very effective tool to always achieve good sensitivity for different defect types. For test objects with regular geometries, such as plates with uniform thicknesses, beams, or tubes, it is possible to first calculate the appropriate loading functions based on the wave mechanics theories that have also been developed in this project. For test objects with irregular geometries, it is necessary to perform loading function tuning to identify the appropriate ones for different defects.

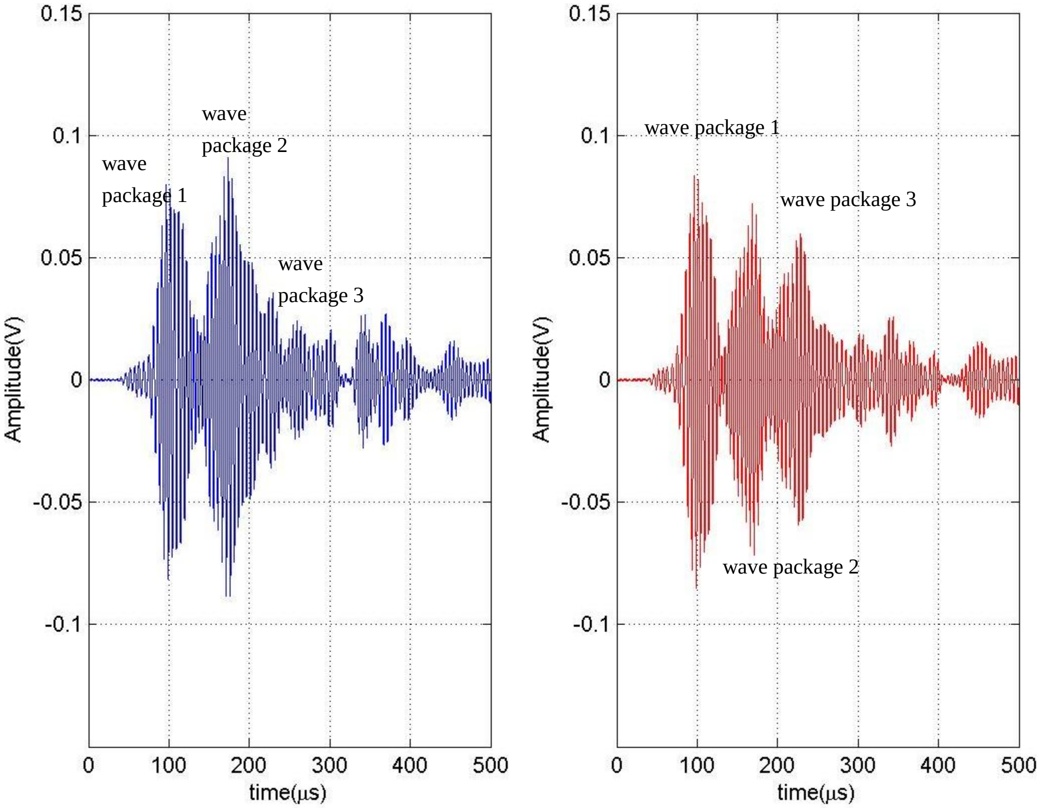

Figure 8.51. Transient guided wave signals for the test sample with only the first defect (left) and the test sample with 2 defects (right). The loading frequency was 0.21 MHz and phase delay was 240 degrees.

UMAT experiments were also conducted using the similar experimental setup as transient guided wave test. In order to study the effect of different loadings, the loading frequencies were swept from 0.2 MHz to 0.4 MHz with an increment of 1 kHz while phase delays were tuned from 0 degree to 360 degrees with a step of 15 degrees. To check the consistency of the experiment system, baseline data were taken twice with a one-day interval. A broadband sensor was used as the receiver. The amplitudes and phases obtained by the receiver under different loadings are recorded in Figure 8.52. As can be seen, both amplitudes and phases are identical in two baseline tests, which yielded very good consistency in our experiments. Moreover, the amplitude figure in Figure 8.52 showed that the receiver can get relatively strong signals when the loading frequency was between 0.295 MHz to 0.31 MHz while the phase delay was between 0 degree and 120 degrees. Another effective loading region was when frequency was between 0.327 MHz to 0.357 MHz while the phase delay was between 150 degrees to 285 degrees.

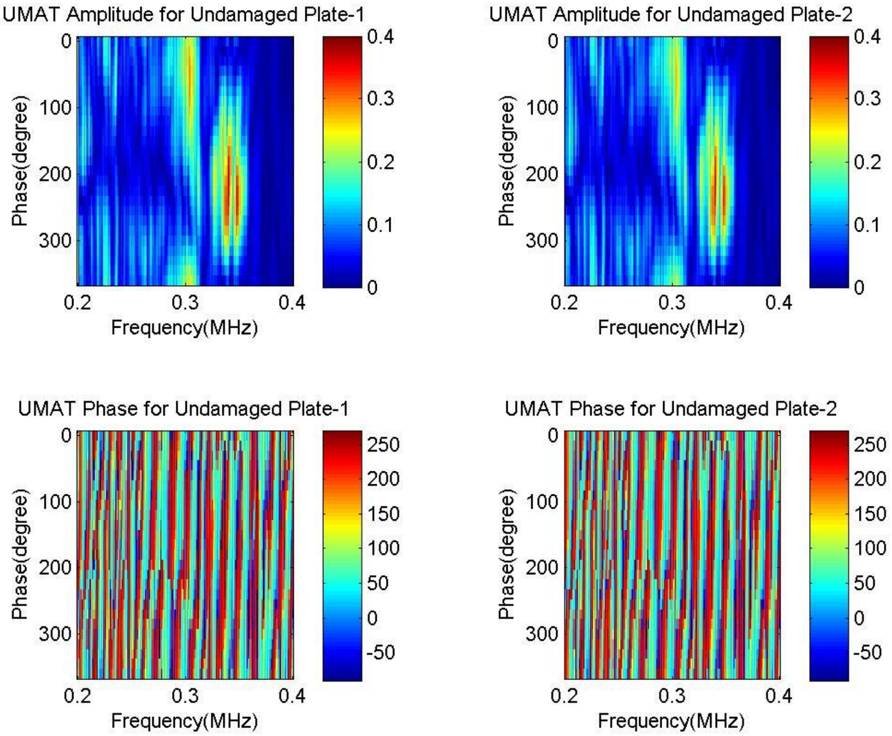
UMAT Amplitude for Undamaged Plate-1

UMAT Amplitude for Undamaged Plate-2

UMAT Phase for Undamaged Plate-1

UMAT Phase for Undamaged Plate-2

Figure 8.52. UMAT signals for two baseline tests: (a) UMAT amplitude for test 1; (b) UMAT amplitude for test 2; (c) UMAT phase for test 1; (d) UMAT phase for test 2.

Comparisons of the baseline and the test results for the new defect are given in Figure 8.53. Under those loading functions, the amplitudes of the UMAT signals varied after the defect was introduced. The average of the amplitude variation was about 24.81%. Note that the phases did not change a lot. This implied that a localized defect will not destroy the ODS tremendously under such loading functions. However, the variations of UMAT amplitudes provided an indication of the defect. The overall UMAT amplitude increased after the new defect was introduced. It is believed that such an amplitude increase was due to the fact that strain energy always intends to concentrate around structural discontinuities. Thus, a sensor closed to damaged region can detect such defects under appropriate loadings. By putting more sensors on the sample, it is feasible to detect and possibly locate a defect.

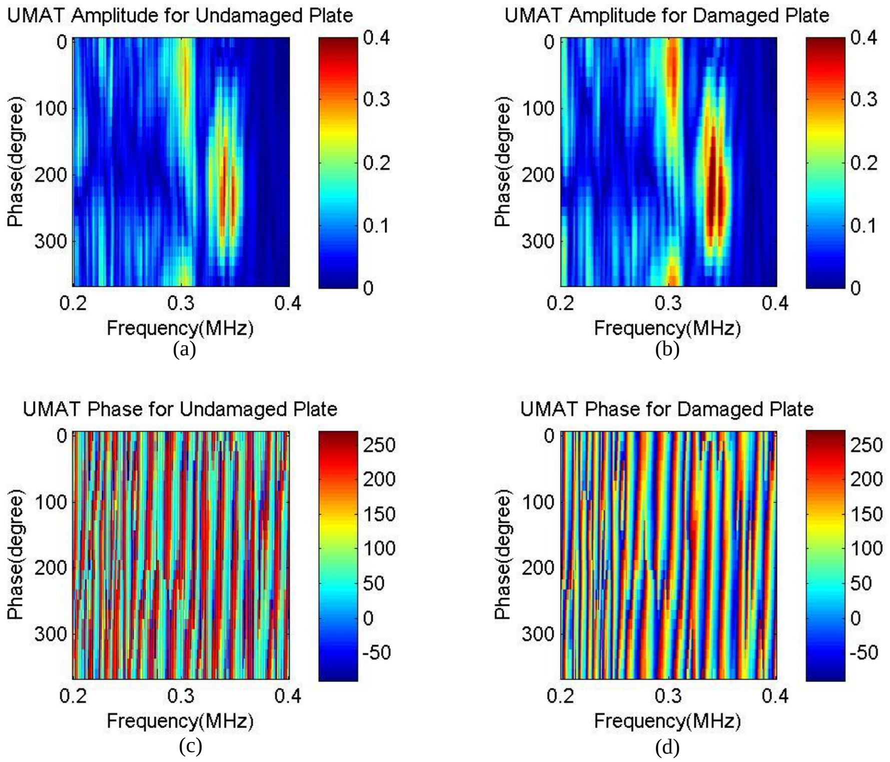

Figure 8.53. UMAT signals for two baseline tests: (a) UMAT baseline amplitudes; (b) UMAT amplitudes for the test sample with a new defect; (c) UMAT baseline; (d) UMAT phases for the test sample with a new defect.

9. Concluding remarks

A new concept of ultrasonic vibration for damage detection was developed. Theoretical foundation for ultrasonic vibration was laid through the developments of a guided wave mode decomposition method for investigating the connections between guided wave propagations and steady-state vibrations. It was demonstrated that, via selections of different guided wave loading functions, specific vibrations that are associated with the guided waves can be selectively excited to produce high sensitivity to specific types of damage. Annular array actuators were designed as a powerful tool for tuning guided wave loading functions. The actuators were designed based on the theories for guided wave excitations by annular arrays which were also developed in this project. A unique UMAT system was developed and demonstrated on various test samples. The UMAT technique developed in this project can serve as a good alternative damage detection method to traditional vibration measurements and transient guided wave techniques. The damage detection sensitivity of UMAT is superior compared to traditional vibration measurements. Compared to transient guided wave tests, UMAT provides better coverage and faster inspection speed for inspecting a large area and also requires much less accessible locations.

10. Key Personnel supported at Penn State University

Dr. Joseph L. Rose
Yue Liang
Cody Borigo

11. Key Publications

- ***Defect detection using a new ultrasonic guided wave modal analysis technique (UMAT)***
  Fei Yan and Joseph L. Rose, (2010), *Proc. SPIE*, Vol. 7650, 76500R.

- ***Ultrasonic Vibration Modal Analysis Technique (UMAT) for Defect Detection***
  J. L. Rose, F. Yan, C. Borigo, and Y. Liang
  Conference Proceedings of the Society for Experimental Mechanics Series, 2011, Volume 4, 25-32

- ***Ultrasonic vibration method for damage detection in composite aircraft components***
  J.R. Rose, F. Yan, Y. Liang, and C. Borigo
  Conference Proceedings of the Society for Experimental Mechanics Series
  Volume 31, 2012, pp 359-367

- ***Phased annular array transducers for ultrasonic guided wave applications***
  Fei Yan, Cody Borigo, Yue Liang, Jaya P. Koduru, and Joseph L. Rose
  Proc. SPIE 7984, 79840S (2011)

- ***Ultrasonic Guided Wave Vibration Formulation***
  Cody Borigo, Yue Liang, Fei Yan, and Joseph L. Rose
  REVIEW OF PROGRESS IN QUANTITATIVE NONDESTRUCTIVE EVALUATION: Volume 31, pp. 225-232

- ***A spacing compensation factor for the optimization of guided wave annular array transducers***
  Cody Borigo, Fei Yan, and Joseph Rose
  Submitted to the *Journal of the Acoustical Society of America,* under review

- ***Analytical separation and prediction of the inward- and outward-propagating guided waves from a phased annular array transducer***
  Cody Borigo, Fei Yan, and Joseph L. Rose
  Submitted to *Wave Motion*, under review

12. References

1. Fei Yan and Joseph L. Rose, “Defect detection using a new ultrasonic guided wave modal analysis technique (UMAT)”, (2010), *Proc. SPIE*, Vol. 7650, 76500R.
2. Rose, J.L. (2004), “Ultrasonic Guided Waves in Structural Health Monitoring,” *Key Engineering Materials* Vol. **270-273**, 14-21.
3. Fei Yan and J.L. Rose, Time delay comb transducers for aircraft inspection, *The Aeronautical Journal*, Vol. **113 (1144)**, 2009: 417-427.
4. Rose, J.L., (1999), *Ultrasonic Waves in Solid Media*, Cambridge University Press, New York, NY.
5. J. Li and J.L. Rose, “Implementing guided wave mode control by use of a phased transducer array,” *IEEE Trans. Ultrason., Ferroelect., Freq.*, Vol. 48, No. 3, pp. 761-768 (2001).
6. Yan, F., *Ultrasonic guided wave phased array for isotropic and anisotropic plates*, The Pennsylvania State Ph.D. Thesis, 2008.
7. H. Gao, M.J. Guers, J.L. Rose, G. (Xiaoliang) Zhao, and C. Kwan, “Ultrasonic guided wave annular array transducers for structural health monitoring,” *Review of Progress in Quantitative Nondestructive Evaluation*, Vol. 25, pp. 1680-1686 (2006).
8. P.D. Wilcox, “Omni-Directional Guided Wave Transducer Arrays for the Rapid Inspection of Large Areas of Plate Structures,” *IEEE Trans. Ultrason., Ferroelect., Freq.* **50(6)**, 699-709 (2003).
9. P. Wilcox *Modeling the excitation of Lamb and SH waves by point and line sources* Review of Quantitative Nondestructive Evaluation Vol. 23, pp. 206-213, American Institute of Physics, 2004.
10. K.I. Salas and C.E.S. Cesnik, “Guided wave excitation by a CLoVER transducer for structural health monitoring: theory and experiments,” *Smart Materials and Structures*, Vol. 18, 075005 (2009).
11. K.I. Salas and C.E.S. Cesnik, “Guided wave structural health monitoring using CLoVER transducers in composite materials,” *Smart Materials and Structures*, Vol. 19, 015014 (2010).
12. E.V. Glushkov, N.V. Glushkova, O.V. Kvasha, and R. Lammering, “Selective Lamb mode excitation by piezoelectric coaxial ring actuators,” Smart Materials and Structures, Vol. 19, 035018 (2010).
13. L. Meirovitch, *Principles and Techniques of Vibration*, Prentice Hall, Upper Saddle River NJ (2000), pp. 443-461.

14. R.D. Mindlin, "Waves and Vibrations in Isotropic, Elastic Plates", *Proc. of 1st Symposium on Naval Structural Mechanics,* Ed. J.N. Goodier and N.J. Hoff, Pergamon Press, Oxford (1960).

15. S. Srinivas, C.V. Rao, A.K. Rao, "An Exact Analysis for Vibration of Simply-Supported Homogeneous and Laminated Thick Rectangular Plates", *J. Sound Vib.,* vol. 12, no. 2, pp. 187-199 (1970)

16. D. Zhou, Y.K. Cheung, F. Au, and S.H. Lo, "Three-Dimensional Vibration Analysis of Thick Rectangular Plates using Chebyshev Polynomial and Ritz Method", *Int. J. Solids Structures,* vol. 39, pp. 6339-6353 (2002).

17. K.M. Liew, K.C. Hung, and M.K. Lim, "A Continuum Three-Dimensional Vibration Analysis of Thick Rectangular Plates", *Int. J. Solids Structures,* vol. 30, no. 24, pp. 3357-3379 (1993).

18. S. Ljunggren, "Forced Vibrations of Infinite Plates", *J. Sound Vib.,* vol. 121, no. 2, pp. 221-236 (1988).

19. I. Bartoli, A. Marzani, H. Matt, F.L. di Scalea, and E. Viola, "Modeling Wave Propagation in Damped Waveguides of Arbitrary Cross-Section", *J. Sound Vib.,* vol. 295, no. 3, pp. 685-707 (2006).

20. T. Hayashi, W.J. Song, J.L. Rose "Guided Wave Dispersion Curves for a Bar with an Arbitrary Cross-section, a Rod and Rail Example" *Ultrasonics,* vol. 41, pp. 175-183, Elsevier (2003).

21. L. Gavric, "Computation of Propagative Waves in Free Rail Using a Finite Element Technique", *J. Sound Vib.,* vol. 185, no. 3, pp. 531-543 (1995).

22. V. Damljanovic and R.L. Weaver, "Propagating and Evanescent Elastic Waves in Cylindrical Waveguides of Arbitrary Cross Section", *J. Acoust. Soc. Am.,* vol. 115, no. 4, pp. 1572-1581 (2004).